Massachusetts Institute of Technology

Woods Hole Oceanographic Institution
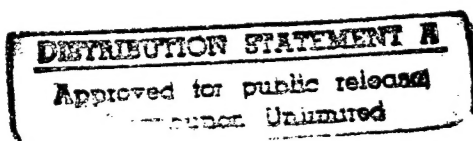
Joint Program
in Oceanography/
Applied Ocean
Science
and Engineering

DOCTORAL DISSERTATION

Baroclinic Vortices Over a Sloping Bottom

by

Joseph H. LaCasce, Jr.

September 1996

MIT/WHOI

97-03

Baroclinic Vortices Over a Sloping Bottom

by

Joseph H. LaCasce, Jr.

Massachusetts Institute of Technology
Cambridge, Massachusetts 02139

and

Woods Hole Oceanographic Institution
Woods Hole, Massachusetts 02543

September 1996

DOCTORAL DISSERTATION

Approved for publication; distribution unlimited.

Approved for Distribution:

Philip L. Richardson

Philip L. Richardson, Chair
Department of Physical Oceanography

Marcia K. McNutt

Marcia K. McNutt
MIT Director of Joint Program

John W. Farrington

John W. Farrington
WHOI Dean of Graduate Studies

BAROCLINIC VORTICES OVER A SLOPING BOTTOM

by

Joseph H. LaCasce, Jr.

A.B., Bowdoin College, 1986
M.S., Johns Hopkins University, 1988

Submitted in partial fulfillment of the
requirements for the degree of

Doctor of Philosophy

at the

MASSACHUSETTS INSTITUTE OF TECHNOLOGY

and the
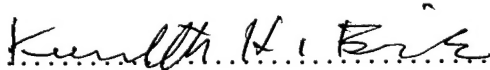
WOODS HOLE OCEANOGRAPHIC INSTITUTION

September 1996

The author hereby grants to MIT and to WHOI permission to reproduce
and to distribute copies of this thesis document in whole or in part.

Signature of Author . . . .
Joint Program in Physical Oceanography
Massachusetts Institute of Technology
Woods Hole Oceanographic Institution
August 23, 1996

Certified by . . . .
Dr. Kenneth H. Brink
Senior Scientist, W.H.O.I.
Thesis Supervisor

Accepted by . . . .
Professor Paola Malanotte-Rizzoli
Chairman, Joint Committee for Physical Oceanography
Massachusetts Institute of Technology
Woods Hole Oceanographic Institution

BAROCLINIC VORTICES OVER A SLOPING BOTTOM

by

Joseph H. LaCasce, Jr.

Abstract

Nonlinear quasigeostrophic flows in two layers over a topographic slope are considered. Scaling the lower layer potential vorticity equation yields two parameters which indicate the degree of nonlinearity in the lower layer. The first, $\frac{U_2}{\beta_2 L^2}$ (the strength of the deep flow divided by the product of the effective bottom slope and the squared length scale), is related to the advection of relative vorticity, and the second, $\frac{F_2 U_1}{\beta_2}$ (the product of the inverse square deformation radius of the lower layer and the strength of the surface flow divided by the effective slope), to the advection of vorticity due to interfacial stretching.

Two types of isolated vortex are used to examine the parameter dependence. An initially barotropic vortex remains barotropic only when $\frac{U_2}{\beta_2 L^2} \gg 1$; otherwise topographic waves are favored at depth, and the vortex separates into a surface vortex and waves. In the latter case, the surface vortex is weakened, consistent with a simple linear theory. An initially surface-trapped vortex which is larger than deformation scale is baroclinically unstable when $\frac{F_2 U_1}{\beta_2} > 1$. If $\frac{F_2 U_1}{\beta_2} < 1$, radiation of disturbances hinders or even blocks unstable growth, permitting the existence of large, stable surface vortices.

Both parameters are also relevant to cascading geostrophic turbulence over a slope. If $\frac{F_2 U_1}{\beta_2} > 1$, a "barotropic cascade" occurs at the deformation radius (Rhines, 1977) and the cascade is arrested at the scale at which $\frac{U_2}{\beta_2 L^2} = O|1|$. The resulting flow is dominated by large scale, anisotropic topographic waves. If $\frac{F_2 U_1}{\beta_2} < 1$, layer coupling is hindered and the cascade is arrested at the deformation scale. The flow then is dominated by isotropic surface vortices which continually "leak" energy to topographic waves at a rate proportional to Λ.

In both single vortex and turbulence cases, the distinction between vortices and waves is more transparent when viewing potential vorticity. It is more difficult to identify waves and vortices from the streamfunction fields, because the waves are present in both layers.

3

Thesis Supervisor: Kenneth H. Brink
Senior Scientist, Department of Physical Oceanography
Woods Hole Oceanographic Institution

Acknowledgements

I am grateful to Ken Brink for much good advice, patience and many interesting conversations. I am also indebted to committee members Dave Chapman, Glenn Flierl, Joe Pedlosky and Steve Lentz for numerous thought-provoking suggestions which greatly improved the work. Glenn's numerical model worked like a well-oiled machine, which freed up time for thinking about the dynamics. Paola Rizzoli was a delightful chairperson for the defense, and cheerfully agreed to sign a wicker blind when I told her that the Institution was out of archival bond.

Many people allowed me to moonlight on their computers for my calculations, which was tremendously beneficial to the work. Linda Meinke and Charmaine King were wonderful, and forgiving of exceeded quotas. Terry Joyce let me use the WOCE computer, which was much faster than my previous machines, and Jane Dunworth was always cheerful and helpful when there were problems. Higher resolution required even faster machines. Edmund Chang at MIT let me use his alpha to do some of the 256^2 grid point calculations, and Mike Spall lent his Silicon graphics machine for a blissful month while he was in Florida; many of the single vortex runs were calculated then. Audrey Rogerson has the same machine, and let me do many calculations, including the "strong slope run" which took 6 days. Audrey also introduced me to the numerical filter used in all of the runs in this thesis. Finally, Jamie Pringle kept me out of trouble by allowing me to store data on a disc he set up.

I have been fortunate to have many good and interesting friends while in the department who helped make my time here so enjoyable; in fact, I might have finished faster if I hadn't been so content here. When we arrived at the generals, there were two of us, and my only classmate, Young-gyu Park, has been a constant friend and great resource. Bruce Warren has also been a close friend with whom I've enjoyed many chats on topics ranging from the ACC to the best Boris Gudonov. I've had frequent talks with many students in the department which were often enlightening, and only once came down to a bet for beer. Barbara Gaffron always guided me when I was lost, and has also been a good friend.

In terms of distractions, I've spent much time (and even lived with) a group of close friends who were able to maintain what I considered to be a "healthy" lifestyle, despite work requirements. Even if the water wasn't actually "boiling" with bluefish, we always had a superb time waiting. Thanks also to the group of regulars who kept the Journal Club afloat and the discussions lively, even when the articles were, well, less so. The movie club (president, Birgit Klein) also suffered through several less inspired pieces, and had fun doing it. The soccer players (president, Debbie Smith) were always ready for a game, even when it looked like sleet was inevitable. And participating in the present incarnation of

the Woods Hole chamber music society has been great fun.

Finally, thanks to my two families. Cecilie Mauritzen is not only a dear wife, but she is a good and critical audience for ideas about oceanography. Johannes is a delight; he had lots to say about the thesis, though I couldn't understand most of it. Its been wonderful being so near my other family for the last few years as well: my parents and my two sisters. They have always been supportive and loving, for which I am very grateful.

Contents

Chapter 1

Introduction

The variation of the Coriolis parameter with latitude, the so-called β-effect, has a profound effect on oceanic flows. In particular, the variation produces a restoring force which opposes meridional motion and therefore supports Rossby waves. These waves are dispersive, and the phase speed is always westward. This westward orientation has been linked to the western intensification of the wind-forced currents in the ocean, i.e. the reason the Gulf Stream lies off the eastern coast of North America rather than the western coast of Europe. It is also known that larger scale motion "feels" the β-effect more than does small scale motion, a fact which makes the larger scales more wave-like but permits nonlinearity at smaller scales (Rhines, 1975).

In a barotropic fluid, topography acts in an analogous manner, i.e. it yields a restoring force which opposes cross-isobath motion. However, the orientation of this "topographic β-effect" can change, so that the "westward" propagation of the waves relative to the topography could in fact be in any direction. Secondly, the strength of the topography can vary, and in many cases can greatly exceed the planetary β. A stronger β favors linear motion at smaller and smaller scales, leading to an expectation of predominantly wave-like motion over steep slopes.

With the introduction of stratification, the problem changes considerably. In

particular, stratification can "shield" flow at the surface from the effects of the topography, perhaps negating its influence. Put another way, if a flow does not advect fluid across the topography, it cannot generate waves and therefore does not interact with the topography. This suggests that a steep slope no longer necessitates wave-like flow, because flow at the surface may be nonlinear. Unlike the planetary β-effect, the effect of topography in a stratified fluid varies in the vertical. This vertical asymmetry of the topographic β can yield interesting results.

As an example, consider a system in which the stratification is approximated by two immiscible layers. In the planetary β case, a meridional restoring force exists in both layers. One says that such motion induces changes in perturbation potential vorticity (PV) in both layers. Two types of Rossby wave are supported: one with parallel particle meridional displacements in each layer (the barotropic mode), and another with anti-parallel motion (the baroclinic mode). Any initial disturbance can be broken into these two types of waves.

In contrast, and as noted above, only motion across the slope in the lower layer is opposed by the topographic β (if one assumes the planetary gradient is zero); motion in any direction at the surface is unopposed, i.e. causes no change in PV. A result is that topographic waves have only one propagating mode. This mode actually has particle displacements in each layer which are parallel, but the amplitude of the surface displacements is always smaller than at depth, and more so for small-scale waves (which are bottom-trapped) (Rhines, 1970). An initial value problem on the topographic β plane thus has a very different outcome: a portion of the disturbance propagates away, but a portion may be left behind. This fact has profound effects in what follows.

A similar comparison is between a two-layer system in which Ekman damping acts in both layers and another in which it only acts at the bottom. In particular, consider the effects on a (baroclinically) unstable flow. In the symmetric damping

10

case, damping inhibits the growth of disturbances, i.e. it stabilizes the flow (Pedlosky, 1987). In the asymmetric case the dissipation actually *destabilizes* the flow, so that the small disturbances grow before eventually decaying, leaving the original flow altered (Pedlosky, 1983). Anticipating the latter result given only the outcome of the symmetrically damped case would be difficult.

There are numerous examples of strong surface flows adjacent to or over strong topography in the ocean. Rings which pinch off from the Gulf stream are known to migrate back towards the continental slope, and cross severe topographic features (Joyce, 1983; Cheney and Richardson, 1976). Likewise, the large Agulhas Eddies which migrate across the South Atlantic must pass over severe ridges, and are occasionally blocked there (van Ballegooyen et al., 1994). The California Current is an intense Eastern boundary current which lies adjacent to the continental slope and spawns eddies which may even move on to the shelf nearby (Largier et al., 1993). With the large number of unstable boundary currents in the ocean, interactions between intense eddies and strong topography are expected to be common.

The present work seeks to characterize the evolution of such eddies in the presence of stratification and bottom topography. In addition, I examine how flows which are familiar on the β-plane are altered on the topographic β-plane. Two specific cases are considered: a single vortex and a turbulent flow (multiple vortices). As explained below, there are numerous studies of both flows with the planetary β, but much less is known about how they evolve over topography.

The specific questions addressed are: 1) under what conditions do the symmetric and asymmetric β cases agree? 2) in cases in which they don't agree, how does one characterize the evolution and, in particular, the baroclinicity of the resulting flow? The more specific questions focus on whether an eddy can move across topography, perhaps from offshore into shallower water, or how cascading turbulence "arrests" over a slope.

11

1.1 Previous work

The single vortex over a slope has been studied previously primarily as a model for large oceanic rings. However, the barotropic case with β has been even more widely examined as a model for self-induced hurricane motion. A linear vortex of either sign drifts westward (Flierl 1977) and disperses rapidly, suggesting that meridional motion and the observed longevity of rings (of order several years, e.g. Cheney and Richardson, 1976) are likely the results of nonlinearity. McWilliams and Flierl (1979) found that a strongly nonlinear vortex decayed at a slower rate, and found a meridional component of translation velocity. The latter was first postulated by Rossby (1948) who noted that a vortex causes a deflection of the mean PV field and thus will tend to migrate meridionally to reduce this deflection. Adem (1956) showed by means of a Taylor expansion in time that a cyclonic vortex drifts initially to the northwest.

Subsequent work (e.g. Chan and Williams, 1987; Fiorini and Elsberry, 1991; Resnik and Dewar, 1995) has sought to explain the self-induced motion in the strongly nonlinear limit, and to predict the initial velocity. The mechanism (now widely accepted) is related to the development of asymmetries in the vortex shape; as fluid on the sides of the vortex is advected meridionally, it acquires relative vorticity. A negative vorticity anomaly develops to the east of a cyclone, and a symmetric positive anomaly to its west, making the positive vortex appear stretched to the west and compressed to the east. The (dipolar) anomaly field can advect the primary vortex and the whole system will translate; by the signs of the anomalies, one deduces that a cyclone moves northward, and an anti-cyclone southward. Rossby waves are generally found in the wake, indicating decay and dispersal of the eddy.

Warren (1967) was apparently the first to note that similar self-induced motion could occur over topography. In agreement with this, Carnevale et al. (1991)

found that a cyclonic vortex moves to the local "northwest", or towards shallower water and to the left (facing shallower water), over a variety of sloping bottoms in the laboratory. Others have then sought to understand the specific influence of the continental slope on barotropic rings. Wang (1992) considered such a case with a hierarchy of models, and Grimshaw et al. (1994) approached the problem with the shallow water equations.

Others have considered stratified vortices on a β-plane, often with either an infinitely deep lower layer or a flat bottom, e.g. McWilliams and Flierl (1979), Mied and Lindemann (1979) and McWilliams and Gent (1986). All find a north-westward/southwestward drift for cyclones/anti-cyclones. However, the addition of baroclinicity can alter the dynamics. The elimination of the barotropic mode (in the deep lower layer or the one and a half layer case) appears to significantly reduce the speed of translation. In the flat bottom case, the vortex may evolve to a baroclinic dipole (e.g. Flierl et al., 1980) with an eastward velocity, though this typically occurred with an initial vortex with no barotropic component. For the more general initial vortex with some barotropic flow, the evolution closely resembled that of the one layer experiments.

Previous baroclinic eddy studies over topography fall into two categories. In the first, the eddy is bottom-trapped on a slope beneath an infinitely deep upper layer, often as a blob of dense fluid. The theoretical studies of Nof (1983) and Killworth (1984) are examples, as are the laboratory studies of Mory et al. (1987) and Whitehead et al. (1990). Nof (1983) argued that the (cyclonic) vortex would drift westward under the influence of gravity and predicted a velocity consistent with that observed in Whitehead et al. (1990). Interestingly, Mory et al. (1987) found a northwestward drift with their cyclonic vortex, much more like the Carnevale et al. (1991) vortex (see Chapter 3 for more discussion of the discrepancy.)

In the second category, the eddy is usually surface-intensified. Smith and

O'Brien (1983), following on initial numerical work by Haustein (1981), studied a two-layer ring impacting a strong linear slope using a primitive equation model. They suggested that the effects of the planetary and topographic β effects would be additive (as one might expect in a barotropic fluid). They found that a vortex with zero initial deep flow was not affected by the slope. In a similar vein, Kamenkovich et al. (1995), in a two layer, primitive equation study, noted the degree of interaction between a steep ridge and an Agulhas eddy depended on how barotropic the vortex was, but that the vortex became "compensated" (zero deep flow) after hitting the ridge. Strongly barotropic vortices could stall over the ridge, as they are sometimes observed to do in the South Atlantic.

In relation to the continental shelf, the important question is whether offshore eddies can influence currents over the continental slope and shelf. Washburn et al. (1993) examined an anticyclone that essentially hovered over the Northern California shelf for two months, transporting suspended sediment offshore. Largier et al. (1993) found that a significant portion of the current variability there was due to offshore eddies. In terms of modelling, Chapman and Brink (1987) found in the linear case that offshore forcing of shelf currents was greatest when coastal trapped waves were excited. Qiu (1990) found that the addition of planetary β allowed for surface wave motion which in turn could induce surface variability over the shelf.

A closely related area of study has focussed on intense topographic waves over the Continental slope, e.g. the slope off the east coast of the U.S. (Thompson and Luyten, 1976). Hogg (1981), Welsh et al. (1991) and Pickart (1995) have found evidence linking the waves with Gulf Stream meanders. Louis and Smith (1982), Shaw and Divakar (1987) and others have suggested that the waves may be generated by rings impacting the slope. A detailed review is given in Smith (1983).

Thus significant work has been done on single eddies over topography, both

in the linear and nonlinear limits. Fewer results exist for more complicated nonlinear flows over topography. However, there is a large body of literature on two dimensional or "geostrophic" turbulence, both with and without a β effect.

In contrast to three dimensional turbulence in which energy is transferred to small scales where it is dissipated by viscous processes, energy in two-dimensions is transferred to large scales. The possibility of such an inverse cascade of energy was apparently first postulated by Onsager (1949) and Fjortoft (1953). Simultaneous with the energy cascade is a forward cascade (towards small scales) of enstrophy (squared vorticity), which is also dissipated by viscous action. Spectral aspects of both cascades (in particular the details of the cascading inertial subranges for enstrophy and energy) were postulated by Kraichnan (1967, 1971) and Batchelor (1969). Recent work on the subject has focussed on the effects of intermittency, in the form of coherent vortices; Basdevant et al. (1981) showed that intermittency led to a steepening of spectra in the enstrophy inertial range, McWilliams (1984, 1990) demonstrated that coherent vortices dominate the dynamics of freely evolving turbulence at later lates and Babiano et al. (1987) illustrated the importance of vortices in forced-dissipative turbulence.

Related research has focussed on how various imposed effects could alter the barotropic cascade. Rhines (1975) found that the β-effect led to an arrest of the inverse cascade, at a scale at which Rossby wave processes dominate advective processes, as waves are much less efficient at transferring energy. His numerical simulations moreover suggested the formation of zonally-oriented jets. Holloway (1978) and Herring (1977) found that small-scale bottom bumps could cause a flux of energy toward the scale of the topography, via nonlinear (triad) interactions. They also found a stationary, topographically-locked component of the flow, predicted as a state of "minimum enstrophy" (Bretherton and Haidvogel, 1976) or maximum entropy (Holloway, 1978). Shepherd (1987) found that the presence of a large scale zonal jet (as in the atmosphere) affected the arrest of

energy both by altering the effective β and by direct shearing of the vorticity field by the jet.

The other significant complication which has been explored is stratification. Charney (1971) showed that under the quasigeostrophic approximation and the assumption of homogeneity, the conservation of potential vorticity guaranteed an inverse cascade to larger horizontal *and* vertical scales. He also suggested that enstrophy in such a case be replaced by potential enstrophy, or squared potential vorticity, but that otherwise the 2-D formalism carried over. Rhines (1977) suggested, along similar lines, that small-scale baroclinic energy in a two-layer flow would undergo a "barotropic cascade" upon reaching the deformation radius. Thereafter, the cascade to larger scales was essentially as in the one layer case. Noting that wind forcing of the ocean is generally baroclinic and at large scales, Salmon (1980) showed that the initial baroclinic cascade of energy was actually forward, but that the late evolution corresponded to that of Rhines (1977). From the vortex point of view, McWilliams (1990b) has suggested that the barotropic cascade occurs as coherent vortices at different depths *align* (e.g. Polvani, 1994) to make barotropic vortices.

The problem of stratified turbulence over topography can be seen as a combination of two lines of study, i.e. stratified turbulence and topographic effects. Consistent with this, most previous work on the subject has focussed on the effect of *bumps* on stratified flows, either in layered systems or continuously stratified representations with truncated vertical modes. Rhines (1977) found that bottom bumps inhibited the barotropic cascade of baroclinic energy; however, he also found that the degree of barotropy depended on the initial vertical structure of the flow. Treguier and Hua (1987) found barotropy was achieved when the turbulence was forced at the surface, but that the bumps yield smaller horizontal scales than would be found over a flat bottom. Treguier and McWilliams (1990) also observed barotropic small scales, and suggested a link to the stationary topo-

graphic mode discussed by Herring (1977). Vallis and Maltrud (1994) considered other types of topography, and found jet formation to occur over a ridge, as well as the development of a temporal mean "westward" component of the flow. The latter they linked to the stationary topographic mode, and the former to the jets observed on the β-plane by Rhines (1975).

1.2 Thesis approach

The examples considered hereafter are quite similar to the stratified topographic cases above: I examine a two-layer single vortex over a slope, as did Smith and O'Brien (1983) and Kamenkovich et al. (1995), and two-layer turbulence over a slope like Vallis and Maltrud (1994). But while the examples are similar, the approach is somewhat different. In particular, I restrict attention to the f-plane over a slope so that the only waves present are topographic waves. This permits a clearer picture of evolution by allowing for a separation into waves and "vortices", in most cases, and also aids the comparison to the purely barotropic case. Moreover, I will employ a quasigeostrophic model, rather than the primitive equations.

The specific approach is to examine numerical initial-value problems in two-layer flows, with an idealized slope (a linear gradient). Under quasigeostrophy the flow is assumed to be geostrophic at lowest order (Pedlosky, 1987); specific restrictions are discussed in the model section, Chapter 2. Quasigeostrophy is adopted essentially for practical reasons: the simplified calculations permit a more thorough examination of parameter space than would a primitive equation study. The two-layer approximation similarly shortens computations, but also the simpler vertical structure is easier to interpret. One nevertheless finds considerable complexity, even with this simplified system.

In addition to the general object of characterizing the differences obtained by

introducing baroclincity to the problem, there are also several additional specific goals. As the single vortex case has relevance to the motion of oceanic rings, the self-induced translation of the vortex over the slope with varying stratification and slope is quantified. The baroclinic stability of the vortex is also of great importance, for ocean rings and for interpreting the results of the more general, turbulent case. In the latter case, the arrest of the inverse cascade is sought under varying stratification and steepness of the slope.

The equations and model used for the numerical runs are described in Chapter 2. Scalings of the two-layer equations are discussed, as are particulars about the numerical implementation. Chapter 3 reviews the case of an isolated single vortex on the β-plane, then discusses the fate of an initially barotropic vortex and a surface vortex over the slope. An appendix (A) is included which discuss the related case of a non-isolated vortex. In Chapter 4, turbulence over a slope discussed, with comparisons to the better known two-layer case with a flat bottom, as well as to the case with an infinitely deep lower layer. An appendix (B) follows which presents results from a another asymmetric case, one with only a bottom Ekman layer (no bottom slope). Chapter 5 concludes the work, and discusses the results in light of previous findings, as well as highlights specific shortcomings.

Chapter 2

Model

The equations which were used are presented below and several nondimensional parameters are found by scaling these equations. The spectral model used for the calculations is also explained, with some discussion of resolution issues and of the damping ("sponging") of waves. Unlike many contemporary numerical studies, a numerical filter is used rather than so-called "hyperviscosity", and the benefits (and drawbacks) of the filter are discussed in the final section.

2.1 Equations

The model is one of the simplest which incorporates advection, stratification and topography: a two-layer, quasigeostrophic model with a linearly sloping bottom. The quasigeostrophic (QG) limit implies a small Rossby number, small interface displacements and weak topographic slopes (Pedlosky, 1987) and thus is not strictly valid for oceanic regions with fronts and/or large bottom slopes. This will be discussed more below.

The relative simplicity of quasigeostrophy makes analytical solutions more tractable, and permits higher horizontal resolution in numerical experiments, compared to comparable primitive equation models. Higher resolution allows for

a reduction of lateral damping effects and is thus desirable in simulations of inviscid fluids. An additional numerical benefit of QG is that the vorticity equations are advanced in time rather than the momentum equations. This in turn allows the inclusion of a mean PV gradient, such as due to the β effect or a slope, in a periodic domain, i.e. one without lateral boundaries and boundary layers. In the case of homogeneous turbulence, this is a considerable simplification.

The inviscid, dimensional equations for the layer potential vorticities in the case of topography which only varies in the y direction are (e.g. Pedlosky 1987):

$$\frac{\partial}{\partial t} q_1 + J(\psi_1, q_1) = 0 \tag{2.1}$$

$$\frac{\partial}{\partial t} q_2 + J(\psi_2, q_2) + \beta_2 \frac{\partial}{\partial x} \psi_2 = 0 \tag{2.2}$$

with $q_i \equiv \nabla^2 \psi_i + F_i(\psi_{3-i} - \psi_i)$ the "perturbation potential vorticity" and ψ_i the streamfunction for layers i=1,2 with ∇^2 the horizontal (two dimensional) Laplacian operator. The (squared) inverse of the deformation radius in each layer is $F_i = \frac{f^2}{g' H_i}$ with $g' = \frac{\rho_2 - \rho_1}{\rho_0} g$ the reduced gravity (ρ_i is the density in layer i, ρ_0 a reference density, and g the acceleration due to gravity), f the Coriolis parameter, and H_i the depth of the layer. The Jacobian is defined as $J(a, b) \equiv \left(\frac{\partial a}{\partial x} \frac{\partial b}{\partial y} - \frac{\partial b}{\partial x} \frac{\partial a}{\partial y} \right)$. Here q_1 is conserved on fluid parcels, but q_2 is not, but changes as the parcels move across isobaths. Rather the "total potential vorticity" in layer two $(q_2 + \beta_2 y)$ is conserved on parcels.

One can define $F_2 \equiv \delta F_1$ where $\delta \equiv \frac{H_1}{H_2}$ is the ratio of layer depths. In the ocean, δ might be the ratio of the depth of water above the thermocline to that below, and, if so, has a typical value of about 0.2. The ratio is generally assumed

to be unity in the numerical runs for simplicity, but I will retain unequal layer depths in the expressions discussed hereafter for generality.

The slope is taken to be linear and shallowing in y, so that $\beta_2 \equiv -\frac{f(\partial_y H_2)}{H_2}$. Note that on the f-plane, there is no loss of generality in orienting the slope in this direction. The expression for β_2 can be found in a manner analagous to the one layer case, where the full PV is given by:

$$q = \frac{\epsilon \nabla^2 \psi + f}{h} \qquad (2.3)$$

where $\epsilon = \frac{U}{fL}$ is the Rossby number, assumed small. If $h = h - \frac{\partial h}{\partial y}y$ and $\frac{\partial h}{\partial y}\frac{L}{h} = O|\epsilon|$ (L being the horizontal scale of motion), the PV can be rewritten:

$$q \approx \frac{1}{h}(\epsilon \nabla^2 \psi + f - \frac{f\frac{\partial h}{\partial y}}{h}y). \qquad (2.4)$$

The definition of β_2 given above then follows. Note that the expansion is carried out in the lower layer in the two layer case, so that h is replaced by H_2. The PV gradient in layer two resembles the traditional β-effect and so is called the "topographic β" (Faller and VonArx, 1955). The small slope requirement is that the variation in depth is no greater than $\frac{\epsilon H_2}{L}$; assuming a Rossby number of order .1, a lower layer depth of 1 km and a scale of motion of 10 km yields a maximum grade of about 1%, a not unreasonably small number. However, QG is often avoided precisely for this limitation. Results presented later on will show that the *effects* of the slope can be large, even within QG.

In previous studies, both planetary and topographic gradients were included (Smith and O'Brien, 1983; Kamenkovich et al.,1995). Wang (1992) contrasted results obtained on the barotropic f-plane with those found on the β-plane with

topography. The planetary β is nevertheless neglected here because its inclusion obscures the interaction with the topography. Expected modifications due to the planetary β-effect are discussed in Chapter 5.

2.2 Scalings

The equations are scaled assuming motion with velocity scales U_1 and U_2 and a length scale L, and time scales T_1 and T_2 (subscript denoting layer). In the upper layer, an advective time scale is appropriate since the surface PV at a given location can only change under the influence of advection. Thus in layer one, $T_1 \propto \frac{L}{U_1}$. In the lower layer, cross-slope motion also leads to temporal changes in PV, so one may choose an advective time scale or a time scale proportional to the period of the bottom waves. Many of the cases of interest below have little or no bottom flow, so the second choice is more desirable, i.e. $T_2 \propto \frac{1}{\beta_2 L}$. Hence there are possibly *different* time scales in each layer. The difference is due to the vertical asymmetry of the PV gradient, and will be found to have profound effects.

Scaling the potential vorticities in each layer, one finds that the measure of the relative importance of stretching and relative vorticity is determined by:

$$ F_1 L^2 \quad , \quad F_2 L^2 \,. \tag{2.5} $$

These terms are the squared ratio of the scale of motion to the internal radius of deformation in each layer. As mentioned, in most of the numerical examples the layer depths are equal, and so there is only one parameter. In the flat-bottom case, the size of the parameters generally indicates the degree of layer coupling.

Scaling the bottom PV equation, (2.2), yields two parameters:

22

$$\frac{U_2}{\beta_2 L^2} \tag{2.6}$$

and

$$\frac{F_2 U_1}{\beta_2} = \frac{\delta F_1 U_1}{\beta_2} = \frac{f U_1}{g'(\partial_y H_2)} . \tag{2.7}$$

The first parameter is the ratio of PV changes due to the advection of relative vorticity and waves. Equivalently, it compares the deep advective time scale to the topographic wave phase speed, or the ratio of particle to wave speeds. It is the slope analog of the barotropic parameter, $\frac{U}{\beta L^2}$ discussed by, among others, Rhines (1975). In the barotropic case, the size of the parameter indicates the relative importance of advection and waves to changes in the Eulerian PV. Alternately, it indicates how "strong" the planetary restoring force is for given particle velocities. Similarly, the slope parameter indicates the effective severity of the slope. Note that it depends not only on the slope but the size and strength of the motion, i.e. a larger/weaker vortex "sees" a larger slope than a smaller/stronger vortex.

The second parameter is the ratio of PV changes due to the advection of thickness and waves. The ratio of the first parameter in (2.6) and that in (2.7) is $\frac{U_2}{U_1} \frac{1}{F_2 L^2}$, and is small when there are large scales of motion and/or when the deep flow is weak. The thickness parameter is found to be central to baroclinic instability, and thus important in both single and multiple vortex cases.

If both advective parameters are small, the contours of total PV in the lower layer are "open" since they are dominated by the slope contribution. As seen in Chapters 3, the degree of openness of the PV contours in the barotropic, β-plane case indicates how linear the evolution is. Likewise, when the contours are open in the two-layer case, one finds the deep evolution to be more wavelike, and the surface flow to be more baroclinically stable.

2.3 Numerical method

The PV equations in (2.1-2.2) were stepped forward in time with a Fortran code written by Glenn Flierl. Equations (2.1-2.2)were solved spectrally on a doubly-periodic domain (e.g. Canuto et al., 1988), so that all variables are Fourier decomposed in both directions:

$$(\hat{q}_i, \hat{u}_i) = \frac{1}{N_x N_y} \sum_k \sum_l (q_i, u_i) \, exp(ikx + ily) \qquad (2.8)$$

where N_x and N_y are the number of grid points (real space). As such, the model has no boundaries, so the region of ocean represented is far from coasts. Moreover, the double periodicity implies that energy which exits one side of the domain enters the opposite side, so waves generated in the domain can re-enter and interact with the original flow. This aspect is perhaps the largest drawback of the model, and is discussed below. The length scale is chosen so that the domain dimensions are 2π by 2π, a common choice which results in integral wavenumbers in spectral space. Variables are alternately referred to by their Fourier and real representations, so the hat distinguishes the Fourier transform (as in (2.8)).

The single vortex runs required fewer grid points than the turbulence runs, as the latter often had of order one hundred vortices. In most cases with the single vortex, using 64^2 and 128^2 grid points (with maximum wavenumbers 32 and 64) yielded quantitatively similar and qualitatively identical results. The model runs were rapid with 64^2, so that resolution was used most often. In one region of parameter space however, the vortex broke up into smaller vortices, and 128^2 points were required. Of course, the required resolution depends on the choice of initial conditions because a smaller initial vortex requires more grid points. But

24

the vortex used here filled a large portion of the domain, so that there were of order 20 grid points across the diameter of the vortex with 64^2 points.

The turbulence cases on the other hand required greater resolution. The amount required depended on the initial conditions, but it was desirable to have initial flow with relatively small scales (to yield a larger population of vortices— see for example Santangelo et al., 1989) so more grid points were required. Therefore, the primary runs were made with 256^2 grid points. Though this is modest resolution in comparison to recent barotropic calculations (1024^2 in Santangelo et al., 1989), higher resolution was not feasible given the computer resources available, and the fact that fast waves required a small time step. Many additional runs were made with 128^2 points and the qualitative aspects were generally reproduced. Additional details on resolution are presented in Chapter 4.

The model was advanced in time with a standard leap-frog scheme, with an Euler step applied periodically to stabilize the computational mode (e.g. McWilliams, 1990). More sophisticated routines might be required for more quantitative representations of observed flows, but this technique was judged sufficient for the results sought here.

Spectral dealiasing, a technique which removes contributions to the Jacobian from unresolved wavenumbers (Patterson and Orszag, 1971), was also employed. However, the results were nearly identical with and without dealiasing, so long as the resolution was fine enough. The single vortex runs were negligibly altered by de-aliassing (differences in the calculated position of the center of the vortex for a typical set of parameters were in the fourth decimal place), but turbulence runs with 128^2 grid points benefited somewhat (dissipation was decreased by a few percent). The higher resolution turbulence runs were not significantly improved. As dealiassing lengthened the computational time by roughly 50%, it was not used.

2.4 Sponge

As mentioned, a drawback of double periodicity is that waves may exit one side of the domain and re-enter the other side, leading to multiple interactions with the primary flows (vortices). Often the interaction was weak enough to ignore, but in some cases the primary flow was severely distorted by the waves. In the single vortex cases, the problem was remedied with a "sponge" layer, of the following form:

$$sponge = .5 + .25 * (\tanh((x - .3)/10) + \tanh((2\pi - x + .3)/10)) \qquad (2.9)$$

This function, which is basically unity over most of the domain but decays to .5 in a boundary layer of half-width .3 at the left and right edges of the domain, multiplied the perturbation potential vorticity in the lower layer (for reasons discussed below) at each time step. The sponge only decays to .5 because the vortex was found to excite domain-scale normal modes with more severe filters. The sponge was more successful with smaller scale waves, which had a strong signature in vorticity, than with larger scale waves. In most cases, the sponge sufficiently weakened the re-entrant waves, but in one case more drastic measures were required, as discussed in Chapter 3.

A sponge was not used with the turbulence runs. By removing vorticity at the edges of the domain, the sponge catalyzed the rapid formation of zonal jets, i.e. structures with no zonal gradient of vorticity. As mentioned in Chapter 4, using a bottom Ekman layer is one way to damp the waves, but the Ekman layer itself changes the stability properties of the surface flow (Pedlosky, 1983). Therefore, the base runs were made with no Ekman damping. However, additional runs

were made in which layer decoupling was accomplished solely by a bottom Ekman layer, for comparison. The details are given in Appendix B.

2.5   Damping

When the inviscid potential vorticity equations (2.1-2.2) are advanced in time, numerical instability often results as energy accumulates at the smallest scales. This is usually avoided by including a diffusion term on the right hand side of the equations, as a model for unresolved small scale dissipative processes. Common forms are a Laplacian diffusion, $\nu_2 \nabla^2 q_i$, or a "bi-harmonic" diffusion, $\nu_4 \nabla^4 q_i$ (e.g. McWilliams 1984), although higher order schemes are often used. Generally ν_j is adjusted to minimize viscous damping of the flow and, with sufficient numerical resolution, the effects on the larger scale dynamics usually are generally small. However, there are negative aspects. Diffusion causes decay, albeit slow, of energy at even the largest scales. It also acts to smooth sharp gradients in vorticity, such as those that appear under the action of strong straining. The effects are sometimes undesirable, as discussed below.

An alternate means of achieving numerical stability is by the use of a low-pass wavenumber cut-off filter, widely used in spectral simulations of compressible flow (see Canuto et al., 1988) wherein the streamfunction is periodically multiplied by a specified function. A low-pass filter generally tends to unity at small wavenumbers and zero at large wavenumbers, and the transition at intermediate wavenumbers, as well as the frequency of application, determine the strength of the filter. A broader filter smooths and weakens discontinuities, whereas filters which only remove the very smallest scales may suffer Gibbs-like oscillations in the vicinity of a discontinuity in the flow, such as a strong front or shock. Different filters are desirable for different flows, and in the absence of analytical solutions, a filter is generally chosen by trial and error.

The effect of filtering is similar to that of the diffusion operators; both lead to a reduction of energy at small scales. In fact, the action of the commonly used "raised cosine" filter is formally equivalent to Laplacian damping when converted to finite differencing (Canuto et al., 1988). Filters which are less invasive at lower wavenumbers are analagous to higher-order diffusion schemes. The advantage of the filter is that the there will be a range of wavenumbers, chosen *a priori*, which will be formally undamped. This can lead to qualitative improvements in the numerical representation at a given resolution.

The filter employed here is the exponential cut-off filter:

$$filtr(i,j) = \begin{cases} \exp(-18.4((x_\phi^2 + y_\phi^2)^{\frac{1}{2}} - c_\phi)^4) & \text{if } (x_\phi^2 + y_\phi^2)^{\frac{1}{2}} > c_\phi \\ 1.0 & \text{if } (x_\phi^2 + y_\phi^2)^{\frac{1}{2}} \preceq c_\phi \end{cases}$$

where $(x_\phi, y_\phi) \equiv (k\triangle x, l\triangle y)$ with (k, l) the horizontal wavenumbers in spectral space and $(\triangle x, \triangle y)$ the grid spacings. The exponent, 4, is chosen to yield a filter which decays over a wide enough range of wavenumbers and the factor of -18.4 $(\ln(10^{-8}))$, is determined by the machine accuracy, which was single precision for these runs. The cut-off wavenumber, c_ϕ, is chosen so that the filter is zero to machine accuracy at the maximum wavenumber of the grid. Setting $c_\phi = .65\kappa_{max}$ with $64^2/128^2/256^2$ grid points results in damping of the wavenumbers above 21/42/83, with those above 27/53/106 decreased by more than 50 percent (recall the maximum wavenumbers are 32/64/128). Wavenumbers below 21/42/83 are multiplied by one, and thus undamped.

The principal difference between using a numerical filter and a low-order diffusion operator is a non-zero decay of the middle wavenumbers under diffusion. The effects of this selective decay can be illustrated as follows. A typical simulation with 128^2 grid points and biharmonic diffusion (∇^4) requires $\nu_4 \cong 2.3 \times 10^{-6}$

for numerical stability. With this value, the e-folding time scale for wavenumber 10 is roughly 29 time units. In figure (2.1), two Gaussian "vortex" profiles are shown with their corresponding profiles reconstructed from a Fourier series truncated at wavenumber 10. The upper profile has $\zeta = 5.25 \ e^{-(\frac{x}{0.3})^2}$ and the lower has $\zeta = 21 \ e^{-(\frac{x}{0.16})^2}$, where ζ is the relative vorticity. The reconstructed profiles are indicated by dashed lines.

The severe truncation has little impact on the broader vortex, but the narrower profile is altered by the loss of the higher wavenumbers. In particular, one finds that the truncation has 1) weakened the vorticity maximum and 2) introduced Gibbs oscillations on the wings of the vortex. In plan view, the latter would appear as rings of oppositely-signed vorticity around the vortex.

The diffusive effects in an actual run may be less dramatic since different wavenumbers decay at different rates, nevertheless both the side lobes and the decrease in the maximum often appear in the calculations with hyperviscosity. An example is shown in figure (2.2) in which a barotropic dipolar vortex ("modon") is translating to the east from its initial position at the center of the domain. The individual vortices have a Gaussian profile identical to the lower profile in figure (2.1). The modon motion was calculated with three types of damping, the traditional Laplacian damping $(\nu_2 \nabla^2 \zeta)$, hyperviscous damping $(\nu_8 \nabla^8 \zeta)$ and with the numerical filter shown in (2.5). The viscosities used were representative of the values usually chosen to insure numerical stability in turbulence calculations, specifically $\nu_2 = 9.82 \times 10^{-4}$ and $\nu_8 = 1.37 \times 10^{-11}$. At left are contours of vorticity at $t = 0$ and $t = 15$ for the respective cases, and at right are meridional profiles of the modons at the later time. All calculations used 128^2 grid points.

The position of the vortices is nearly identical in all three cases, suggesting that the gross dynamics are not affected by the choice of damping. However, the decay of the vortex amplitudes is evident in the hyperviscous case, and drastic in the Laplacian damping case. In fact the amplitude has been decreased by 72%
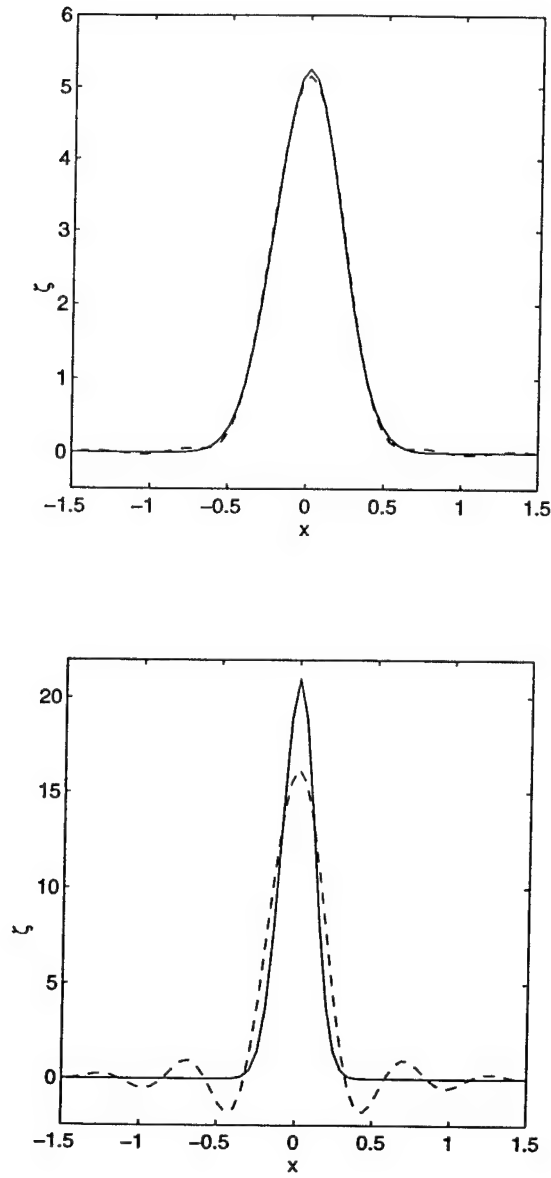
Figure 2.1: A Gaussian profile (solid line) with the same profile reconstructed from a Fourier series truncated at wavenumber 10 (dashed line). The upper profile has $\zeta = 5.25 \exp -(\frac{x}{0.3})^2$ and the lower has $\zeta = 21 \exp -(\frac{x}{0.15})^2$. A decrease in amplitude and Gibbs effects are evident in the lower case.
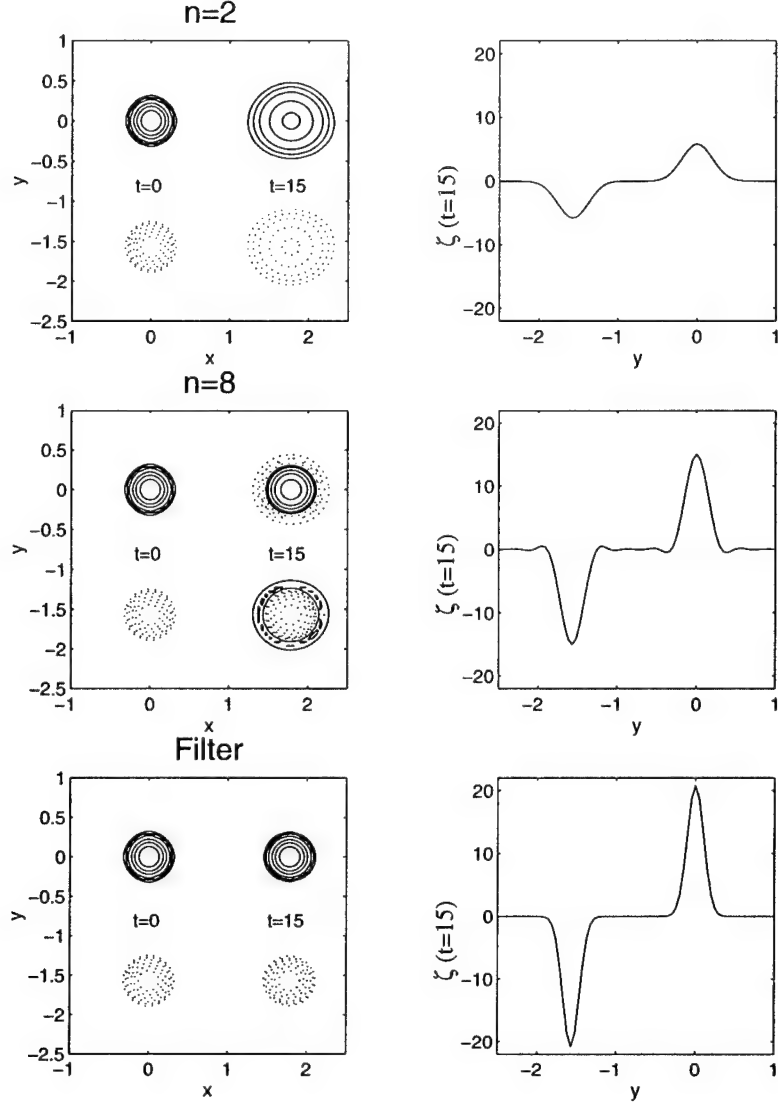
30

Figure 2.2: An eastward translating barotropic dipole under the influence of three types of damping: Laplacian damping $\left(\nu_2 \nabla^2 \zeta\right)$ with $\nu_2 = 9.82 \times 10^{-4}$, hyperviscous damping $\left(\nu_8 \nabla^8 \zeta\right)$ with $\nu_8 = 1.37 \times 10^{-11}$, and with an exponential cut-off filter applied at each time step. At left are contours of vorticity at $t = 0$, 15, and at right are cross sections of vorticity at the later time. The vorticity contour levels $(\pm[.25.512.5510])$ were chosen to highlight the outer structure of the compact vortices.

in the Laplacian case, 28% in the hyperviscous case, and about 1% in the filtered case. Ideally, the latter decrease ought to be zero since the grave wavenumbers are undamped, but the vortex maxima are found to fluctuate, and to decrease somewhat.

In addition, the hyperviscous run is found to develop weak external lobes or rings of oppositely signed vorticity. The contours at left were chosen to highlight this feature, but the lobes are also visible in the profile at right. The Laplacian run does not exhibit the ring formation; rather the diffusive decay simply flattens the profile and causes it to spread out laterally. The filtered vortices apparently do not develop the lobes at all, but rather retain their original shape.

Mariotti et al. (1994) document similar effects due to hyperviscous damping in the case of a vortex in an external shear. As they note, changes in vortex amplitude can alter its longevity under shear, since the shear required to destroy a vortex is proportional to its maximum value of vorticity. They also document an *increase* in amplitude under hyperviscosity in some cases when the vortex was strongly deformed by the shear. I have found similar behavior with the wavenumber filter, and I believe the effect is inevitable with a truncated spectral representation. The effect is undesirable in a model which supposedly conserves potential vorticity, but the impact of a fluctuating peak amplitude was found to be less problematic than a rapid decay of the vortex.

If the resolution were substantially greater, one could use smaller viscosities and the results would be more nearly the same. Likewise, if the vortex were larger, as in the upper panel of figure (2.1), the differences would be less. However, the filter yields a more nearly "inviscid" response at a given resolution than does hyperviscous diffusion.

2.6 Vortex counting

As mentioned, McWilliams (1984) found freely evolving turbulence is dominated by coherent vortices at later times. Using an automated vortex counting routine to locate and characterize the vorticity extrema, McWilliams (1990) discovered an apparent power law decay of the vortex population, with $N \propto t^{-.75}$. This prompted Carnevale et al. (1991b) to propose a scaling theory which related mean vortex quantities (area, circulation, peak vorticity) to the number of vortices.

Vortices likewise play an important role in the baroclinic turbulence experiments in Chapter 4, and vortex statistics are a useful way to quantify their evolution, as well as providing a point for comparison with the McWilliams (1990) results. The method used is very similar to that described in some detail in McWilliams (1990). The potential vorticity at each grid point is tested to see whether it is greater than the threshold value, q_{min}, then the qualifying grid points are grouped into simply connected regions. This was done by a repetitive process of checking neighboring points and labeling connected groups. Some care was required as the domain is doubly periodic, so single vortices could straddle borders.

After the groups have been selected, those with less than five grid points are rejected as too small. Also, groups which were too elongated were rejected, basically to remove filaments from the population, via a rough axisymmetry test. The (x, y) aspect ratio was computed for each vortex, and vortices with a ratio less that $1/5$ or greater than 5 were rejected. This procedure is more crude than that of McWilliams, but was preferable in this case due to vortex deformation by topographic waves.

Areas were calculated by multiplying the grid area, $\triangle x \times \triangle y$, by the number of vortex grid points. The circulation was found by multiplying the vorticity at each grid point by the grid area and summing over all points. The peak

vorticity was simply the maximum vorticity in the vortex. Additional quantities (maximum area, integrated squared vorticity, etc.) are easily found, but not reported in the text.

2.7 Quadratic Invariants and Spectral Fluxes

The two-layer QG equations possess several quadratic invariants which are useful in evaluating nonlinear baroclinic flows. For the sake of unity, the invariants referred to in the text are presented here. The single layer case is shown first, for illustration as well as for reference to a case in Chapter 4. Then the two layer invariants are derived.

The one layer PV equation in the absence of β may be written:

$$\frac{\partial}{\partial t}q + J(\psi, \nabla^2\psi) = 0 \qquad (2.10)$$

where $q = \nabla^2\psi$ in the barotropic case, or $q = (\nabla^2 - F)\psi$ in the case of a single layer of fluid overlying a motionless deep layer (the so-called one and a half layer case). Equation (2.10) is equivalent to equation (2.1) with ψ_2 set to zero. The energy equation is derived by multiplying the Fourier-transform of equation (2.10) by $\hat{\psi}^*$, where the asterisk indicates complex conjugate and the hat accent denotes transform. Taking the real part of the result yields an equation for the total energy (which is real):

$$\frac{\partial}{\partial t}(KE(\kappa) + PE(\kappa)) = \Re\{\hat{\psi}^* J(\hat{\psi}, \kappa^2\hat{\psi})\} \qquad (2.11)$$

where $KE \equiv \frac{1}{2}\kappa^2|\hat{\psi}|^2$ is the kinetic energy, $PE \equiv \frac{1}{2}F_1|\hat{\psi}|^2$ the potential energy, $\Re$ is the real part and $\kappa^2 = k^2 + l^2$ is the total (squared) wavenumber. The nonlinear term on the right hand side permits transfer of energy between different wavenumbers, but does not alter the total energy, i.e.

$$\sum_k \sum_l \Re\{\hat{\psi}^* J(\hat{\psi}, \kappa^2\hat{\psi})\} = 0 \qquad (2.12)$$

so that the sum over all wavenumbers of the sum of kinetic and potential energy is conserved, although of course there can be exchange of energy between the two components. Note that the nonlinear term derives solely from the advection of relative vorticity. In other words, there is no advection of thickness in the one and a half layer case, which is the same as saying there is no baroclinic instability (Pedlosky, 1987). The spectral transfer is mostly of interest in Chapter 4 since there is an active shift in scales due to turbulent interactions. In the case of the single vortex, the scales are essentially fixed so that the transfer is weak if not zero.

The conservation of PV also implies conservation of q^n where n is any number. A frequently used quantity is the squared potential vorticity or the "potential enstrophy" (Charney, 1971). An equation for this quantity is found by multiplying equation (2.10) by $\hat{q}^* = -(\kappa^2 + F_1)\hat{\psi}^*$ and then taking the real part of the resulting equation:

$$\frac{\partial}{\partial t}\frac{1}{2}|\hat{q}|^2 = -\Re\{\hat{q}^* J(\hat{\psi}, \kappa^2\hat{\psi})\}. \qquad (2.13)$$

The transfer on the right also vanishes when summed over wavenumber, so that the total enstrophy is conserved. Again note that changes in the quantity are

35

brought about solely by advection of relative vorticity. The addition of β changes neither conservation equation, (e.g. Rhines, 1977); however, with the addition of a bottom slope, enstrophy is no longer conserved in the lower layer.

The total energy for a two-layer flow is derived in a similar fashion. The Fourier-transformed upper layer equation (2.1) is multiplied by $\delta\psi_1^*/(1+\delta)$ and the transformed lower equation (2.2) by $\psi_2^*/(1+\delta)$, the asterisk again indicating the complex conjugate. The real part of the sum of the resulting equations is:

$$\frac{\partial}{\partial t}TE(\kappa) = \Re\{\hat{\psi}_1^* J(\hat{\psi}_1, \kappa^2\hat{\psi}_1)\} + \Re\{\hat{\psi}_2^* J(\hat{\psi}_2, \kappa^2\hat{\psi}_2)\} + \Re\{F\hat{\psi}_1^* J(\hat{\psi}_1, \hat{\psi}_2)\} \quad (2.14)$$

where $TE = KE_1 + KE_2 + PE$. The spectral transfers written in this way will be referred to as the "layer-wise" transfers because the first two terms derive from advection of relative vorticity in each layer. Note the first is the same as the transfer for the one and a half layer energy. The presence of a thickness transfer indicates the possibility of baroclinic instability (e.g. Salmon, 1980) when there is a correlation between temperature (thickness) and the perturbation velocity field (Pedlosky 1987). The sum over all wavenumbers of the transfers is zero, so again the total energy is conserved.

An alternate method, and one more commonly used with two layer models, is to break the total energy into barotropic and baroclinic parts (e.g. Salmon, 1980). One first adds and subtracts equations (2.1-2.2) to obtain equations for the barotropic and baroclinic vorticity. With equal layer depths, the result is (using the notation of Larichev and Held (1995)):

$$\frac{\partial}{\partial t}\nabla^2\psi + J(\psi, \nabla^2\psi) + J(\tau, \nabla^2\tau) + \beta_2\frac{\partial}{\partial x}(\psi - \tau) = 0 \qquad (2.15)$$

$$\frac{\partial}{\partial t}(\nabla^2 + 2F)\tau + J(\psi, \nabla^2\tau) + J(\tau, \nabla^2\psi) + J(\psi, -2F\tau) - \beta_2\frac{\partial}{\partial x}(\psi - \tau) = 0 \quad (2.16)$$

36

where $\psi \equiv \frac{1}{2}(\psi_1 + \psi_2)$ is the barotropic streamfunction and $\tau \equiv \frac{1}{2}(\psi_1 - \psi_2)$ the baroclinic streamfunction. The energy equations follow after multiplying (2.15) by $\hat{\psi}^*$ and (2.16) by $\hat{\tau}^*$, and taking the real parts:

$$\frac{\partial}{\partial t} \kappa^2 |\hat{\psi}|^2 = \Re\{\hat{\psi}^* J(\hat{\psi}, \kappa^2 \hat{\psi})\} + \Re\{\hat{\psi}^* J(\hat{\tau}, \kappa^2 \hat{\tau})\} - \beta_2 \Re\{ik\hat{\psi}^*\hat{\tau}\} \qquad (2.17)$$

$$\frac{\partial}{\partial t}(\kappa^2 + 2F)|\hat{\tau}|^2 = \Re\{\hat{\tau}^* J(\hat{\tau}, \kappa^2 \hat{\psi})\} + \Re\{\hat{\tau}^* J(\hat{\psi}, \kappa^2 \hat{\tau})\} + \Re\{\hat{\tau}^* J(\hat{\psi}, -2F\hat{\tau})\} + \beta_2 \Re\{ik\hat{\psi}^*\hat{\tau}\} \,.$$
$$(2.18)$$

The first transfer term in the barotropic equation represents barotropic self-advective changes and the second is due to transfers to/from the baroclinic mode. One finds that the sum over wavenumbers of the first is zero, but may be non-zero for the second as there may be a net exchange of energy between baroclinic and barotropic modes. Likewise, the first transfer term of the baroclinic equation is the baroclinic self-advective term and the second the transfer to/from the barotropic mode, the sum of the first over wavenumbers being zero, but not necessarily zero for the second. However, the sum of the second term is the negative of the sum of the second barotropic transfer term, as is required by conservation of total energy. The two intermode transfers are not equal at every wavenumber as energy may be removed and injected at different scales (a striking example is found in Larichev and Held (1995)). The third baroclinic transfer term represents changes to the spectrum due to the advection of thickness by the barotropic field, and can be shown to be identical to the thickness transfer term in the total energy equation (2.14). The final terms in both equations represent wave-induced transfers of energy between the barotropic and baroclinic modes. They cancel wavenumber by wavenumber, i.e. they are equal and opposite in the two budgets.

37

The barotropic/baroclinic formalism tends to be more illustrative of baroclinic instability, evidenced in particular by a conversion of baroclinic to barotropic energy. However, it will be seen that in cases of severe layer decoupling, the layer-wise transfers are preferable.

The equations for the two-layer potential enstrophies and transfers are found by multiplying equations (2.1-2.2) by $\hat{q}_1^*$ and $\hat{q}_2^*$ respectively, and taking the real parts:

$$\frac{\partial}{\partial t}|\hat{q}_1|^2 = -\Re\{\hat{q}_1^* J(\hat{\psi}_1, \hat{q}_1)\} \tag{2.19}$$

$$\frac{\partial}{\partial t}|\hat{q}_2|^2 = -\Re\{\hat{\psi}_2^* J(\hat{\psi}_2, \hat{q}_2)\} - \beta_2 \Re\{ik\hat{q}_2^*\hat{\tau}\}. \tag{2.20}$$

Again, the sum over all wavenumbers of the first transfer term in each equation is zero, implying conservation of the surface enstrophy in the absence of small-scale dissipation. But the lower layer enstrophy is not conserved due to the slope term (which need not sum to zero). The breaking of the conservation of enstrophy by topography has been noted before (e.g. Rhines, 1977). When the bottom is flat and dissipation present, the enstrophy monotonically decays in both layers.[1]

In forced-dissipative studies, the transfer terms are generally averaged over a long period because they tend to be noisy (e.g. Treguier and Hua, 1987; Larichev and Held, 1995). Averaging in time is less appealing for initial value problems because if the spectra are shifting in time, averaging tends to smear out the transfers. An alternative is to calculate the spectral fluxes, defined as :

---

[1] The equations shown here are inviscid, and thus do not represent the dissipation due to the filter. This could be done by adding a higher-order diffusion term. Then it would be clear that one obtains a monotonic decay of enstrophy.

$$flux(\kappa) = \sum_{\kappa=0}^{\kappa} transfer(\kappa).$$ (2.21)

The flux represents the net amount of energy entering or leaving the inner volume of wavenumber space. By virtue of being an integral quantity, the flux is less noisy than the transfer. It has the additional benefit of revealing immediately which terms have non-zero total integrals over all wavenumbers (the barotropic-baroclinic transfers). The spectral flux is by definition an isotropic quantity (averaged over all directions) and thus must be viewed cautiously in anisotropic flows. However, like the quadratic quantities in general, they provide a useful means of extracting information from the sometimes complicated flow fields.

Chapter 3

A single vortex over a slope

As explained in Chapter 2, the scaling of the lower layer PV equation yields two advective parameters: $\frac{U_2}{\beta_2 L^2}$ and $\frac{F_2 U_1}{\beta_2}$. The size of these parameters determines the degree of openness of the contours of the total lower layer PV, and is related to the importance of nonlinearity at depth. Both parameters will be examined in turn below. The first is studied using an initially barotropic vortex, which has no interfacial deformation and thus zero (initial) advection of thickness. The second parameter is then considered by looking at the evolution of a surface-trapped vortex, in which the interfacial displacement may be large, but relative vorticity at depth is initially zero.

The barotropic vortex case lends itself naturally to comparison with a single layer case. The barotropic case, from which much of our present intuition into the baroclinic problem derives (e.g. Smith and O'Brien, 1983), is therefore discussed first. Here, $\frac{U}{\beta L^2}$ determines the degree of openness and linearity of the ensuing evolution. One finds that the vortex *motion* is an indicator of the nonlinearity, as has been discussed before.

The primary difference in two layers is that the PV gradient is now non-uniform in the vertical. This asymmetry "favors" baroclinicity as one might expect. Particular questions which will be addressed are: 1) when is the evolution

40

barotropic? 2) if baroclinic, what is the ensuing motion? and, 3) how do the single layer results help in our understanding of the problem? Inherent in the third is the validity of using intuition from barotropic problems to diagnose the motion of baroclinic rings over topography.

The barotropic results, and thus the importance of $\frac{U_2}{\beta_2 L^2}$, form the central portion of the chapter. However, the second parameter, $\frac{F_2 U_1}{\beta_2}$, is also important and one finds that it is related to vortex stability because a large bottom slope works against layer coupling. Several examples are presented, and the general importance of the parameter deduced.

3.1 Initial conditions

The vortex used in both one and two-layer examples discussed hereafter has a Gaussian streamfunction profile, i.e.

$$\psi = Aexp(-(\frac{r}{2r_0})^2) = -0.7exp(-(\frac{r}{0.6})^2) \tag{3.1}$$

and is shown in figure 3.1. A Gaussian streamfunction vortex is a common choice in numerical studies (e.g. McWilliams and Flierl, 1979) as well as in laboratory studies (e.g. Carnevale et al. 1991a) because its azimuthal velocity decays exponentially in the far field, thereby minimizing interactions with the boundaries. Such a vortex is "isolated" because the vanishing of the azimuthal velocity implies zero circulation:

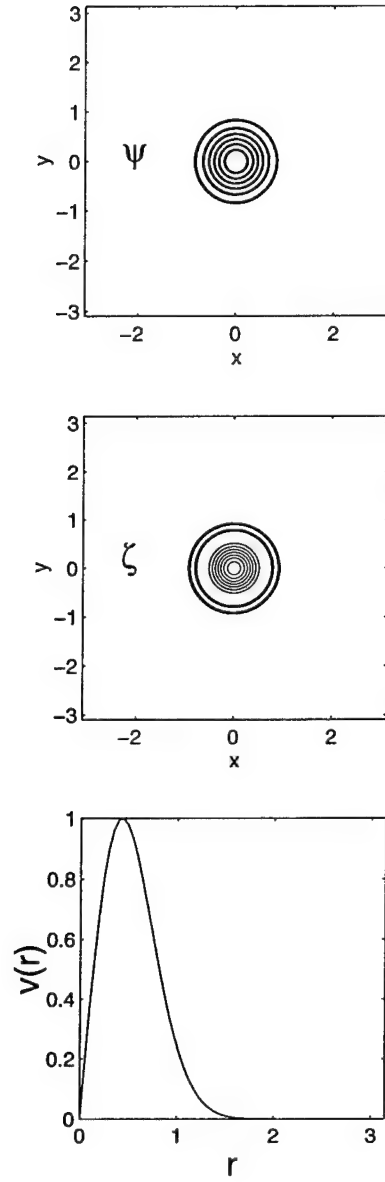$$lim_{r\to\infty} \int\int \nabla^2\psi \, dA = lim_{r\to\infty} \oint v(r) \, r \, d\theta = 0 \tag{3.2}$$

41

Figure 3.1: The initial vortex. The streamfunction is shown at top, with contour interval C.I. = ±[.1 : .1 : 1]; the vorticity is in the middle panel, with C.I. = ±[1 : 1 : 10]; and the azimuthal velocity profile at bottom. The bold contours are negative values, the thin are positive.

so that a monopolar vortex is nested in a ring of oppositely-signed vorticity, as seen in the middle panel of figure 3.1. The Gaussian vortex is known to be weakly barotropically unstable, with the result that the outer ring rolls into two "satellite" vortices yielding a "tripolar" structure (Kloosterziel and van Heijst, 1991). This was found in some cases discussed below, but generally did not alter the qualitative aspects of the evolution.

Note r_0 is the radius to the velocity maximum, chosen so that the vortex was well-resolved but did not extend too close to the boundaries of the domain. The length scale was chose so that the latter had dimensions 2π by 2π. The amplitude was chosen so that the maximum azimuthal velocity was approximately 1.0. As stated above, the vortex is taken to be initially barotropic and so has the same velocity profile in each layer.

In addition, only cyclonic vortices are considered. However, the quasigeostrophic equations are isomorphic under the change $\psi(y) \to -\psi(-y)$, so the results for an anticyclone are exactly the same with the reversal of the effective "north" and "south", i.e. if the cyclone moves toward shallower water, the equivalent anticyclone moves to deeper water.

3.2 One layer results

Scaling the barotropic quasigeostrophic vorticity equation with the wave period as a time scale $(T \; \alpha \; (\beta L)^{-1})$ and the vortex radius (r_0) as a length scale yields a single parameter: $\frac{U}{\beta_{dim} r_0^2}$. The inverse of this parameter defines a non-dimensional effective slope. Both quantities will be used hereafter. However, when the dimensional version of β is required, it will be denoted β_{dim}. The size of β is an approximate indication of linearity of the vortex evolution. Which radius to use in this expression is somewhat subjective; the convention adopted here is the

43

same as used in the observational literature (e.g. Joyce and Kennelly, 1985), specifically the distance to the maximum azimuthal velocity, or r_0.

Four examples of single-layer vortices on the β-plane are shown in figure 3.2 for a large range of values of $\beta = \frac{\beta_{dim} r_0^2}{U}$; in particular, the relative vorticity is shown after the vortex has evolved from its initial position in the center of the domain. In the strong β limit, shown in the lower right panel, the evolution is nearly linear and the vortex disperses rapidly as a packet of Rossby waves. The decay of the peak value of vorticity is correspondingly rapid. This approximates the case of a fully linear ring, considered in detail by Flierl (1977). The direction of "vortex" translation is exclusively westward, due to the north-south symmetry of the initial profile (see Flierl, 1977).

The opposite extreme, in which advection dominates changes in the relative vorticity, is seen in the upper left panel. Note that this figure shows the vorticity at $t = 36$, as compared to the strong β case at $t = .18$; as β is 10^3 times smaller in this case, the wave phase speeds are correspondingly slower. However, there are qualitative differences from the linear case. For one, the vortex motion is predominantly meridional, with only a weak westward drift. The northward drift is due to an interaction with the perturbed background vorticity field, and is described below and briefly in Chapter 1. The strength of the cyclone has decreased only marginally during the evolution, due to the meridional displacement and the (weak) mean PV gradient. Note that the outer ring of vorticity has begun to roll up into two satellites, due to the barotropic instability described earlier.

With intermediate values of β the response falls between the two extremes described above. There is less meridional motion and more westward motion than in the weak β case, and an increasing rate of decay of the original cyclone. There is also a more pronounced "wake" of Rossby waves at larger values of β. In the $\beta = 0.18$ case, the pools of vorticity resemble similar structures found
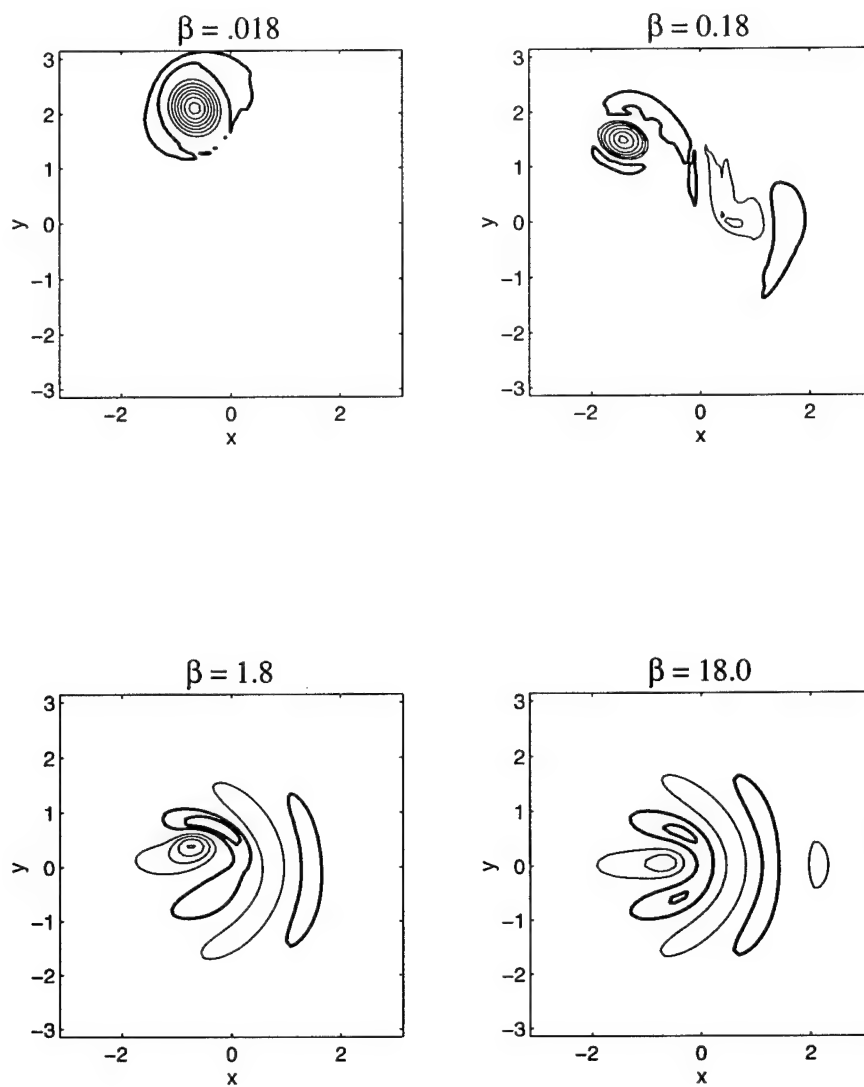
44

Figure 3.2: The vorticity at later times in the one layer runs. The corresponding times are $t = 36$ ($\beta = .018$), $t = 16$ ($\beta = .18$), $t = 4.5$ ($\beta = 1.8$), $t = .18$ ($\beta = 18$) and C.I. $= \pm[1:1:10]$.

by Carnevale et al., (1991a). The qualitative transition from nonlinear to linear behavior appears to occur around $\beta = 1$ (consistent with the scaling), but it is a gradual transition.

The relative vorticity is not conserved on the β-plane, but rather the total vorticity, $\nabla^2\psi + \beta y$, is. Plots of this quantity for the initial vortex in the four cases are shown in figure 3.3. Here the cyclonic vortex is seen as a downward deflection of the isocontours of barotropic potential vorticity, and the degree of the deflection depends on the relative strengths of the cylcone and the background gradient. The deflection is strong enough to yield closed contours of PV in three of the cases; indeed, it is so strong in the $\beta = 0.018$ case that the background gradient is not visible with the contours drawn. The transition between closed and open contours, around $\beta = 1$, reflects the degree of nonlinearity of the resulting evolution. The figure qualitatively suggests that northward motion will occur as the deflected contours relax towards their equilibrium positions (latitude lines), as noted by Rossby (1948). Indeed, the integral theorem of Flierl et al. (1983) states that such a monopolar vortex experiences an unbalanced "Rossby" force on the β plane, indicating that the deflection must relax. McWilliams and Flierl (1979) noted this tendency, but found that a vortex with weak β turned westward before reaching the "rest latitude".

The vortex translation is thus due to a combination of wave dispersion which yields westward motion and a nonlinear mechanism which gives meridional motion. In the weak β case, the Rossby phase speeds are so slow that the meridional drift dominates, but when β is large, the meridional drift is inconsequential. The nonlinear mechanism for meridional self-advection was discussed briefly in chapter 1, and hinges on the generation of a perturbed dipolar background field, the so-called "β-gyres" (e.g. Sutyrin and Flierl, 1994), which in turn advect the primary vortex. The gyres are initially oriented east-west, but acquire a tilt as the vortex begins to move so that the resulting path is more northwestward.
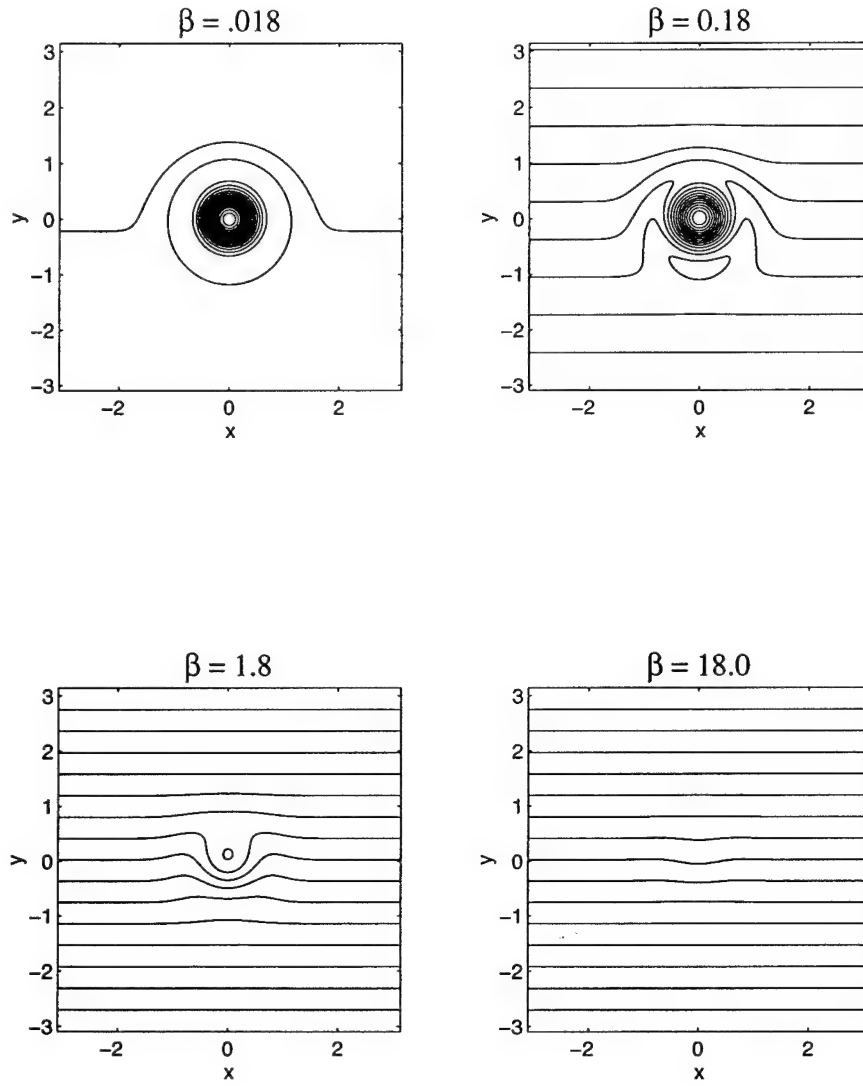
Figure 3.3: The total vorticity $\nabla^2 \psi + \beta y$ at $t = 0$ for the one-layer vortex. The contours are chosen so that15 contours span the range $[\zeta_{min}, \zeta_{max}]$.
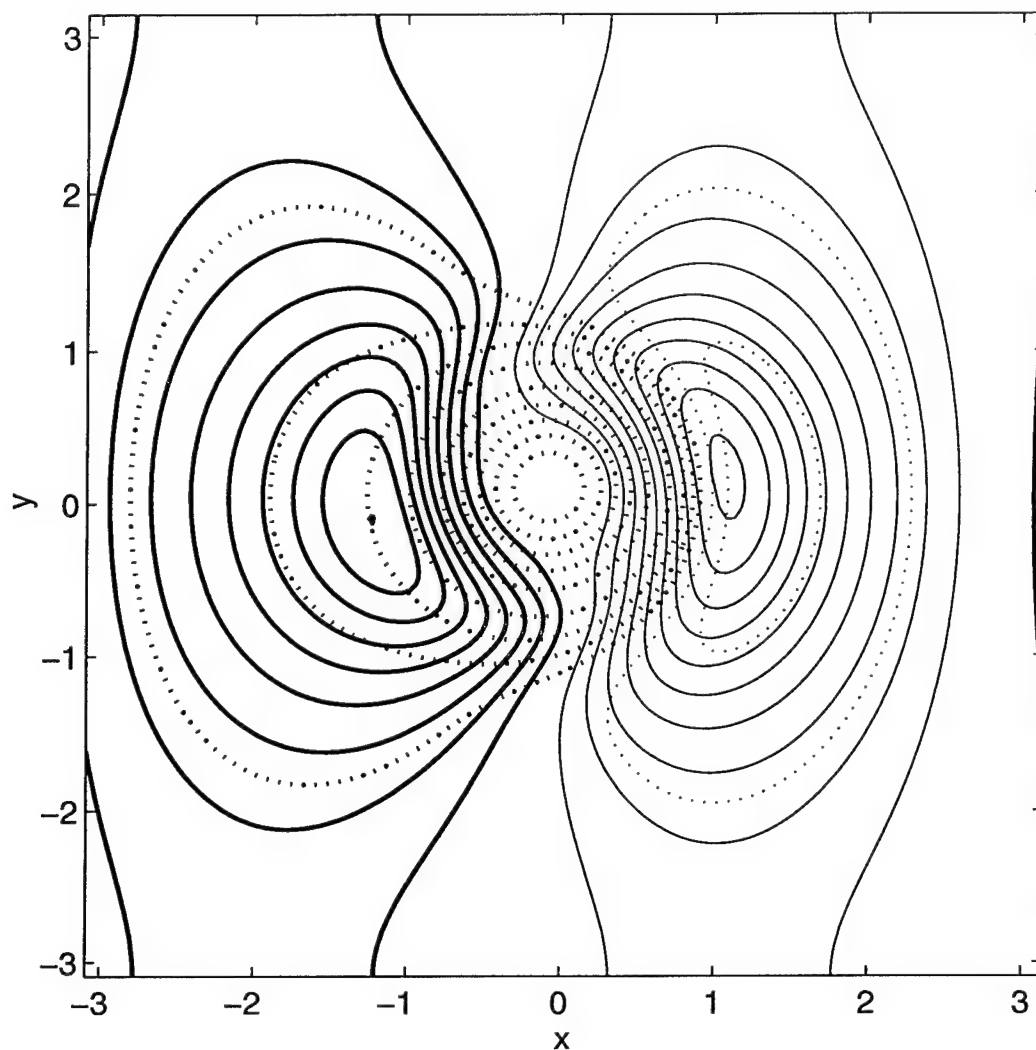
Figure 3.4: The asymmetric streamfunction for a one-layer vortex run with $\beta = .018$; fields shown at $t = 5$. The actual streamfunction is superimposed, in dots. For the asymmetric field, the CI $= \pm[1 : 1 : 10]/250$ and for the actual streamfunction, the CI $= \pm[.01.025.05.1 : .1 : 1]$.

As demonstrated in Fiorini and Elsberry (1991), the gyres are clearly visible in plots of the streamfunction with the radially symmetric portion removed. Such a plot for the $\beta = 0.018$ case at an early time is shown in figure 3.4 with the streamfunction superimposed. The gyres were found by first locating the streamfunction maximum using two perpendicular spline fits in Matlab (The Mathworks, Inc.) (the maximum may not fall on an actual grid point), and then subtracting from the streamfunction the original Gaussian profile with the amplitude scaled to match. This method was found to be more accurate than calculating the actual radially symmetric portion of the streamfunction by averaging on the grid.

The gyres are seen to straddle the vortex, so that the center of the primary vortex lies at the velocity maximum for the dipole (figure 3.4). The vortex translates under the influence of these gyres, and the gyres move with it, evolving in time and eventually developing a more complicated modal structure (Willoughby, 1994) so that the path becomes more complicated. The mechanism is nonlinear because it hinges on the interaction between the perturbed gyres and flow which generated them. For more detailed accounts, consult Fiorini and Elsberry, 1991; Willoughby, 1994; Sutyrin and Flierl, 1994; Resnik and Dewar, 1995.

Numerical simulations of the weak β vortex suggest that the vortex accelerates from rest before reaching a relatively constant velocity (e.g. McWilliams and Flierl, 1979; Fiorini and Elsberry, 1989). This can be seen in plots of the position of the vortex, $(x(t), y(t))$, as in figure 3.5. The duration of this state of steady translation is not known, because the vortex usually encounters boundaries, and higher order effects eventually alter the trajectory (Willoughby, 1994). However, this velocity is easy to measure and provides a useful tool for gauging the dependence on $\beta_{dim} r_0^2 / U$. Smith (1993) argued dimensionally that the translation velocity ought to vary as $u_\theta (\frac{\beta r_0}{u_\theta})^n$ (where u_θ is the azimuthal or swirl velocity scale and n is some number) because these are the only important parameters for the case of an isolated vortex. Moreover, he found, by comparing data from pub-
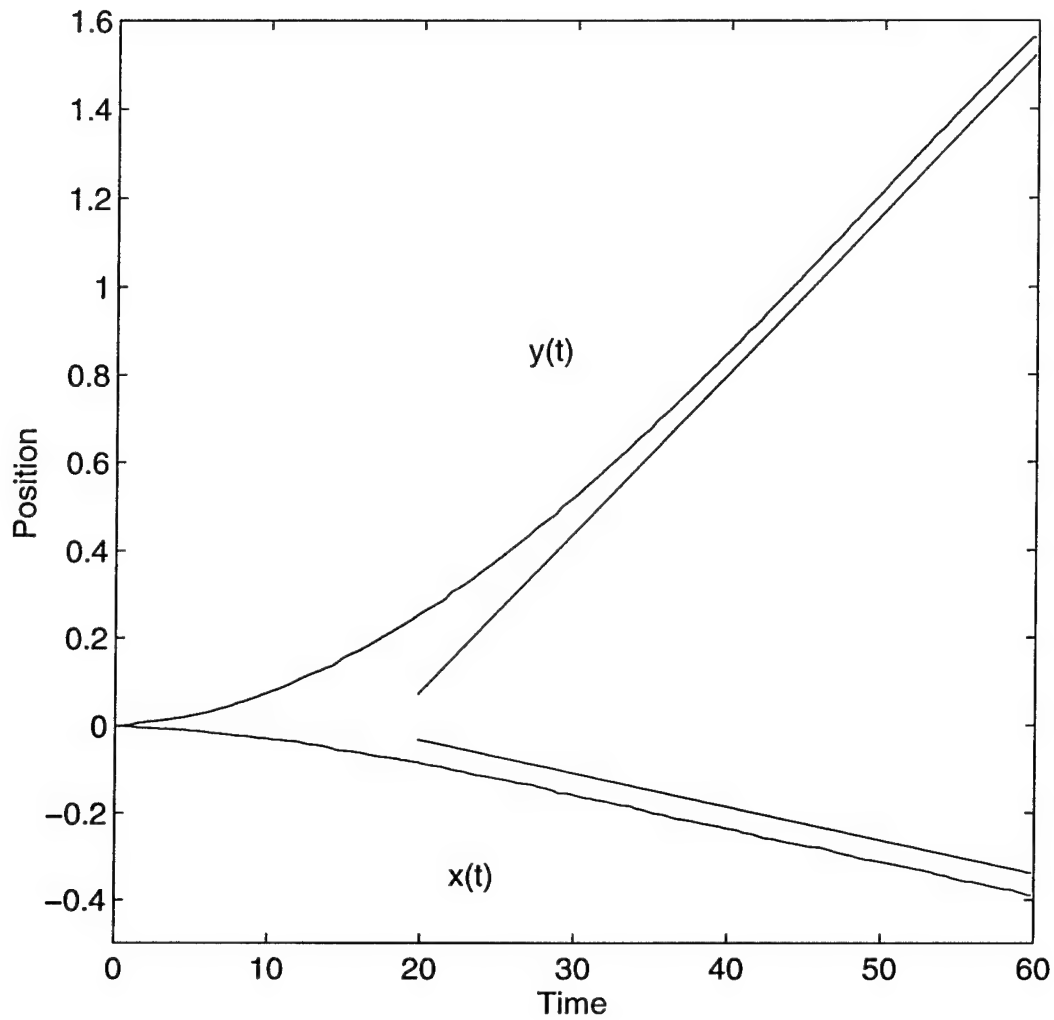
49

Figure 3.5: The position of the vorticity centroid in (x, y) vs. time for a single layer vortex case with $\beta = .0018$. The lines are drawn to indicate a constant velocity.

lished studies, that the *magnitude* of the velocity, i.e. $\sqrt{(\frac{\partial x}{\partial t})^2 + (\frac{\partial y}{\partial t})^2}$, appears to vary as $\beta^{\frac{1}{2}}$ so that $n = .5$.

The translation velocity was calculated with this model over a range of β and the results are shown in figure 3.6. The upper panel shows that the dependence is roughly linear for $\beta > .25$. This is to be expected in this limit for the velocity is simply the Rossby group velocity, linearly dependent on β. The middle panel, a magnified view of the plot in the top panel, illustrates the nonlinear dependence for smaller values of β. The bottom panel is a logarithmic plot of the small β velocities and the solid line the result of a least-squares fit, with slope $m = .45 \pm .05$, consistent with the empirical result of Smith (1993). Figure (3.6) also suggests a transition from nonlinear to linear behavior for $\beta = O|1|$.

To summarize the one layer case, the evolution is found to depend on the value of the nondimensional parameter, $\beta = \beta_{dim} r_0^2 / U$. If large (compared to unity), the vortex moves westward or along the isobaths, dispersing rapidly as Rossby waves. If β is small, meridional motion is found and the dispersal is slower. The more nonlinear the vortex, the greater the number of closed contours of total PV, $\nabla^2 \psi + \beta y$. Note that the parameter depends strongly on vortex size and inversely on vortex strength, so stronger, smaller vortices are more likely to be nonlinear.

It should be emphasized that the monopole on a β-plane is not a steady solution (Flierl et al., 1983), so that in all cases the vortex must either disperse into waves or evolve to a state which is no longer monopolar. A detailed discussion of steady, isolated vortices can be found in Flierl (1987).
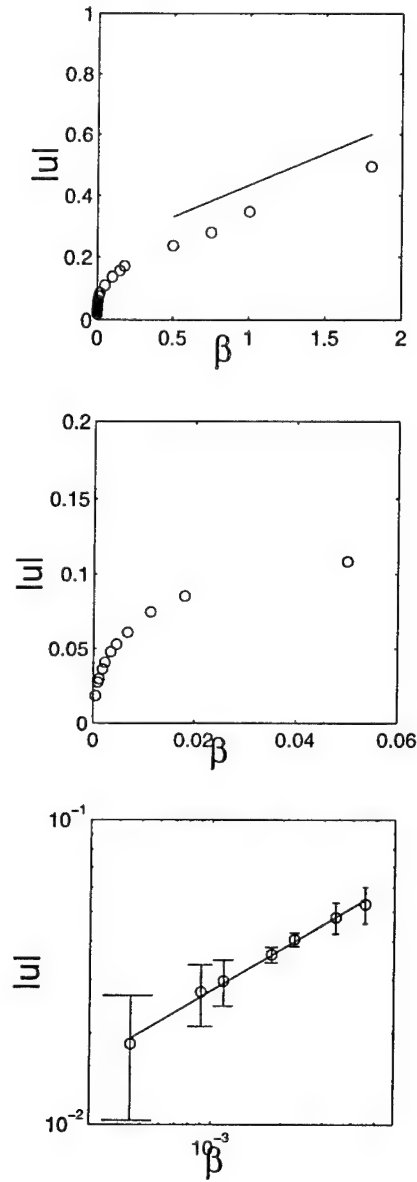
Figure 3.6: The translational velocity as a function of β. The upper plot is the full range (with line to indicate a linear dependence), the middle plot is the small β range of the upper plot, and the bottom plot is a logarithmic plot of the points in the middle plot. The error bars at the bottom are from the least squares fits of the vortex position curves. The straight line is the best fit, with slope $m = .45 \pm .05$.

3.3 Two-layer results: A barotropic vortex

The barotropic Gaussian vortex with the same amplitude and horizontal scale was also used for the two-layer f-plane runs. Thus the streamfunction and vorticity shown in figure 3.1 are also the streamfunction and the layer potential vorticity in the two-layer runs.

With an initially barotropic vortex ($U_1 = U_2$) and equal layer depths ($F_1 = F_2$), there are two important parameters: Fr_0^2 and $\beta_{2dim}r_0^2/U$. As before, the radius to the maximum azimuthal velocity indicates the vortex scale so that $r_0/\lambda_i \equiv r_{vmax}\sqrt{F_i}$ hereafter. Also as before, it is useful to define a nondimensional PV gradient relative to the vortex scales, $\beta_2 \equiv \frac{\beta_{2dim}r_0^2}{U}$. Though the layer depths are assumed equal in most of the numerical examples, the scalings and expressions derived in the chapter retain unequal F_1 and F_2.

The resulting parameter space is sketched in figure 3.7. Again the behavior in the limits of weak and strong slopes will be addressed first, before considering the evolution over intermediate slopes. The first case (A) is that of a vortex larger than deformation scale over a weak slope and the second (B) of a vortex smaller than deformation scale over a weak slope. Then the case of a small vortex over a strong slope (C) is considered before examining the intermediate slope response for the small vortex. The large vortex over a strong slope (D) and a discussion of the intermediate slope behavior for the large vortex follow. The latter transition region exhibits rich dynamics, so additional time is spent examining the behavior there. Finally, the single vortex results are summarized and discussed.

3.3.1 Case A: $r = 2.5\lambda$, $\beta_2 = .02$

The total PV in each layer at a late time are shown in figure 3.8; the position of the vorticity centroid $(x_i, y_i) \equiv \frac{\int\int (x,y)q_i dA}{\int\int q_i dA}$ (where $q_i \equiv \nabla^2\psi_i + F_i(\psi_{3-i} - \psi_i)$ is
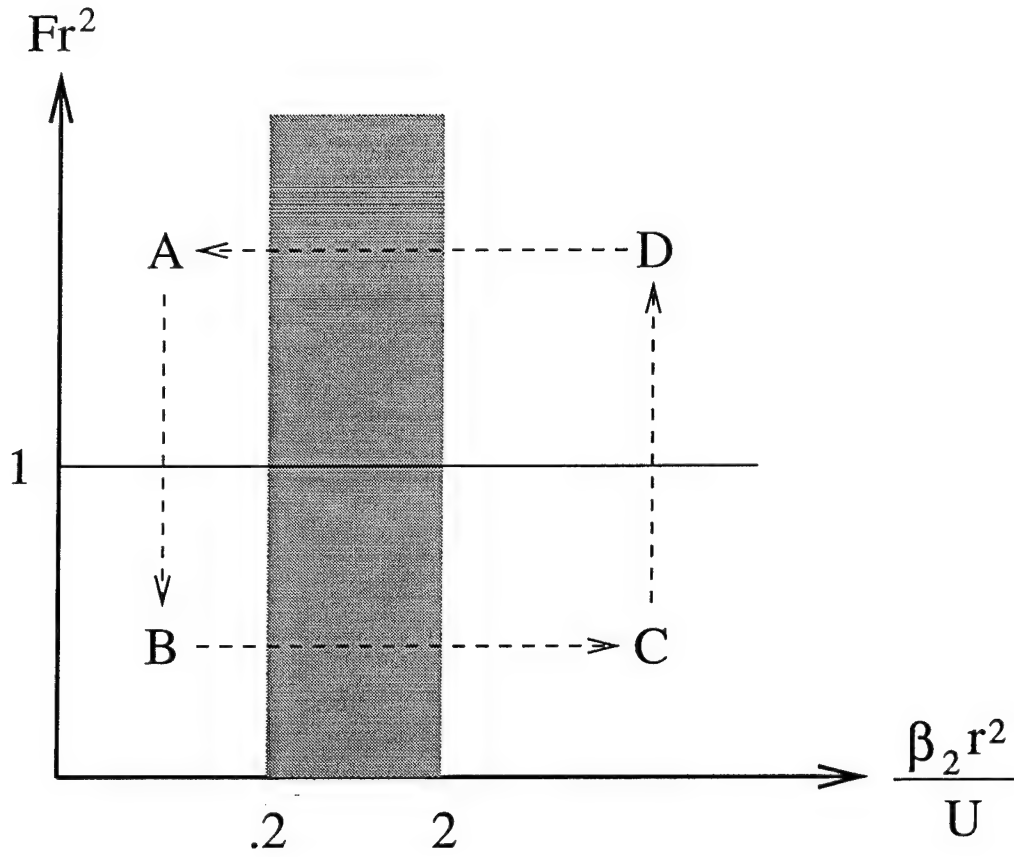
Figure 3.7: The two-layer parameter space. The x-axis is the non-dimensional slope parameter, and the y-axis is the (squared) ratio of vortex radius to the deformation radius. The cases A, B, etc. are labeled in order of appearance in the text.
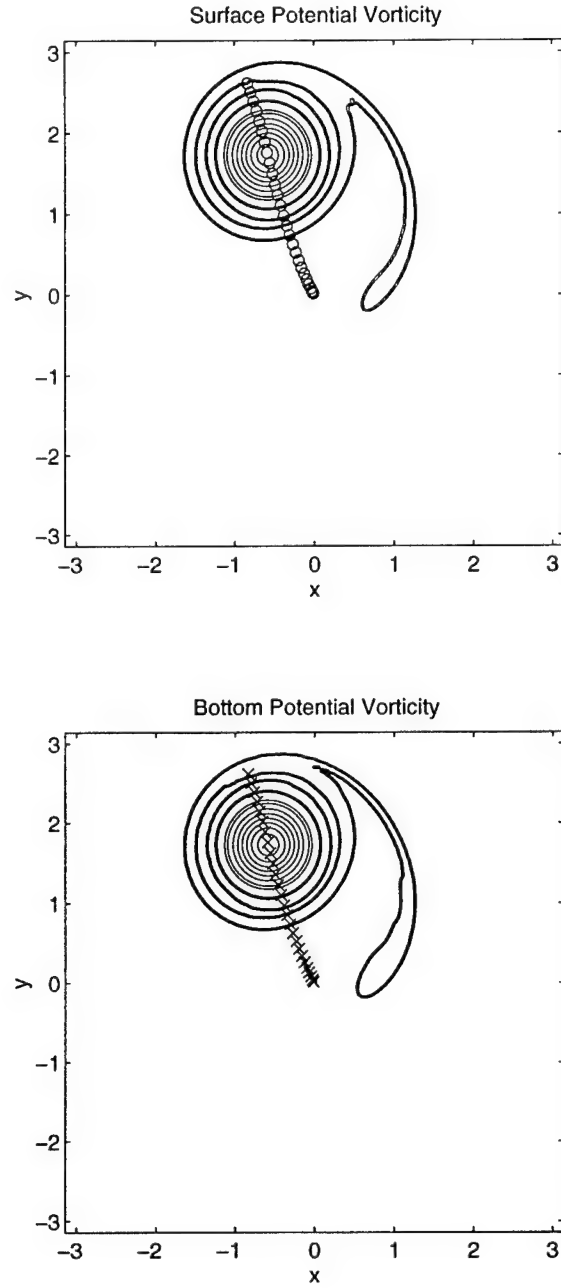
Figure 3.8: The upper and lower layer potential vorticity for the two-layer vortex with $r_0 = 2.5\lambda$ at $t = 37.5$ and $\beta_2 = .02$. The CI $= \pm[.51 : 1 : 10]$. Also shown are the centroid positions drawn every two time units. The slope is shallowing towards the top of the figures.

the perturbation PV in each layer), is indicated every two time units, the upper layer with an (o) and the lower layer with an (x). The vortex is larger than deformation scale $(r_0/\lambda = 2.5)$, and is clearly translating as a barotropic vortex. The upper and lower centroids are aligned, and the specific features in the upper layer are mirrored in the lower layer. The vortex moreover strongly resembles its one-layer counterpart shown in the upper left panel of figure 3.2 in that it is in nearly the same location. The direction is nearly cross-isobath, with a weak "westward" drift.

As in the one-layer case, one can calculate the asymmetric portion of the streamfunction in both layers. This was done by subtracting the original Gaussian (with the amplitude adjusted to match) from that of the vortex at the later time. The upper and lower centers of the vortex did not exactly coincide at any given time, so the process was carried out separately in each layer. The result, with the streamfunction superimposed, is shown at two different times in figure 3.9. The gyres are found to intensify with time (as can be seen in the barotropic case) and are symmetric in the vertical. Thus while the perturbed vorticity field is entirely in the lower layer, the gyre streamfunction or flow field is equal in both layers and so are able to advect surface and bottom portions of the vortex equally.

The gyres are comparable in intensity to those in the one-layer case, and thus the translation velocity comparable. The magnitudes of the translation velocity for the two-layer vortex and the one-layer vortex were compared and are shown in figure 3.10. The (x) in the figure is the two-layer translation velocity, and the (o) is the one-layer. β_2 has been scaled by a factor of $\frac{1}{1+\delta} = \frac{1}{2}$ for the comparison with the barotropic case, because $\beta_2 = \frac{f\partial_y H}{H_2} = (1+\delta)\frac{f\partial_y H}{H}$.

The magnitudes of the translational velocities are equal within error, as is the dependence on the PV gradient, so that for the two-layer vortex on a weak slope, $|u| \propto \beta_2^{\frac{1}{2}}$. The agreement is perhaps not surprising, as one would expect
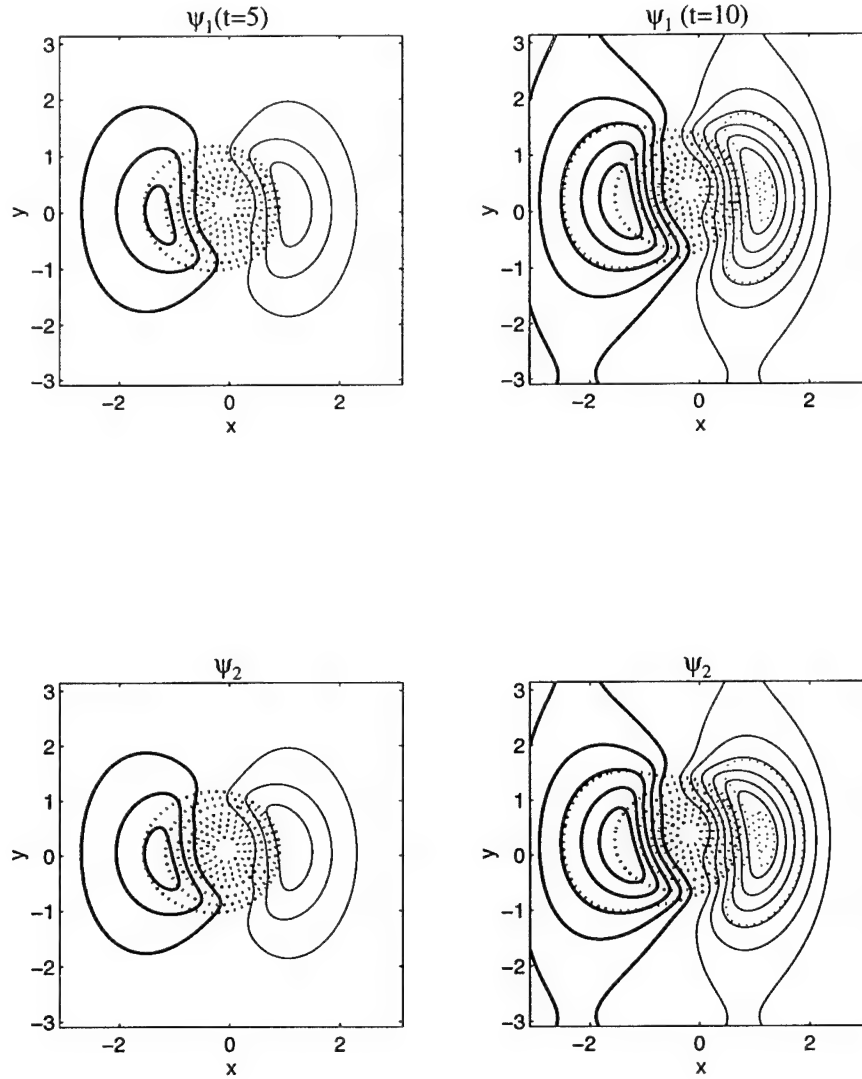
Figure 3.9: The upper and lower layer asymmetric streamfunction for the two-layer vortex with $r_0 = 2.5\lambda$ and $\beta_2 = .2$ at $t = 5$ and $t = 10$. For the asymmetric field, the CI $= \pm[1 : 1 : 10]/125$ and for the actual streamfunction, the CI $= \pm[.025 .05 .1 : .1 : 1]$.
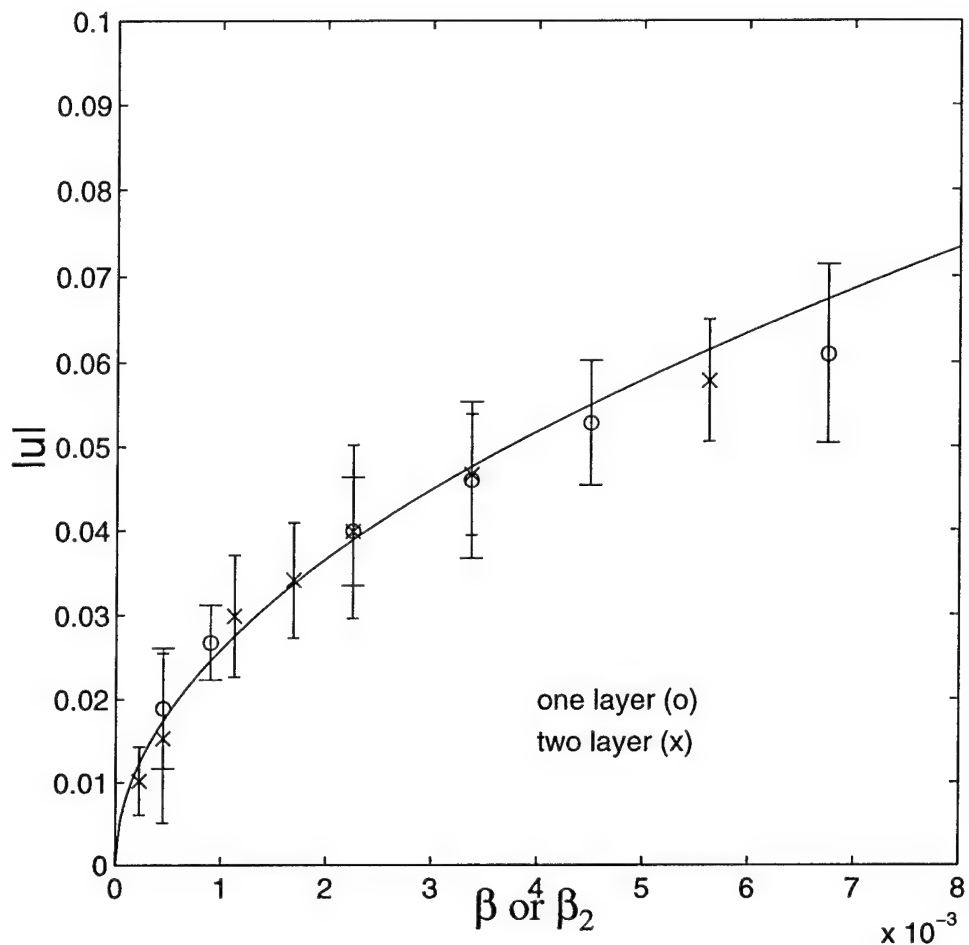
Figure 3.10: The translation velocity obtained from fits of $(x(t), y(t))$ for the one and a two-layer vortex with $r_0 = 2.5\lambda$. The 'x' indicates the two-layer velocity, the 'o' the one-layer velocity. β_2 has been scaled by a factor of 2 for the comparison—see text. The solid curve varies as $\beta^{\frac{1}{2}}$. The error bars are from the least square fits of the vortex position in time.

the dynamics in the deep layer to mimic those in the one-layer case. Of interest is that the top half of the vortex is carried along at the same speed. There does appear to be a systematic deviation of the observed velocities from the curve, suggesting that a more complicated nonlinear relation may be required to capture fully the actual dependence; however, a $\beta_2^{\frac{1}{2}}$ dependence is correct within the accuracy of the experiments.

The evolution of the components of the energy balance (Chapter 2) can also be considered. The energy components are shown in figure 3.11. A barotropic initial state has no potential energy and, with equal layer depths ($\delta = 1$), equal layer kinetic energies. There is a slight increase in potential energy and loss of kinetic energy due to the weakening of q_2 from the cross-isobath motion, though the changes are very small because β_2 is small. More substantial changes are found later, in more baroclinic examples.

3.3.2   Case B: $r_0 = .64\lambda$, $\beta_2 = .02$

A late-time plot of the PV in each of the two layers for the case of a vortex with $r_0 = .64\lambda$ is shown in figure 3.12 and the evolution is clearly much different than that found in the previous example. The motion of upper and lower cores is no longer aligned, with the lower core moving to shallower water and eastward, and the upper portion arcing towards deeper water. The outer rings of vorticity have been strongly deformed, and also have no apparent vertical coherence. In addition, the translation speeds (inferred from the spacing of the centroid markings) are more erratic and rapid.

The vortex has separated into layer-trapped *potential* vortices, or vortices with layer-trapped expressions of potential vorticity. As discussed below, such vortices have nonzero flow in the opposite layer. This can be seen in plots of relative vorticity (figure 3.13); both vortices have relative vorticity of the same
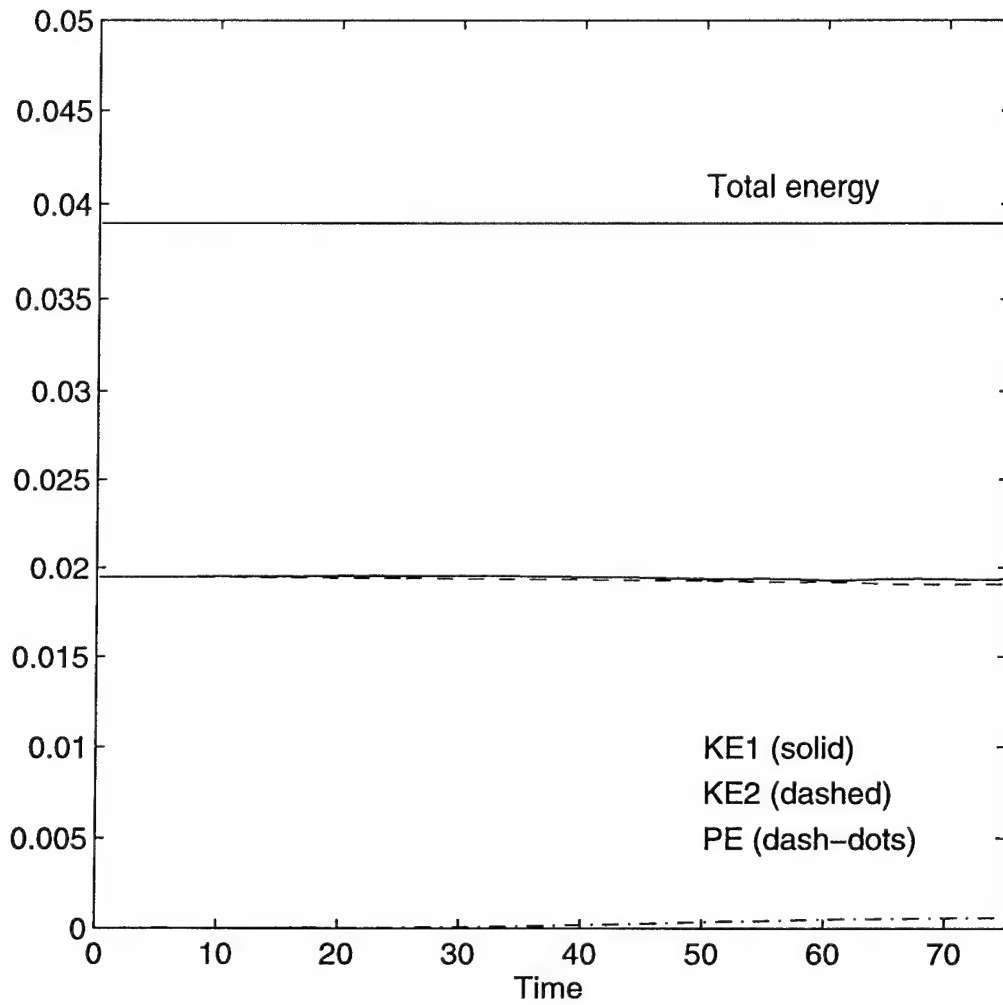
59

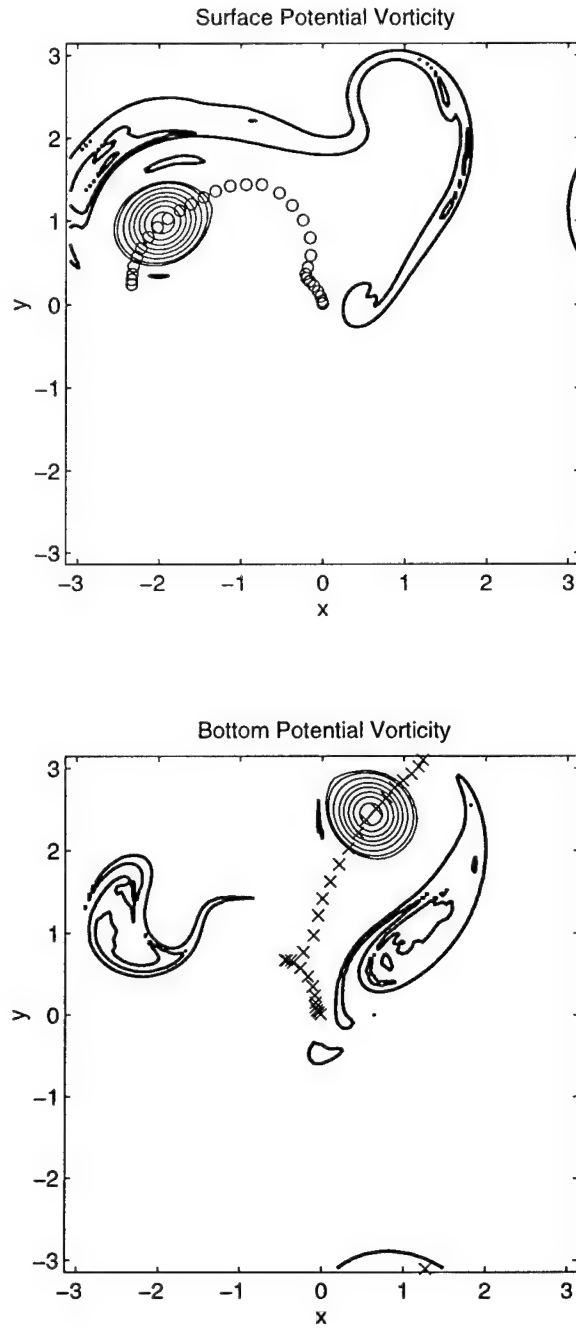Figure 3.11: The components of the total energy for the $r_0 = 2.5\lambda$ vortex with $\beta_2 = .018$.

Figure 3.12: The upper and lower layer potential vorticity for the two-layer vortex with $r_0 = .64\lambda$ at $t = 45$. The CI $= \pm[.51 : 1 : 10]$. Also shown are the centroid positions drawn every two time units.

61

sign in the opposite layer. With both vortices having non-zero flow at depth, each are able to self-advect over the slope. However the motion is more rapid and erratic than in case A.

The separation is an example of the "twisting instability" of Flierl (1988), first noted by Gent and McWilliams (1985). The mechanism is clearly explained in a schematic in figure 7 of the former reference, and affects sub-deformation scale, isolated, barotropic vortices. Under the influence of a baroclinic perturbation (here the influence of the slope), the unstable vortex experiences a vertical misalignment between vortex cores and the outer ring. The misalignment between surface and bottom portions of the vortex leads to a dipolar coupling between ring and core in each layer with a velocity vector which is generally not parallel to that of the corresponding dipole in the opposite layer, so that the upper and lower portions move off in different directions. Here we find that the dipolar structure persists at finite amplitude, causing the rapid translation seen in figure 3.12.

Further numerical runs revealed that the line dividing case A and case B vortices is fairly distinct; a vortex with $r_0 = .82\lambda$ separated, albeit more slowly than with $r_0 = .64\lambda$, whereas one with $r_0 = .9\lambda$ did not. Gent and McWilliams (1985) calculated growth rates for a linearly unstable Gaussian vortex with continuous stratification and a constant Brunt-Väsälä frequency. They found that the maximum growth rate occurred when the vortex horizontal scale was roughly .8 times the deformation radius, and that the vortex was stable if the scale was greater than $1.7NH/f$. Flierl's (1988) stability calculations were for two-layer vortices, but with nested contours of uniform PV. However, if one assumes that his inner ring of vorticity extends to r_0 and the outer ring to roughly $3r_0$, a reasonable choice, one finds his condition for instability is roughly $(r_0/\lambda)^2 < .8$. The results here for two-layer Gaussian vortices are in rough agreement with the latter result, but differ somewhat from the Gent and McWilliams result. The disagreement
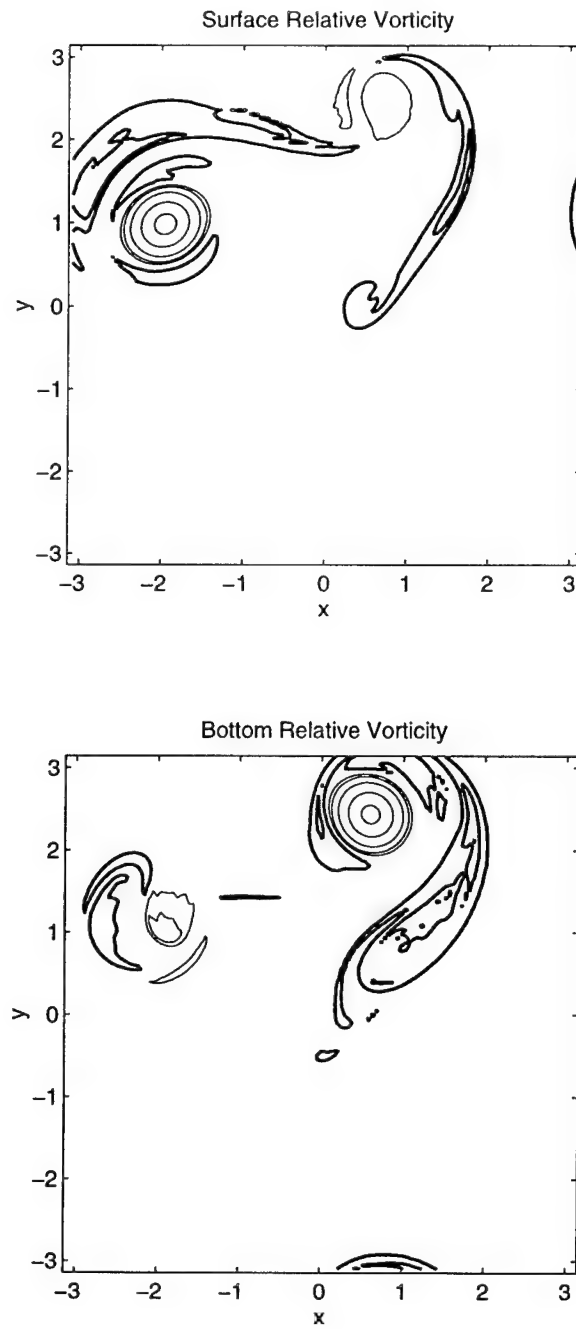
Figure 3.13: The upper and lower layer relative vorticity for the two-layer vortex with $r = .64\lambda$ and $\beta_2 = .02$ at $t = 45$. The CI $= \pm[.51 : 1 : 10]$.

appears to be related to the difference in stratification, as seen below.

As mentioned, potential vortices have a non-zero streamfunction in the opposite layer; the strength of that flow is weaker when the vortex is smaller than deformation scale. Consider a surface-trapped potential vortex; inverting the perturbation vorticity relations, one finds expressions for the (transformed) streamfunction in each layer:

$$\hat{\psi}_1 = \frac{-(\kappa^2 + F_2)\hat{q}_1}{\triangle} \tag{3.3}$$

$$\hat{\psi}_2 = \frac{-F_2\hat{q}_1}{\triangle} \tag{3.4}$$

where $\triangle \equiv \kappa^2(\kappa^2 + F_1 + F_2)$ and $F_1 = F_2 = F$ by assumption.[1] One sees that if $\kappa^2 \ll F$, $\psi_1 \approx \psi_2$ the *streamfunction* is nearly barotropic, though the potential vorticity is layer-trapped.

Thus if the vortex in case A is thought of as an aligned pair of potential vortices, the streamfunctions strongly "overlap" in each layer. However, the overlap is markedly less in case B, because the vortex is smaller than deformation scale. So one might expect that the latter vortex will be less cohesive under the action of a perturbation. The "overlap" argument is insufficient to predict instability, in that it does not predict a sharp transition at $r_0 = \lambda$ nor require the presence of the outer ring of oppositely-signed vorticity, a necessary component for the formation of layer dipoles. However, it does suggest that the "overlap" is

---

[1]The expressions are undetermined at $\kappa = 0$ as $\hat{q}_1(\kappa = 0) = \hat{q}_2(\kappa = 0) = 0$ due to isolation (the $\kappa = 0$ mode represents the domain-average). On the other hand, the Gaussian streamfunction does have a non-zero domain average, or "angular momentum" in the language of Flierl et al. (1985). But as the constant portion of the streamfunction does not alter the velocity field, it is not of concern here.
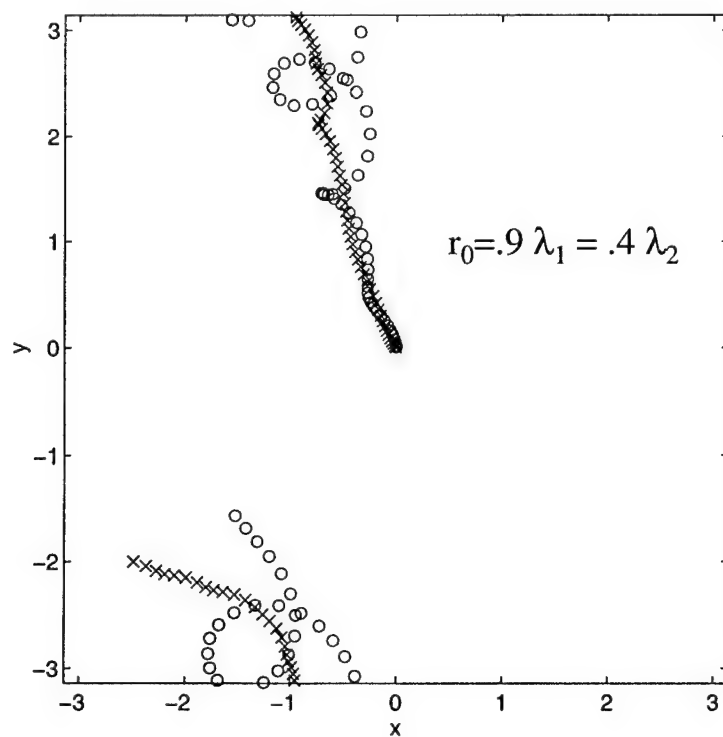
Figure 3.14: A run with with unequal layer depths, $r_0 = .90\lambda_1 = .40\lambda_2$. The upper (x) and lower (o) potential vorticity centroids are shown every time step.

decreased if F_2 is smaller, which is the case when the lower layer is deeper than the upper layer.

Therefore an additional numerical run was made in which the vortex was the same size relative to the upper deformation radius as in case A, but in which the lower layer was four times deeper than the surface layer. The trajectories of the upper and lower PV centroids are shown in the lower panel of figure 3.14. The vortex does separate, as suggested by the above argument. A larger vortex is therefore required for stability, which may partially explain the higher cut-off predicted for the vortex with constant stratification by Gent and McWilliams.

The Gaussian vortex is weakly barotropically unstable to azimuthal mode 2 perturbations (Carton, 1989). However, the twisting instability is a mode 1 barotropic instability, and stabilizing the $m = 2$ mode apparently does not damp it. An additional run was made with a $r_0 = .64\lambda$ vortex with $\psi \propto exp(-(\frac{r}{r_0})^{1.75})$, which is stable to the $m = 2$ instability (Carton, 1989). The vortex also separated (not shown), and on the same time scale as the Gaussian vortex. In fact, the only case found in which the sub-deformation scale vortex did not separate involved a vortex with no outer ring of vorticity (see Appendix A).

As in case A, the components of the total energy for the $r_0 = .64\lambda$ vortex were computed, and are shown in figure 3.15. The separation into baroclinic vortices at $t = 30$ appears as a loss of kinetic and growth of potential energy, but thereafter the components are relatively constant. Recall that the terms represent domain averages, so that each term has contributions from both vortices. The potential energy is less than either kinetic energy term. This is a general feature of layer-trapped potential vortices with equal layer depths; using the expressions for the streamfunctions for the surface vortex in (3.3-3.4), one can write the contribution to the potential and upper layer kinetic energies at wavenumber κ as:
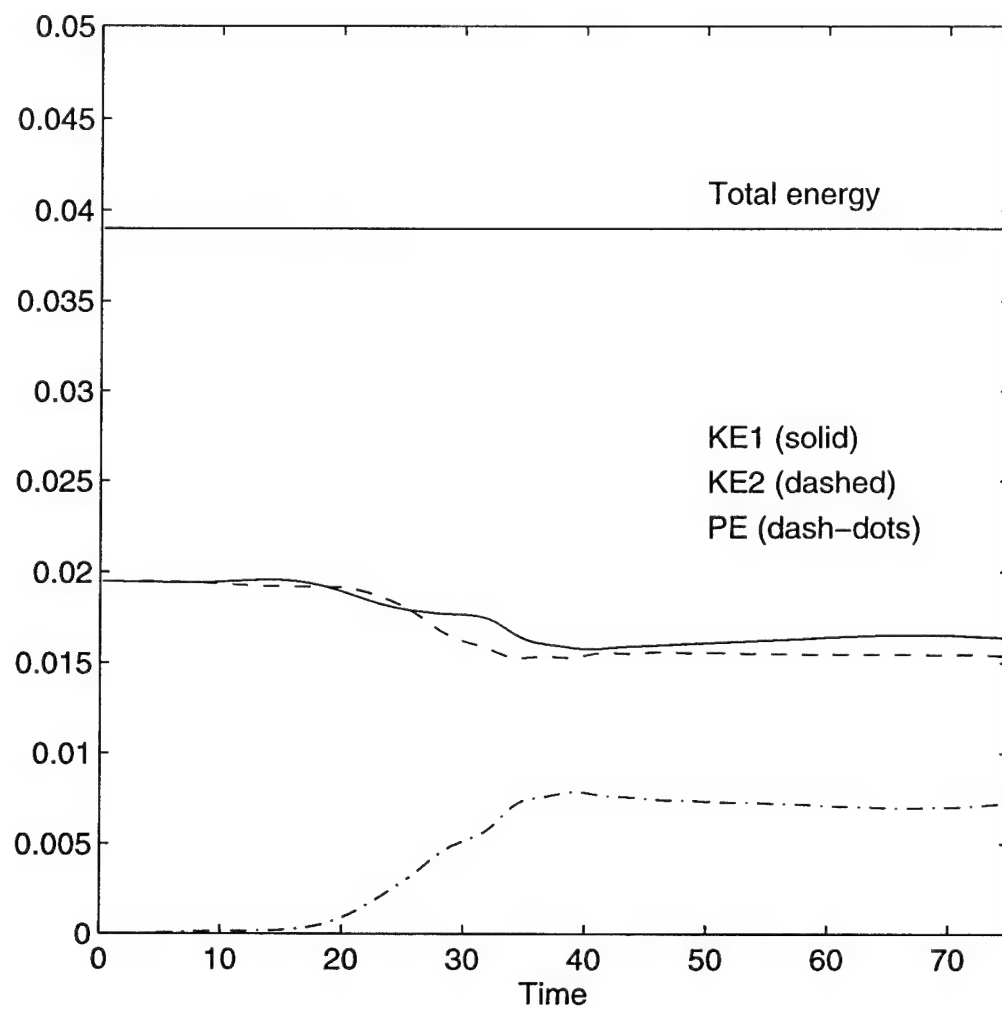
Figure 3.15: The components of the total energy for the $r = .64\lambda$ vortex with $\beta_2 = .018$.

$$KE_1(\kappa) = \frac{\delta}{1+\delta}\kappa^2|\hat{\psi}_1|^2 = \frac{\delta}{1+\delta}\frac{\kappa^2(\kappa^2+F_2)^2\hat{q}_1^2}{\triangle^2} \qquad (3.5)$$

$$PE(\kappa) = \frac{F_2}{1+\delta}|\hat{\psi}_2 - \hat{\psi}_1|^2 = \frac{F_2}{1+\delta}\frac{(\kappa^2\hat{q}_1)^2}{\triangle^2} \qquad (3.6)$$

so that the ratio of $KE_1(\kappa)$ to $PE(\kappa)$ is

$$\frac{(\kappa^2+F_2)^2}{\kappa^2 F_1}. \qquad (3.7)$$

If $F_1 = F_2$, this is always greater than one and so the the sum over all wavenumbers is also greater than one. Thus the potential vortex has more kinetic energy in the primary layer than potential energy.

A subtle aspect of the energy plot in figure 3.15 is that the upper layer kinetic energy and the potential energy oscillate slightly, and are out of phase. This is a result of the conservation of potential vorticity in the surface layer, where changes in relative vorticity must be offset by equal changes in stretching, and is primarily due to undulations in the shape of the surface vortex. The effects of this and the exchange in energy it represents are small in this case, but they will be found to be important in the case of many surface vortices, as seen in the following chapter.

To summarize the results thus far, one finds that the two-layer vortex over a weak slope can be regarded as a pair of vertically aligned potential vortices. If the pair are larger than deformation scale, they remain aligned and move over the topographic slope almost exactly as a one-layer vortex. But if smaller than

68

deformation scale, they separate into layer-trapped potential dipoles, and move rapidly away from one another. The point of transition from barotropic to baroclinic motion at $r_0 \approx \lambda$ is predicted by the linear instability analysis of Gent and McWilliams (1985) and Flierl (1988). The transition was explained here in terms of a heuristic argument about the "overlap" of the constituent vortex streamfunctions.

3.3.3 Case C: $r_0 = .64\lambda$, $\beta_2 = 36$

The potential vorticity and streamfunction fields at an early time and later on are shown in figure 3.16 for the case of the $r_0 = .64\lambda$ vortex with $\beta_2 = 36$. Note that the left hand panels are not at $t = 0$, but shortly thereafter; the $t = 0$ fields are identical to those in figure (3.1). The numerical sponge layer (Chapter 2) was used for this run, due to the great velocity of the departing waves. While the sponge greatly damps re-entrant waves, weak, large-scale waves remain; so the $t = 2.0$ field has been averaged with the fields at $t = 1.9, 2.1$ to reduce the wave contributions. One can see that the temporal evolution is much different than in the previous case (compare the potential vorticity to that in figure 3.12). In particular the lower layer perturbation PV disperses rapidly into topographic waves, while the upper layer potential vorticity remains essentially unchanged. The $t = 0.1$ frame of the lower layer perturbation PV strongly resembles the one-layer case shown in the lower right panel of figure 3.2, and, as in that case, the initial perturbation to the total lower layer PV due to the bottom vortex only weakly disturbs the strong background gradient. Indeed, one might have anticipated a similar evolution in the lower layer, but the stationarity of the upper layer potential vorticity is perhaps less expected. The lower layer streamfunction rapidly disperses also, while the upper streamfunction is only weakly perturbed.

The final state has a surface-trapped vortex which appears to have zero flow

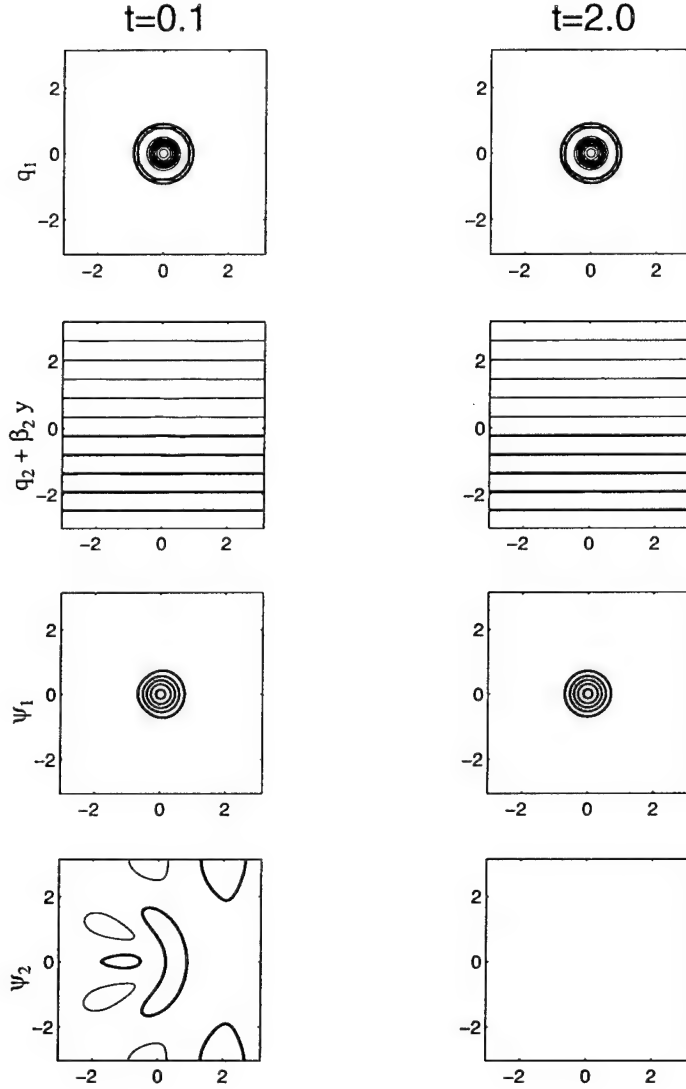Figure 3.16: The fields for the two-layer vortex with $r_0 = .64\lambda$ and $\beta_2 = 36$ at $t = .1$ and $t = 2$. The initial fields, not shown, are identical to those in cases A and B. The upper PV CI $= \pm[1 : 1 : 10]$, the bottom PV CI$= \pm[.3 \ .9 \ 1.5 \ 2.1 \ 2.7]$ and the streamfunction CI $= \pm[1 : 1 : 10]/10$. The $t = 2$ fields are averaged from three realizations, at $t = 1.9, 2, 2.1$.

at depth [2]. In other words, the surface vortex differs from that found in the weak slope case which had zero potential vorticity but non-zero flow in the opposite layer; this vortex does have a slight expression in potential vorticity in the opposite layer, and it is negative.

Due to the severity of the slope, the temporal changes in potential vorticity are essentially linear, which prompts consideration of the linear solution. The linear versions of the two-layer equations (2.1-2.2) are:

$$\frac{\partial}{\partial t} q_1 = 0 \tag{3.8}$$

$$\frac{\partial}{\partial t} q_2 + \beta_2 \frac{\partial}{\partial x} \psi_2 = 0 \,. \tag{3.9}$$

Substituting in $(\psi_1, \psi_2)\ \alpha\ exp(ikx + ily - i\omega t)$ yields two solutions. The first is a propagating mode, the topographic Rossby waves, with

$$\omega = \frac{-\beta_2 k}{\kappa^2} \frac{\kappa^2 + F_1}{\kappa^2 + F_1 + F_2} \tag{3.10}$$

and

$$\hat{\psi}_1 = \frac{F_1}{\kappa^2 + F_1} \hat{\psi}_2 \,. \tag{3.11}$$

---

[2]A choice of weaker contours would reveal an averaged wave signal, but no apparent flow associated with the vortex.

The latter relation signifies that the waves are bottom-intensified, because $\psi_1 \leq \psi_2$. These waves have zero surface potential vorticity, i.e. $q_1 = 0$ identically. This solution is well-known (e.g. Rhines 1970; Pedlosky 1987), however, the equations have a second solution which is less frequently discussed, i.e. a stationary mode with $\omega = 0$. This mode carries the surface potential vorticity. It also has zero lower layer streamfunction, for if not, fluid could move across isobaths which would generate waves, violating stationarity.

An initial value problem on a two-layer topographic β-plane is characterized by the separation into propagating and stationary modes. In other words, the lower layer streamfunction disperses into propagating waves, leaving the surface potential vorticity unchanged. The remaining properties of the stationary flow can be predicted, given these two fields:

$$\hat{\psi}_1 = \frac{-\hat{q}_1}{\kappa^2 + F_1} \tag{3.12}$$

and

$$\hat{q}_2 = F_2\hat{\psi}_1 = \frac{-F_2\hat{q}_1}{\kappa^2 + F_1}. \tag{3.13}$$

The upper layer streamfunction is equivalent to $\hat{\psi}_1(t = 0) - \frac{F_1}{\kappa^2 + F_1}\hat{\psi}_2(t = 0)$, or the portion of the initial streamfunction left over after removal of the projection of the waves onto the surface layer, and is therefore weaker than the initial streamfunction if the lower layer streamfunction is of the same sign. For the barotropic vortex, the upper layer streamfunction is decreased by a factor $\frac{\kappa^2}{\kappa^2 + F_1}$

72

so that vortices larger than deformation scale have less than half the initial flow at the surface, but the loss is less for smaller vortices. Note also that the final lower layer PV is solely due to interfacial stretching caused by the upper layer flow, and therefore reflects the final vortex potential energy.

An important consequence of this prediction for the form of the final vortex is that it does not depend at all on the initial lower layer PV, only on q_1. Thus an initially barotropic vortex and one which initially has no flow at depth will yield the same final vortex (identical to the latter vortex) if the two have the same surface PV. This does not, of course, imply an independence of ψ_2 because ψ_2 in part determines q_1, and the loss of the ψ_1 to waves is directly proportional to ψ_2. However, the importance of q_1 must be emphasized.

The actual surface layer streamfunction and that predicted by linear theory are shown in figure 3.17; again the late observed field is averaged to remove re-entrant waves which are roughly 5% the amplitude of the vortex. The amplitude and scale of the two agree quite well, though the predicted amplitude is somewhat less than observed and the predicted upper layer azimuthal velocity, $\frac{\partial \psi_1}{\partial r}$ changes sign, unlike the observed vortex. These differences persist in runs made without a sponge layer and with higher resolution (128^2 grid points as opposed to 64^2), but are not substantial. The final streamfunction is somewhat weaker than the initial profile, shown at upper left and as the solid line in the cross-section profile at lower right.

The total energy and its components are shown in figure 3.18. Unlike in the $\beta_2 = .018$ case, the total energy is not conserved, owing to removal of the waves by the sponge layer. [3] Likewise, KE_2 is decreasing, but note that it does not decay to zero, revealing that the while the waves have been damped, they have not been obliterated. The waves also contribute to KE_1 and PE (see below),

---

[3] It was noted in Chapter 2 that the sponge only acts on the lower layer perturbation PV. The reason for this is clear now; as the waves have zero surface PV, there is no need to damp q_1.

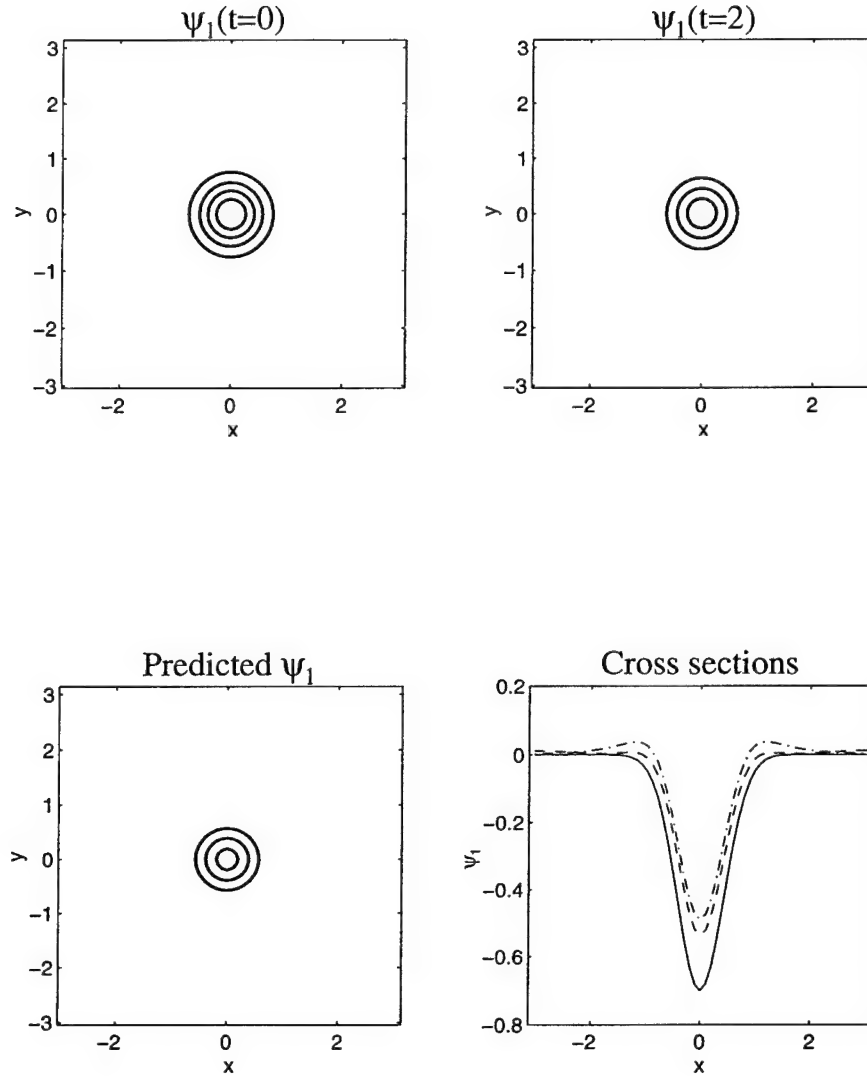Figure 3.17: The initial and final streamfunction with that predicted by a linear evolution; the $r_0 = .64\lambda$ vortex with $\beta_2 = .018$. The CI $= \pm[1 : 1 : 10]/10$. The $t = 2$ fields are averaged from three realizations, at $t = 1.9, 2, 2.1$. In the cross section plot, the solid curve is the inital vortex, the dashed curve is the vortex at $t = 2$ and the dash-dot curve is the predicted profile.

but the largest contribution to these terms in this case is from the vortex itself.

The vortex has more kinetic energy than potential, owing to the fact that it is smaller than deformation scale (see also below). This fact is reflected in the small amplitude of q_2 under the vortex, seen on the right in figure 3.16. The vortex energy components are seen to be oscillating out of phase, as was suggested in Case B; this is due to undulations in the vortex shape, due primarily to continued perturbations by re-entrant waves. As stated before, the fact that the oscillations are out of phase is required by conservation of the surface potential vorticity. The re-entrant waves are weaker than the surface vortex, so that the perturbations to the shape of the latter are fairly small. The deformations are more severe when the vortex is weaker, as in case D.

Vortex and wave energy in the linear case

It is simple to derive the energy of the waves and the vortex from the linear solution, and those terms are presented here for completeness; the uninterested reader may skip ahead to the discussion of intermediate slopes at $r_0 = .64\lambda$.

The question of how much wave energy is generated when a ring impacts a slope has been of some interest, for energetic topographic waves are often witnessed on the continental slope and may play a significant role in variability there (e.g. Thompson and Luyten, 1976; Hogg, 1981; Smith, 1983; Pickart, 1995). Louis and Smith (1982) and later Shaw and Divakar (1991) addressed the issue with models and found significant wave energy generated by a ring on the shelf (the latter authors also noted that one should expect compensation of the vortex after radiation). The energy which is carried off by the waves is easily found from the linear solution discussed above. It is assumed that all of ψ_2 and a portion of $\hat{\psi}_1 = \frac{F_1}{\kappa^2 + F_1}\hat{\psi}_2$ projects onto the waves. Given this, the wavenumber components of the total wave energy follow:
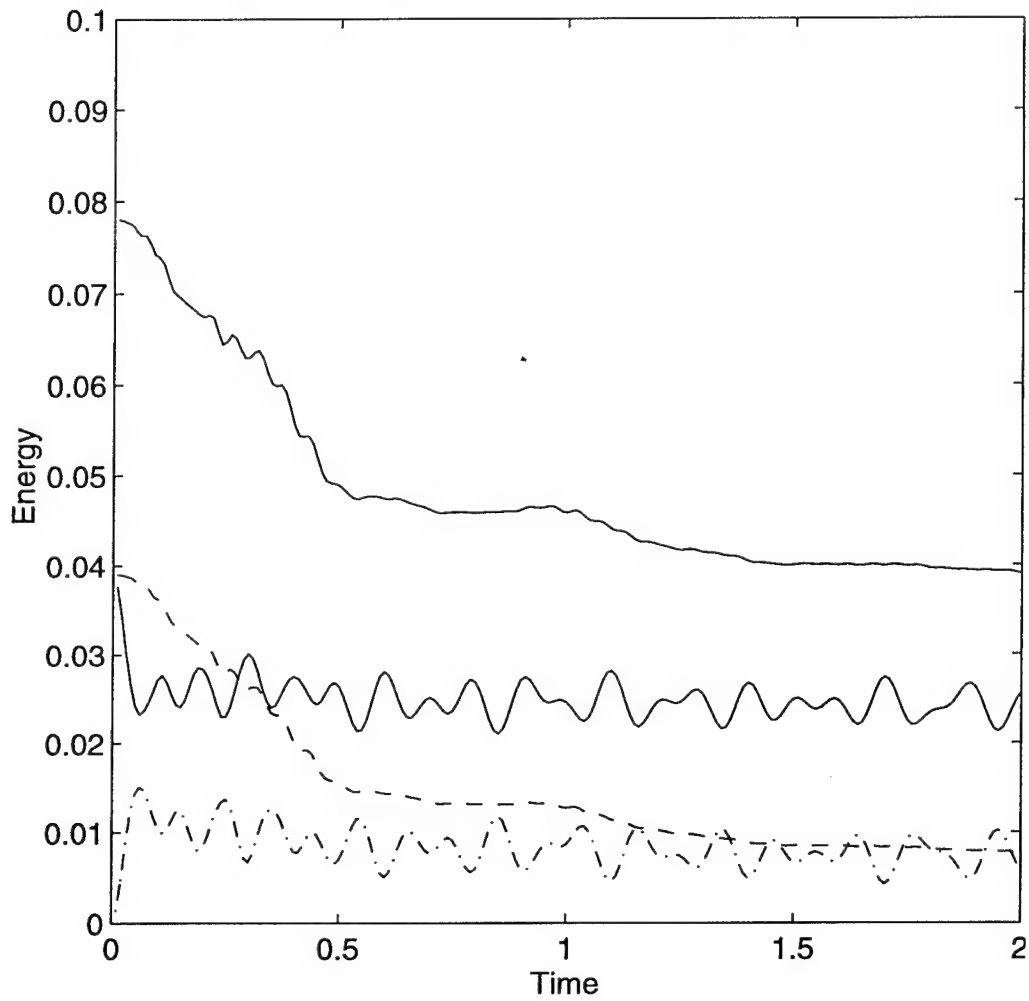
Figure 3.18: The components of the total energy for the $r_0 = .64\lambda$ vortex with $\beta_2 = 36$. The upper solid curve is the total energy, the lower solid curve is KE_1, the dashed curve is KE_2, and the dash-dot curve is PE.

$$KE_{1w}(\kappa) = \frac{\delta}{1+\delta} \frac{\kappa^2 F_1^2}{(\kappa^2 + F_1)^2} |\hat{\psi}_2|^2 , \tag{3.14}$$

$$KE_{2w}(\kappa) = \frac{1}{1+\delta} \kappa^2 |\hat{\psi}_2|^2 , \tag{3.15}$$

$$PE_w(\kappa) = \frac{1}{1+\delta} \frac{\kappa^4 F_2}{(\kappa^2 + F_1)^2} |\hat{\psi}_2|^2 , \tag{3.16}$$

where the subscript (w) denotes wave. The total wave energy is then:

$$TE_w = \sum_k \sum_l \frac{1}{1+\delta} \left(\frac{(\delta F_1^2 + \kappa^2 F_2)\kappa^2}{(\kappa^2 + F_1)^2} + \kappa^2 \right) |\hat{\psi}_2|^2 . \tag{3.17}$$

Thus in the linear system, the total wave energy is not known unless the initial vortex flow at depth is known. This construction is useful if one knows the profile of the vortex prior to its impacting the slope, however it is less useful if the ring is actually formed over topography. The latter scenario may be important as well because Gulf Stream meanders are also suspected to generate topographic waves (Hogg, 1981; Pickart, 1995),

The remaining (vortex) energy can likewise be found:

$$KE_{1v}(\kappa) = \frac{\delta}{1+\delta} \frac{\kappa^2}{(\kappa^2 + F_1)^2} |\hat{q}_1|^2 , \tag{3.18}$$

$$PE_v(\kappa) = \frac{1}{1+\delta} \frac{F_2}{(\kappa^2 + F_1)^2} |\hat{q}_1|^2 , \tag{3.19}$$

77

$$TE_v = \sum_k \sum_l \frac{1}{1+\delta} \frac{(\delta\kappa^2 + F_2)}{(\kappa^2 + F_1)^2} |\hat{q}_1|^2 , \qquad (3.20)$$

where the (v) denotes vortex. Note that the ratio of vortex kinetic energy to potential energy at wavenumber κ is just:

$$KE_{1v}(\kappa)/PE_v(\kappa) = \frac{F_2}{\delta\kappa^2} = \frac{F_1}{\kappa^2} \qquad (3.21)$$

or the (squared) ratio of the deformation radius to vortex scale. For the vortex in Case C, one expects then an excess of KE, as seen in figure 3.18. Vortices larger than deformation scale on the other hand are expected to have an excess of potential energy (see below).

One can also calculate the ratio of wave energy at a given wavenumber to vortex energy, assuming the initially barotropic vortex, as in the numerical examples. This ratio is:

$$TE_w(\kappa)/TE_v(\kappa) = \frac{1}{\delta}(1 + \frac{F_1 + F_2}{\kappa^2}) \qquad (3.22)$$

or $(1 + \frac{2F}{\kappa^2})$ for equal layer depths. This ratio is always greater than one, as the waves take all of the lower layer streamfunction and a portion of the upper. The only case in which the vortex might have more total energy is when the lower layer is shallower than the upper ($\delta > 1$). Other relations may be derived for vortices with different initial vertical structure.

78

3.3.4 Intermediate slopes with $r_0 = .64\lambda$

The case of a sub-deformation scale vortex over two extremes of topographic slope has been considered. Over a weak slope, the initially barotropic vortex was found to break apart by a barotropic instability, and over a strong slope, the vortex rapidly split into a surface vortex and bottom-intensified waves. How do these two scenarios merge over intermediate slopes? Figure 3.19 presents PV plots which are representative of the barotropic vortex after its initial adjustment over various grades of slope. One finds less and less perturbation to the upper layer potential vorticity over steeper slopes, with less translation of the upper vortex. One also finds a more rapid transition to waves in the lower layer.

The differences are related to the interaction between the surface and bottom PV anomalies. As might be deduced from the one-layer case (figure 3.2), increasing $\beta_2 r_0^2/U$ increases the decay rate of the vorticity anomaly in the lower layer; over extreme slopes, the decay effectively occurs before the upper layer PV can react. Over a weak slope, the decay rate is gradual, so that the lower vortex, displaced from the upper vortex as it begins to translate, can interact with the upper vortex. The result is the severe deformation of the outer rings of vorticity, and the formation of layer-trapped dipoles.

Over intermediate slopes, one finds that the lower anomaly separates faster from the upper vortex, due to the greater translational velocity (recall $|u| \propto \beta_2^{1/2}$). This, coupled with the faster decay time of q_2, decreases the impact on the surface vortex. The outer ring of vorticity is disrupted in the $\beta_2 = .18$ case, and less so in the $\beta_2 = 1.8$ when the decay of the lower vortex is even more rapid. Thus the change in evolution can be linked to changes in the lower layer vortex, which in turn could be inferred from the one-layer vortex results. The shift in the character of the runs thus also occurs around (non-dimensional) $\beta_2 = 1$.

In the weak slope case, the initially barotropic vortex can be conceptualized as a pair of aligned *potential* vortices, so that the surface vortex has a non-zero

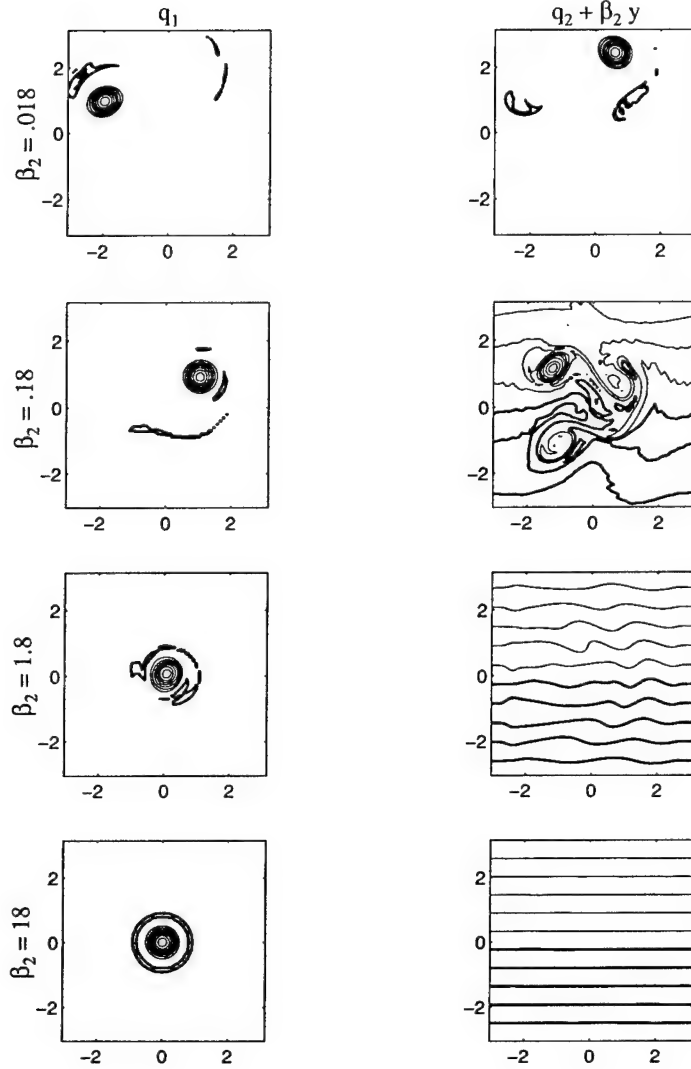Figure 3.19: The upper and lower potential vorticity for the $r_0 = .64\lambda$ vortex with various bottom slopes. The upper PV CI $= \pm[1:1:10]$ for q_1 and bottom PV CI were chosen to yield 15 contours in the range of the minimum and maximum values of $q_2 + \beta_2 y$. The corresponding times are $t = 45$ ($\beta_2 = .018$), $t = 20$ ($\beta_2 = .18$), $t = 4$ ($\beta_2 = 1.8$), $t = .5$ ($\beta_2 = .018$).

flow at depth if the vortex separates. In the strong slope case however, the vortex is really a surface-trapped *relative* vortex because the flow at depth must cease if the vortex is to be steady. Thus the transition in slope heralds a transition in the vertical structure of the resulting vortex or vortices as well.

Visually, the transition would be far less dramatic if the vortex were smaller. As shown by Flierl (1988), the twisting instability is also bounded by a neutral stability curve for smaller vortices; this is because the interaction between surface and bottom anomalies is weaker for vortices progressively smaller than the deformation radius, as one can readily see in the expression for ψ_2 for the surface potential vortex in (3.4); $\hat{\psi}_2 \propto \frac{F_2}{\kappa^4}$ when $\kappa^2 >> F_1, F_2$, so that the surface vortex has vanishing flow at depth and is consequently unable to advect the lower vortex, and vice versa for the bottom vortex. Thus if the runs had been made with a sufficiently small vortex, q_1 would not have evolved. In this case, varying β_2 would not have affected the surface vortex.

3.3.5   Case D: $r = 2.5\lambda$, $\beta_2 = 36$

It was noted in the previous sections that the loss of ψ_1 to the waves and the strength of interaction between the upper and lower portions of the vortex depend on the ratio r_0/λ. Thus it is of interest to consider a vortex which is substantially larger than the deformation radius, to see what happens when the surface vortex is greatly weakened by the radiation.

The potential vorticity plots in figure 3.20 are from such a run, with $r_0 = 2.5\lambda$ and $\beta_2 = 36$. Note again the late time plot shows an average of the fields at $t = 1.9, 2.0, 2.1$. The propagating waves are now nearly barotropic, as can be seen in the streamfunction plots at $t = 0.1$, and thus the final surface vortex streamfunction is greatly weakened ($t = 2.0$). However, again there is little change in q_1; the loss in surface relative vorticity has been balanced by a gain

in stretching. Thus, although the vortex is substantially larger than deformation scale, the decoupling effect of the slope is strong enough to prevent barotropy. This effect is considered more quantitatively in what follows.

One can again apply the linear model to predict the final streamfunction, and the result is shown in figure 3.21. The amplitude and size of the vortex is predicted well, again suggesting that linear dynamics are appropriate. The observed streamfunction at $t = 2$ has been averaged as in the previous figure, because the residual waves now have an amplitude in layer one comparable to that of the vortex.

This can also be seen in the plot of the energy components, shown in figure 3.22. The upper plot shows the full components, while the lower plot shows only the vortex contributions to the potential and surface kinetic energy (as shown above). The greater decline in KE_1 reflects the loss to the near-barotropic waves, and the loss of total energy is thus also greater than in the $r = .64\lambda$ case. The energy appears roughly equipartitioned by $t = 1$, but in fact the vortex potential energy exceeds its kinetic energy, as shown in the lower panel and as one would expect for surface-trapped vortex larger than deformation scale, given the previous energy arguments (see 3.21). The vortex kinetic energy is less than half the total surface kinetic energy; the residual waves are thus equally energetic and the departed waves far more energetic. As before, the vortex energy oscillations are clearly evident. In contrast, the wave energies are not oscillating (note that KE_2 is much "flatter") because perturbation PV is not conserved in layer 2 (which has consequences in the turbulence experiments of the following chapter).

It is interesting to contrast the changes due to the transition in r_0/λ in the $\beta = 36$ case with that in the $\beta = .018$ case. In the latter, the boundary between translating barotropic solutions and solutions which separated into baroclinic vortices was found to be quite distinct; under the criteria of separation during
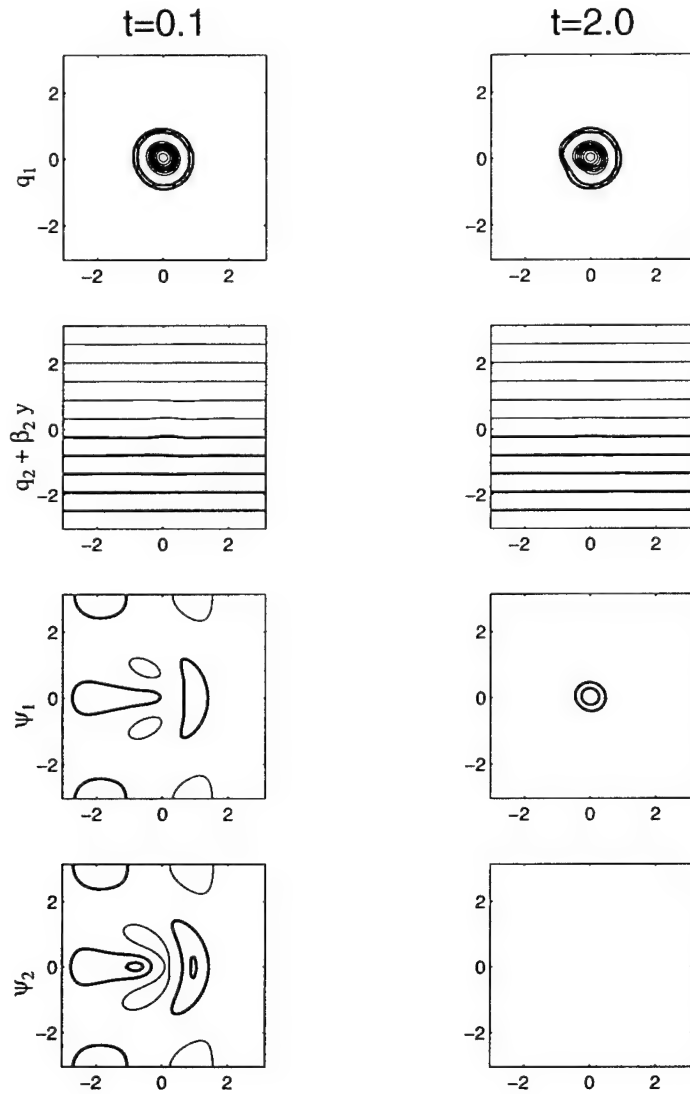
82

Figure 3.20: The fields for the two-layer vortex with $r_0 = 2.5\lambda$ at $t = .1$ and $t = 2$. The upper PV CI $= \pm[1 : 1 : 10]$, the bottom PV CI$= \pm[.3 \ .9 \ 1.5 \ 2.1 \ 2.7]$ and the streamfunction CI $= \pm[1 : 1 : 10]/10$. The $t = 2$ fields are averaged from three realizations, at $t = 1.9, 2, 2.1$.
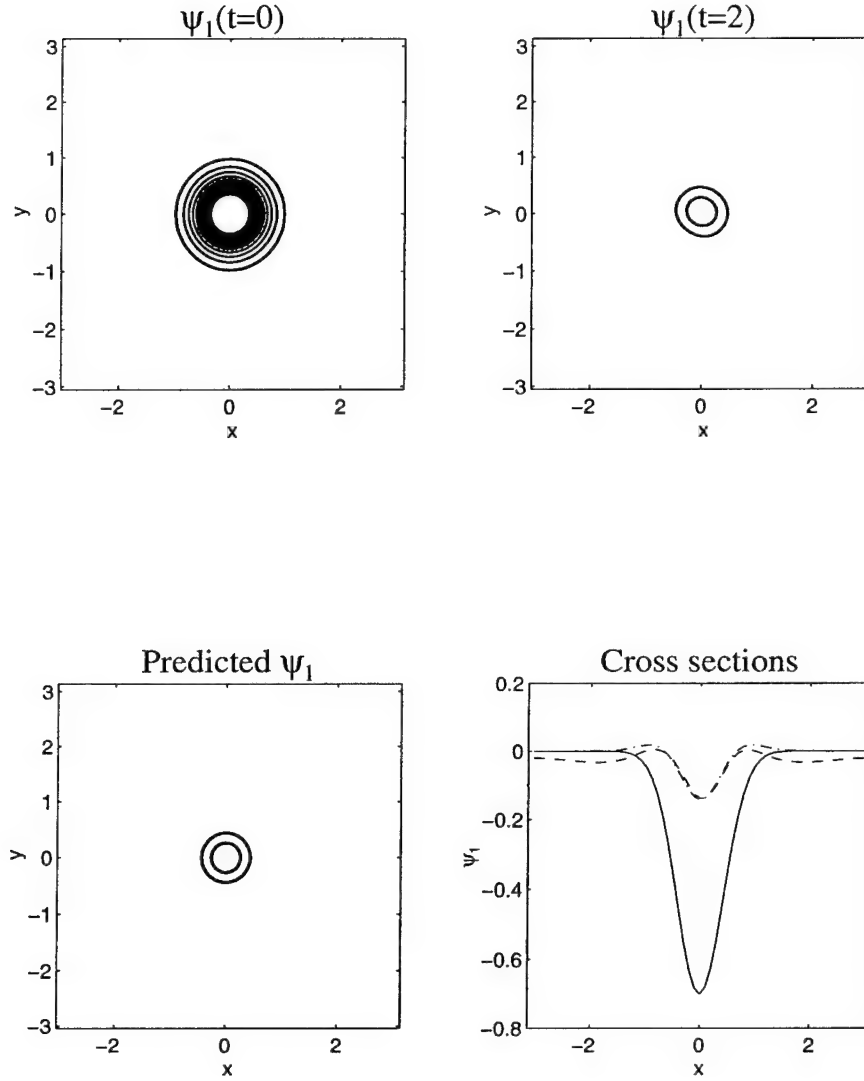
Figure 3.21: The initial and final streamfunction with that predicted by a linear evolution, for the $r_0 = 2.5\lambda$ vortex with $\beta_2 = 36$. The CI $= \pm[1:1:10]/20$. The $t = 2$ fields are averaged from three realizations, at $t = 1.9, 2, 2.1$. In the cross section plot, the solid curve is the inital vortex, the dashed curve is the vortex at $t = 2$ and the dash-dot curve is the predicted profile.

84

Figure 3.22: The components of the total energy (upper panel) for the $r = 2.5\lambda$ vortex with $\beta_2 = 36$. Shown are total energy (upper solid), KE_1 (lower solid), KE_2 (dashed), and PE (dash-dot). The lower panel shows the vortex energies, KE_1 (solid) and PE (dash-dot). The negative energies in the lower plot are an artifact of subtracting the waves from ψ_1 to determine the vortex energies.

85

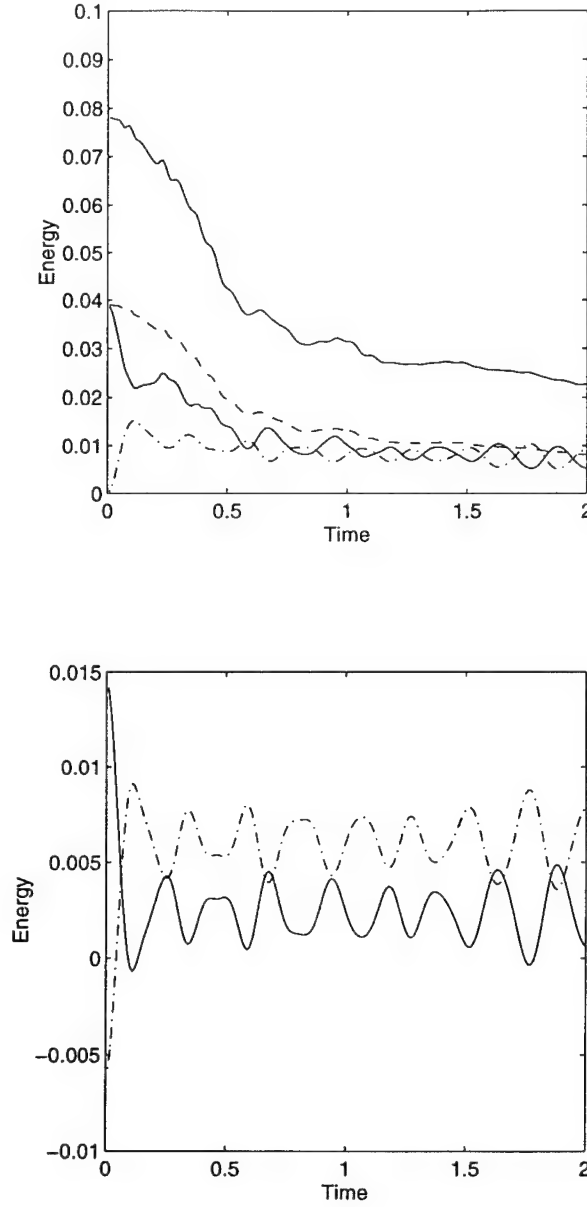the length of the numerical run, vortices with $r_0 = .82\lambda$ separated and those with $r_0 = .9\lambda$ did not. The figure 2 of Gent and McWilliams (1985) shows a similarly rapid variation in growth rate over a small range of vortex sizes. In contrast, essentially the only difference between the $r_0 = .64\lambda$ and $r_0 = 2.5\lambda$ cases over the steep slope is the relative amount of energy taken up by the stationary vortex and the propagating waves. Both cases yield a baroclinic vortex and bottom-intensified waves. This reflects the fact that when $\beta_2 > 1$, the slope favors baroclinic surface motion, regardless of the scale of motion. This is examined further below, when the role of the slope in baroclinic instability is discussed.

3.3.6 Intermediate slopes with $r_0 = 2.5\lambda$

Representative late-time PV plots in four cases spanning weak to strong slopes for the $r_0 = 2.5\lambda$ vortex are shown in figure 3.23. The behavior in the $\beta_2 = .18$ case appears similar to that in the weaker slope case, i.e. the vortex is aligned vertically and translating to the northwest. However, the cross-isobath displacement has weakened the lower core, suggesting that the coupled motion must cease at a later time when the lower vortex disperses (this could not be proven with this run however because the vortex soon after began to interact with its own wake, which altered its trajectory). The vortex is much more deformed than in the weaker slope case, and the outer ring of vorticity has been stripped off as a consequence.

When the slope is $O|1|$ or larger, the decay of the bottom vortex happens more rapidly. One might expect only a surface vortex after some initial adjustment. However, as seen in the figure, the transition over the $O|1|$ slope is found to be a destructive one for the surface vortex. At the late time, the surface vortex has fissioned into two portions, and the lower layer is still active, suggesting wave radiation from the surface vortices.

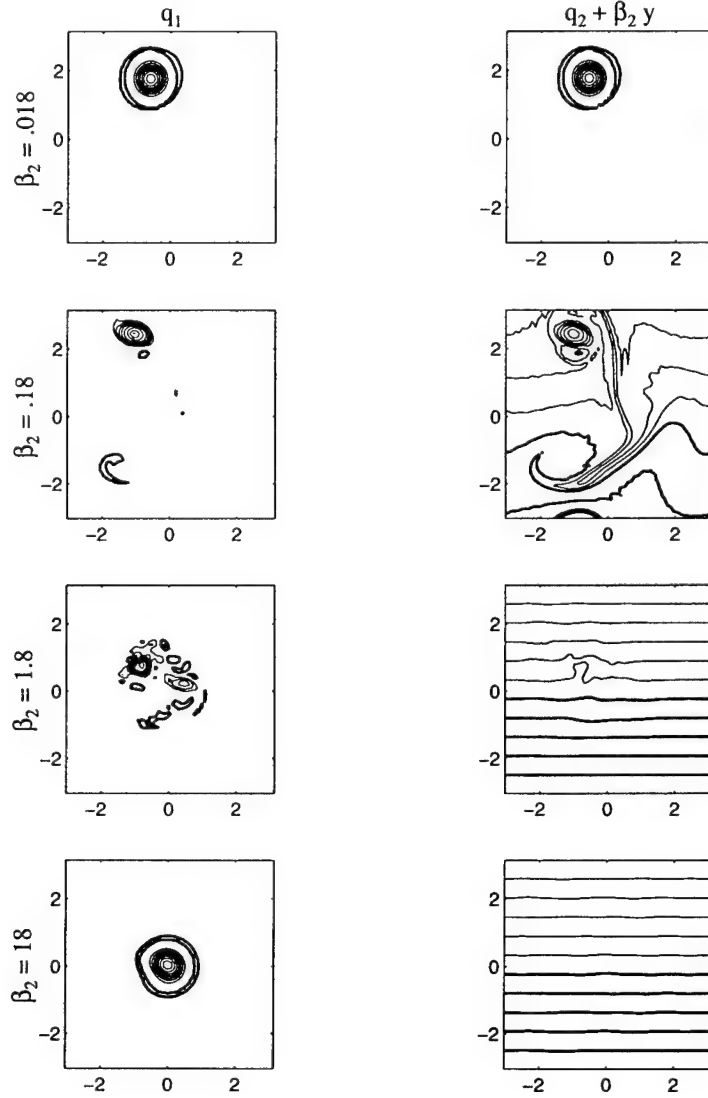Figure 3.23: The upper and lower potential vorticity for the $r_0 = 2.5\lambda$ vortex with various bottom slopes. The CI $= \pm[1:1:10]$ for q_1 and the bottom PV CI were chosen to yield 15 contours in the range of the minimum and maximum values of $q_2 + \beta_2 y$. The corresponding times are $t = 37.5$ ($\beta_2 = .018$), $t = 20$ ($\beta_2 = .18$), $t = 10$ ($\beta_2 = 1.8$), $t = .5$ ($\beta_2 = .018$).

The potential vorticities for the case with $\beta_2 = 1.8$ at several successive times are shown in figure 3.24. In addition to the sponge, a filter was applied at $t = 5$ to remove the energetic re-entrant waves, [4] so that flow in the lower layer after this time was directly forced by the upper vortices. Initially, the upper vortex is displaced and deformed. The stretched surface vortex then appears to break into two portions, with significant simultaneous filamentation and dissipation of the surface PV. Thereafter, the stronger vortex rotates and is deformed further, and appears to be radiating waves in the lower layer.

There are two phenomena which contribute to the complicated evolution in this case. First, there is the intense shearing of the upper vortex during the separation from the lower. Secondly, the final vortex is surface-trapped and larger than deformation scale, and is thus potentially baroclinically unstable.

Figure 3.25 shows the shearing of the upper potential vorticity anomaly by the dispersing lower vortex. The left column is the surface potential vorticity, the center column is the vortex streamfunction defined as $\hat{\psi}_{1v} \equiv \frac{-\hat{q}_1}{\kappa^2 + F_1}$, and the right column the upper layer portion of the "waves", $\hat{\psi}_{1w} \equiv \frac{F_1 \hat{\psi}_2}{\kappa^2 + F_1}$. The latter decomposition is only strictly valid after the lower vortex has dispersed, but is useful for illustration. Clearly the wave portion of the upper layer streamfunction is more intense than the vortex portion, so that one could approximate the surface PV equation with the linear approximation:

$$\frac{\partial}{\partial t} q_1 + J(\psi_{1w}, q_1) = 0 .$$ (3.23)

Such an equation describes the advection of a passive tracer by a background

---

[4]Specifically, the lower layer PV was "reset": $\hat{q}_2 \rightarrow \frac{-F_1 \hat{q}_1}{\kappa^2 + F_1}$ so that only the stretching due to the vortices in the upper layer is retained. This may be justified because, in the ocean, topographic waves generally radiate far from the vortex rather than circulating and re-interacting.
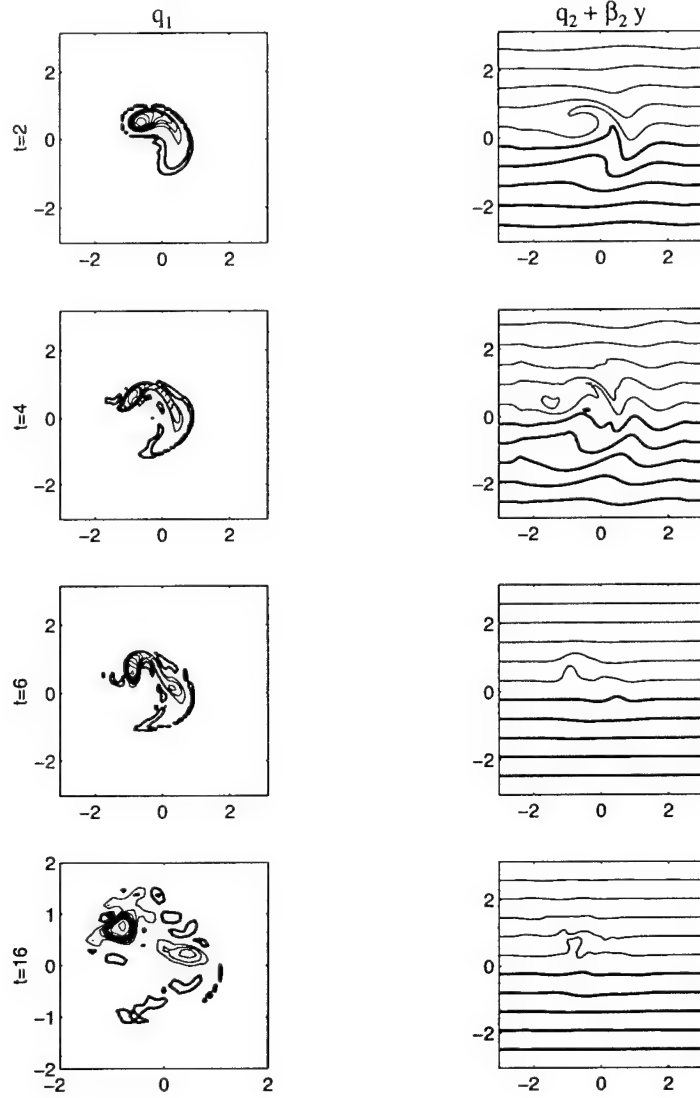
Figure 3.24: The upper and lower PV for the $r_0 = 2.5\lambda$ case with $\beta_2 = 1.8$. The q_1 CI $= \pm[1 : 1 : 10]$ and the q_2 CI $= \pm[.3.81.422.6]$. Note that the scale is expanded in the lower left figure for detail. The wave field has been removed at $t = 5$ (see text).
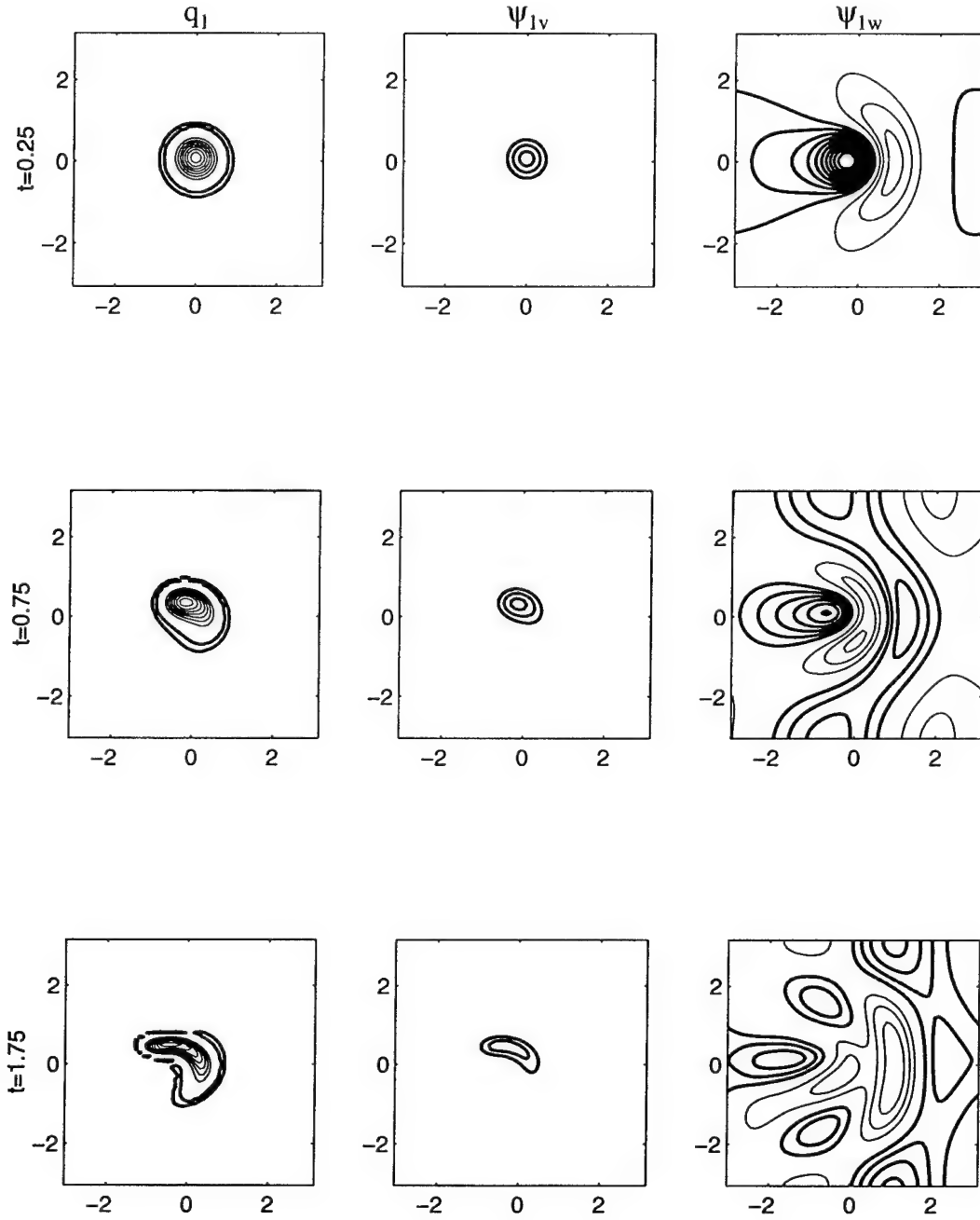
Figure 3.25: The shearing of the upper vortex during separation for a vortex with $r_0 = 2.5\lambda$ and $\beta_2 = 3.6$. The larger slope was chosen to accentuate the effect. The upper layer PV is at left, the vortex streamfunction is in the middle, and the "wave" projection in layer one at right. The q_1 CI= $\pm[1:1:10]$ and the stream CI $= \pm[1:1:10]/10$.

flow (e.g. Babiano et al., 1987), and the $t = 1.75$ frame also seems to suggests the straining of a passive tracer.

Given the wave/vortex streamfunction decomposition, one can derive an approximate scaling for the deformation of q_1. Under the decomposition, the upper layer PV equation becomes:

$$\frac{\partial}{\partial t}q_1 + J(\psi_{1v}, q_1) + J(\psi_{1w}, q_1) = 0 \,. \tag{3.24}$$

Scaling the terms again assuming the time scale of the waves, one obtains parameters for the Jacobians: $\frac{U_{1v}}{\beta_2 r^2}$ and $\frac{U_{1w}}{\beta_2 r^2}$. For deformation to occur, the third term is larger than the second and must be $O|1|$ (or else $\frac{\partial}{\partial t}q_1 \approx 0$). Using $\hat{\psi}_{1w} = \frac{F_1}{\kappa^2 + F_1}\hat{\psi}_{2w}$, these conditions reduce to the simultaneous necessary conditions:

$$\frac{F_1 r_0^2}{1 + F_1 r_0^2}\frac{U_2}{\beta_2 r_0^2} = O|1| \tag{3.25}$$

and

$$F_1 r_0^2 \frac{U_2}{U_1} > 1 \,. \tag{3.26}$$

If the vortex is barotropic, it must be larger than deformation scale and the nondimensional β_2 must be $O|1|$. If $\beta_2 \gg 1$, then the waves disperse too rapidly

91

to affect q_1 as in case D; if $\beta_2 \ll 1$, the wave decomposition is not proper because the lower vortex is not dispersing, and we find the vortex translates barotropically as in the weaker slope cases. In other words, deformation occurs in a relatively small region of the barotropic vortex parameter space (and may not occur at all for vortices with initially weak deep flow.)

In the second portion of this chapter, the relationship between the slope and baroclinic instability is examined, and it is found that a strong slope ($F_2 U_1 / \beta_{2dim} \ll 1$) can stabilize a surface vortex. One has two choices for U_1 with the initially barotropic vortex: the initial value, or that after wave radiation. The latter can be predicted by the linear model: $\hat{\psi}_{1f} = \frac{\kappa^2}{\kappa^2 + F_1} \hat{\psi}_{1i}$. Wave radiation causes about a 70% decrease in the magnitude of ψ_1 (and U_1) for the vortex with $r_0 = 2.5\lambda$. The vortex in case D has $F_2 U_1(0)/\beta_2 \approx 0.18$ and $F_2 U_1(t_f)/\beta_2 \approx 0.05$ and thus is likely to be stable. However, the $\beta_2 = 1.8$ case has $F_2 U_1(0)/\beta_2 \approx 3.6$ and $F_2 U_1(t_f)/\beta_2 \approx 1$ and is thus likely to be unstable, even after radiation. One finds that the vortex of figure 3.24 appears to radiate waves (and so lose energy) later on, but does not break up further.

To summarize the large vortex runs, again there is a qualitative change in behavior around $\beta_2 = 1$. The barotropic vortex remains barotropic when $\beta_2 \ll 1$; when $\beta_2 \gg 1$, the behavior is similar to that of the $r = .64\lambda$ vortex, but for the greater weakening of the surface vortex by wave radiation. However, the transition region is quite different as two additional effects become important: shearing of the surface vortex by the near-barotropic waves, and baroclinic instability of the final vortex. The former effect was argued to be pronounced due to the strength of the deep vortex (due to the choice of an initially barotropic vortex). For the more commonly found surface-intensified oceanic ring, the instability is more likely to be important.

3.4 Two-layer results: A surface vortex

In cases in which the vortex is initially surface-intensified, or when the bottom slope is large enough to disperse the lower portion of the initial vortex, and in which the vortex scale exceeds the deformation scale, baroclinic instability of the surface vortex may be important. If the vortex is unstable, energy will be lost to the lower layer or the surface vortex may break into smaller vortices, but as will be seen, a steep bottom slope tends to stabilize the vortex.

The stability of a baroclinic vortex has been studied previously in the laboratory by Saunders (1973) and Griffiths and Linden (1981), and theoretically by Ikeda (1981), Pedlosky (1985), Flierl (1988) and Helfrich and Send (1988). The general picture which emerges is that vortices which are sufficiently larger than deformation scale and in which the barotropic circulation is not overly strong are baroclinically unstable. The most unstable azimuthal mode increases with vortex scale. In the finite amplitude state, the larger vortices may break into separating baroclinic dipoles (Ikeda, 1981; Helfrich and Send, 1988) of the sort categorized by Flierl et al. (1980), finite-area versions of the "hetons" of Hogg and Stommel (1985).

The stability of a vortex over a slope has received less attention. Hart (1975) considered the linear stability of a surface-trapped circular flow in two layers in a circular basin. He found that a weak slope tended to destabilize the surface flow by shifting the short wave cut-off for instability to smaller wavelengths. However, he also noted that steeper slopes damped growth rates, and postulated that the vortex would become completely stable in the limit of a very large slope when fluid trajectories would be constrained to be along isobaths.

One can see similar slope-induced effects in the (simpler) case of a surface-trapped parallel flow at an angle to the isobaths. The linear growth rate is found exactly as with a non-zonal flow on the β-plane (Pedlosky, 1987, section 7.13).

The absence of a PV gradient in the surface layer means that a constant flow at the surface is a steady solution and need not be balanced by a forcing function. Following Pedlosky (but with a slope) the linearized two-layer equations with $\bar{u}_1 = U$, $\bar{v}_1 = V$, $\bar{u}_2 = 0$, $\bar{v}_1 = 0$, and a disturbance $(\psi_1, \psi_2) = (A_1, A_2) \, e^{ikx+ily-i\sigma t}$ are:

$$A_1[(\sigma - U_1 k - V_1 l)(\kappa^2 + F_1) + F_1(U_1 k + V_1 l)] - A_2 F_1[\sigma - Uk - Vl] = 0 \quad (3.27)$$

$$A_2[\sigma(\kappa^2 + F_2) + \beta_2 k - F_2(U_1 k + V_1 l)] - A_1 F_2 \sigma = 0 \qquad (3.28)$$

where $\kappa^2 = k^2 + l^2$ is the total squared wavenumber. As in Pedlosky, the following substitutions are made to simplify the equations:

$$c \equiv \frac{\sigma}{\kappa} \quad , \quad U \equiv \frac{U_1 k + V_1 l}{\kappa} \quad , \quad \eta_2 \equiv \frac{\beta_2 k}{\kappa} \qquad (3.29)$$

so that (3.27-3.28) become:

$$A_1[(c - U)(\kappa^2 + F_1) + F_1 U] - A_2 F_1(c - U) = 0 \qquad (3.30)$$

$$A_2[c(\kappa^2 + F_2) + \eta_2 - F_2 U] - A_1 F_2 c = 0 \,. \qquad (3.31)$$

Non-trivial solutions for the A_i are obtained when:

$$c = \frac{U(\kappa^2 + 2F_2)}{2(\kappa^2 + F_1 + F_2)} - \frac{\eta_2(\kappa^2 + F_1)}{2\kappa^2(\kappa^2 + F_1 + F_2)} \pm \frac{\sqrt{\gamma}}{2(\kappa^2 + F_1 + F_2)}. \qquad (3.32)$$

where the radical, γ, is given by:

$$\gamma \equiv (\kappa^2 + F_1)^2\eta_2^2 + 2U\kappa^2[\kappa^4 + F_1\kappa^2 - 2F_1F_2]\eta_2 + U^2\kappa^4[\kappa^4 - 4F_1F_2]. \qquad (3.33)$$

Growth of the disturbance occurs when $\gamma < 0$. For the flat bottom case, this requires $\kappa^2 < 2\sqrt{F_1F_2}$ or the scale of motion exceeds the mean deformation scale. Small values of η_2 can destabilize the flow, as in Hart (1975), because the term linear in η_2 in (3.33) is negative when U is negative; thus smaller scales (larger κ^2) may be unstable over a weak slope. A strong slope can stabilize the flow by making (3.33) always positive. Assuming equal layer depths and a vortex approximately deformation scale, the ratio of the third and first terms is $(\frac{FU}{\eta_2})^2$, so if Λ (defined with η_2) is smaller than one, the radical is likely to be positive.

However, there is a catch because the stabilizing effect depends on the orientation of the flow due to the k-dependence of η_2 (in relations 3.29). In particular, a disturbance with $k = 0$ is always unstable if $l^2 < 2\sqrt{F_1F_2}$. In this case the particle motion is parallel to the isobaths, so that the disturbance effectively does not feel the slope. The same is true on the β-plane, a central reason for why nonzonal flows are more unstable than their zonal counterparts (Kamenkovich and Pedlosky, 1996).

While the zonal flow instability predicts similar slope-induced effects to those described by Hart for a vortex over a slope, one expects that the vortex case

95

may be more complicated. For instance, the sign of the "meridional" gradient of surface PV is different on the "north" and "south" sides of the vortex, so it might seem that a slope would only be able to stabilize one side of the vortex. Also, the orientation of growing disturbances with respect to the isobaths will change if the azimuthal phase speed is nonzero, which in turn could alter the instability of the $k = 0$ mode.

Several numerical runs were made with surface vortices. The streamfunction ($\psi_1 = -.7exp(-(\frac{r}{0.6})^2)$, and $\psi_2 = 0$) is the surface portion of the previous barotropic vortex. Zero bottom flow was chosen to avoid wave-induced deformation of the surface vortex. The main case had a vortex equal in size to the "large" vortex, i.e. $r_0 = 2.5\lambda$. In addition, a perturbation of azimuthal mode 2 was added to the resulting surface relative vorticity at 20% of the amplitude of the surface relative vortex (mode 2 is the fastest growing for this size vortex over a flat bottom; Flierl (1988)). The vortex is stronger than that obtained after wave radiation in the barotropic $r_0 = 2.5\lambda$ cases, but will suffice to illustrate the dependence of the instability on the slope.

Three representative cases are presented in figures (3.26, 3.27, 3.28). The flat bottom case (fig 3.26) is representative of the instability: the large surface-trapped vortex splits into two deformation-scale baroclinic dipoles which move away from one another. Each dipole consists of a surface cyclonic potential vortex and a bottom anti-cylconic vortex displaced horizontally from it. A small surface-trapped potential vortex remains behind, at center, so three surface vortices have been produced by the instability. In general the evolution here closely resembles that in figures (7-8) of Ikeda (1981) and figure 6 of Helfrich and Send (1988).

Over a moderate slope instability still occurs, and on the same time scale (figure 3.27)[5]. The slope was such that $\Lambda = 1.8$, or alternately $\frac{\beta_{2dim}r_0^2}{U_1} = 3.6$.

---

[5]This run is not meant to illustrate destabilization by the slope. To illustrate that effect, one would have to consider a smaller vortex which was stable over a flat bottom.
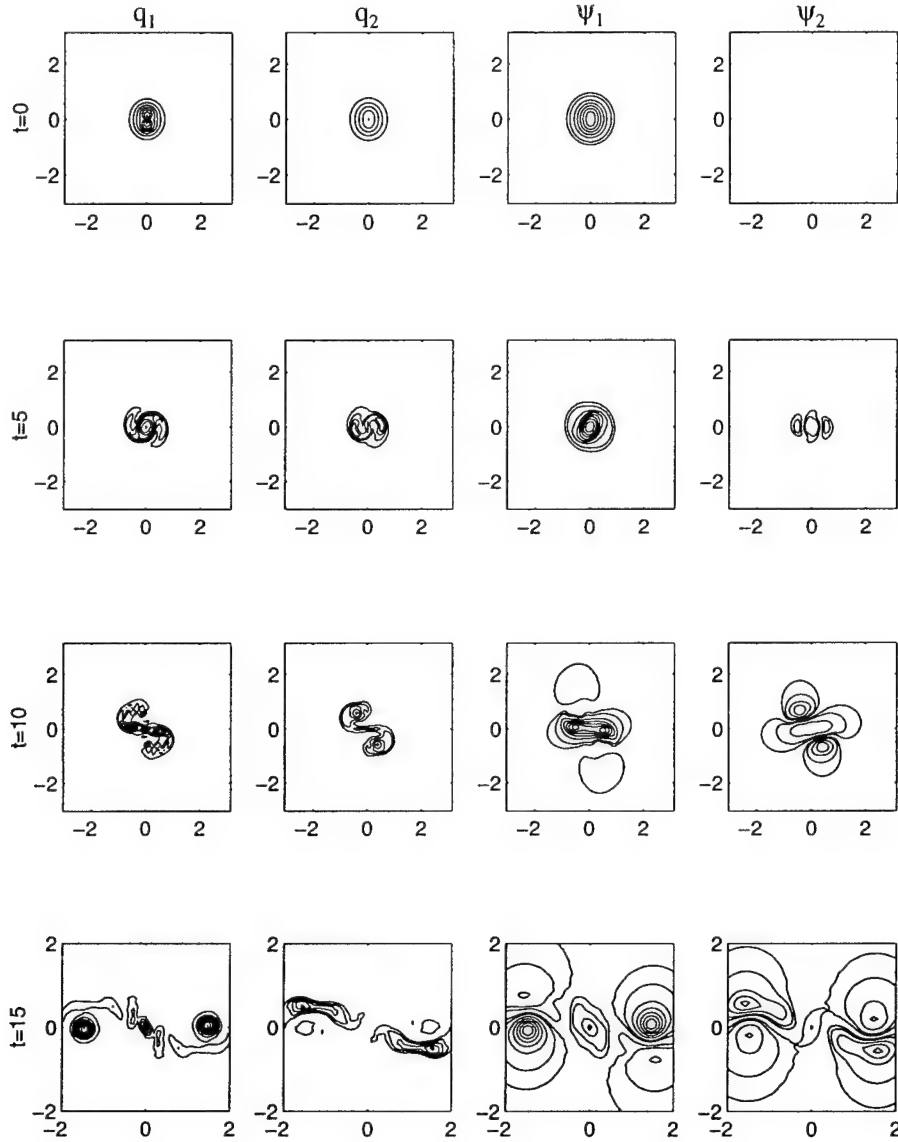
Figure 3.26: A surface-trapped vortex ($\psi_1 = -.7exp(-(\frac{r}{2r_0})^2)$, and $\psi_2 = 0$) over a flat bottom with $r_0 = 2.5\lambda$. From left to right are the surface PV, deep PV, surface streamfunction, and deep streamfunction. The surface PV contour intervals are C.I. = $\pm[5 : 5 : 50]$; the bottom PV CI= $\pm[.3 \ .9 \ 1.5 \ 2.1 \ 2.7]$; the streamfunction C.I. = $\pm[.05 \ .1 : .1 : 1]$. Different axes are used in the bottom row for detail.

There are closed contours of lower layer PV at $t = 0$ as the interface contribution to q_2 overwhelms the slope contribution immediately beneath the vortex, and indeed the slope does not block instability. Plots of the energy (see below) reveal that the loss in potential energy in this case is of the same magnitude and occurs as rapidly as in the flat-bottom case. Thus the slope has not appreciably altered the domain-averaged transfer of energy.

However, there are qualitative differences between this and the flat-bottom cases. Unlike the flat-bottom case, instability does not yield baroclinic dipoles; rather, the slope is large enough ($\frac{\beta_{2dim} r_0^2}{U_2} > 1$; Chapter 3) so that radiation at depth is favored over coherent vortex formation, hence the lower vortices disperse. Likewise, the surface vortices are unable to move without the deep vortices; the surface PV is fractured, but remains more or less local. The break-up of the q_1 field is apparently quite turbulent, because there is much more small-scale structure than in the flat-bottom case. At later times, one finds that three long-lived surface vortices remain, however they are smaller than their flat-bottom counterparts.

The defeat of baroclinic dipole formation does not imply that the energy remains local however, for the dispersing topographic waves carry off energy, as in the strong slope cases in Chapter 3. These waves can be seen in the streamfunction fields at $t = 10$ and $t = 15$ in figure (3.27)[6]. In that the deep disturbances are radiated away, the instability resembles the "radiating instability" on the β-plane discussed by Dickinson and Clare (1973), Talley (1983) and Kamenkovich and Pedlosky (1996). As discussed in the last reference, unstable flows generally have trapped and untrapped growing disturbances, but only the latter can transport energy away from the primary current. Non-trapped disturbances may be important in explaining eddy kinetic energy in parts of the ocean far from the unstable boundary currents. The radiating modes also reduce available potential

---

[6]No sponge was used in this case, the waves are seen to re-enter the right side of the domain.
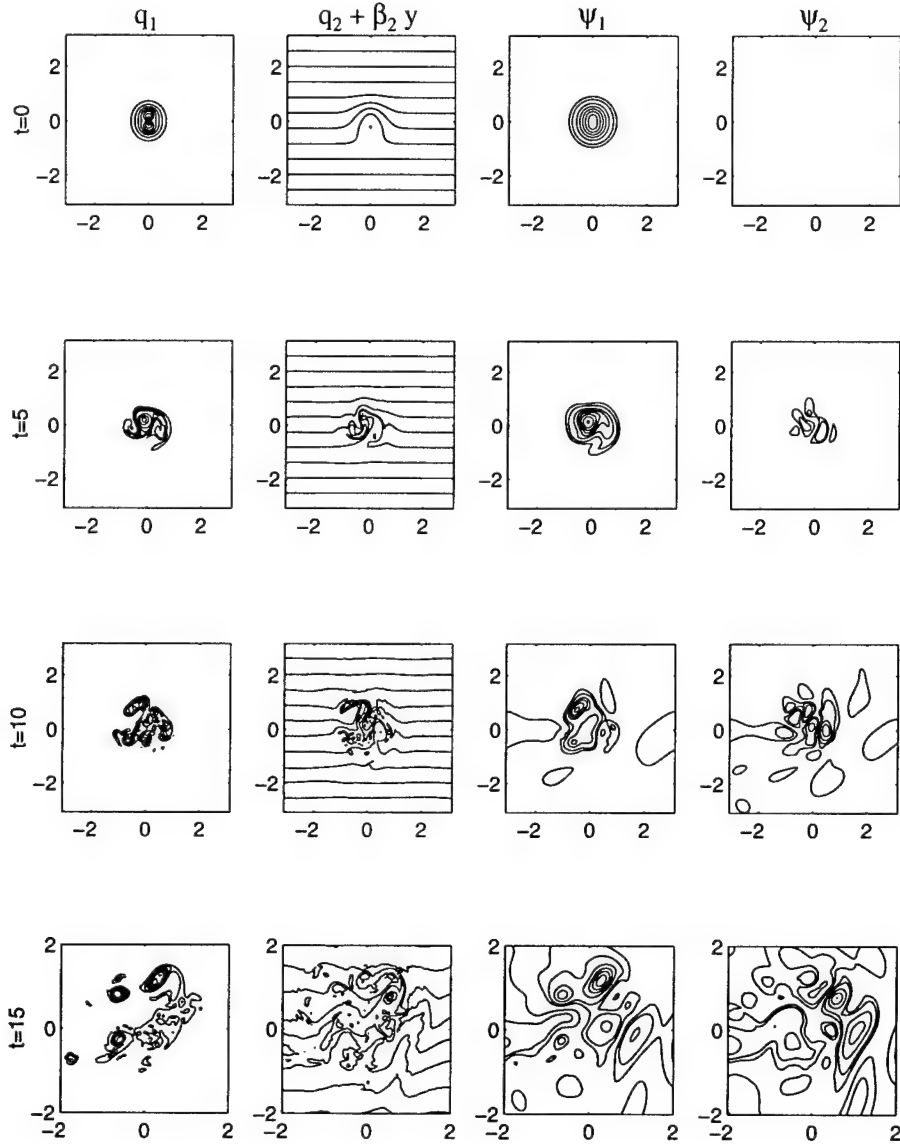
Figure 3.27: A surface-trapped vortex ($\psi_1 = -.7exp(-(\frac{r}{2r_0})^2)$, and $\psi_2 = 0$) over a moderate slope ($\Lambda = 1.8$) with $r_0 = 2.5\lambda$. The surface PV contour intervals are C.I. $= \pm[5 : 5 : 50]$; the bottom PV CI$= \pm[.3 \ .9 \ 1.5 \ 2.1 \ 2.7]$; the streamfunction C.I. $= \pm[.05 \ .1 : .1 : 1]$. The axes have been adjusted in the bottom row for details.

energy locally, but serve to redistribute that energy laterally. In the slope case, the radiating modes are bottom-intensified topographic waves which one expects will be eventually damped by bottom drag.

The parameter which determines whether the deep flow is "local" or radiating is $\frac{\beta_{2dim}r_0^2}{U_2}$, as in the barotropic cases of Chapter 3. The difficulty in this case is that $U_2 = 0$ initially, complicating the *a priori* determination of radiation. However, the deep velocities in this case are comparable to the initial surface velocities, due to the large size of the vortex and thus the large amount of available potential energy. Thus $\frac{\beta_{2dim}r_0^2}{U_2} \approx 3.6$. Given the previous results, one expects waves to dominate at depth, and hence the instability is primarily radiating.

This case illustrates that understanding the evolution requires knowledge of two parameters, Λ and $\beta_2 = \frac{\beta_{2dim}r_0^2}{U_2}$. This slope was termed "moderate" above because it was weak enough to permit instability ($\Lambda > 1$), but strong enough to inhibit vortex motion at depth ($\beta_2 > 1$). A weaker slope (not shown) also permits instability, but is less inclined to radiation of perturbation energy at depth and thus more closely resembles the flat bottom case.

A case with a larger slope is shown in figure (3.28). Here $\Lambda = .18$, and the vortex appears to be stable. Some wave energy is radiated as the vortex adjusts to axisymmetry from its initial perturbed state, but thereafter remains circular. Plots at later times reveal the vortex does not change, and no further energy is lost to waves. A sponge was used in this run, so the waves generated initially do not re-enter the domain and perturb the vortex further. The radiation of waves during the initial adjustment is explained in Chapter 4; unsteady surface motion implies interfacial motion, which must be accompanied by motion at depth. But as the sponge absorbs the waves, the vortex is able to achieve a *steady* state which does not require motion at depth.

Another run, in which the sponge was not used, is shown in figure (3.29). In this case the perturbation-generated waves re-enter the domain and disturb

Figure 3.28: A surface-trapped vortex ($\psi_1 = -.7exp(-(\frac{r}{2r_0})^2)$, and $\psi_2 = 0$) over a strong slope ($\Lambda = .18$) with $r_0 = 2.5\lambda$. The surface PV contour intervals are C.I. $= \pm[5 : 5 : 50]$; the bottom PV CI$= \pm[.3\ .9\ 1.5\ 2.1\ 2.7]$; the upper layer streamfunction C.I. $= \pm[.05\ .1 : .1 : 1]$ and the lower layer contours are one-fifth those, due to the weak flow at depth. The axes have been expanded in the bottom row for detail.

the vortex. Thus more potential energy is lost to the waves, and the $k = 0$ mode intensifies. However, less potential energy is lost than in the $\Lambda = 1.8$ case, suggesting the release of APE is bounded. The late stages are characterized by a vortex embedded in a zonal jet of a comparable width, with the vortex elongated in the direction of the jet. Jets and zonally-elongated vortices are also found in the case of evolving surface-trapped geostrophic turbulence over a slope (chapter 4). The case is mentioned here only to illustrate the potential growth of the $k = 0$ mode in a re-entrant domain, a fact anticipated in the discussion of the parallel flow above.

The effect of increasing Λ is illustrated in figure 3.30. The plot shows potential energy and the centroid wavenumber of the surface potential vorticity. The latter, a mean wavenumber, resembles the barotropic vorticity centroid of McWilliams (1984) and is defined as:

$$\mu_{q1} \equiv \frac{\sum_k \sum_l \kappa |\hat{q}_1(k, l)|^2}{\sum_k \sum_l |\hat{q}_1(k, l)|^2}).\tag{3.34}$$

Since the waves have zero surface PV, μ_{q1} only reflects the mean scale of the surface vortices and filaments. When Λ is large, the potential energy decreases rapidly while μ_{q1} increases. The latter asymptotes to the deformation wavenumber, $\sqrt{F} = 6$ where it remains thereafter. In the $\Lambda = 1.8$ case there is overshoot, consistent with the "turbulent" evolution observed in the moderate slope case (figure (3.27)). But as noted above, the release of potential energy in this case is nearly the same as in the flat bottom case.

With smaller values of Λ, less potential energy is lost and the surface scale does not decrease to deformation scale. In the intermediate cases, the surface vortex is deformed by the initial perturbation, but relaxes thereafter toward axisymmetry
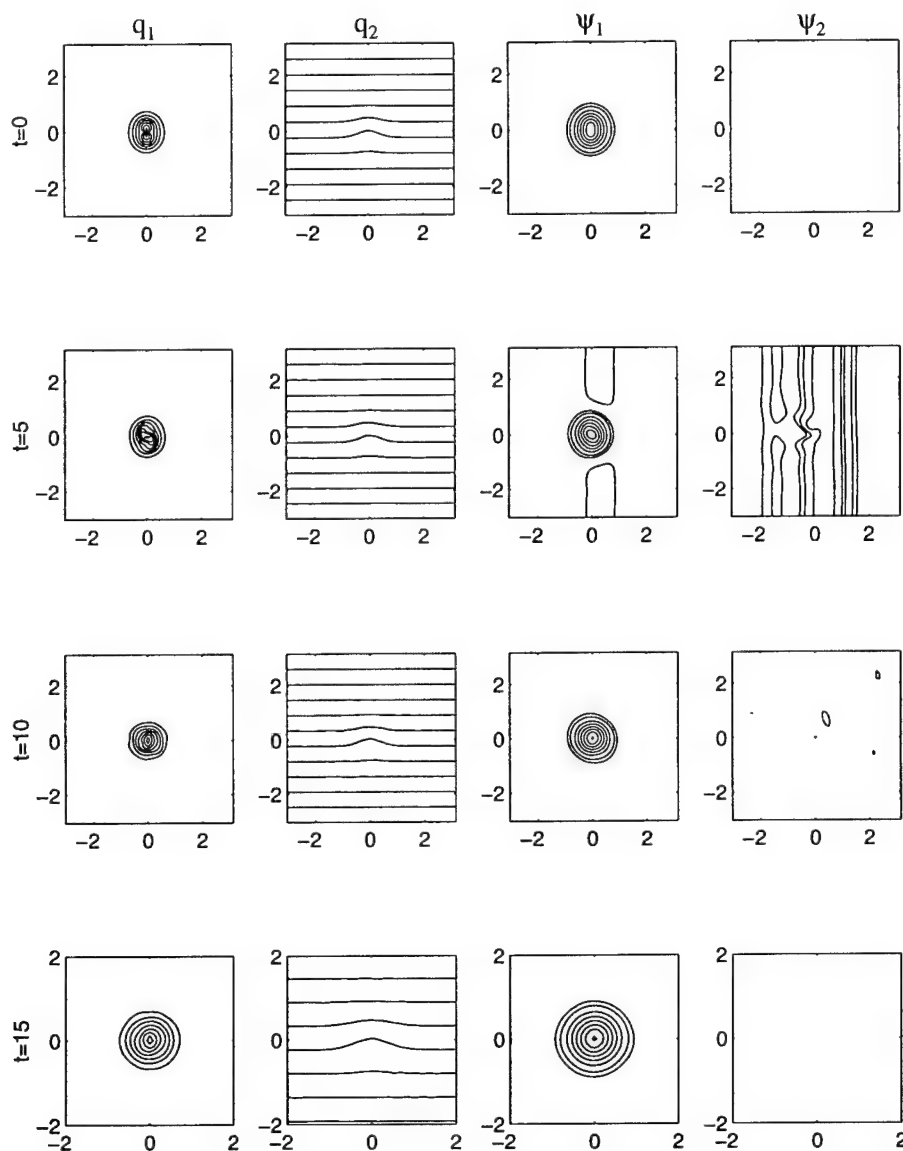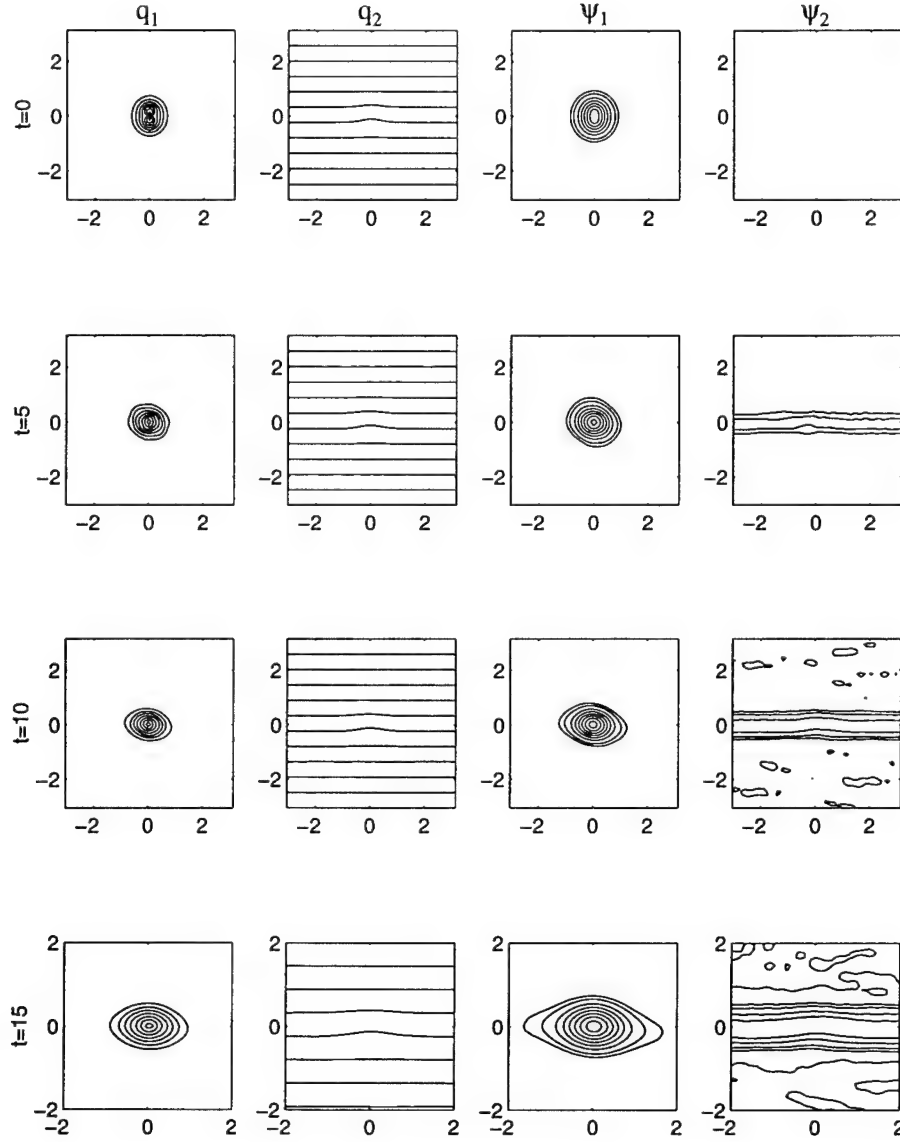
Figure 3.29: A surface-trapped vortex ($\psi_1 = -.7exp(-(\frac{r}{2r_0})^2)$, and $\psi_2 = 0$) over a strong slope ($\frac{\beta_2 r^2}{U_1} = 36$) with $r_0 = 2.5\lambda$. The surface PV contour intervals are C.I. $= \pm[5 : 5 : 50]$; the bottom PV CI$= \pm[.3 \ .9 \ 1.5 \ 2.1 \ 2.7]$; the upper layer streamfunction C.I. $= \pm[.05 \ .1 : .1 : 1]$ and the lower layer contours are one-fifth those, due to the weak flow at depth. The axes have been shifted in the bottom row for detail.

103
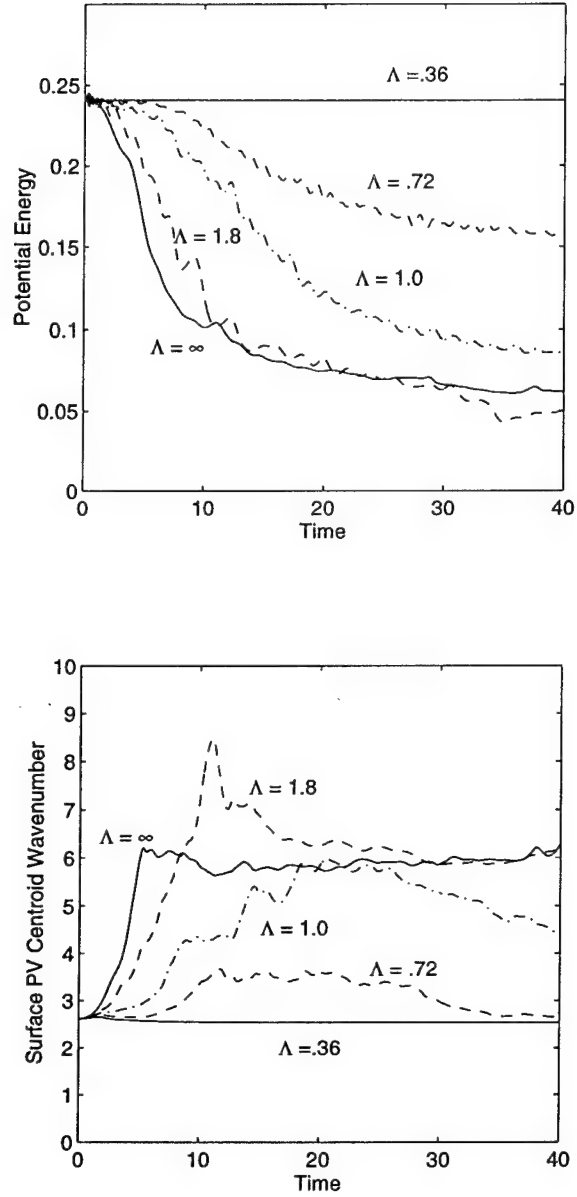
Figure 3.30: Potential energy and the surface PV centroid for the surface-trapped initial vortex with $r_0 = 2.5\lambda$ and various bottom slopes. The deformation wavenumber is 6.

(much like a subcritical case considered in Ikeda, 1981). The return to the initial scale of the surface PV is seen in particular in the $\Lambda = .72$ case. At the smallest value of Λ, the scale does not change appreciably, and there is no discernable loss of potential energy.

As in Flierl (1988) and Helfrich and Send (1988), larger vortices are unstable to higher azimuthal wavenumbers. Given this, and the fact that the slope cannot stabilize disturbances with $k = 0$ (from the parallel flow discussion above), one suspects that larger vortices might be unstable. This is indeed the case. In figure (3.31), a somewhat larger vortex ($r = 3.3\lambda$) is shown with $\Lambda = .36$. Small perturbations are found to grow on sides of the vortex (the cross slope flow) and generate similar disturbances at depth. The latter radiate quickly away, and so never grow to an extent to break the surface vortex up, but the edge of the potential vorticity breaks off into smaller filaments. Unlike the $r = 2.5\lambda$ case, potential energy is continually lost.

The latter can be seen clearly in a plot of potential energy, shown in figure (3.32). The PE does decline for this vortex, and does so even more rapidly with a larger vortex. The upper layer scale increases initially, but then nearly returns to the initial scale, consistent with the idea that energy is being radiated away to waves without breaking up the surface vortex.

In summary, one finds that a steeper slope tends to inhibit the baroclinic instability of a surface vortex. The key parameter, suggested from parallel flow linear instability arguments as well as from numerical runs, is $\Lambda \equiv \frac{F_2 U_1}{\beta_2}$. When larger than one, the growth of energy in the deep layer occurs faster than wave radiation and in the ensuing development the surface vortex breaks up. If $\Lambda < 1$, the loss of potential energy is inhibited. For vortices somewhat larger than deformation scale, instability can be blocked. But larger vortices which are unstable to higher azimuthal wavenumbers are not stabilized due to the inability of the slope to affect disturbances whose particle trajectories are parallel to the isobaths

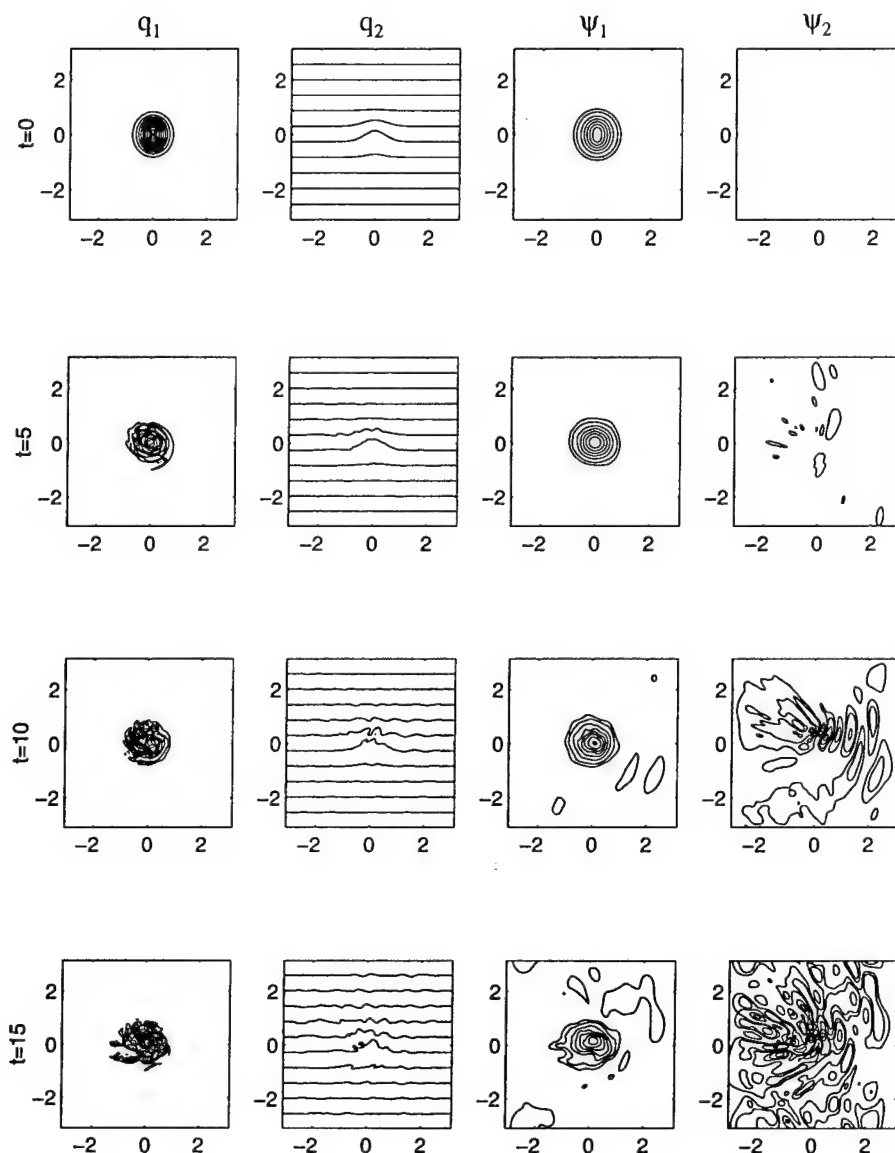Figure 3.31: A surface-trapped vortex with $r = 3.3\lambda$ and $\Lambda = .36$. The surface PV contour intervals are C.I. $= \pm[5 : 5 : 50]$; the bottom PV CI$= \pm[.3\ .9\ 1.5\ 2.1\ 2.7]$; the upper layer streamfunction C.I. $= \pm[.05\ .1\ :\ .1\ :\ 1]$ and the lower layer contours are $1/2.5$ times the latter.
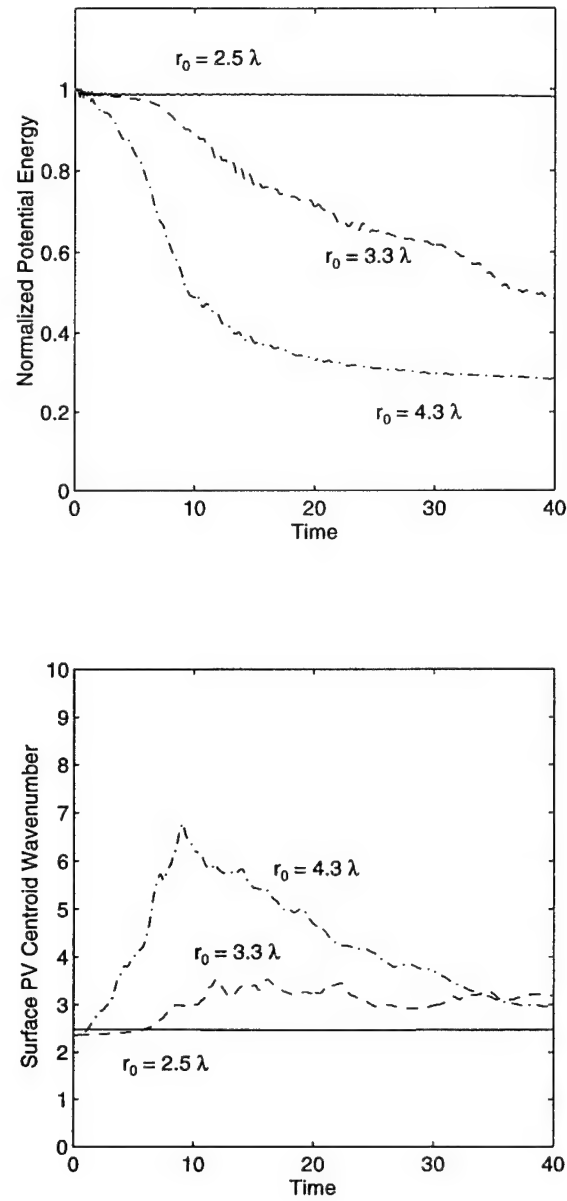
Figure 3.32: Potential energy and the surface PV centroid for the surface-trapped initial vortex with various radii.

(perturbations with $k = 0$).

In unstable cases, it was argued that $\frac{\beta_2 r_0^2}{U_2}$ is important to the finite amplitude state obtained. For small values, the formation of baroclinic dipoles was observed, but at large values, the deep energy was radiated away.

3.5   Discussion

The evolution of a single vortex depends strongly on two parameters: $\frac{U_2}{\beta_{2dim}r_0^2} \equiv 1/\beta_2$ and $\Lambda \equiv \frac{F_2 U_1}{\beta_2}$. They indicate the strength of the advection of relative vorticity and stretching respectively; if either is greater than one, nonlinearity is likely to be important at depth. If $\frac{U_2}{\beta_{2dim}r_0^2} > 1$ ($\beta_2 < 1$), the lower portion of an initially barotropic vortex remains coherent, and able to couple with the surface portion; otherwise, the deep flow is wave-like. If $\Lambda < 1$, the deep flow beneath a surface vortex is also wave-like which inhibits baroclinic instability.

A unique aspect of f-plane flow over a topographic slope is that there is no wave dispersion of surface PV. Thus if a flow has PV at the surface initially, it will retain that PV after radiation of topographic waves. Of course the surface PV may evolve due to advection by the waves, but it nevertheless remains "local".

The planetary and topographic β cases agree best in the lower layer, where the PV gradient exists in both cases. The only case in which there is complete agreement is when the initial vortex is barotropic, larger than deformation scale ($r_0 > \lambda$), and the slope is very weak ($\beta_2 \ll 1$). Then the vortex remains barotropic and translates meridionally or cross-isobaths. In a sense, the barotropic case predicts the fate of the vortex when $\beta_2 \gg 1$ and $r_0 > \lambda$ in that most of the surface streamfunction is lost to wave radiation. However, the choice of an initially barotropic vortex optimizes the comparison; a vortex with weaker deep flow, such as oceanic rings are known to have, would radiate away less of the surface vortex over a steep slope. Ultimately, as the surface potential vortic-

ity dynamics are not captured, the single layer simplification fails to capture the whole evolution.

One can find approximate values for the two-layer parameters from values of the deformation radii, velocities and bottom slopes given in some observational and modeling papers. This is done with the caveat that oceanic depth changes are probably too large to be strictly consistent with QG.

Given the estimates of velocities for warm core ring 82B prior to its intersection with topography (Joyce, 1983) and from stratification in Olson et al. (1985):

$$U_1 \approx 1.0 m/s \ \ U_2 \approx .05 m/s \ \ f \approx 10^{-4} \ \ g' \approx 0.01 m^2/s \ \ H_y \approx 0.025 \,,$$

$$r_0 \approx 50,000m \ \ \beta_2 = \frac{f \partial_y H}{H_2} \approx \frac{(10^{-4}/s)(.025)}{2000m} = 1.25 x 10^{-9}/ms \,.$$

This leads to estimates of the two values:

$$\frac{U_2}{\beta_2 r_0^2} \approx 0.008 \ \ , \ \ \Lambda \approx 0.4 \,.$$

Warm core ring 82B appears thus to be unlikely to translate barotropically over topography as a Case A vortex. It also appears that it will be stable after radiation of topographic waves (which will decrease U_1 somewhat), so that the Case D seems a reasonable expectation. The smallness of both parameters suggests open PV contours at depth, and linear dynamics there. A similar example was the cold core ring observed by Cheney and Richardson (1976). The vortex, known to have non-zero flow as deep as 2000m, crossed the Blake escarpment on its journey to the southwest. This feature rises to only 1000m below the surface, and so is likely a "strong slope". Interestingly, the vortex continued on its original path, moving right over the escarpment. Cheney and Richardson found that the decay of the ring accelerated drastically as the vortex passed over the escarpment (see their figure 7), consistent with a weakening of the surface streamfunction.

Of course, the topography in that case was hardly consistent with QG, but the changes were consistent with a stable (Case D) evolution outlined here.

Agulhas eddies migrate to the northwest across the South Atlantic, and must pass over steep topography such as the Walvis ridge on their way. Values for vortex scale and velocity and the Walvis ridge are given in Kamenkovich et al. (1996) and Clement and Gordon (1995):

$$\frac{U_2}{\beta_2 r_0^2} = \frac{H_2 U_2}{f \, \partial_y H \, r_0^2} \approx \frac{(4000)(.1)}{(10^{-4})(.0125)(10^{10})} = .032$$

and

$$\Lambda = \frac{fU_1}{g'H_y} \approx \frac{10^{-4}(.5)}{(.04).0125} = .10$$

so that, apparently, the Agulhas eddy will be undeformed and stable as well over the Walvis ridge, i.e. also as in Case D. Kamenkovich et al. (1996) varied the strength of the deep flow so that $.05 \le |U_2| \le .35$ which leads to a range of β_2 parameters from .016 to .112, all of which are in the steep slope range. Interestingly, they noted that the (model) eddy was found to stall over the ridge in the case of the strongest deep flow, and was "practically destroyed before reaching the axis of the ridge". Given the results of Case D, one might guess that, due to the nearly barotropic initial profile, topographic wave radiation carried off a significant portion of the surface streamfunction. Indeed, the vortex ψ_1 is very weak in their figure (16) after impacting the ridge. One might speculate further that the loss of ψ_1 would impair the translation on the planetary β-plane by inhibiting the maintenance of the "β-gyres", producing the "stall" seen there and in observations (VanBallegooyen et al., 1994). Further details about the inclusion of the planetary β effect are given in Chapter 5.

Lastly, the Smith and O'Brien (1983) study of Loop Current Eddies impacting the slope in the Gulf of Mexico employed layer-trapped and barotropic vortices, as I have in this chapter. Representative velocities and scales yield the following parameters:

$$\frac{U_2}{\beta_2 r_0^2} = \frac{H_2 U_2}{f\, \partial_y H\, L^2} \approx \frac{(3000)(.5)}{(10^{-4})(.01)(50000)^2} = .6$$

for the barotropic and bottom-trapped vortex, and

$$\Lambda = \frac{fU_1}{g'H_y} \approx \frac{10^{-4}(.5)}{(.025).01} = .20$$

for all vortices. Again the vortices (approximately deformation scale) appear to fall into the stable, large slope category, although the β_2 parameter is the largest of the examples considered, suggesting that the barotropic vortex might be significantly deformed during wave radiation. The occurrence of closed contours of bottom potential vorticity in their figure 7 is consistent with this, but it is difficult to say whether the surface vortex has been deformed by waves or is interacting with the edge of their domain.

A recent observational study of a Loop current eddy (Vidal et al., 1992) witnessed its impact on the continental slope. A primary finding was that the vortex lost about $\frac{1}{3}$ of its "mass" on impact, but remained in tact. This obviously fits with the steep slope scenario detailed in the chapter. Because the surface vortex was weakened, one can deduce that it had a significant deep flow prior to impact.

The results may also suggest the reason the laboratory experiments of Mory et al. (1987) and Whitehead et al. (1990) disagreed. Both examined vortices formed by the convection of dense fluid onto a sloping shelf. In the Mory study, a nearly barotropic cyclonic vortex formed above the dense fluid and the vortex migrated slowly to the northwest. Whitehead et al. on the other hand found a surface-intensified cyclonic vortex over the dense fluid, one which drifted due west at a speed which agreed with the predictions of Nof (1983). The "lower layer" in both cases is completely contained in the vortex (the dense water at the base of the vortex), so applying the QG results of this chapter is questionable

at best, nevertheless the cyclonic circulation experiences the slope PV gradient, so it is reasonable to ask how large β is. This can be done approximately given their experimental parameters, and taking the water depth to be that of the tank and the swirl velocities at the surface. One obtains (quantities shown are in cgs units):

$$\beta = \frac{fH_y r_0^2}{HU} \approx \frac{(2)(.14)(3.5)^2}{(25)(.5)} = .27 \quad (Mory\ et\ al.,\ 1987),$$

$$\beta = \frac{fH_y r_0^2}{HU} \approx \frac{(.83)(.2)(5)^2}{(13)(.5)} = .62 \quad (Whitehead\ et\ al.,\ 1990),$$

so that the effective slope in the Whitehead et al. case more than two times larger than in the Mory et al. case. Of course, both estimates are less than one, however they are near enough to one that they ought to fall in the "transition" region (and slightly smaller estimates of velocity or larger radii would shift the slopes closer to unity). The Whitehead et al. slope might actually be larger because the observed surface speeds would be representative post-wave radiation flow.

Whitehead et al. demonstrated that the vortex flow at the bottom was about zero, so their vortex was compensated. And the vortex in figure 3c of Mory et al. (1987) has a trailing wake of smaller vortices, as in figure 4 of the barotropic experiment of Carnevale et al. (1991a). The picture is more complicated than suggested here, because of the effect of gravity on the deep fluid (Nof, 1983), but the observed baroclinicity is consistent with the results of this chapter.

In the numerical experiments discussed, the deep flow was so weak that the lower portion of the vortex should have radiated away as waves. As seen in cases C and D, when this occurs the vortex is *unable* to self-advect over topography. The expectation that the vortex will migrate in a direction which is the weighted average of the topographic and actual northwest (expressed in figure 3 of Smith and O'Brien 1983) is thus incorrect. Rather, the vortex simply loses its lower

half, only continuing to move if the surface vortex is able to generate (planetary) β-gyres, or if the surface vortex is moving under the influence of an ambient flow.

Saying whether rings move under the influence of a mean flow or the planetary β-effect is beyond the scope of this work. It appears that the mechanism likely depends on the local flow. Joyce and Kennelly (1985) contended that Warm Core ring 82B was simply advected by the background flow when over the continental slope. However, the results of Cornillion et al. (1989) clearly suggest translation of the ring at a velocity different from that of the slope flow, at least away from the shelf. It should be noted that mean advection rather than topographic translation might explain why anticyclonic Warm core rings migrate to the topographic west, whereas anticyclonic Loop current eddies drift to the topographic east. Agulhas eddies on the other hand experience weaker mean flows translating across the South Atlantic, and appear to move at a speed and in a direction compatible with β-induced translation (Clement and Gordon, 1995).

A final point concerns the question of whether a surface vortex which is offshore of the continental shelf could move onto the shelf. The answer appears to be that the topography may not prevent it from doing so, but that the vortex will be unable to self-propel across. In variable regions such as the California coast, interactions with other vortices could advect a vortex up over the topography after radiation of the deep flow. A striking example of an eddy on the shelf is the 45 km radius anticyclone described by Washburn et al. (1993) which moved on to the Northern California shelf/slope and stayed there for two months, drawing tons of sediment off the shelf. In fact, Largier et al. (1993) contend that offshore eddies may be responsible for a sizable portion of the shelf variability in this region. Vortex interactions over topography are considered in more depth in the following chapter.

Appendix A: Non-isolated Vortex

In the following a non-isolated vortex over a topographic slope is considered. The primary motivation is to identify elements in chapter 3 which depend solely on vortex isolation. However, the work is also intended as a baroclinic extention of the barotropic laboratory study of Carnevale et al., (1991a).

A non-isolated vortex has a non-zero circulation and thus a slowly-decaying velocity field, with $lim_{r\to\infty} v(r) \; \alpha \; \frac{1}{r}$. The wider field of influence increases the likelihood of boundary effects. Indeed Carnevale et al. (1991a) attributed the arcing trajectory of their laboratory non-isolated vortex to the influence of the boundary.

The following is divided into subsections. In the first, the effect of confining the vortex to a doubly periodic domain is discussed. In the second, a β-dependence of the translation velocity in the barotropic case is sought. In the third, the non-isolated vortex in two layers over a weak slope is examined. One finds the twisting instability is absent in this case so that even small barotropic vortices translate vertically aligned. In the fourth, the evolution over a large slope is briefly discussed, and isolation is found to be unimportant. Finally, the translation of a surface-trapped potential vortex over a slope is discussed. This last category is provided for comparison with a recent study by Pankratov (1994) of a point potential vortex over a slope.

Initial condition

The vortex has a Gaussian vorticity profile, i.e. $\zeta = \nabla^2 \psi = A e^{-(\frac{r}{r_0})^2}$, and is shown in figure (3.33). Different parameter values were used, but the vortex always had a maximum swirl speed of roughly one. A typical example is shown in figure (3.33).

A difficulty with confining such a vortex to a doubly periodic domain is that the total circulation in the domain must be zero, as noted by Mariotti et al.

(1994). This can be seen in the area-average of the Fourier expansion of vorticity:

$$\int_0^{2\pi} \int_0^{2\pi} \nabla^2 \psi \, dx \, dy = \int_0^{2\pi} \int_0^{2\pi} \sum_k \sum_l -\kappa^2 \hat{\psi}(k,l) e^{ikx+ily} \, dx \, dy = -(0) \, \hat{\psi}(k,l) = 0$$

(3.35)

In practice, the model effectively adds a background vorticity equal (and opposite) to the domain average circulation of the vortex. The result is that the azimuthal velocity decays to zero at the edge of the domain, as one expects from Gauss's Theorem, so the far-field velocity is truncated. The dotted line in the bottom panel of (figure (3.33)) is the actual velocity of a Gaussian vortex:

$$v(r) = \frac{Ar_0^2}{2r}(1 - e^{-(\frac{r}{r_0})^2})$$

(3.36)

The model and actual profiles agree except in the outer region where the model velocity falls off too rapidly. In their study of a non-isolated vortex exposed to shear, Mariotti et al. (1994) chose to add negative vorticity to the boundary to balance the circulation of the vortex. In comparing results to a similar contour dynamical simulation, they claimed that the effect of the additional vorticity was weak. I have chosen not to add such a boundary layer of vorticity, but rather to use smaller vortices, as the velocity scales as r_0^2. The hope is that the *local* interactions between surface and bottom vortices and with waves will be captured. Carnevale et al. (1991a) found qualitative agreement between the laboratory vortex and a numerical vortex in a doubly periodic domain. Althought the total circulation will be zero in a laboratory tank as well if the no-slip condition applies, the agreement with two different sized domains is reassuring.
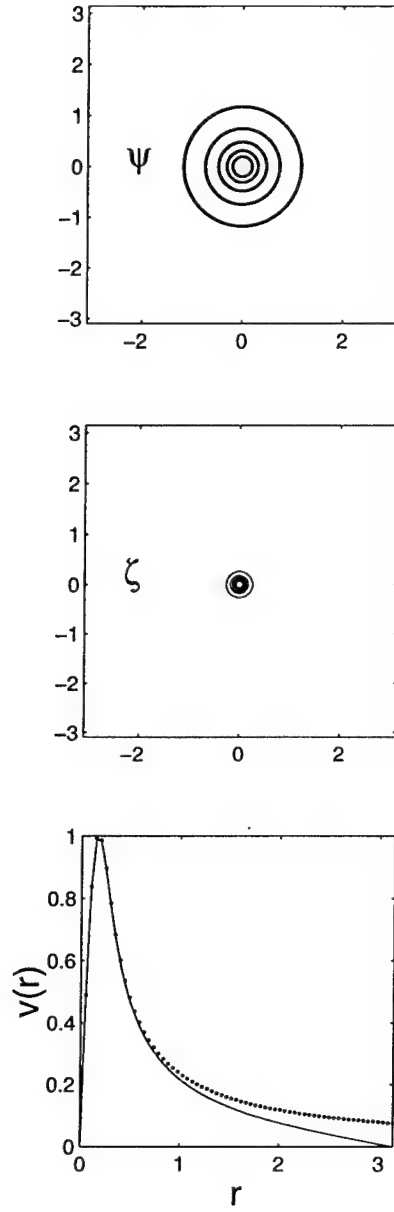
115

Figure 3.33: The initial vortex. The streamfunction (top) has contour interval
C.I. = −[.1 : .1 : 1] and the vorticity (middle) C.I. = [1 , 5 , 9 , 13 , 17]. The
bottom panel shows the azimuthal velocity on a doubly periodic domain (solid)
and the analytical velocity (dotted). The bold contours are negative values, the
thin are positive.

<u>One layer</u>

As in the isolated vortex case, the vortex was found to accelerate to an approximately constant translation velocity. However, the translational velocity was found to be more rapid and the trajectory arcing from northwest to nearly westward in many cases. An example is shown in figure (3.34). The evolution is qualitatively consistent with that of Carnevale et al. (1991a), and the vorticity in figure (3.34) closely resembles their figure (3a).

As in Chapter 3, one can seek the β-dependence of the translation velocity for this vortex as well. Several single layer runs were made and the translation velocity was obtained by approximate linear fits of the centroid position in time. The results, shown in figure (3.35), indicate that $|u| \alpha \beta^{.85}$. Furthermore, in the small β limit, the dependence appears to be approximately linear. Similar tests with different sized vortices indicate almost no dependence on vortex scale.

These results may be understood by appealing to the asymmetric streamfunction (defined in Chapter 3) shown in figure (3.34). One sees that the advecting gyres are domain-filling. The gyres appear to intensify, fill the domain, then propagate westward as Rossby waves, carrying the vortex along with them. Moreover, this type of evolution was observed with all vortices which could be resolved by the model; in each case, the vortex was advected by domain-filling waves. The response then is apparently a consequence of the larger horizontal scale of the velocity field.

If the vortex is transported by a large-scale wave field, then the dependence of that velocity on β and r makes more sense. The dependence on β probably only reflects the linear dependence of the wave phase speed on β. The approximate independence on r could be explained by noting that L, the size of the domain, may be the important length scale. Perhaps the efficiency of vortex propulsion by the wave should vary somewhat with vortex size, but it appears, to first order at least, that the variation is weak. Of course, if the domain were much larger, one

117
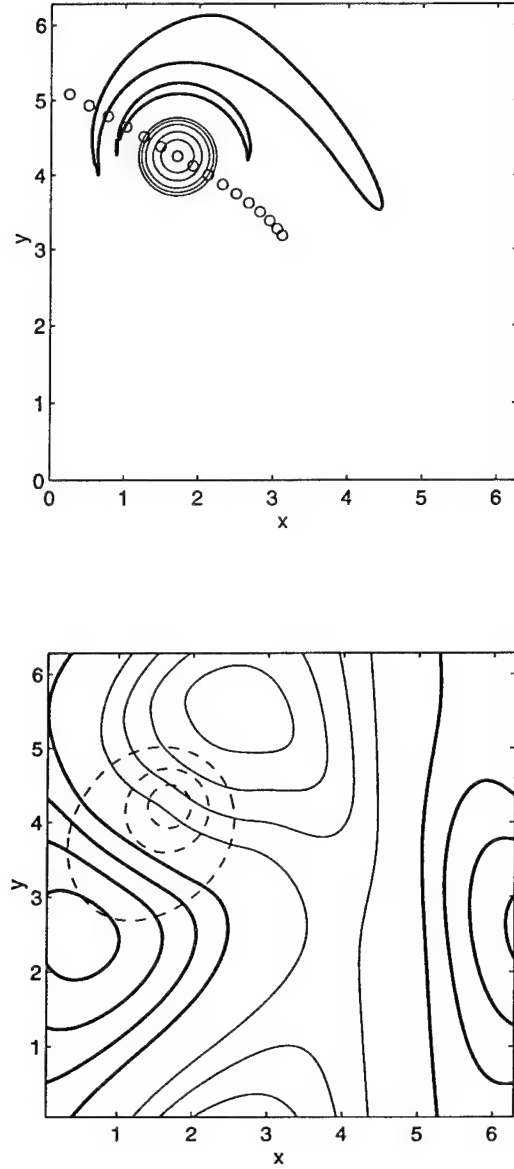
Figure 3.34: In the upper panel, the vorticity for a non-isolated vortex with $\frac{\beta r_0^2}{U} = .01$ at $t = 20$. The CI $= [.25\ .5\ 1\ 2.5\ 5\ 10]$. The centroid position is drawn every two time units. The asymmetric streamfunction at $t = 20$ is below. The actual streamfunction is superimposed (dashed). The CI $= \pm[1:1:10]/25$ (asymmetric field) and CI $= \pm[1:1:10]/5$ (streamfunction).

118

Figure 3.35: The translation velocity of the non-isolated vortex as a function of β (top panel) and vortex e-folding radius (bottom). The velocity was determined by linear fits to the vortex position in time; the error bars are from the fits. The vortex amplitudes and radii were $(A, r_0) = (7, .45)$, $(11, .3)$, $(14, .225)$, $(21, .15)$, $(42, .075)$. The last vortex was used for the upper cases.

might expect variations with vortex size, but computational constraints limited the range of accessible vortex sizes.

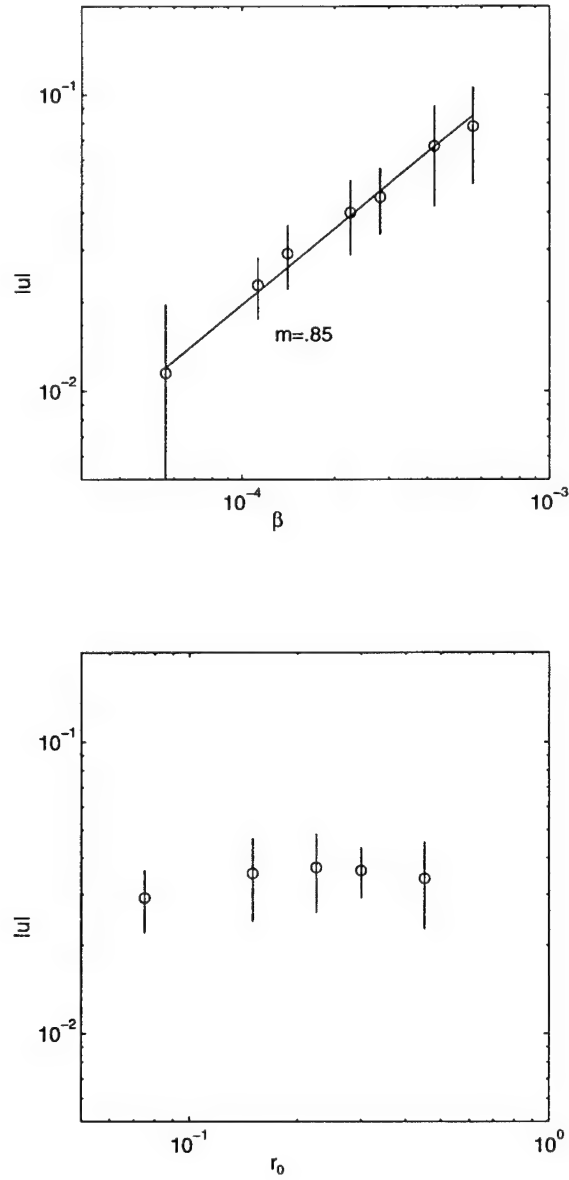Therefore, the barotropic non-isolated vortex translates in this doubly periodic model by exciting domain-filling Rossby waves. Carnevale et al. (1991a) postulated that the arcing trajectory of the non-isolated vortex in the lab was due to boundary influences so the present findings are then consistent with that notion.

Two layers, weak slope

Two layer, non-isolated barotropic vortices were considered as in cases A and B in chapter 3. The slope again was weak, $\frac{\beta_2 r_0^2}{U_2} \approx .009$ (although this value may be misleading due to the large scale velocity field). Several different vortices were allowed to evolve from rest over the slope, and the trajectories of the upper and lower potential vorticity centroids are shown in figure (3.36). Of interest is the fact that the vortices shown are all *smaller* than deformation scale, but are nevertheless translating vertically aligned. As noted above, the radius to the velocity maximum tends to underestimate the scale of the non-isolated vortex, but even taking three times r_0 would yield sub-deformation scale vortices. The trajectories all closely resemble that found in the one-layer case, and are consistent with trajectories obtained in the laboratory (Carnevale et al., 1991).

As explained by Flierl (1988), the twisting instability requires vortex isolation. The outer ring of oppositely-signed vorticity permits the formation of layer-trapped dipoles and in turn the separation of the upper and lower vortices. Without the ring of negative vorticity, the upper and lower vortices will simply co-rotate with a frequency which varies with the separation of their centers. This can be seen approximately by inverting the potential vorticity of one of the layer-trapped potential vortices to find the streamfunction in the other layer, i.e.
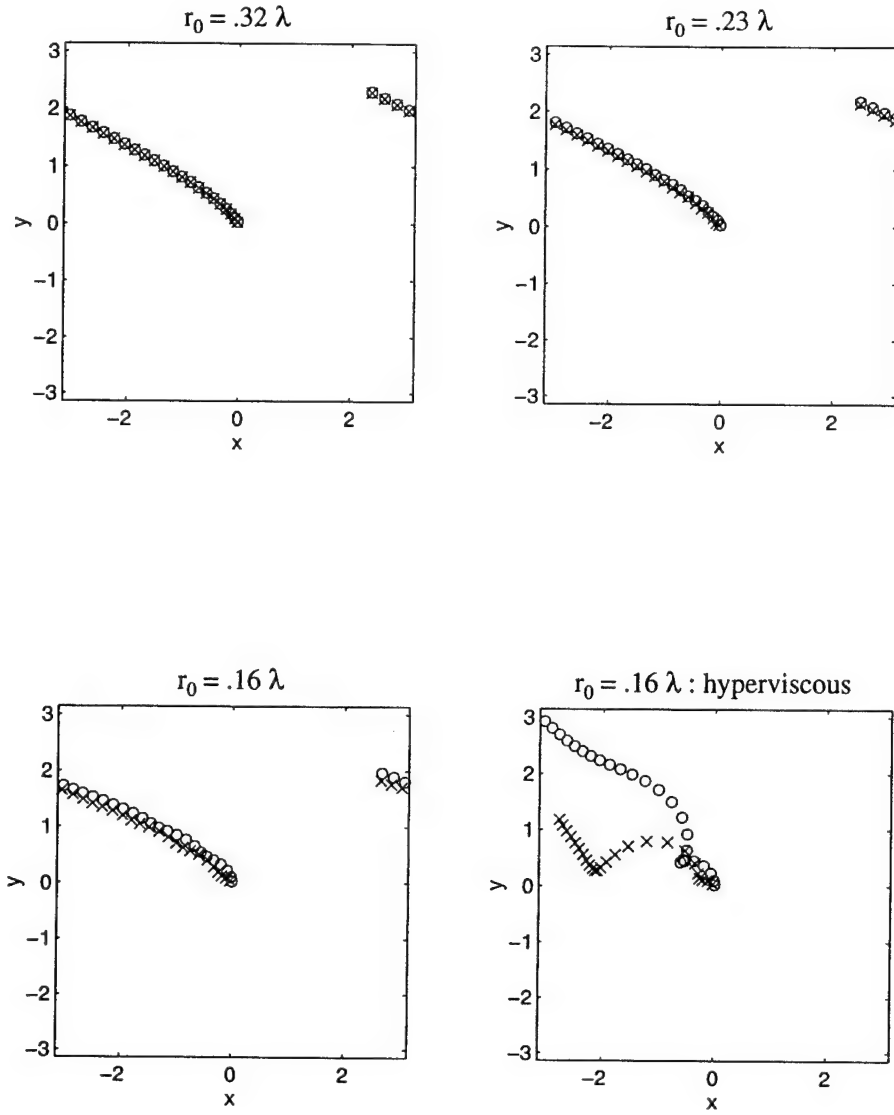
Figure 3.36: The positions of the potential vorticity centroids, as defined in chapter 3, for non-isolated vortices of varying scale with $\frac{\beta_2 r_0^2}{U} = .002$. The (o) is the upper potential vortex and the (x) is the lower vortex. The lower right panel is an additional run done with $\nabla^8 q_i$ damping with a coefficient of 1.758×10^{-9}.

the flow responsible for advecting the other vortex. For simplicity, assume that the vortex profile is fixed, i.e. undeformed by the other vortex, and confined to the upper layer. Then if $q_1 = Ae^{(-\frac{r}{r_0}^2)}$ and $q_2 = 0$, the corresponding barotropic vorticity (e.g. Hogg and Stommel, 1985) is:

$$q_{BT} = \nabla^2(\psi_{BT}) = \nabla^2(\psi_1 + \psi_2) = Ae^{(-\frac{r}{r_0}^2)} \tag{3.37}$$

and the baroclinic vorticity is:

$$q_{BC} = (\nabla^2 - 2\,F)(\psi_{BC}) = (\nabla^2 - 2\,F)(\psi_1 - \psi_2) = Aexp(-\frac{r^2}{r_0}). \tag{3.38}$$

Equations (3.37) and (3.38) can be inverted with the Green's functions corresponding to the ∇^2 and the $\nabla^2 - 2\,F$ operators in two dimensions:

$$\psi_{BT}(r) = -\frac{1}{\pi}\int_0^{2\pi}\int_0^\infty Aexp(-\frac{r'^2}{r_0})log(r-r')r'dr'd\theta' \tag{3.39}$$

and

$$\psi_{BC}(r) = -\frac{1}{\pi}\int_0^{2\pi}\int_0^\infty Aexp(-\frac{r'^2}{r_0})K_0(\sqrt{2F}(r-r'))r'dr'd\theta' \tag{3.40}$$

122

where K_0 is a modified Bessel function. The streamfunction in the upper/lower layer is half the sum/difference of (3.39) and (3.40), and the azimuthal velocity in layer two is the radial derivative, $\partial_r \psi$:

$$
v_1(r)/v_2(r) = -\frac{1}{2\pi} \int_0^{2\pi} \int_0^\infty A exp(-\frac{r'^2}{r_0})(\frac{1}{r-r'} \pm K_1(\sqrt{2F}(r-r')) \cos(\alpha(r,r',\theta'))r'dr'd\theta'
$$

$$(3.41)$$

where $cos(\alpha) = \frac{r\dot{r}'}{|r||r'|}$ results from the projection onto the azimuthal velocity (the radial velocity is identically zero), and where K_1 is the modified Bessel function of first order. Equation (3.41) was solved by integrating numerically using a two-dimensional trapezoidal rule. The velocity for a vortex with the same amplitude and radius as those in the figure (3.36) calculations is shown in figure(3.37). The solutions asymptotically approach point potential vortex solutions (e.g. Hogg and Stommel, 1985) as $r/r_0 \to \infty$ due to the non-zero circulation, $\Gamma = \pi A r_0^2$. Unlike in a point vortex solution, the velocity is bounded at $r = 0$.

If the upper and lower portions of the barotropic vortex become displaced by a distance r, they will advect one another with a velocity $v_2(r)$. Two characteristics of this velocity are evident in figure (3.37): for larger vortices, the flow is stronger and the radius of maximum velocity closer to the center of the vortex. Under the influence of a vertically sheared impulse, the upper and lower potential vortices will experience less horizontal separation if they are large. Smaller vortices will separate more, but the azimuthal velocity is non-zero even when the vortices are smaller than deformation scale, so such vortices may translate aligned.

In the topographic case, the initially barotropic vortex perturbs bottom-intensified β_2-gyres which are more bottom-trapped when the vortex is small. However, the shear is too weak to separate the vortices in the cases shown in
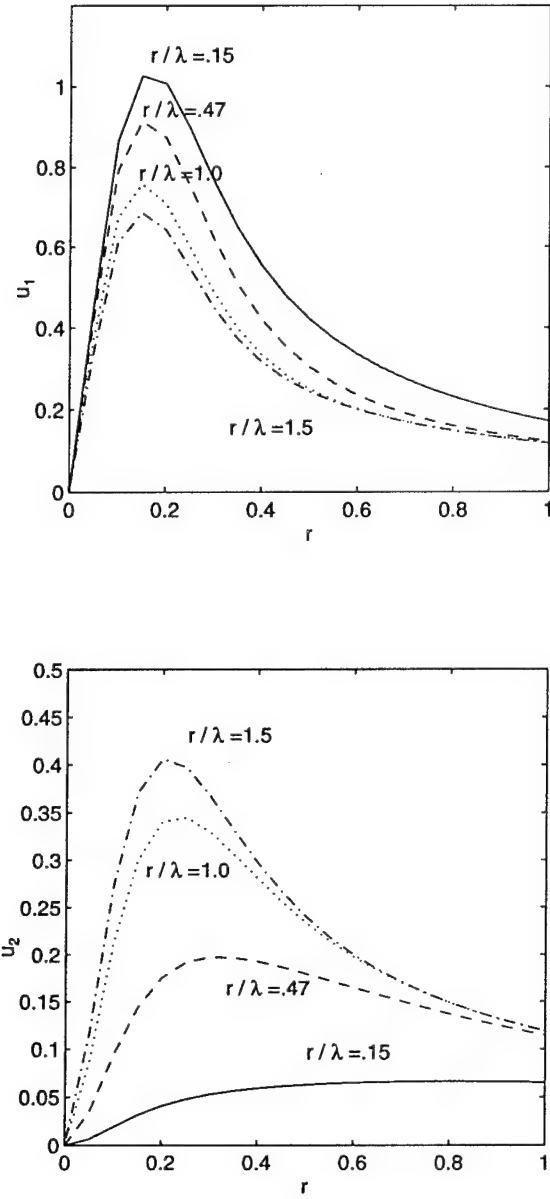
Figure 3.37: The azimuthal velocity field of a surface Gaussian potential vortex vs. distance from the vortex center. The vortex parameters are the same as those in the simulations, i.e. $A = 21$ and $R_0 = .15$. The upper layer velocity is shown at top and the lower layer velocity at bottom.

figure (3.36). On close inspection, the small vortex trajectories in figure (3.36) are found to be misaligned, and weakly co-rotating. One expects that a much smaller vortex will separate, when the co-rotating flow is much weaker.

If the vortex is larger than deformation scale, then the surface and bottom vortices would deform significantly if laterally separated, and would "align" as discussed by Polvani et al. (1994). Thus using a fixed PV profile to derive the velocity in the opposite layer would be inappropriate. But alignment ceases to occur at scales smaller than the deformation radius, so cohesion due to co-rotation is the dominant effect.

Interestingly, under hyperviscous damping the sub-deformation scale vortex ceases to translate aligned. The centroid trajectories for such a case are shown in the final panel of figure (3.36). Unlike the filtered case, the upper and lower vortices rapidly separate. This is a result of the formation of a weak negative ring of vorticity around the vortex, a Gibbs effect from the hyperviscous damping as described in Chapter 2. The rings are quite weak in this case, but nonetheless strong enough to couple with the primary vortices and cause separation. This case suggests that the twisting instability can occur even when the vortices are only weakly shielded, and that sub-deformation scale barotropic vortices are unlikely to be found in nature.

Non-isolated barotropic vortices over a large slope

The evolution in the case when $\beta_2 r_0^2 \gg U_2 = U_1$ is essentially the same as in the isolated case. An example with a vortex with $r_0 = 1.8\lambda$ and $\frac{\beta_2 r_0^2}{U} = 18$ is shown in figure (3.38), and may be compared to figure(3.20). As in the isolated cases, the portion of the vortex projecting onto the topographic waves radiates away leaving the surface potential vorticity unperturbed. As in case D in Chapter 3, the radiating waves are nearly barotropic so that surface streamfunction which remains is substantially weakened.

A surface-trapped non-isolated vortex

A vortex which has non-zero potential vorticity only in the surface layer (a surface potential vortex in the language of chapter 3) is an interesting special case because the contours of total potential vorticity at depth are open initially. In other words, the relative vorticity and stretching cancel one another, and thus do not deflect contours. At first glance one might expect a linear evolution. However, as there is non-zero flow at depth, waves will be generated and the vortex vertical structure must evolve. Over a flat bottom, a surface potential vortex is baroclinically stable because there is no change in sign of PV in the vertical (Flierl, 1988). But over a slope, the deep flow can be lost, potentially allowing instability.

The azimuthal velocities in both layers are shown in figure (3.37). The vortices larger than deformation scale are more nearly barotropic, and the smaller vortices have weaker deep flow. From this alone, one expects that smaller vortices are more prone to radiation of their deep flow since β_2 is larger. They will therefore come to rest sooner than would a large vortex.

Surface-trapped potential vortices were allowed to evolve over a weak slope, and the tracks are shown in figure (3.39). The vortex amplitudes were adjusted so that the maximum surface velocity was 1.0 in all cases. Translation is more rapid for the larger vortices, and is comparable to the barotropic case in magnitude and direction. The small vortices on the other hand undergo a small cross-slope migration, with an unsteady and vanishing velocity.

Pankratov (1994) studied a freely evolving surface potential vortex with continuous stratification and a slope. The density contours on the slope were modelled via a modified contour dynamics scheme, and were coupled to the velocity field of the surface vortex[7]. The density contours were assumed to be only weakly

---

[7]Inherent in Pankratov's formulation was the fact that a surface vortex would conserve its
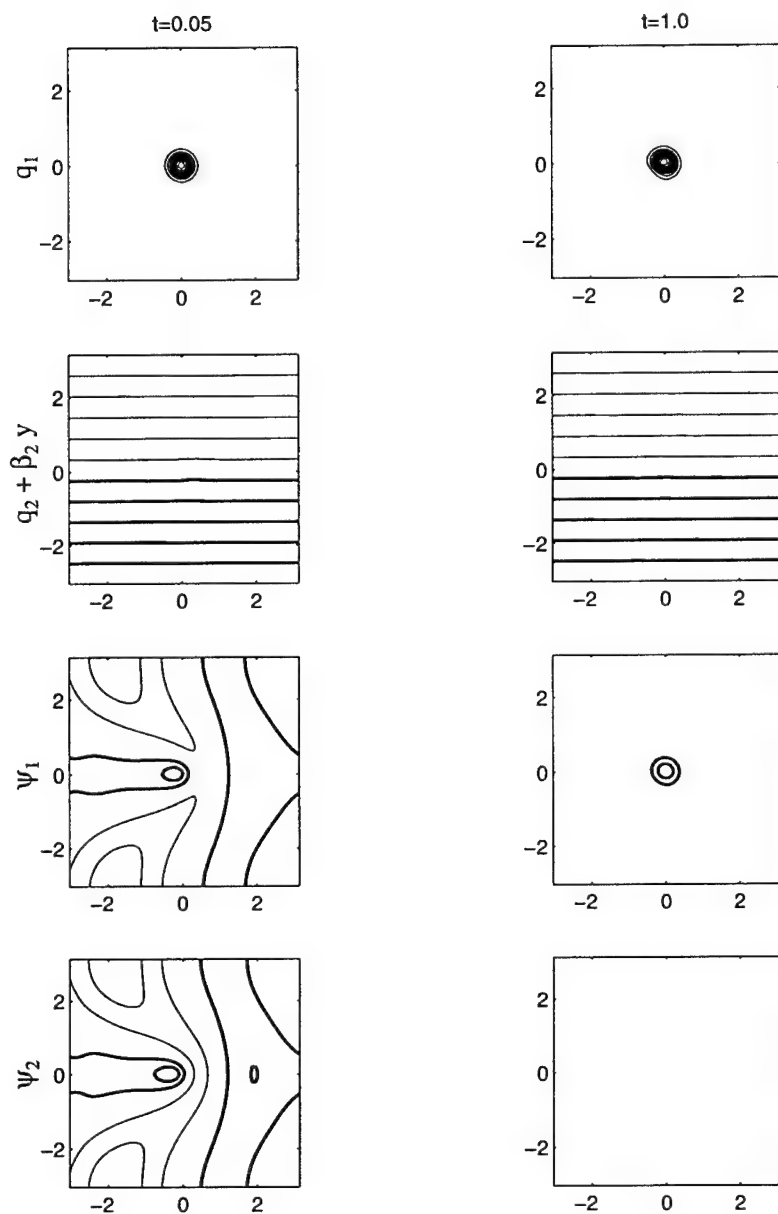
Figure 3.38: The fields for the two-layer non-isolated vortex with $r_0 = 1.8\lambda$ and $\beta_2 = 18$ at $t = .5$ and $t = 2$. The PV CI $= \pm[1:1:10]$ and the streamfunction CI $= \pm[1:1:10]/10$. The $t = 2$ fields are averaged from three realizations, at $t = 1.9, 2, 2.1$.

127
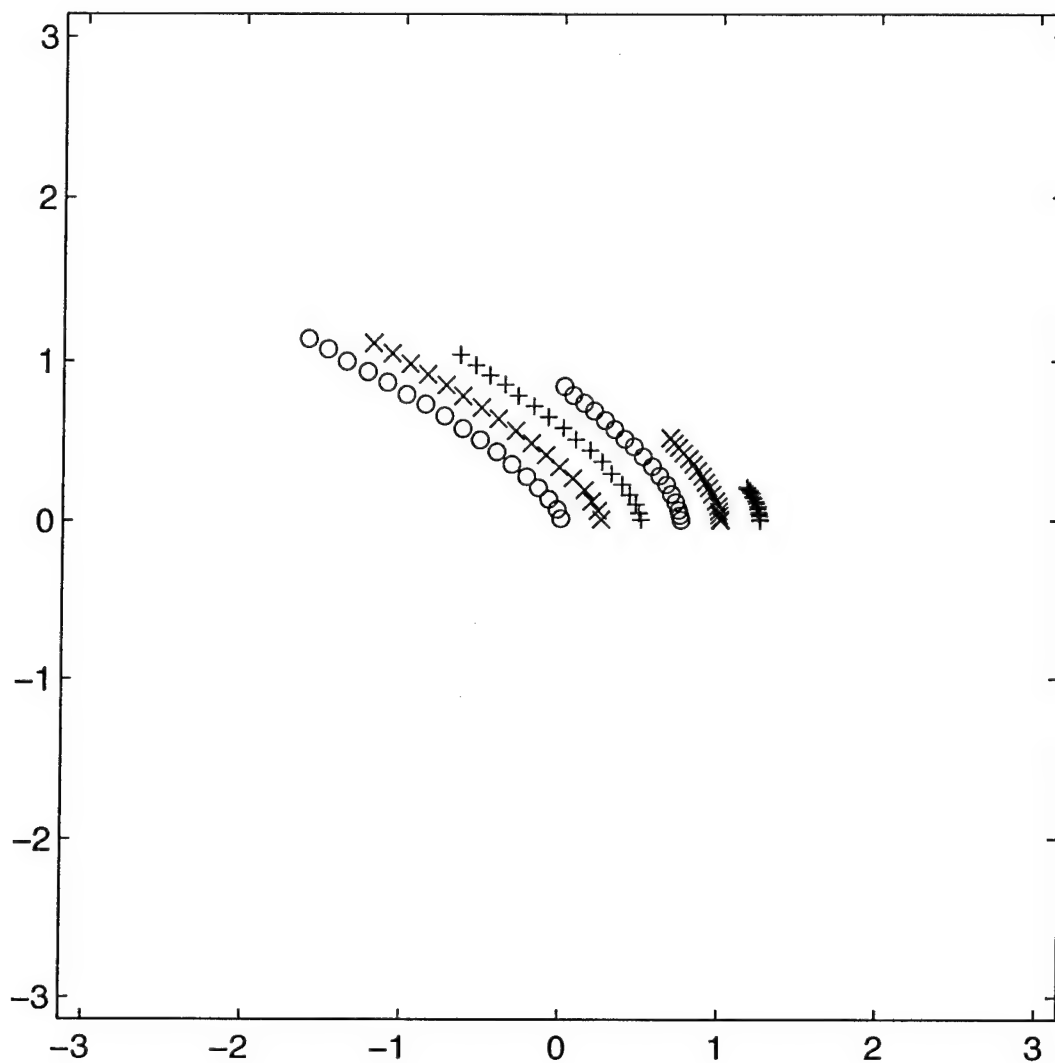
Figure 3.39: Non-isolated, surface-trapped potential vortex tracks with $\frac{\beta_2 r_0^2}{U_1} = .009$. The tracks from left to right correspond to sizes $r_0 = .9\lambda$, $.64\lambda$, $.45\lambda$, $.32\lambda$, $.23\lambda$, $.16\lambda$, . Positions are indicated every 3 time units.

perturbed by the vortex.

Of interest was that he found *eastward* motion of the vortex over the slope. In all cases above, as well as in all cases in chapter 3, the vortices always moved westward. Pankratov explained the motion by saying that the gyre to the west of the vortex was radiated away while that to the east remained and coupled with the surface vortex in such a way to yield steady northeastward transla- tion. The present results suggest that vortices with strong deep flow couple to the large scale wave field as do barotropic vortices and thereby move westward. Small vortices suffer radiation of the advecting gyres, but then stall. Pankra- tov maintained that the motion depended on continuous stratification and thus not captured in a layer model. One expects that both approaches should yield westward drifts with vanishing stratification, but perhaps differences are found with strong stratification (small vortices). The answer awaits a study in another continuously stratified model.

In summary, the non-isolated vortex differs from the zero circulation vortex in two principal ways: in the larger extent of its velocity field and in its immunity to the twisting instability. The consequence of the former is that the transla- tion velocity is found to be approximately independent of vortex size since the advecting gyres fill the domain. The vortex stability permits vertically aligned translation of sub-deformation scale barotropic vortices. However, the far field velocity of the non-isolated vortex is found to be truncated in a doubly-periodic model, and as such the results may disagree with predictions for a vortex on an infinite domain.

---

potential vorticity on the f-plane. Thus he assumed the point which was exploited in Chapter 3 to predict the final streamfunction in the strong slope cases.

Chapter 4

Geostrophic turbulence over a slope

Previously, it was found that the two lower layer advective parameters, $\frac{U_2}{\beta_2 L^2}$ and $\Lambda = \frac{F_2 U_1}{\beta_2}$ dictated the character of the single vortex evolution. The barotropic vortex became baroclinic when the former parameter was less than unity, and large surface vortices were baroclinically stable if the second was less than one. In the large slope cases, the upper vortex was found to be *steady* as it was unperturbed by the rapid waves and was stable.

A turbulent flow, in contrast, is not steady as vortices continually merge and shear one another apart. Neither are the scales of motion in freely evolving turbulence fixed, but are continually increasing. So it is reasonable to wonder whether the previous results carry over to this case. It will be seen that the basic ideas do carry over, with the exception that the slope is no longer able to stabilize the surface flow. In that case, however, Λ determines the rate at which available potential energy is lost.

In addition, the specific impact of the slope on the spectral cascade is of interest. As noted in Chapter one, β has a significant impact on two-dimensional turbulence as the inverse cascade of energy is arrested when turbulent vortices

disperse into Rossby waves. Determining whether such an arrest occurs and where is one of the goals of this chapter.

The chapter organization is as follows. A short section reviewing relevant aspects of cascading barotropic turbulence is given, and then the initial conditions in the slope case are discussed. The slope results are presented by looking in detail at a case in which the slope is "weak" (in a sense to be explained) and then at one in which it is "strong". Comparisons to a two layer run with a flat bottom and a run with a motionless lower layer are shown for comparison. Finally, a brief appendix is included in which similar results are obtained with only a bottom Ekman layer.

4.1   Background: Barotropic turbulence

As mentioned in Chapter 1, a singular and important aspect of two-dimensional turbulence is that energy cascades from small to large scales, the so-called "inverse cascade" of energy. In a numerical experiment, a finite domain is the only impediment to even larger scale motion. This tendency towards domain-filling motion can be seen in the streamfunction fields shown in figure (4.1). The initial flow, with energy sharply peaked at wavenumber 14 (see below), evolves to a field of eddies which span the doubly-periodic domain.

A second relevant point is that enstrophy or squared vorticity cascades to smaller scales where it is dissipated, here, by the numerical filter described in Chapter 2. What typically remains are the strongest maxima present in the initial vorticity field. These *vortices* last for many eddy turnover times and merge with like-sign features to produce larger (area) vortices. As suggested by McWilliams (1984), the forward enstrophy cascade is prevented in the interior of the vortices as vorticity there essentially is unable to be sheared out. The vortices
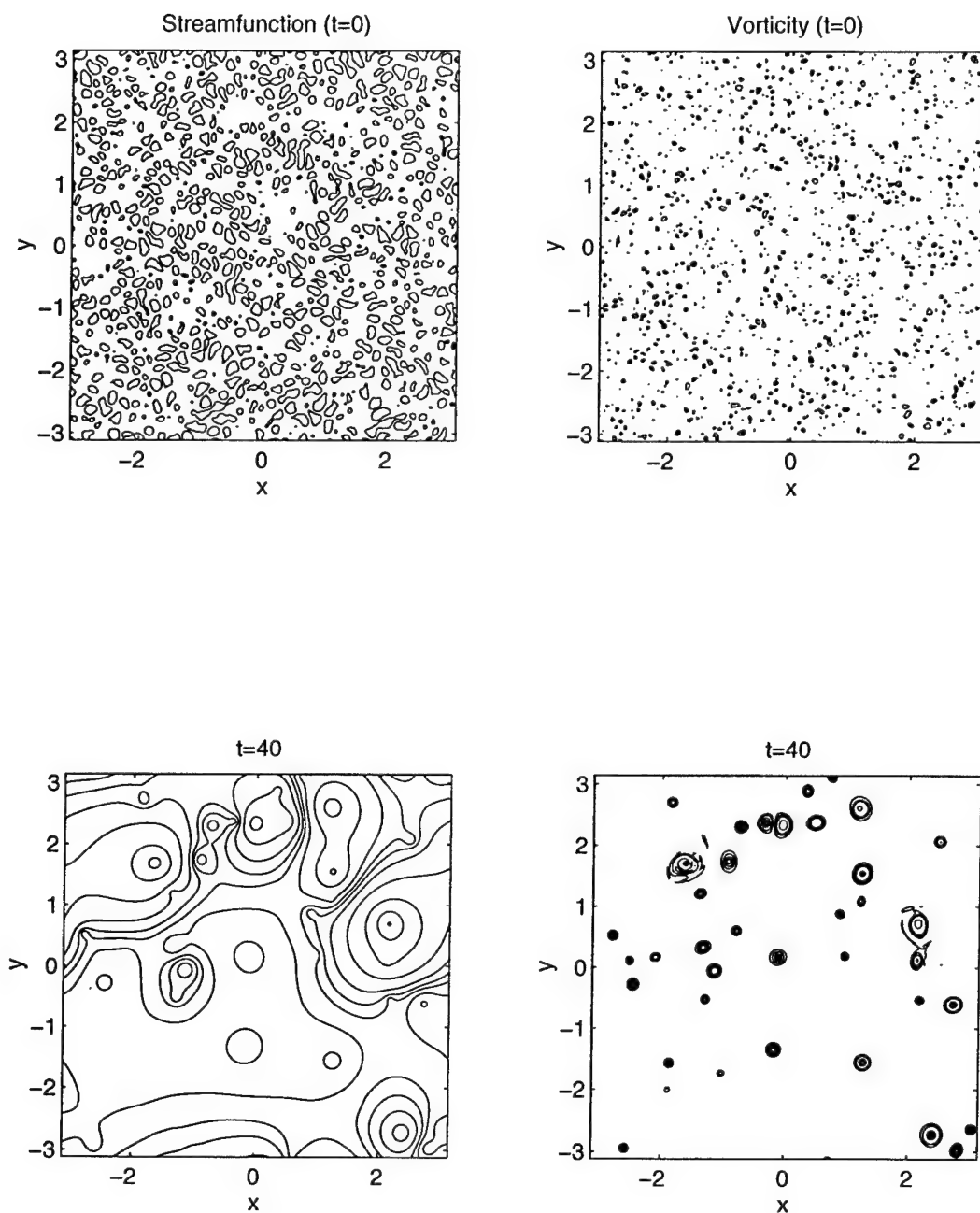
131

Figure 4.1: The streamfunction (left) and vorticity (right) fields for a barotropic turbulent run with $\beta = 0$. The initial fields are at the top, the late fields ($t = 40$) at the bottom. The streamfunction contour values were $\pm[.05\,.2\,.5\,1\,1.5\,2]$, the initial vorticity contour values $\pm[60\,100]$ and the late contour values $\pm[15\,30\,60\,100\,150]$.

dominate the dynamics after the bulk of the enstrophy has been dissipated, here about 5 eddy turnover times.

The barotropic evolution in the presence of a β-effect is different, as illustrated first by Rhines (1975). As seen in figure (4.2), the streamfunction also evolves to larger scales, but the late flow is anisotropic and not domain-filling. As argued by Rhines, when the motion reaches a certain scale, the dynamics are dominated by Rossby waves which are less efficient at transferring energy. This *arrest* scale is predicted by a simple scaling. The barotropic vorticity equation is:

$$\frac{\partial}{\partial t} \nabla^2 \psi + J(\psi, \nabla^2 \psi) + \beta \frac{\partial}{\partial x} \psi = 0. \tag{4.1}$$

If the β term is assumed order one, the advective term has a scale $\frac{U}{\beta L^2}$. This is the inverse of the nondimensional β discussed in Chapter 3. If the scale of motion is small, advection dominates and the cascade proceeds as if in the absence of β. But when $L \approx L_\beta \equiv \sqrt{\frac{2U}{\beta}}$,[1] advection and the β term are comparable and transfers are found to slow greatly. Though Rhines' argument is essentially isotropic, the resulting flow is generally *anisotropic*. This can be related to the anisotropy of the Rossby dispersion relation, i.e. to the fact that the wave frequency is proportional to the zonal wavenumber (see Vallis and Maltrud, 1994). The zonal scale exceeds the meridional scale, and the latter is of the same order of magnitude as the (isotropic) arrest scale.

One also finds that the coherent vortices disperse when the cascade arrests. As a result, the late vorticity field in figure (4.2) is essentially devoid of closed contours and dominated by the mean PV gradient. Thus β in a sense aids the forward cascade of enstrophy by removing the possibility that vorticity can be "shielded" in the interior of vortices.

---

[1]The factor of two results from the assumption of isotropy. See Rhines (1975).
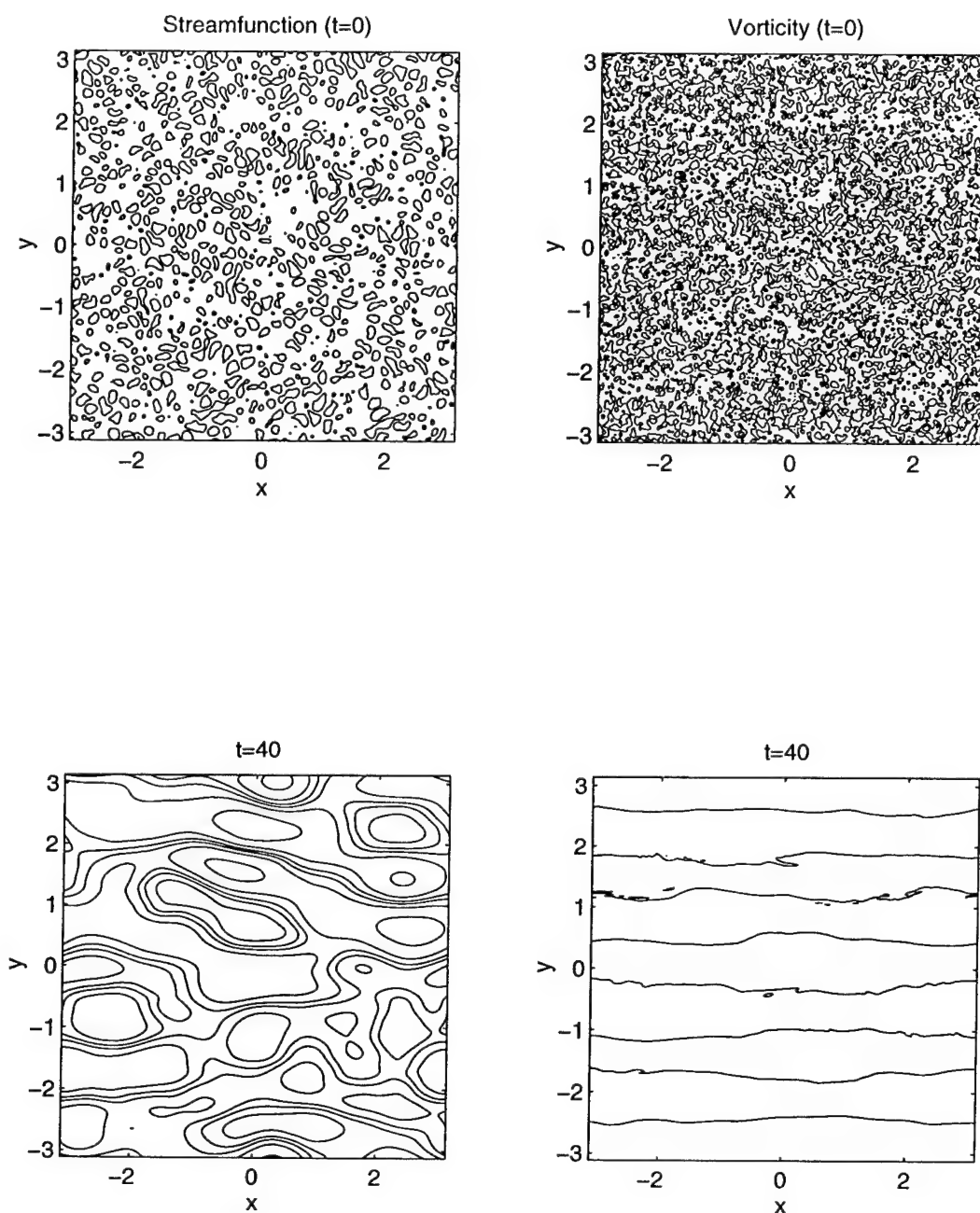
Figure 4.2: The streamfunction (left) and total vorticity (right) fields for a barotropic turbulent run with $\beta = 62.5$. The initial fields are at the top, the late fields ($t = 40$) at the bottom. The streamfunction contour values were $\pm[.05 \,.2 \,.5 \, 1 \, 1.5 \, 2]$; the vorticity contour values are drawn so that 8 contours span the range from maximum to minimum vorticity, roughly ± 307 ($t = 0$) and ± 208 ($t = 40$).

Thus a mean potential vorticity gradient significantly alters the two-dimensional cascades. In a barotropic fluid, a topographic slope acts as a β effect, and one thus expects an arrest with scale $L \approx L_\beta \equiv \sqrt{\frac{2U}{\beta_2}}$. This scale may be smaller than the planetary version because the slope can be steep (β_2 large). The PV gradient in the two-layer, f-plane case over a slope is confined to the lower layer. It is as if the two barotropic cases discussed above were stacked vertically. If the interface between the two layers was rigid, one would find the same evolutions. However, the interface can move, so the cascades will be coupled, and outcome is less obvious.

4.2   Initial conditions

As before, one must specify the initial vertical distribution of energy. Rhines (1977) considered surface-trapped, small-scale turbulence when examining the cascade of baroclinic energy towards the deformation radius. McWilliams (1990b) on the other hand chose an initial spectrum which filled his continuously stratified domain, leading to baroclinic cascades on multiple levels. I have chosen an initial flow which resembles Rhines's: a surface-trapped streamfunction field with a peak scale smaller than the deformation radius. This facilitates observing the spin-up of the lower layer, or the "barotropic cascade" in Rhines's terminology.

The initial surface kinetic energy spectrum used is shown in figure 4.3, and is given by:

$$KE_1(\kappa) = \begin{cases} 0 & \text{if } \kappa < \kappa_0 \\ \frac{KE_{01}\kappa^6}{(\kappa+\kappa_0)^{18}} & \text{if } \kappa \geq \kappa_0 \end{cases}$$

The coefficient KE_{01} is determined by the normalization:

$$\frac{1}{2}\int\int u_1^2 + v_1^2 \; dx \; dy = \frac{1}{2}\sum_k\sum_l KE_1(\kappa) = \frac{1}{2}\sum_k\sum_l \kappa^2|\hat{\psi}_1|^2 = 0.5 \,. \qquad (4.2)$$

135

The normalization constant chosen yields a rms surface velocity of one. The steep spectral tail is the same used in the barotropic study of McWilliams (1990a).[2]. The sharp tail was chosen to minimize energy lost immediatedly to the numerical filter (chapter 2), which in turn permitted taking larger values of κ_0 and $\sqrt{F}$. The vortices which emerge tend to be comparatively uniform in size and strength (McWilliams 1990a), a fact which was of little importance in what follows.

The number of vortices which emerge depends on the resolution, because higher resolution allows decreased lateral damping which, in turn, preserves more small vortices (Benzi et al., 1986). Finer grids also means better resolution of the initial vorticity gradients and thus *stronger* vortices. Because stronger vortices are more resistant to shear (Mariotti et al., 1994), this too increases the vortex population. The main runs discussed below were made with 256^2 grid points, which was sufficient to capture the qualitative vortex dynamics. The small time step required for the large slopes essentially prohibited finer resolution with the computers available. Supplementary runs with coarser resolution were made when longer integrations were required, and for the Ekman cases in Appendix B.

The removal of the long wave portion of the spectrum yields a distribution resembling the "classical" initial spectra used by Rhines (1975), Shepherd (1987) and others. This choice simply aids in observing the changes at the deformation radius.

The dash-dot line in figure 4.3 is the resulting potential energy if the deformation wavenumber is 10, the latter indicated in the plot (and later spectral plots) by the vertical dotted line.

In chapter 3, the slope was defined to be strong when $\frac{U_2}{\beta_2 L^2} < 1$, but such a definition is useless with $U_2(t=0) = 0$. An alternative is to use $\Lambda = \frac{F_2 U_1}{\beta_2}$ which is not only independent of the deep velocities, but is also approximately scale

---

[2]Note however that observed energy spectra are thought to have a decay nearer to κ^{-3} (Stammer and Boning, 1992), but barotropic turbulence calculations generally indicate steeper slopes, possibly due to coherent vortices (e.g. Basdevant et al, 1981; Babiano et al., 1987).
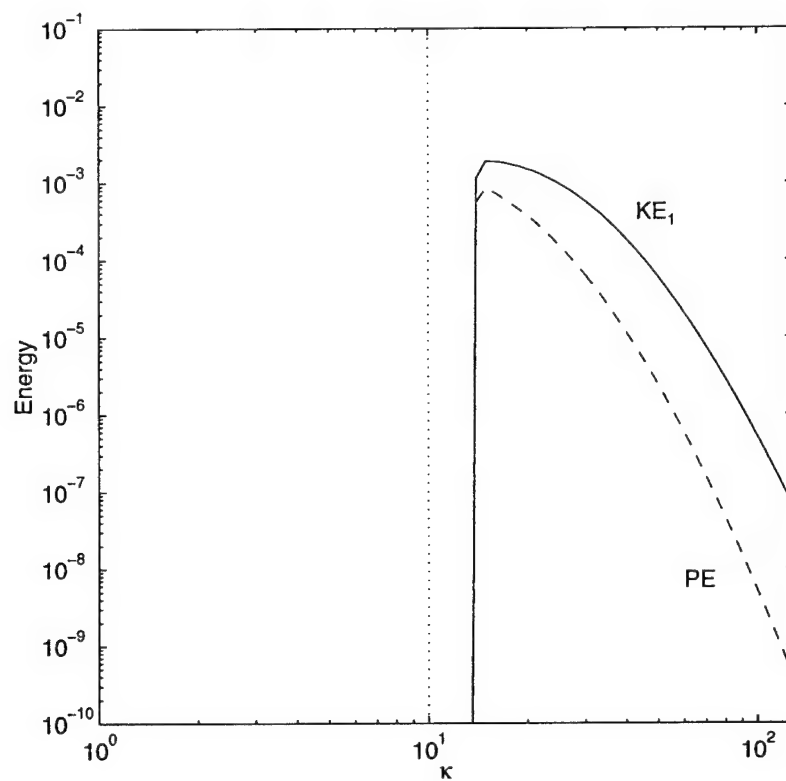
Figure 4.3: The initial spectrum. The surface kinetic energy is (solid) and potential energy is (dash-dot).

independent. Thus, the slope is "strong" when it is steep enough potentially to inhibit baroclinic instability; i.e. the weak slope case has $\Lambda > 1$ and the strong slope case has $\Lambda < 1$.

4.3   Weak slope: $\Lambda = 4$

In this and the following examples, the $F_1 = 100$ so the deformation wavenumber is 10. This choice represents a compromise between the desire to have a large scale separation between deformation and domain scales (to aid observing arrests), with the necessity of keeping the initial scales large enough to avoid dissipation of a significant portion of the energy in the early stages of the integration. In this case, $\frac{\beta_2 L_{domain}^2}{U_1} = 62.5$, which yields a value of $\Lambda \approx 4$ because the *maximum* surface velocities are between $2 - 3$. The strong slope case, discussed below, has a smaller value of $\Lambda = 0.1$. The present case has equal layer depths, so $F \equiv F_1 = F_2$.

4.3.1   Streamfunction and energy

The streamfunction fields for the weak slope case are shown in figure 4.4. As in the previous barotropic cases, the cascade to larger scales is evident. In addition, one finds that the fields become more *barotropic* in that the larger features are nearly identical in the two layers.

The barotropic cascade in two layers over a flat bottom was discussed by Rhines (1977) and can be inferred from the work of Charney (1971). The latter postulated that in a stratified quasigeostrophic flow, the cascade to larger horizontal scales will be accompanied by a cascade to larger vertical scales. Rhines noted that deformation-scale energy is expected to lead to layer coupling (his "barotropic cascade"). One finds that this occurs over the slope also in the case

138

$\Lambda > 1$, consistent with the notion that the slope is not blocking baroclinic instability. However, close examination of the streamfunction fields suggests that the motion is *bottom*-intensified, and that there is small-scale motion at the surface which has no component at depth. As in the barotropic β-plane case above, the late flow is found to be anisotropic and does not fill the domain, suggesting an arrest.

The energy spectra are shown in (figure 4.5). The spectra have been averaged in wavenumber bins for smoothing, and so are isotropic. They suggest a rapid shift towards larger scales (smaller wavenumbers), and the peak in energies has moved past the deformation scale by $t = 5$. However, the arrest clearly ceases and the peak at $t = 20$ lies between $4 - 5$. In contrast, the peak from a flat-bottom experiment (lower right) lies at the gravest scales at the same time. Note that the lower layer kinetic energy exceeds that of the upper layer at the peak, which is also consistent with the bottom-intensification noted above. At larger scales one finds that the potential energy dominates kinetic energies. In contrast, the flat bottom case has $KE_1 \geq KE_2$ at large scales, and weaker potential energy at scales larger than the deformation radius, consistent with barotropic motion.

In the enstrophy cascading range (from the peak wavenumber out to dissipation range beginning at wavenumber 85), the spectral slope is nearly constant for the lower layer kinetic energy, but is curved for the upper layer. The presence of coherent vortices can lead to multiple slopes in the inertial range (e.g. Santengelo et al., 1989); if so, it would appear that there are coherent vortices at the surface, but not at depth. This is indeed the case, as shown below. The slope in both cases is greater than the classical value of κ^{-3} (Kraichnan, 1967).

The rate of spectral evolution can be quantified by considering spectral fluxes, derived in chapter 2. The barotropic and baroclinic fluxes are shown in figure (4.6). The fluxes for the flat bottom case are shown as well for reference. In the flat bottom case, one finds that there is an active transfer of energy from

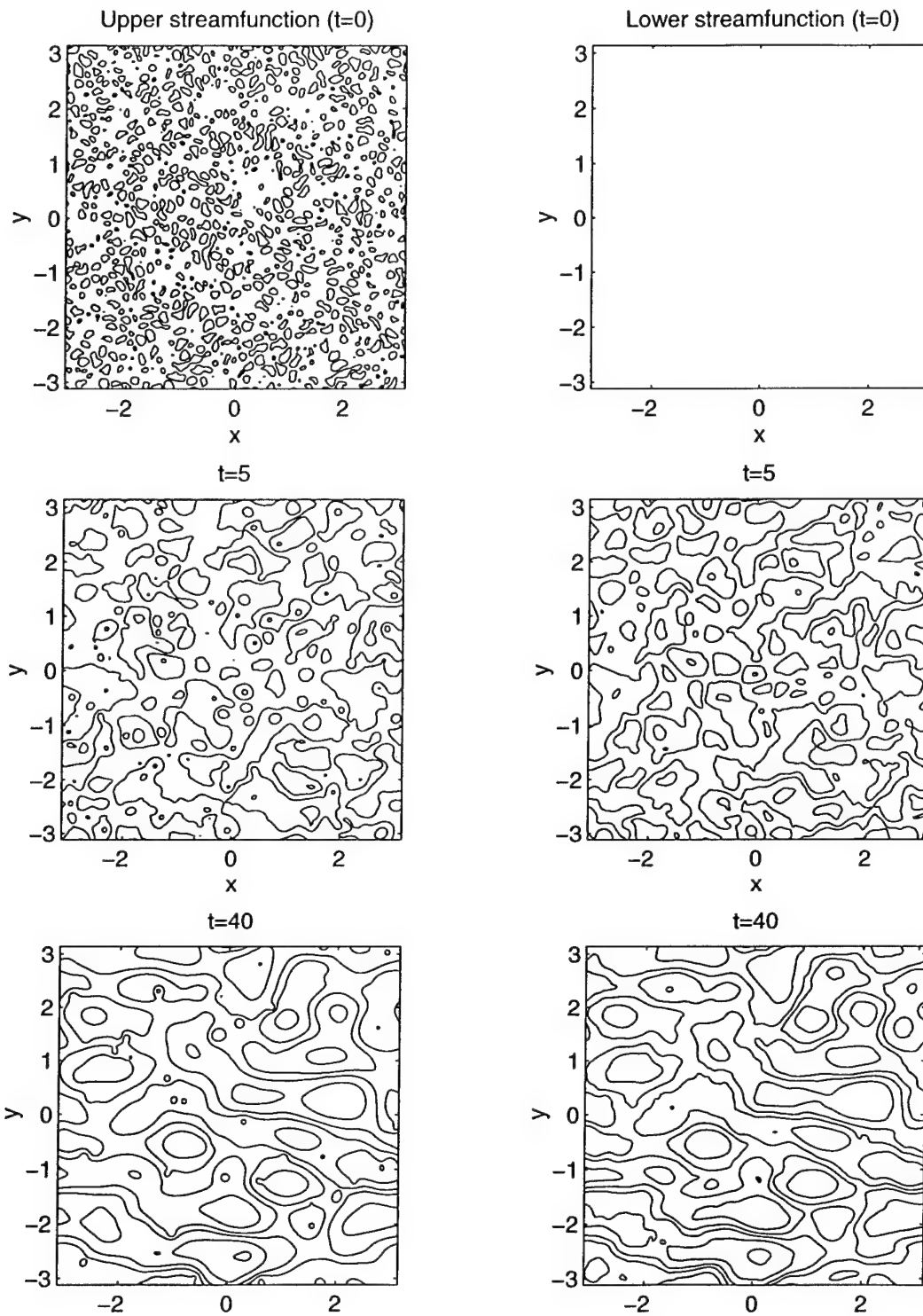139

Figure 4.4: The upper and lower layer streamfunction fields for the weak slope case. The contour values are $\pm[.05\ .2\ .5\ 1\ 1.5\ 2]$.
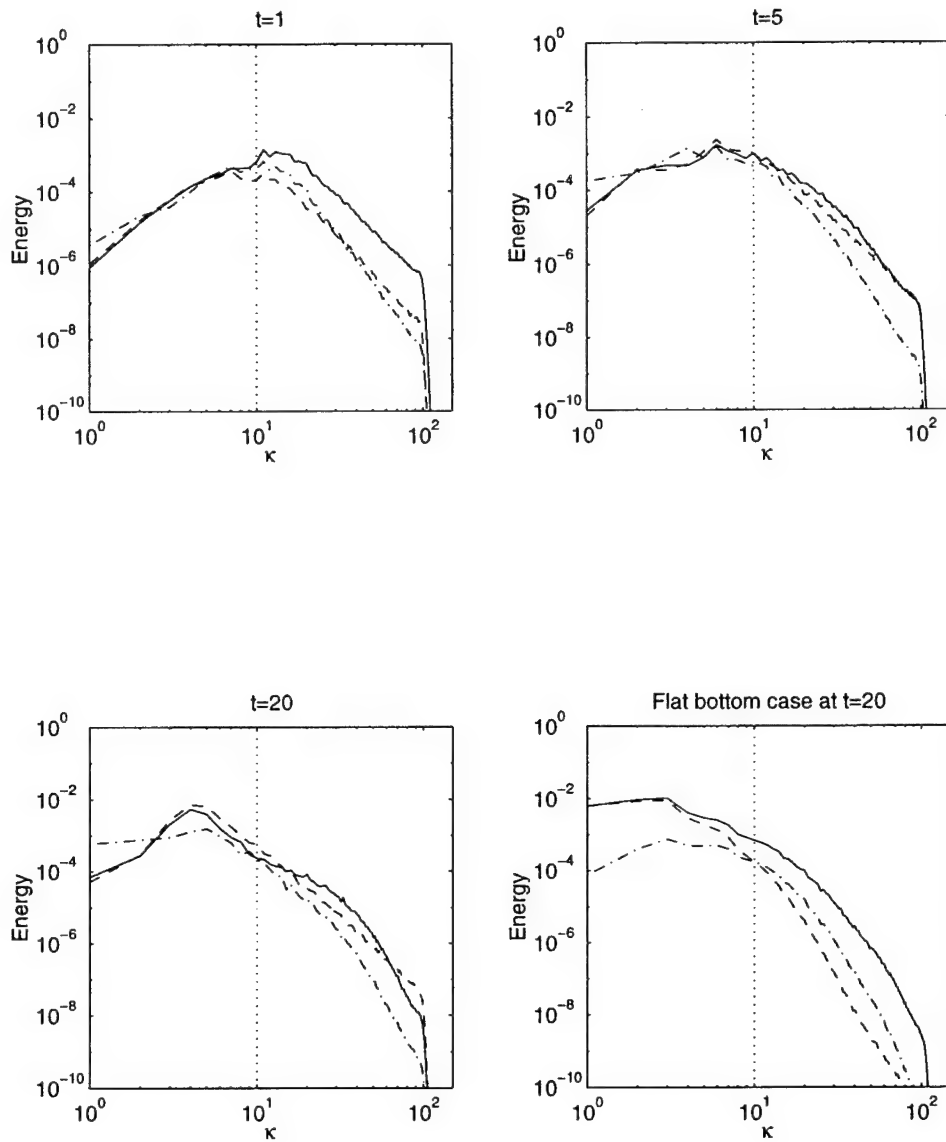
140

Figure 4.5: The energy spectra for the weak slope and flat bottom (lower right) cases. The components are KE_1 (solid), KE_2 (dashed) and PE (dash-dot). The spectra have been averaged in unit wavenumber bins from $[\kappa - .5, \kappa + .5)$.

the baroclinic to the barotropic mode at early times followed by an essentially barotropic flux of energy to large scales which is more episodic, but nevertheless extends to the largest scales. At the same time, a forward (downscale) flux of thickness is approximately balanced by an inverse (upscale) baroclinic self-advective flux, suggestive of an inverse correlation which is found in baroclinic instability (Pedlosky, 1987). The intermode transfer is intense early on due to the proximity of the initial energy peak and the deformation radius.

The slope case differs in that the intermode transfer is greatly prolonged, and still evident even at $t = 20$. However, the flux is nearly balanced by a forward flux due to the topographic term, thereby returning the energy to the barotropic mode. Recall that the sum over all wavenumbers of the baroclinic to barotropic transfer and the barotropic to baroclinic transfer are equal, but that the two may not be equal at every wavenumber. However, the topographic transfer is equal at each wavenumber, so the flux due to the topographic transfer is equal and opposite for the two modes. As explained below, the reason for the balance between intermode and topographic transfers is that energy is being "taken up" by topographic waves, which are bottom-intensified. We see here that the balance occurs *at all times*, i.e. there is no delay in the conversion to wave energy.

The total energy budgets also differ for the flat and sloping bottom cases, as shown in figure (4.7). In both cases, the upper layer kinetic energy decreases rapidly while the lower layer kinetic energy increases. The decrease of KE_1 is a result of the shift to larger scales in the surface layer. With $\psi_2 \approx 0$, $\nabla^2 \psi_1$ must balance $F\psi_1$ to conserve surface PV, implying KE_1 and PE must balance. The ratio PE to KE_1 scales as $F_1 L^2$, so an increase in scale causes a decrease in KE_1.

In the flat bottom case, PE is converted simultaneously to KE_2 due to the conversion of baroclinic to barotropic energy. In the flat bottom case the deep kinetic energy does not exceed the surface kinetic energy (due to dominance of the surface potential vorticity, described below), but in the slope case it does,

142
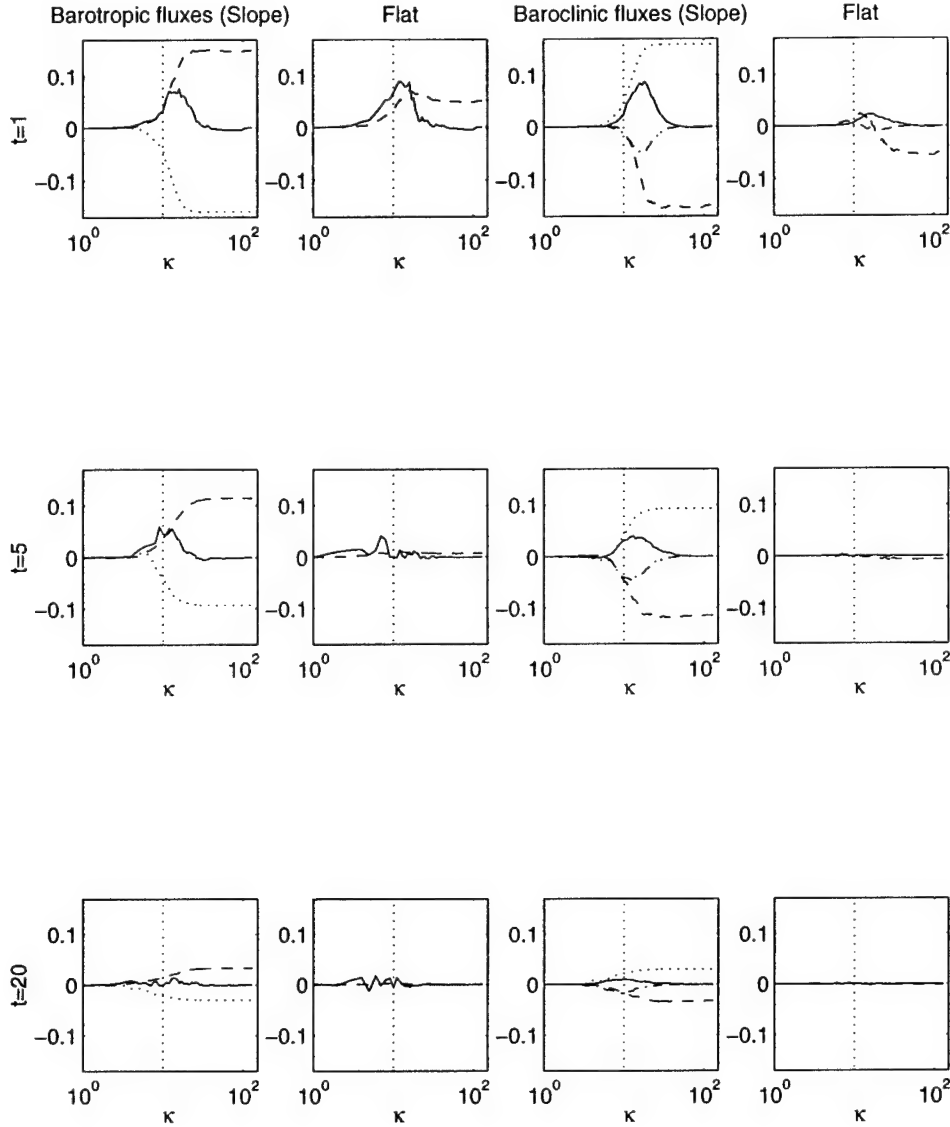
Figure 4.6: The barotropic and baroclinic spectral fluxes for the weak slope and flat bottom cases. The barotropic fluxes are $\Re\{\hat{\psi}^*J(\hat{\psi},\kappa^2\hat{\psi})\}$ (solid), $\Re\{\hat{\psi}^*J(\hat{\tau},\kappa^2\hat{\tau})\}$ (dashed) and $\Re\{-ik\hat{\psi}^*\hat{\tau}\}$ (dotted). The baroclinic fluxes are $\Re\{\hat{\tau}^*J(\hat{\tau},\kappa^2\hat{\psi})\}$ (solid), $\Re\{\hat{\tau}^*J(\hat{\psi},\kappa^2\hat{\tau})\}$ (dashed), $\Re\{\hat{\tau}^*J(\hat{\psi},-2F\hat{\tau})\}$ (dash-dot) and $\Re\{ik\hat{\psi}^*\hat{\tau}\}$ (dotted).

indicating a greater transfer of energy from the surface to bottom layers. A second, subtler difference is that KE_1 and PE are oscillating rapidly and out of phase in the slope case, but not in flat bottom case.

An interpretation which is consistent with these observations is one in which surface-trapped energy cascades to the deformation scale, couples with the lower layer, then cascades barotropically to a topographic arrest scale. The coupling occurs because wave radiation is too slow at deformation scale; if the perturbed lower layer velocities are of the same order as the surface velocities, then $\Lambda > 1$ implies that $U_1 \approx U_2 > \frac{\beta_2}{F}$. Secondly, if the flow is nearly barotropic, advection at depth is primarily advection of relative vorticity, of magnitude $\frac{U_2}{\beta_2 L^2}$ compared to $\beta_2 \frac{\partial}{\partial x} \psi_2$. Hence thereafter the cascade is analogous to the barotropic Rhines case, with an arrest occurring near $\kappa_s \equiv \frac{\beta_2}{2U_2}$. Moreover both barotropic and topographic arrests are anisotropic (Vallis and Maltrud, 1994).

However, there are differences which make the weak slope case interesting. For one, the arrest scale is initially infinite because there is no flow at depth. Thus the arrest scale affectively "sweeps in" past the deformation scale during the spin-up of the lower layer. This is in strong contrast to the barotropic Rhines case in which the arrest scale is fixed because U is fixed by conservation of energy. The fact that the slope cannot block instability essentially guarantees that the arrest scale will move past the deformation radius; if energy becomes predominantly barotropic, then the mean velocity will be conserved thereafter, so $\Lambda > 1$ roughly implies that $\sqrt{\frac{\beta_2}{U_1}} \approx \sqrt{\frac{\beta_2}{U_2}} < \sqrt{F}$.[3] During the early stages of the lower layer spin-up, a degree of wave radiation is expected, dependent on the strength of the slope. In the case considered above, wave radiation apparently occurs all the time as the topographic flux term is always large.

A second fundamental difference with the barotropic case is that the waves

---

[3]This highlights the importance of evaluating Λ with the surface velocity *at deformation scale* rather than at the initial time.
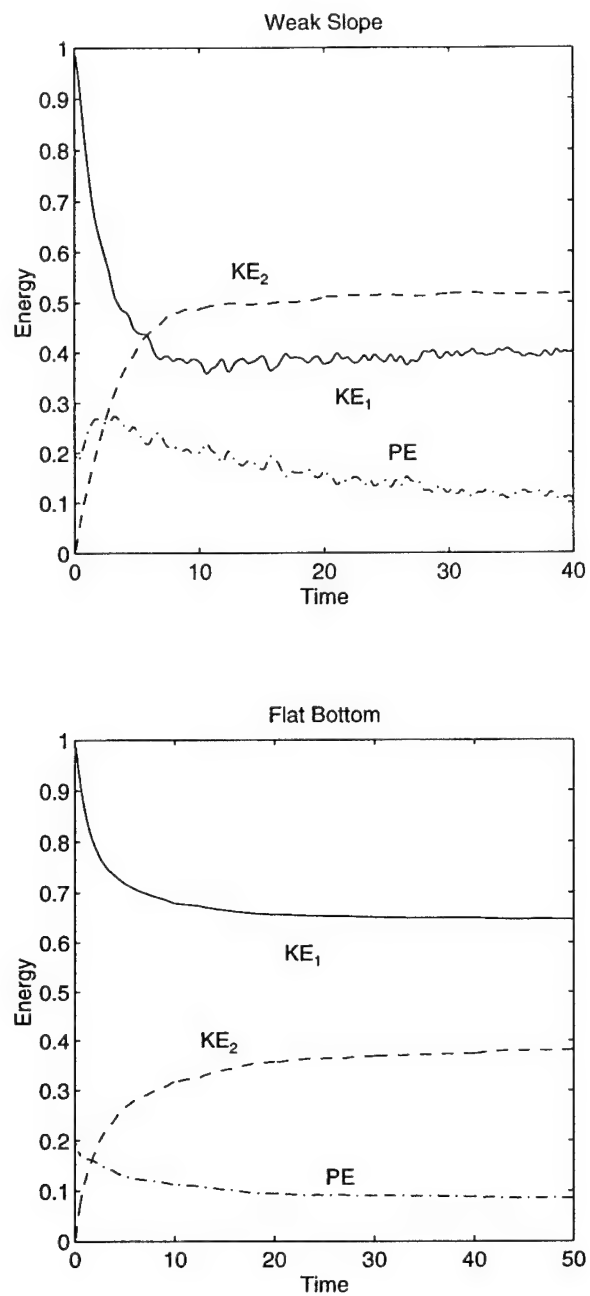
Figure 4.7: The time series of the energy components for the weak slope and flat bottom cases. The components are KE_1 (solid), KE_2 (dashed) and PE (dash-dot). The initial total energy is the same for the two cases.

are not barotropic, but bottom-intensified. As described in chapter 3, as $\hat{\psi}_{1w} = \frac{F}{\kappa^2 + F_1}\hat{\psi}_{2w} \le \psi_{2w}$. This has two implications. First, if the flow evolves to one dominated by topographic waves, the lower layer kinetic energy should exceed that in the upper layer, as found in figure 4.7. Secondly, as seen in chapter 3 with an initially barotropic vortex over a slope, one expects that a surface-trapped component of the flow will be left behind after wave radiation. This portion carries the surface potential vorticity, as described in Chapter 3, since the topographic waves have zero surface PV. Plots of the potential vorticity fields confirm this, as discussed below. Note that the degree of wave baroclinicity depends on their scale, with large scale waves being nearly barotropic. Thus in the limit of vanishing slope or stratification, the arrest becomes more like the Rhines case.

The shifting arrest scale obviously complicates predicting the final scale of motion *a priori*. However, an estimate can be made given this particular initial condition . If $KE_{2f} \approx KE_{1f} \approx \frac{1}{2}TE_0$ where the latter is the total initial energy, then $\kappa_s \approx 6.4$, which is somewhat larger than the observed value of $\sqrt{4^2 + 1^2} = 4.1$. However, the arrest argument is an isotropic one, and so applies to the early arrest (barely visible in the $t = 5$ plot in figure 4.5); one finds that the spectrum does indeed initially arrest at around $\kappa = 6$.

4.3.2 Potential vorticity and surface vortices

As noted above and in chapter 3, topographic waves have zero surface potential vorticity, so one might ask of the fate of that field. The potential vorticities of the weak slope run of figure (4.4) are shown in figure (4.8). Here it is obvious that the flow has broken into two components: the bottom-trapped wave field and a collection of isotropic, surface vortices. In fact, in terms of PV the weak slope case resembles *both* the $\beta = 0$ and the $\beta \ne 0$ barotropic cases in that vortices are present where the mean PV gradient vanishes. The contrast between the $t = 40$

146

plots in figure (4.8) and figure (4.4) is striking.

Some differences with the barotropic cases are evident, though. The slope vortices are smaller than their barotropic components, an aspect which is quantified below. Also, the deep PV contours appear more strongly perturbed, indicating the greater importance of relative vorticity and/or stretching in the slope case. Note that the perturbations are the most severe at $t = 5$, or shortly after the period of strongest baroclinic to barotropic energy conversion (figure (4.6)). At the late time the perturbations are smaller, consistent with wave domination.

The differences between upper and lower perturbation PV fields are highlighted in plots of the enstrophy spectra, shown in figure(4.9). The two dimensional enstrophy is shown in the upper panels; the isotropic spectra are superimposed at lower left, with the flat bottom spectra at lower right for comparison. The two dimensional spectra show that the upper field is nearly isotropic and covers a broad range of scales, whereas the lower field is anisotropic and dominated by a strong peak at $(k, l) = (1, 4)$. Plots of the two dimensional kinetic and potential energy spectra (not shown) reveal a similar peak, so that the peak is representative of the dominant wave harmonic.

The band-averaged spectra similarly suggest a broad range of scales for the upper layer enstrophy and an "arrested" lower layer enstrophy (compare $|q_2|^2$ with the kinetic energy spectra in figure (4.5)). Of interest though are the significant differences from the flat bottom case. In the latter case, the upper layer enstrophy is peaked, and at scales somewhat smaller than the domain scale; this is due to the compactness of the vorticity field compared to the streamfunction field which does fill the domain. In contrast the lower enstrophy is *vanishing*. In the absence of topography enstrophy decreases monotonically due to numerical dissipation, and the choice of a sub-deformation scale, surface-trapped flow yields a weak initial lower layer PV field. Thus, no coherent vortices emerge in the lower layer and the deep enstrophy is strained out by the upper layer vortices. In other
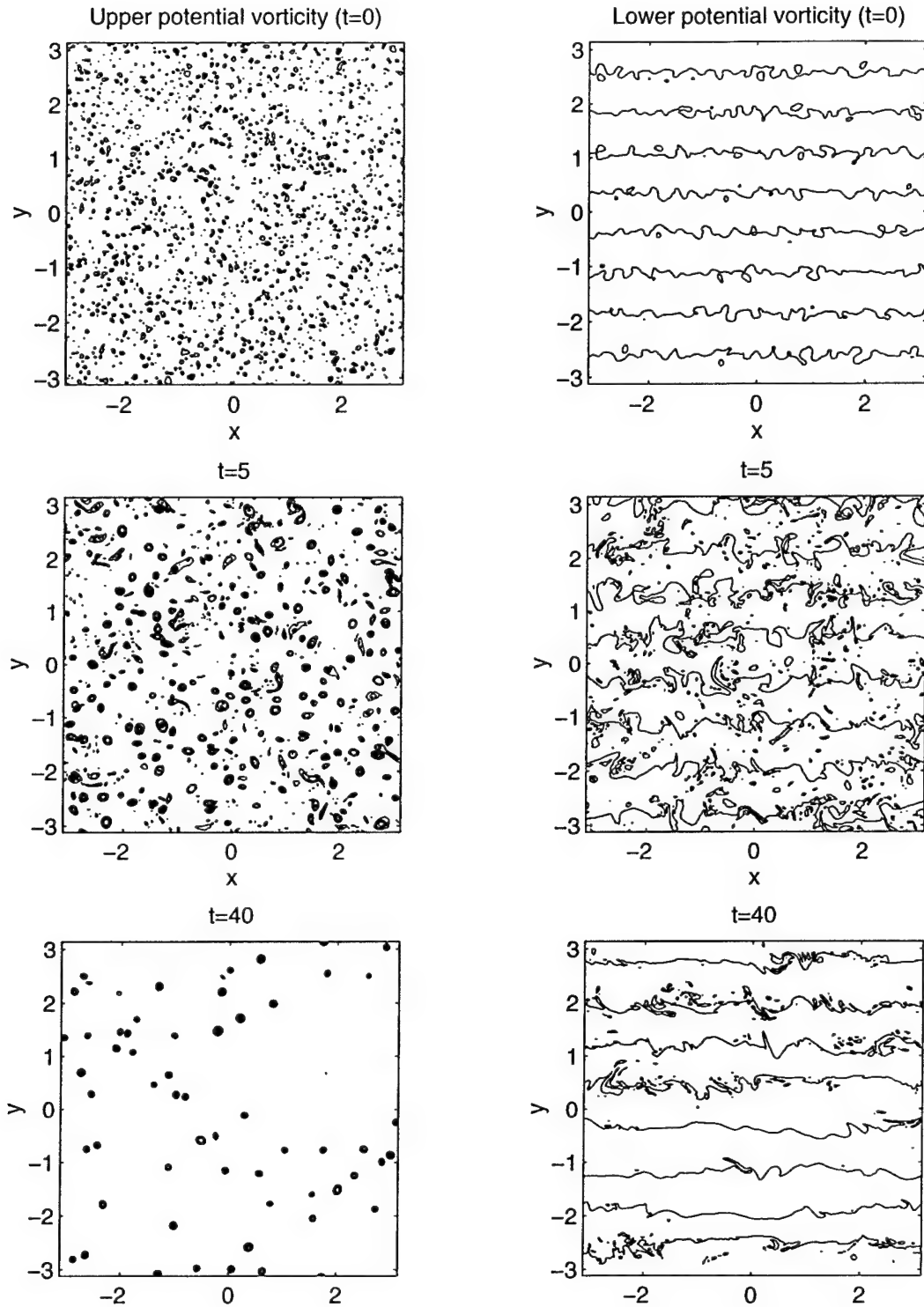
147

Figure 4.8: The upper and lower layer potential vorticity fields for the weak slope case ($\beta_2 = 62.5$). The contour values were $\pm[60\,100]$ at the upper left, $\pm[15\,30\,60\,100\,150]$ in the lower left plots and $\pm[50\,100\,150\,200]$ in the right-hand plots.

148

words, the flat bottom case evolves to a surface-trapped PV distribution. The deep enstrophy is not conserved over the slope, and actually grows to exceed the total surface enstrophy. The surface vortices are still present, but do not dominate the dynamics as in they are found to in the flat bottom case.

It should be emphasized that the distinguishing feature of the slope case is a *coexistence* between surface potential vortices and arrested waves, and that this coexistence is a consequence of the vertical variation of the mean PV gradient. In the barotropic cases, vortices either merge and grow or disperse into Rossby waves.

McWilliams (1990a, hereafter M90) employed a vortex counting routine to quantify interactions between vortices in the $\beta = 0$ barotropic case, as noted in Chapters 1 and 2. He found that the number of vortices exhibited a power law decay, i.e. $N \propto t^{-.75}$, and that the mean peak vorticity remained nearly constant. All other vortex properties appeared to have power law dependences on time as well. The findings prompted Carnevale et al. (1991b) to propose a scaling theory wherein all vortex properties and global turbulence properties (e.g. total enstrophy) were predicted if the decay rate of the number of vortices was known. A study of a collection of point vortices with a merger law was shown to be consistent with the theory (Weiss and McWilliams, 1993), but it is possible that the decay of the number of vortices is a result of finite numerical resolution (Dritschel, 1994). In any event, it is reasonable to compare the statistics of the surface vortices in these cases with the barotropic case, and the vortex counting approach presents a useful means of examining the results.

The vortex counting routine is described in Chapter 2; essentially the routine identifies simply connected regions which have vorticity greater than a prescribed threshold. The surface potential vorticity is the field analyzed, as opposed to relative vorticity (McWilliams, 1990b), and the threshold value, chosen by examining plots of the field, was set to 10 (see also Benzi et al., 1988). Vortex statistics for
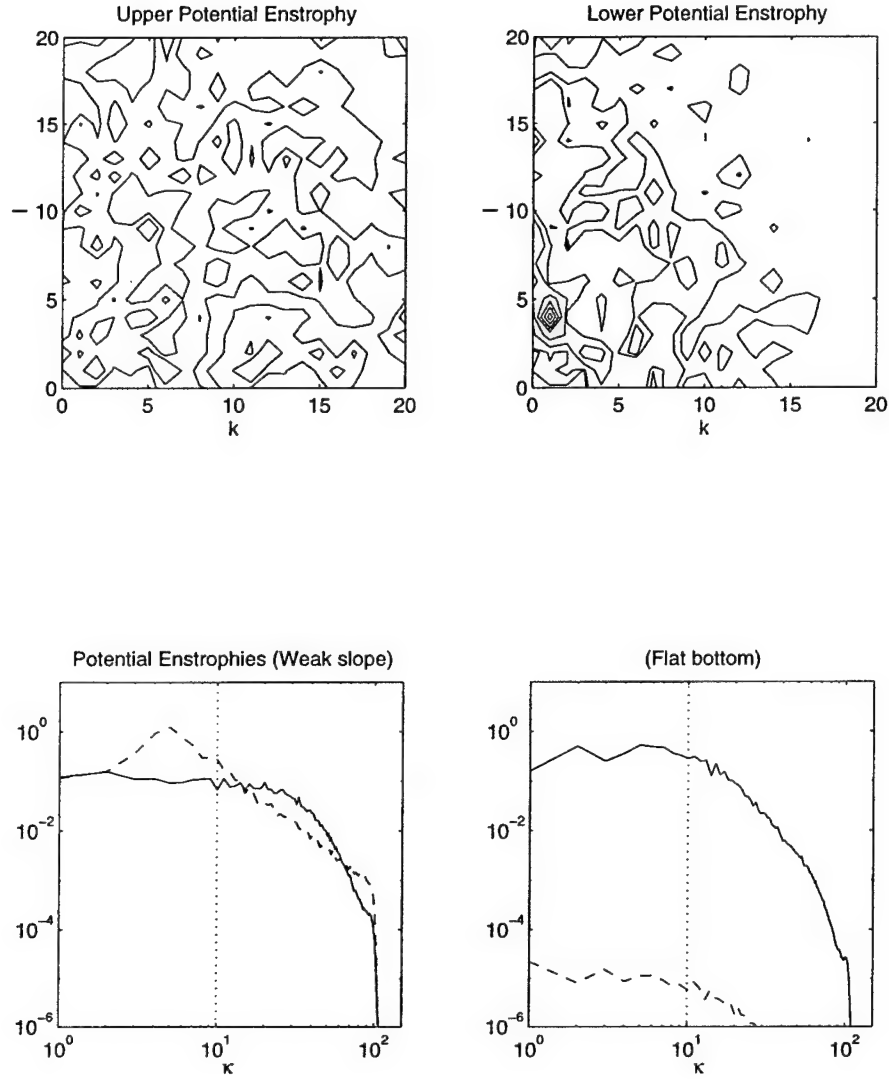
Figure 4.9: The enstrophy spectra for the weak slope case at $t = 20$. The two dimensional spectra are shown at the top, with contours $[.1\,.3\,.5\,.7\,.9]$ of the maximum values: $max(q_1) = .212$, $max(q_2) = 5.16$. The band-averaged spectra at $t = 20$ are shown at lower left, and the flat bottom case at the same time at lower right.

three cases are shown in figure (4.10). The three cases are a flat bottom run, the $\Lambda = 4$ slope case, and a weaker slope case with $\Lambda = 16$; shown are the number of vortices, mean area and mean peak, or absolute maximum, of potential vorticity.

The number of vortices is comparable in all three cases and the runs are nearly indistinguishable at late times, given that the measure is noisy. Moreover, the rate of decay is consistent with the barotropic rate given in M90, indicated by the solid line, suggesting that the merger rate, perhaps surprisingly, is unaffected by the wave field. The only apparent difference is that there are more vortices at early times in the slope cases, particularly noticeable with the $\Lambda = 4$ case.

The mean peak vorticity is also comparable in the three cases, and weakly *increasing.* As noted, M90 held that the mean peak vorticity was approximately constant. He argued that selective losses of weaker vortices to mergers, which would increase the mean, were balanced by a viscous decay of the stronger vortices yielding a nearly constant mean. Weiss and McWilliams (1993) found that the mean decayed slightly, indicating a greater rate of viscous decay. If the increase is significant in these results, one expects that the change due to mergers is dominant. A possible reason for the discrepancy is that M90 and Weiss and McWilliams used hyperviscous damping for their spectral runs, whereas the present runs were made with a numerical filter; the latter was shown in chapter 2 to limit decay of intermediate wavenumbers. However, due to computational limitations, sensitivity to damping schemes were not conducted in the turbulence runs. In any event, the deviation from a constant mean peak vorticity is not large, even in the presence of the slope.

Significant differences between the runs are found with the mean areas. In the flat bottom case, the area is increasing, albeit somewhat less than in the barotropic case of M90, although such a difference is plausible with a single realization. In contrast, the area is found to *decrease* in the slope cases at a rate which depends on the size of the slope. In the $\Lambda = 4$ case, the vortices are

significantly smaller even when counting commences, at $t = 5$. At later times, the $\Lambda = 4$ vortices are roughly one third the size of the flat bottom vortices.

The difference in the areas is linked to the arrest to topographic waves, as explained in the following. The vortex dynamics over a flat bottom and weak slope are examined in more detail, to illustrate the changes incurred by the slope.

Flat bottom

In the flat bottom case, the (initially weak) lower layer enstrophy is strained out and dissipated, as noted above, whereas the surface PV evolves to a collection of isotropic vortices. Thus the surface vortices may be idealized as having only surface potential vorticity. As in Chapter 3, the PV can be inverted to yield the streamfunction of such a vortex:

$$\hat{\psi}_1 = -\frac{(\kappa^2 + F_2)\hat{q}_1}{\triangle} \quad , \quad \hat{\psi}_2 = -\frac{F_2\hat{q}_1}{\triangle} \tag{4.3}$$

where $\triangle \equiv \kappa^2(\kappa^2 + F_1 + F_2)$. Mergers between the vortices increase their size, and so decrease κ. In the limit $\kappa \to 0$ in (4.3), the upper and lower streamfunctions become equal so that the vortex flow approaches barotropy. Thus an increase in horizontal scale automatically entails an increase in vertical scale of motion, as in Charney (1971). That larger vortices have stronger deep flow is evident in plots of the relative vorticity (figure (4.11)). Interestingly, the change in vertical scale apparently does not alter the merger statistics. If one "counts" vortices in the barotropic case shown in figure (4.1), one finds similar numbers, sizes and strengths of vortices; in other words, the M90 results carry over to the two-layer flat bottom case exactly when one considers *potential* vorticity in the latter. However, this fact could be anticipated from the work of Polvani et al. (1991)
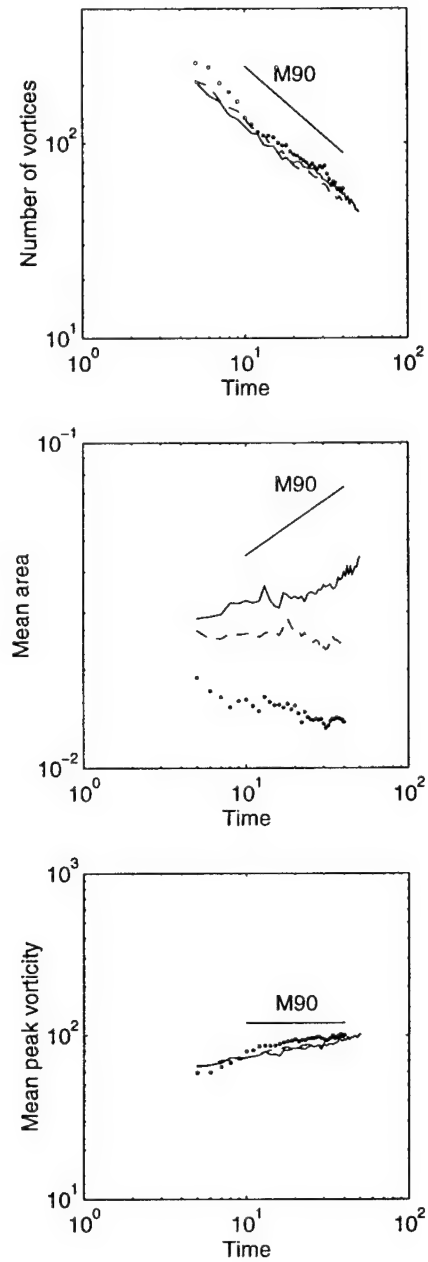
152

Figure 4.10: Vortex statistics for weak slope cases. Shown are runs with $\beta_2 = 0$ or $\Lambda = \infty$ (solid), $\Lambda = 4$ (dots), and $\Lambda = 16$ (dashed). Vortices are connected regions with $q_1 > 10$.

153

who found that mergers between vortices with zero deep potential vorticity occur at the same separation as between barotropic vortices. Merger is the fundamental process occurring in the late stages of the turbulence calculations.

McWilliams (1990b) found that the population of vortices in his stratified calculation decreased faster than in the barotropic case. However, as mentioned in section (4.2) of this chapter, he chose an initial flow which had energy uniformly distributed in the vertical. Thus vortices appeared at multiple levels and could "merge" via the process of alignment (Polvani, 1994). The present results suggest that confining the vortices to one level, i.e. the surface in this case, results in a two-dimensional decay in the number of vortices. Note that McWilliams (1990b) suggested that the alignment process might be to the barotropic cascade what horizontal mergers are to the horizontal cascade. However, the present results illustrate a case in which the vertical scale increases *without* alignment. Here, the streamfunction field approaches barotropy while the PV field remains layer-trapped.

A second point is that the surface kinetic energy must always exceed the deep kinetic energy for a collection of surface potential vortices. The ratio $\frac{KE_1}{KE_2}$ at wavenumber κ is $(1 + \frac{\kappa^2}{F_2})^2$, which is always greater than one except at $\kappa = 0$ where there is no kinetic energy.

Weak slope

The primary difference between the weak slope and the flat bottom case is that at a certain scale (arrest scale) the vortex will "lose" its lower portion to topographic wave radiation. As studied in Chapter 3, when a barotropic vortex undergoes topographic wave radiation, it loses its deep flow *and* a portion of the surface flow. The surface potential vorticity remains unchanged, but the vortex left behind, with a surface-trapped *streamfunction*, is weaker.

Such changes to the surface vortex are found to have two effects. The weak-
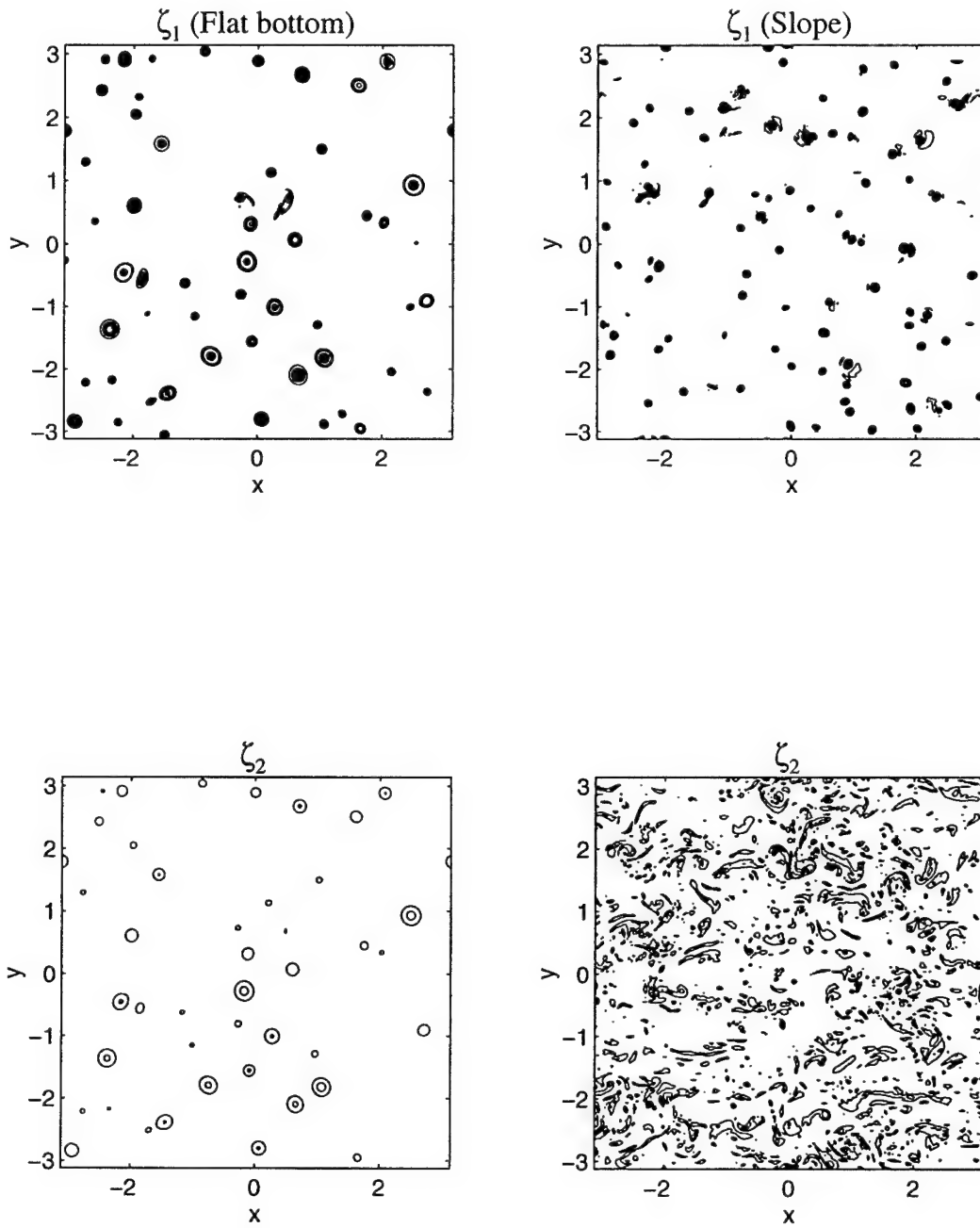
Figure 4.11: The relative vorticity fields at $t = 20$ for the flat-bottom (left) and slope (right) cases. The contour values are $\pm[10 : 10 : 100]$.

155

ening of the vortex favors *filamentation* by neighboring vortices because the potential vorticity is primarily stretching vorticity. This appears to occur until the surface PV is dominated by the relative vorticity, which means the final vortex will be smaller than deformation scale because the ratio of kinetic to potential energy for a surface vortex varies as the ratio of the vortex radius to deformation radius. Plots of relative vorticity such as in figure (4.11) indicate that the scale of the surface relative vorticity is the same as the surface PV, consistent with this notion. Figure (4.11) also shows that it is difficult to identify a lower portion of the surface vortices.

Secondly, it is easy to imagine that radiation of the deep flow enhances baroclinic instability. Radiation and filamentation continually produces sub-deformation scale, surface-trapped vortices which will, in turn, continue to merge and produce larger vortices. The product vortices, deformation scale and surface-trapped, will likely be unstable and thus prone to losing more energy to the lower layer. The process is illustrated schematically in figure (4.12). The figure shows surface potential vorticity and bottom streamfunction, with unshaded indicating zero and shaded non-zero values. In the flat bottom case, shown at the top, small surface vortices merge to yield a larger surface vortex. If this vortex is larger than deformation scale, it becomes unstable and yields two vortices which are more barotropic (C), i.e. have deep flow. These vortices then merge again to produce larger vortices with stronger mean flow (D). However, instability occurs primarily at the second stage, or stage B as indicated.

In the slope case, radiation of the deep flow is now possible. This means that the more barotropic vortices at stage C effectively return to stage A (albeit with weaker ψ_1), and thus can merge (B) and become unstable again. Growth of the surface vortices is defeated because the vortices can never attain stage D. Judging from the spectral fluxes and the integrated lower layer kinetic energy, the enhanced transfer of energy occurs early on, when the density of vortices is higher

156

and mergers more frequent. But instability is also prolonged by the presence of the slope, as indicated by baroclinic to barotropic fluxes at later times.

Note that a weaker slope (the $\Lambda = 16$ case in figure (4.10) for instance) increases the arrest scale, and thereby delays the radiation of the deep flows. This permits the merging vortices to become larger before being weakened by radiation and filamentation, which in turn increases the mean vortex area.

The schematic illustrates that filamentation of the surface potential vortices must occur, or that the area of the potential vortices must decrease, as in figure 4.10. To see this, assume rather that q_1 is conserved exactly during merger and instability. Then the areas of the surface vortices at state C are equal to those in state A; however, as the lower layer streamfunction is now non-zero, the energy at state C must therefore be greater than at state A so that energy is produced during merger and instability. This is certainly not the case (the total energy decreases monotonically), so that q_1 is not conserved, and the vortices at C are smaller than at A. Filamentation must occur during merger and during instability.

In addition, the waves also likely filament the vortices, as with the initially barotropic vortex in the Case A to D transition region discussed in chapter 3. There the surface vortex was strongly deformed by departing waves, to the point of splitting into two smaller vortices. That vortex was 2.5 time deformation scale, but the important point is that near barotropic waves can be destructive to surface vortices, and break them into smaller structures.

Summary: weak slope

The picture which emerges in the case of the weak slope is one in which the upscale cascade is arrested as vortices in the lower layer yield to bottom-intensified topographic waves. Coexisting with the waves is a population of isotropic surface potential vortices, which continue to merge and become unstable, thereby losing
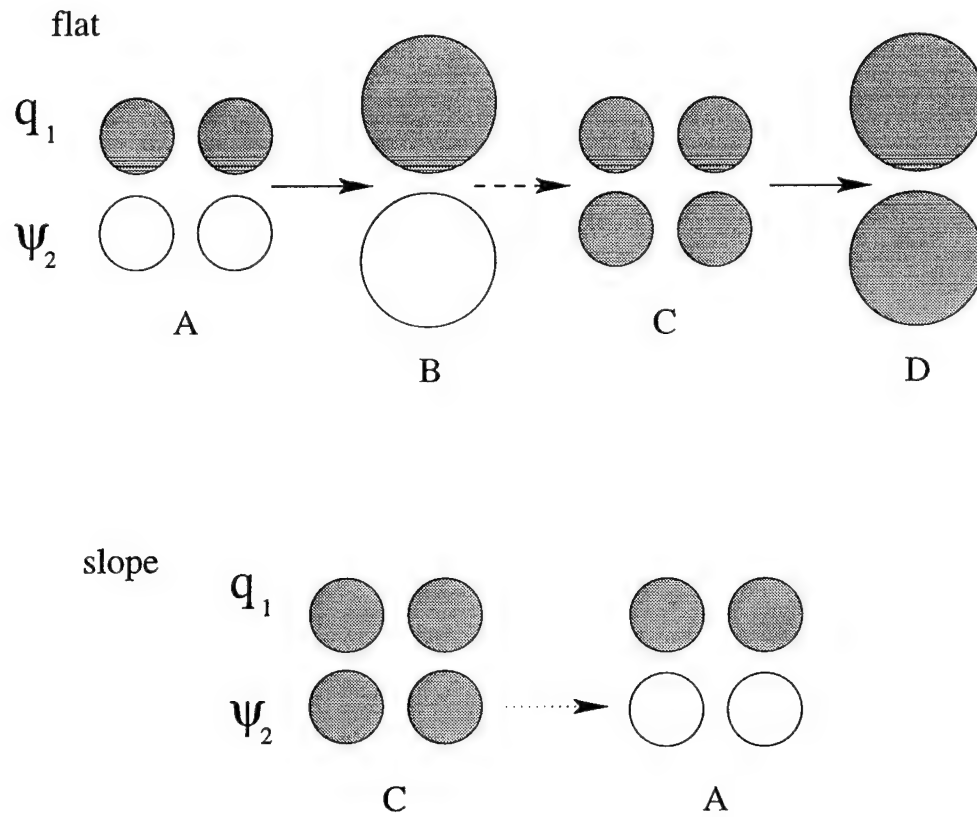
Figure 4.12: A schematic illustrating vortex merger and instability in the flat-bottom and weak slope cases. The shaded region indicates non-zero, and clear is zero. The solid arrows denote merger, the dashed arrow baroclinic instability, and the dotted line dispersion by waves.

energy to the waves and increasing the transfer of energy to the lower layer over that observed in the flat-bottom case.

The strength of the slope in this limit determines at what scale waves become dominant. In the case above, the slope was strong enough to arrest the cascade soon after passing the deformation radius. This was in turn the cause for the sharp reduction in the size of the surface vortices. If the slope had been weaker, the vortices would have reached a larger scale before their lower portions were dispersed. This causes the area on average to be larger (figure (4.10)).

The last point to mention is that the vortices, after releasing energy to the waves, are primarily smaller than deformation scale and baroclinic. Similar features have been studied before under the name "submesoscale coherent vortices" or "SMCV's" in the terminology of McWilliams and Gent, 1986. Here we find that such features evolve naturally in the presence of topographic wave radiation, and so the process outlined above yields a possible explanation of their origin. The fact that they are smaller than deformation scale implies that they are more sensitive to coarse numerical resolution. In fact, in identical runs with 128^2 grid points, the population dwindled to zero in the $\Lambda = 4$ case due to dissipation during straining events. The effect of resolution of the vortex population was also noted in Benzi et al. (1986).

4.4 Strong slope: $\Lambda = .1$

In Chapter 3 it was found that surface vortices slightly larger than deformation scale were stabilized when the slope was large enough so that Λ was smaller than approximately one half. Thus one might expect that such a strong slope will have a similar effect on the merging vortices arriving at deformation scale. As will be seen below, the slope is unable to block the spin up of the lower layer,

but rather slows the rate at which energy is lost to deep flow. Comparisons will be made to case in which the lower layer is infinitely deep and motionless to highlight similarities and differences.

4.4.1   Streamfunction and energy

The numerical run in this case had a lower layer which was four times deeper than the upper layer, so that $\delta = .25$. Numerical limitations made it difficult to retain equal layer depths and have a slope which was strong enough to yield such a small value of Λ. Specifically, to obtain $\Lambda = .1$ with $F_1 = F_2 = 100$ required a (nondimensional) slope of order $2000 - 3000$ which in turn required a prohibitively small time step due to the rapid waves. However, results discussed below reveal that increasing the lower layer depth and increasing the slope have the same effect on the evolving surface flow, with the exception that the evolving deep flow is weaker with a deep lower layer because the initial potential energy is decreased. Thus the primary run had $\delta = .25$ and $\beta_2 = 500$, but a second shorter run with $\beta_2 = 3000$ was made for comparison.

The streamfunction fields for this case are shown in figure 4.13. As in the weak slope case, the cascade to larger horizontal scales is apparent; but in contrast, the flow does not become barotropic. The surface flow at $t = 20$ appears to be nearly isotropic and the deep flow (magnified by a factor of 5 in the figure) is weaker and very anisotropic. The surface flow appears "vortex-like", and the deep flow is "jet-like". The latter is found to have an expression at the surface as well, which is apparent in the lower part of the lower left panel.

Two principle characteristics which will be studied in some depth are the following. The scale of motion at the surface is nearly deformation scale, if slightly larger. And, as is obvious by now, the deep flow is non-zero, so that the slope has not blocked the loss of energy to the lower layer.
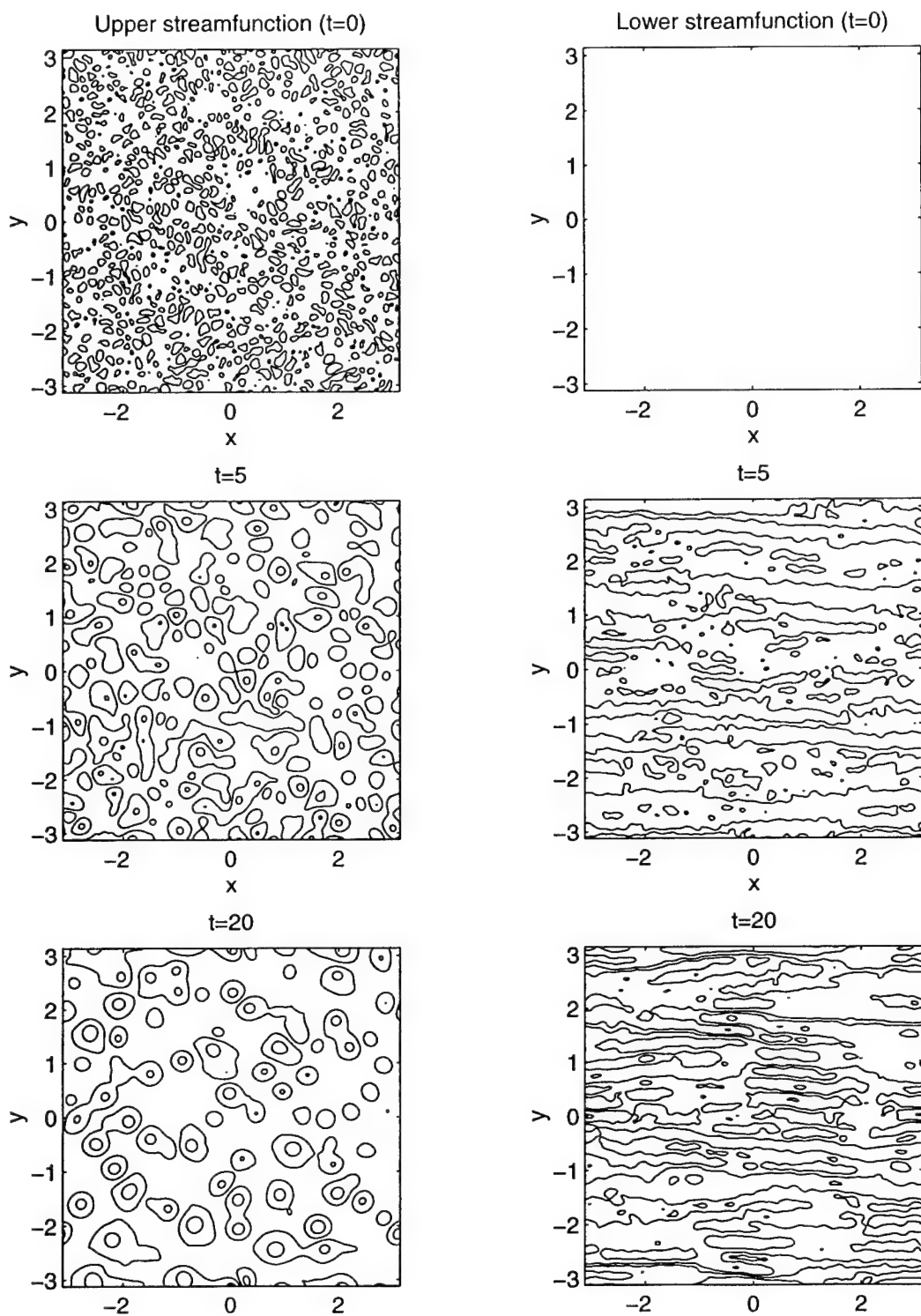
Figure 4.13: The upper and lower layer streamfunction fields for the strong slope case. The contour values were $\pm[.05 \, .2 \, .5 \, 1 \, 1.5 \, 2]$.

161

The "arrest" at the deformation scale can be seen more clearly in plots of the isotropic energy spectra, shown in figure 4.14. The upper layer kinetic energy shifts to the left, but appears to stall at a scale somewhat larger than deformation scale; larger scales are dominated by the potential energy. For comparison, the energy spectrum from a one and a half layer integration ($\psi_2 = 0$) is shown at the lower right. It too shows that the upper layer kinetic energy is peaked near the deformation scale. The potential energy here dominates at all scales larger than the deformation radius; this is reasonable because $\frac{PE}{KE_1} \alpha FL^2$ for a surface-trapped flow. Thus the strong slope case resembles the one and half layer case to a first approximation. The differences between the two cases may be attributed to the deep jets: $KE_2 \neq 0$ and KE_1 is increased at larger scales due to the surface expression of the jets, as seen below.

The "layerwise" spectral fluxes, defined in Chapter 2, are also indicative of an arrest at the deformation scale. In the two-layer case the fluxes comprise self-advective fluxes for each of the two layers, and a thickness flux which is equivalent to that in the barotropic/baroclinic flux formulation; they are shown in figure (4.15). Again the one and a half layer results are included, as are the flat bottom fluxes. In the one and a half layer case, there is no potential energy flux nor lower layer flux, so only the advection of upper relative vorticity contributes. The latter flux is large initially, but decreases substantially at the deformation radius. In the other cases the flux is also surface-trapped and large initially. However, in the flat bottom case the flux passes the deformation scale and is joined by a weaker upscale flux in the lower layer. The strong slope case more closely resembles the one and a half layer case in that the upper layer flux nearly ceases near the deformation scale and the thickness and lower layer fluxes are nearly negligible.

The deformation scale arrest will be examined in more detail later, when the upper layer vortices are considered. First though, the question of the spin-
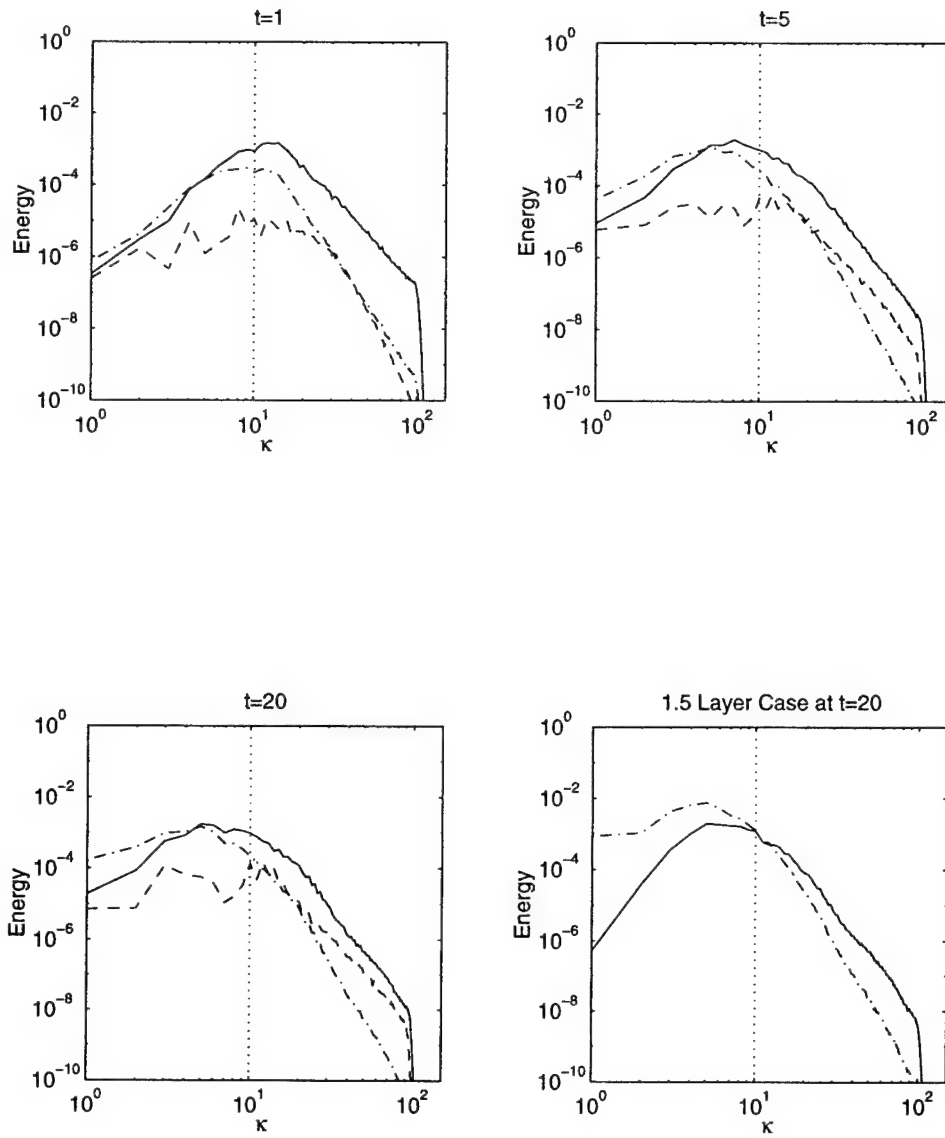
Figure 4.14: The energy spectra for the strong slope case and the one and a half layer case (lower right). The components are KE_1 (solid), KE_2 (dashed) and PE (dash-dot). The spectra have been averaged in unit wavenumber bins from $[\kappa - .5, \kappa + .5)$.
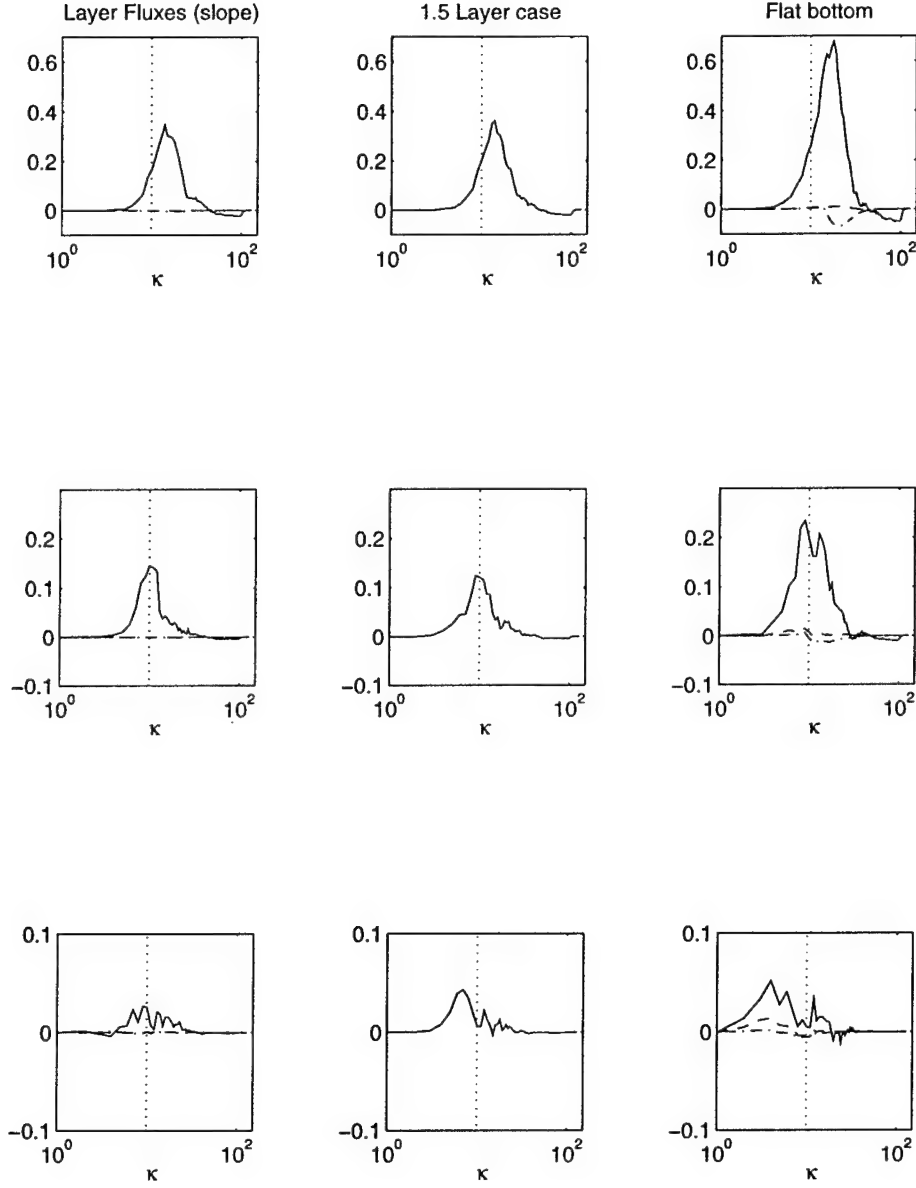
Figure 4.15: The layerwise spectral fluxes for the strong slope case (left), flat bottom case (center) and one and a half layer case (right). The fluxes are $\Re\{\hat{\psi}_1^* J(\hat{\psi}_1, \kappa^2 \hat{\psi}_1)\}$ (solid), $\Re\{\hat{\psi}_2^* J(\hat{\psi}_2, \kappa^2 \hat{\psi}_2)\}$ (dashed), and $\Re F \psi_1^* J(\psi_1, \psi_2)$ (dash-dot). The times are $t = 1$ (top), $t = 3$ (middle) and $t = 10$ (bottom). Note that the scales are different for the different times to facilitate comparison.

up of the lower layer is addressed. Besides the development apparent in the streamfunction plots in figure (4.13), an active "topographic flux" is found in the barotropic/baroclinic spectral fluxes, shown in figure (4.16). As the barotropic/baroclinic flux formalism is more complicated in the case of unequal layer depths, I have used the shorter duration run with equal layer depths and $\beta_2 = 3000$ for this example; the results are qualitatively similar for the unequal layer depth case.

One finds that both barotropic and baroclinic fluxes are dominated at early times by nearly equal self-advective fluxes. This is simply a result of the flux being almost entirely confined to the upper layer, for when $\psi_2 \approx 0$:

$$\Re\{\hat{\psi}^* J(\hat{\psi}, \kappa^2 \hat{\psi})\} \approx \Re\{\hat{\psi}_1^* J(\hat{\psi}_1, \kappa^2 \hat{\psi}_1)\} \tag{4.4}$$

and

$$\Re\{\hat{\tau}^* J(\hat{\tau}, \kappa^2 \hat{\psi})\} \approx \Re\{\hat{\psi}_1^* J(\hat{\psi}_1, \kappa^2 \hat{\psi}_1)\}. \tag{4.5}$$

In addition to this flux, though, one finds a transfer from baroclinic to barotropic modes, and a topographic flux in the opposite direction, as in the weak slope case. Again energy is being lost to bottom-intensified topographic waves. These fluxes are weaker than in weak slope case and noisy, but present even at late times in the run.

Consistent with this, the lower layer kinetic energy is found to increase monotonically throughout the run, as seen in plots of the area-integrated energy components shown in figure (4.17). The one and a half layer case, also shown, is
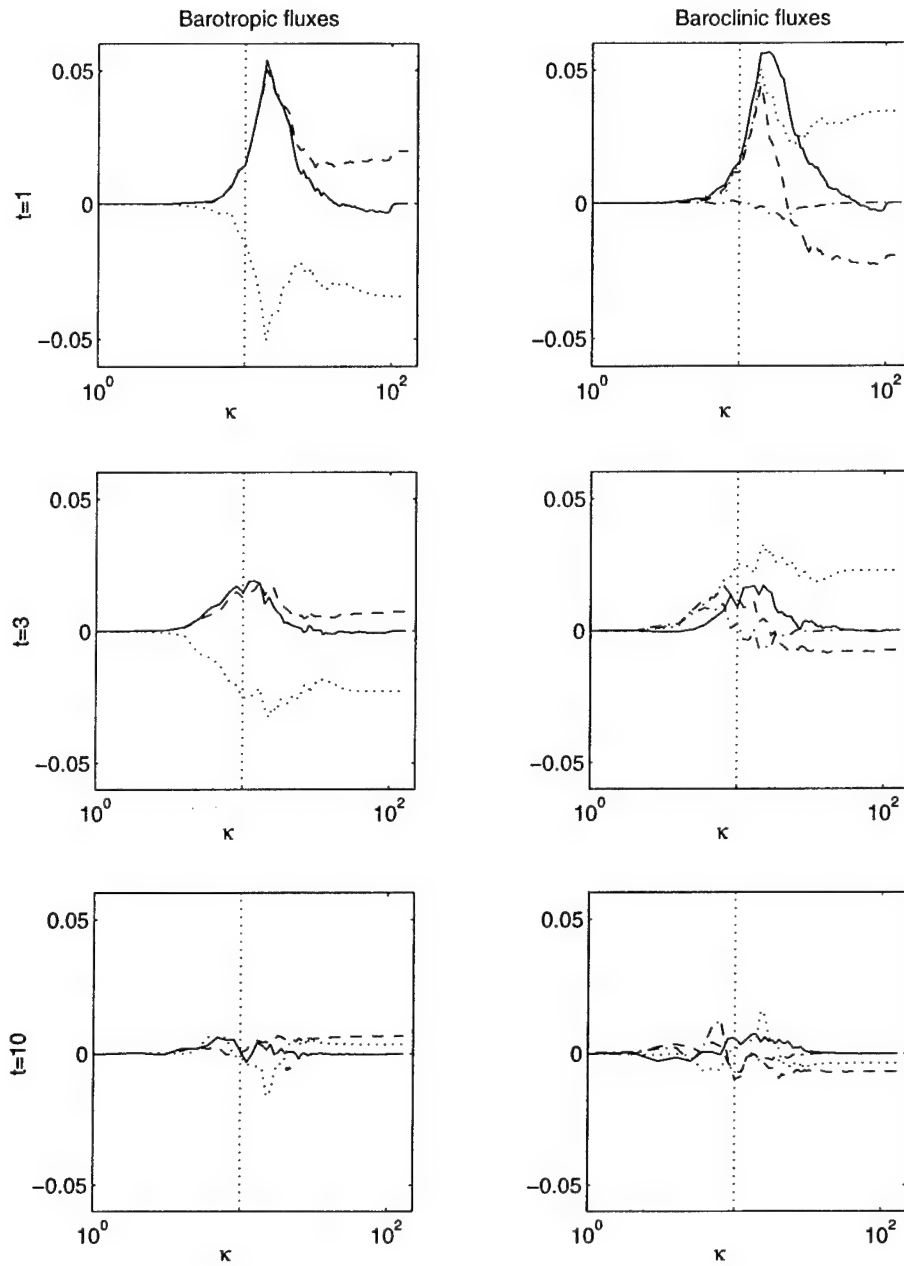
Figure 4.16: The barotropic and baroclinic fluxes for the strong slope case. The flux labelling for the barotropic/baroclinic fluxes is the same as in the flat-bottom case.

useful for comparison. In that case the sum of upper kinetic energy and potential energy are conserved, and a decrease in the former is balanced by an increase in the latter; as noted before, the ratio $\frac{PE}{KE_1}$ varies as FL^2 and so must increase with the scale of motion. The initial changes in KE_1 and PE in the slope case are nearly the same, but at later times potential energy is lost as the lower layer kinetic energy increases.

In Chapter 3 it was found that a strong slope could stabilize a vortex which was marginally larger than deformation scale. In particular, if $\Lambda < .5$, a small initial perturbation caused a small amount of wave radiation, but thereafter the vortex relaxed to an axisymmetric stable state. But in the case of a turbulent surface flow, potential energy is lost even when $\Lambda = .1$; what is the discrepancy?

The fact that waves were radiated when the single vortex was weakly perturbed but not when it relaxed to axisymmetry is telling. The circular surface vortex in the absence of external forcing is a steady solution of the two layer equations over the slope on the f-plane so that relative vorticity and interfacial stretching not only balance, but do not change in time. The surface vortices in the turbulence case are never steady, but are continually advected and perturbed by other vortices. In the process, the interface undulates up and down, generating vorticity at depth. In other words, interfacial motion *requires* motion at depth to conserve PV in the lower layer. With a slope, the interfacial motion can drive cross-isobath motion, which in turn can generate waves, as follows. A parcel in the lower layer must conserve total PV:

$$q_2 + \beta_2 y = \nabla^2 \psi_2 + F_2(\psi_1 - \psi_2) + \beta_2 y \qquad (4.6)$$

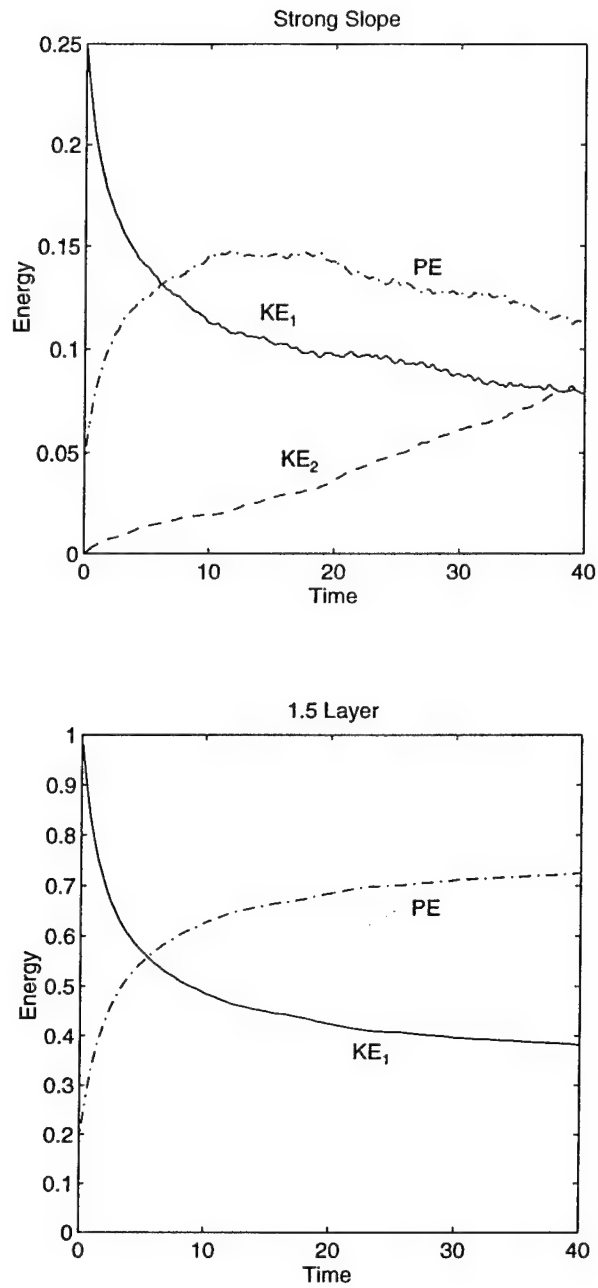so that time changes in the parcel PV are zero, implying:

167

Figure 4.17: The time series of the energy components for the strong slope and one and a half layer cases. The components are KE_1 (solid), KE_2 (dashed) and PE (dash-dot). The initial total energy is smaller for the slope case because of the choice of unequal layer depths.

$$F_2 \frac{\partial}{\partial t}\psi_1 = \frac{\partial}{\partial t}(-\nabla^2 \psi_2 - F_2\psi_2 - \beta_2 y). \qquad (4.7)$$

If ψ_2 is zero initially and the slope large, the cross-slope velocity induced is roughly $v_2 \, \alpha \, \frac{F_2 \frac{\partial}{\partial t}\psi_1}{\beta_2}$. Now the importance of Λ becomes apparent: it is the ratio of the magnitude of interfacial displacements to the size of the slope and thus a measure of the strength of induced cross-isobath flow. In the turbulence case, the velocity scale at the surface is also a measure of the magnitude of the interface driving (this is not the case with the steady vortex where U_1 measures the swirl speed but not the interfacial motion).

From this simple argument, it seems that Λ in the unsteady flow case is a measure of the "ease" with which surface flow can induce motion at depth. To quantify this, a number of runs were made in which slope, lower layer depth (F_2) and U_1 were varied. The results are shown in figure (4.18). As the lower layer kinetic energy increases monotonically, it is the simplest to use. At upper left it is seen that increasing the bottom slope decreases the rate at which KE_2 grows. By measuring the change in slope of the $KE_2(t)$ curves at $t = 0$, one can quantify the dependence of the growth rate on the slope. Thus the initial change in lower layer kinetic energy $((KE_2(t = \triangle t) - KE_2(t = 0))/\triangle t)$ is plotted at upper right. The straight line has slope -1, so the dependence is a simple inverse dependence of growth rate on slope.

Likewise the dependence on F_2 and U_1 can be found, although changes in these parameters mean a change in the total initial energy and in the time scale, which must be corrected for a comparison. The initial energy spectrum may be written as:

$$E(k, l, t = 0) = E_0(\delta\kappa^2|\hat{\psi}_1|^2 + F_2|\hat{\psi}_1|^2 = E_0\delta(\kappa^2 + F_1)|\hat{\psi}_1|^2 \qquad (4.8)$$

with $E_0 \propto U_1^2$, which implies that the energy varies with δ and with the square of U_1. The dependence on δ is slightly more complicated because F_1 is also a function of δ, but with this initial spectrum $(\kappa_0 > \sqrt{F_1})$ it is nearly linear.[4]

The time scale is nondimensionalized by $(\kappa_0 U_1)^{-1}$ where κ_0 is the initial peak wavenumber.[5] Combining this with the energy scaling yields a nondimensional scaling for the growth of deep kinetic energy of $\delta \kappa_0^3 U_1^3$.

The dependence of growth rate on δ and U_1 is shown at the bottom of figure (4.18). One finds a clear linear dependence on U_1 and a nearly linear dependence on layer depth ratio. The deviation from linearity with δ is probably the result of the δ dependence of F_1, mentioned above. Note also that there are slight departures at smaller β_2 and larger U_1 where $\Lambda \to 1$. Thus the growth rate appears to scale linearly with Λ when this parameter is less than unity.

The parameter Λ thus plays a different role in the turbulence cases. It essentially determines how quickly the surface vortex field loses APE to the lower layer flow. As with the single vortex case, a steeper slope and/or deeper lower layer favor surface stability, but in the unsteady case, baroclinic instability is not defeated by the slope, only impeded.

4.4.2   Potential vorticity and surface vortices

The potential vorticity fields are shown in figure 4.19. As in the weak slope case, vortices emerge at the surface, but now the large slope completely dominates the lower layer PV field so that there are no closed contours and only weak perturbations visible. As in the weak slope case the surface vortices are isotropic, but they are somewhat larger in this case. As is seen below, they are also larger

---

[4]If the initial potential energy was larger, a $\frac{\delta}{1+\delta}$ scaling might be more appropriate.

[5]One might think that the initial scale of motion in the lower layer might depend on the deformation radius, and thus the layer depths, but in the experiments the mean scale of motion in layer two varied only weakly under changes in parameters, i.e. it seemed only to depend on the initial scale of motion.
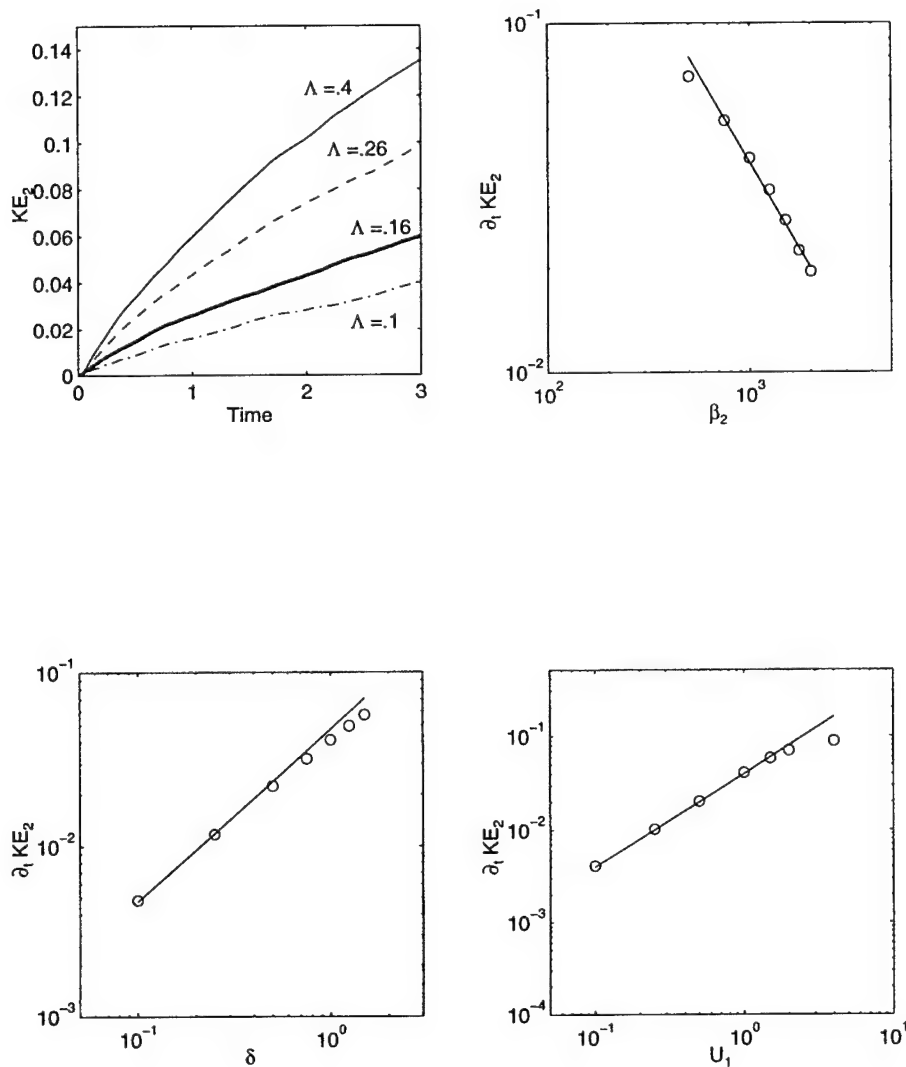
Figure 4.18: The growth of lower layer kinetic energy as a function of Λ. The upper left plot shows KE_2 with $F_1 = F_2 = 100$ for various Λ, with faster growth rates corresponding to smaller slopes. The other plots show $(KE_2(t = \triangle t) - KE_2(t = 0))/ \triangle t$, with $\triangle t = 0.2$, as a function of upper layer velocity, layer thickness and slope. The energy has been nondimensionalized by δU_1^2 and the time step by $(\kappa_0 U_1)^{-1}$. The slopes of the lines shown are -1.0 (U_1), 1.0 (δ) and 1.0 (U_1).

171

than in the flat bottom case. In addition, they are comparable in scale to the isotropic structures seen at $t = 20$ in the surface streamfunction of figure (4.13).

The differences in vortex characteristics can be quantified by using the counting routine; the results for this case as well as for the one and a half layer and flat bottom cases are shown in figure (4.20). As before, the decrease in the number of vortices appears the same for the three cases. This is rather remarkable given that baroclinic instability occurs in one case, not in another and is impeded in the third. There is a faint suggestion of a slowing in the rate of decrease in the one and a half layer case; this is actually what one expects, as discussed below.

Likewise the mean peak PV is nearly the same for the three cases, and certainly equal with the uncertainty of single realizations. There is a weak increase in the mean, as in the weak slope case.

Again the difference comes in the mean area of the vortices, shown in the center panel. In this case, the slope vortices are *larger* than in the flat bottom case. The one and a half layer vortices are larger still, and increasing at a rate which is consistent with the power law of M90. The slope vortices appear to increase in size initially, but then level out and perhaps decline later on.

The larger area and the deformation scale arrest discussed above are linked, and are related to the loss of a barotropic portion of the vortex flow. A barotropic vortex with nonzero circulation has an azimuthal velocity which decays slowly, specifically $v(r) \propto \frac{1}{r}$, as noted in Chapter 3. In contrast, a vortex in one and a half layers has a velocity field which decays exponentially beyond the deformation radius, for $v(r) \propto K_1(\frac{r}{\lambda}) \propto e^{-(\frac{r}{\lambda})}$. This can be seen by inverting the potential vorticity:

$$\nabla^2 \psi - F_1 \psi = q_1 \qquad (4.9)$$

172
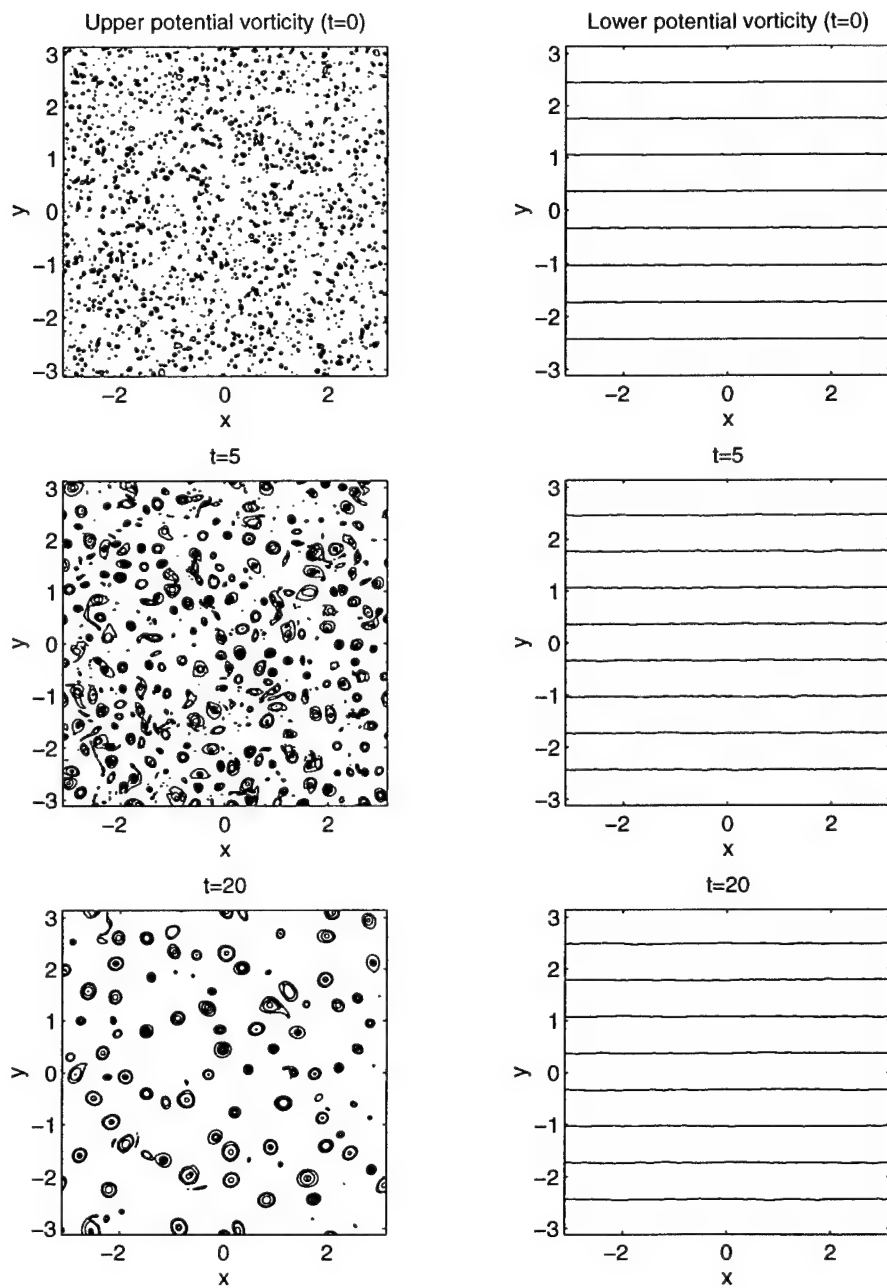
Figure 4.19: The upper and lower layer potential vorticity fields for the strong slope case ($\delta = .25$, $\beta_2 = 500$). The contour values were $\pm[60\,100]$ at the upper left, $\pm[15\,30\,60\,100\,150]$ in the lower left plots and $\pm[390\,780\,1170\,1560]$ in the right-hand plots.
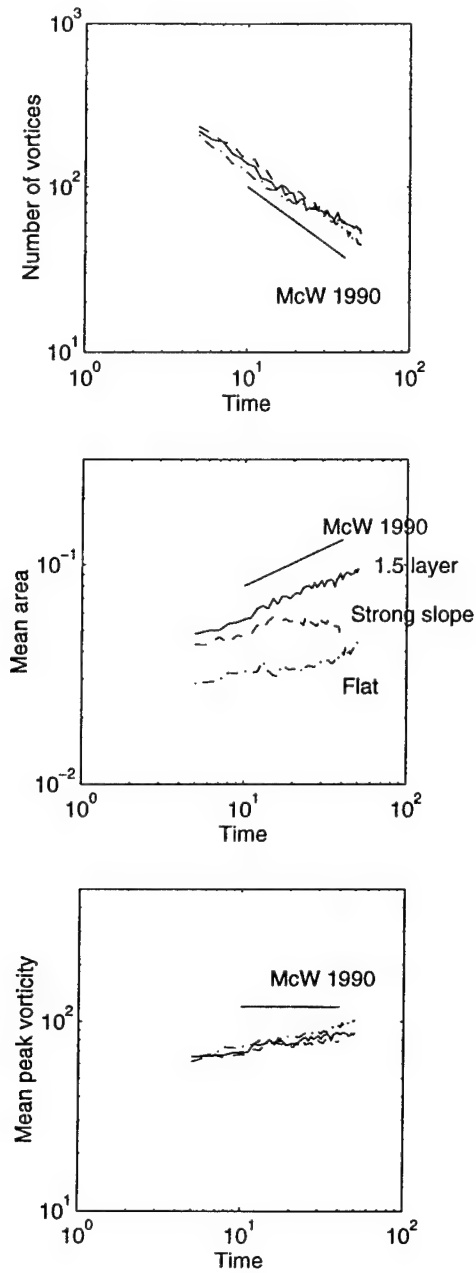
Figure 4.20: Vortex statistics for strong slope cases. Runs shown are the flat bottom case (dash-dot), the $\Lambda = .1$ case (dashed) and the one and a half layer case (solid). Vortices are connected regions with $q_1 > 10$.

174

which yields $\psi \alpha K_0(\frac{r}{\lambda})$. The one and a half layer vortex is a purely baroclinic vortex and has no barotropic flow, and as a result its range of influence is much smaller than a barotropic vortex. It is essentially unable to interact with vortices farther than a deformation radius away. If the vortices are small and densely packed, they will advect and be able to merge. But if the vortex is deformation scale, the velocity field in effect does not extend beyond the edge of the vortex. Thus cascading turbulence in one and a half layers arrests at the deformation scale because the vortices simply cease to merge.[6]

The study of mergers between surface vortices of Polvani et al. (1991) is again of relevance. One aspect they considered is the effect on mergers of increasing the lower layer depth, and in particular mergers in one and a half layers. Of interest for the present results is that they found that vortex *filamentation* was greatly suppressed during interactions in one and a half layers. Vortices at the critical distance for merger would join to form long asymmetric "blobs" and rotate thereafter. The larger area seen in figure (4.20) is likely a consequence of this suppressed filamentation; as vortices coalesce, less vorticity is cast off and so the product vortices are simply larger. If this is so, one must conclude that filamentation is similarly suppressed over a strong slope. A study of mergers over a strong slope would confirm or deny this; that will left for future work.

If the velocity field is localized to the vortex as discussed above, the streamfunction and potential vorticity fields ought to have the same scale; this appears to be the case in one and a half layers, as seen in figure (4.21). The same is true for the strong slope case, shown in the lower half of the figure. The streamfunction in the slope case also has hints of zonal flow (the lower portion of the figure) which is the surface expression of the deep flow which is intensifying and is even more noticeable at later times.

---

[6]The same effect has been noted in the case of cascading turbulence in the shallow water system where energy arrests at the external deformation radius; see Polvani et al., (1994).
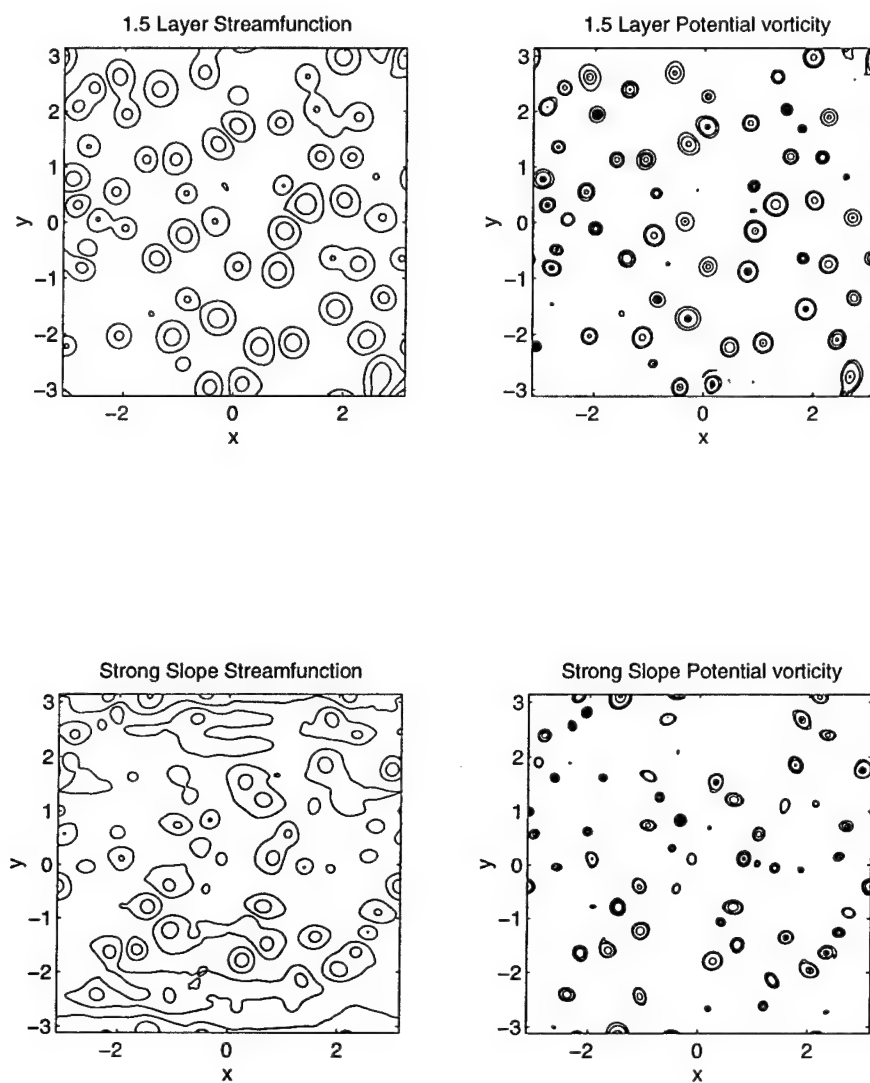
Figure 4.21: Surface potential vorticity and streamfunction for the one and a half layer and strong slope cases at $t = 20$. The streamfunction contour values are $\pm[.05\,.2\,.5\,1\,1.5\,2]$ and the vorticity values $\pm[15\,30\,60\,100\,150]$.

The decline in vortex interactions can be seen quite clearly in overlaid plots of surface PV from a range of times. In figure (4.22) single contours of PV from $t = 30$ to $t = 35$ are shown for the flat bottom, one and a half layer and strong slope cases (two nearly equal values of PV were used to accentuate the lines). Over a flat bottom there is active motion, so much so that it is often difficult to identify single coherent tracks. But in one and a half layers, the vortices are much more sluggish; there are identifiable mergers, but on the whole there is much less interaction. The same is true over the strong slope. Although there is a clear zonal drift due to advection by the intensifying deep flow, the vortices appear to interact very little with one another. Thus one finds an "arrest" in the latter two cases simply because the vortices are becoming more stationary.

One might wonder if the vortices are more stationary, why the number of vortices is decreasing equally as shown in figure (4.20). The answer is partially that the relatively small number of vortices increases the uncertainty of the measure. Alternately, while the one and a half layer vortices are becoming sluggish, the frequency of encounter has decreased in the flat bottom case at the same time, and both have the same effect. However, another reason is that there are a *range* of vortex sizes present at all times; while some of the vortices are deformation scale, others are smaller and still likely to merge with neighbors. If all the vortices were the same size at any one time, the difference between the two cases would be more dramatic.

Deep flow

The last aspect to discuss is the form of the deep flow. The condition $\Lambda \ll 1$ implies $U_1\sqrt{F_2} \ll \frac{\beta_2}{\sqrt{F_2}}$. The latter relation implies that the frequency of the interfacial "forcing" of waves is lower than the approximate isotropic topographic wave frequency at deformation scale. But as the wave dispersion relation is anisotropic, i.e. $\omega \propto \beta_2 k$, waves with low zonal wavenumbers have low frequencies.
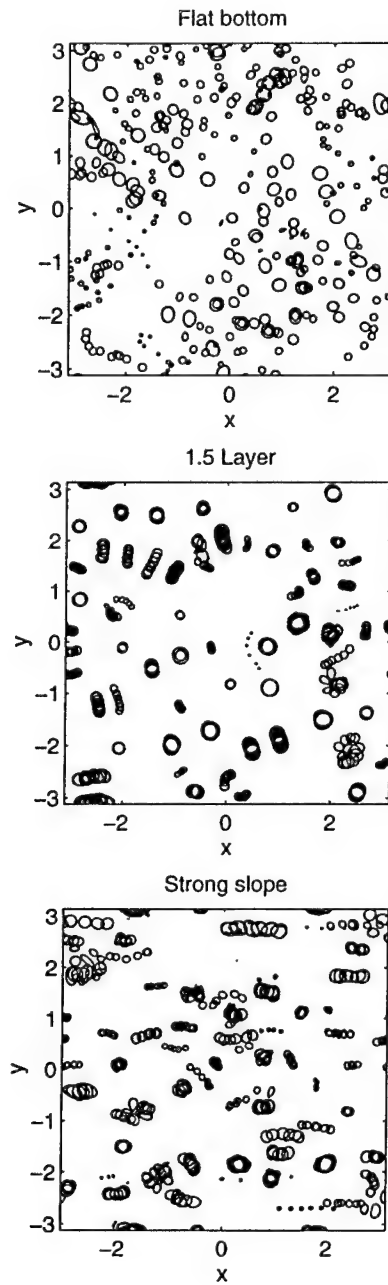
Figure 4.22: Contours of the surface potential vorticity for the flat bottom, one and a half layer and strong slope cases. The contour values are $\pm[30\,35]$.

Thus we expect that the surface forcing to generate waves of long zonal extent.

The zonal elongation is apparent in the streamfunction plots in figure (4.13) as well in the two-dimensional energy spectra shown in figure (4.23). The upper layer kinetic and the potential energies are plainly isotropic, but the lower layer kinetic energy is strongly peaked around wavenumbers $(k, l) = (1, 10) - (1, 12)$, or at a scale comparable to the surface deformation scale, but smaller than the deep deformation scale ($\sqrt{F_2}=5$). There is also a purely zonal (jet) mode around $(k, l) = (0, 4)$ which is at the deep deformation scale. One might imagine that the scale of the deep flow ought to be comparable to the scale of the forcing and therefore at the surface deformation radius, but more numerical runs are required to say with certainty. The jet mode is likely the result of continued forcing and upscale transfer at depth; as described by Vallis and Maltrud (1994), the $k = 0$ mode has zero wave frequency and is thus unable to arrest the cascade. Energy inevitably accumulates in this mode when continued forcing causes the scale to shift upwards.

As the deep waves/jets are deformation scale, they have significant flow at the surface. Thus they can advect the surface vortices, and even cause filamentation of those vortices. The latter is responsible for the decrease in vortex area seen in figure (4.20), a decline which is more dramatic when the waves are stronger, as was the case with the shorter duration run with equal layer depths. The model periodicity permits the waves to re-enter the domain, as discussed before, and with larger slopes the rate of wave/vortex encounters increases, though the waves are weaker due to the inhibition of instability. Nevertheless, the periodicity is central to the weakening of the vortices by the waves. Whether such an effect is realistic in a larger domain with a localized (inhomogeneous) turbulent flow is another question, and is discussed more below. At least the interaction reminds us that the surface vortices may be affected by external agents.

In conclusion, cascading surface turbulence over a strong bottom slope resem-
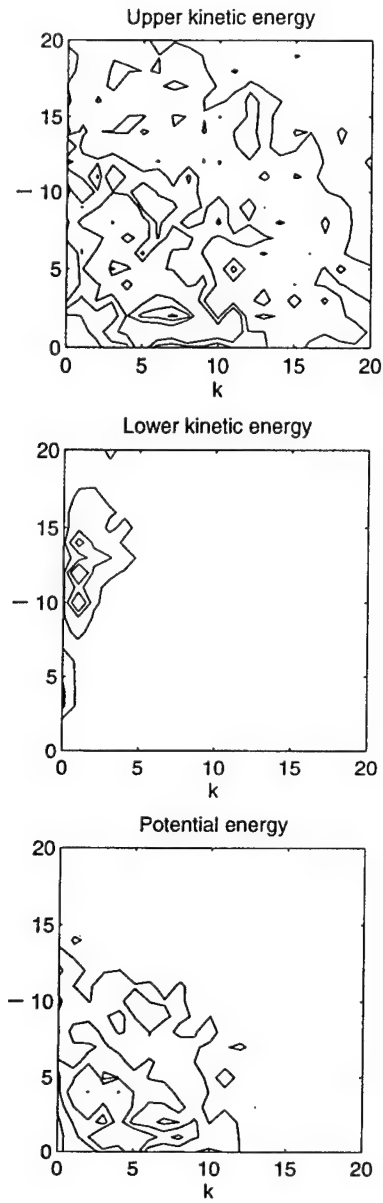
Figure 4.23: The two-dimensional energy spectra for the strong slope case. At left are contours for the $t = 2$ fields, and on the right the $t = 10$ fields. Contours are at $[.1 .3 .5 .7 .9]$ of the maximum of the $KE_1(k,l)$ at each time: $.0055$ ($t = 2$) , $.021$ ($t = 10$).

bles a one and a half layer evolution in that the cascade arrests at the deformation scale, due to the inhibition of coupling with the lower layer. However, unlike that case, energy is continually lost to the lower layer by an interaction between the undulating interface and the bottom slope. The rate at which energy loss occurs scales with the stability parameter Λ, so strong slopes or deep lower layers inhibit the loss. In the late portion of the integration, the intensifying wave field interacts with the surface vortices, advecting them and even possibly inhibiting their growth through filamentation.

4.5   Discussion

4.5.1   Arrest: the Rhines diagram

To summarize the spectral arrest over the topographic slope, I will compare to the arrest in the planetary β in two layers, discussed in Rhines (1977) using diagrams similar to that of Rhines. The planetary arrest is shown in figure (4.24), a redrawing of Rhines's figure for the case of small scale baroclinic flow. The upper plane represents baroclinic motion, the lower barotropic motion. The y-axes are the mean frequency of the motion and x-axes are the mean wavenumber. Assigning a frequency to the turbulence, $\omega \equiv U_1 \kappa$,[7] as in Batchelor (1953), one can plot the inverse cascade. Two cases are shown: one with a higher initial energy, and one lower.

The inverse cascade proceeds as energy moves towards smaller wavenumbers (larger scales) and lower frequencies. In the barotropic case, $\omega = U\kappa$ and U is conserved so that the cascade proceeds on a straight line towards the origin. With stratification, U_1 decreases with increasing scale due to the decrease in KE_1 and increase in PE, seen for example in figure (4.17). Thus the curves curve

---

[7]This is equivalent to assigning an advective time scale $T = \frac{L}{U_1}$.

181
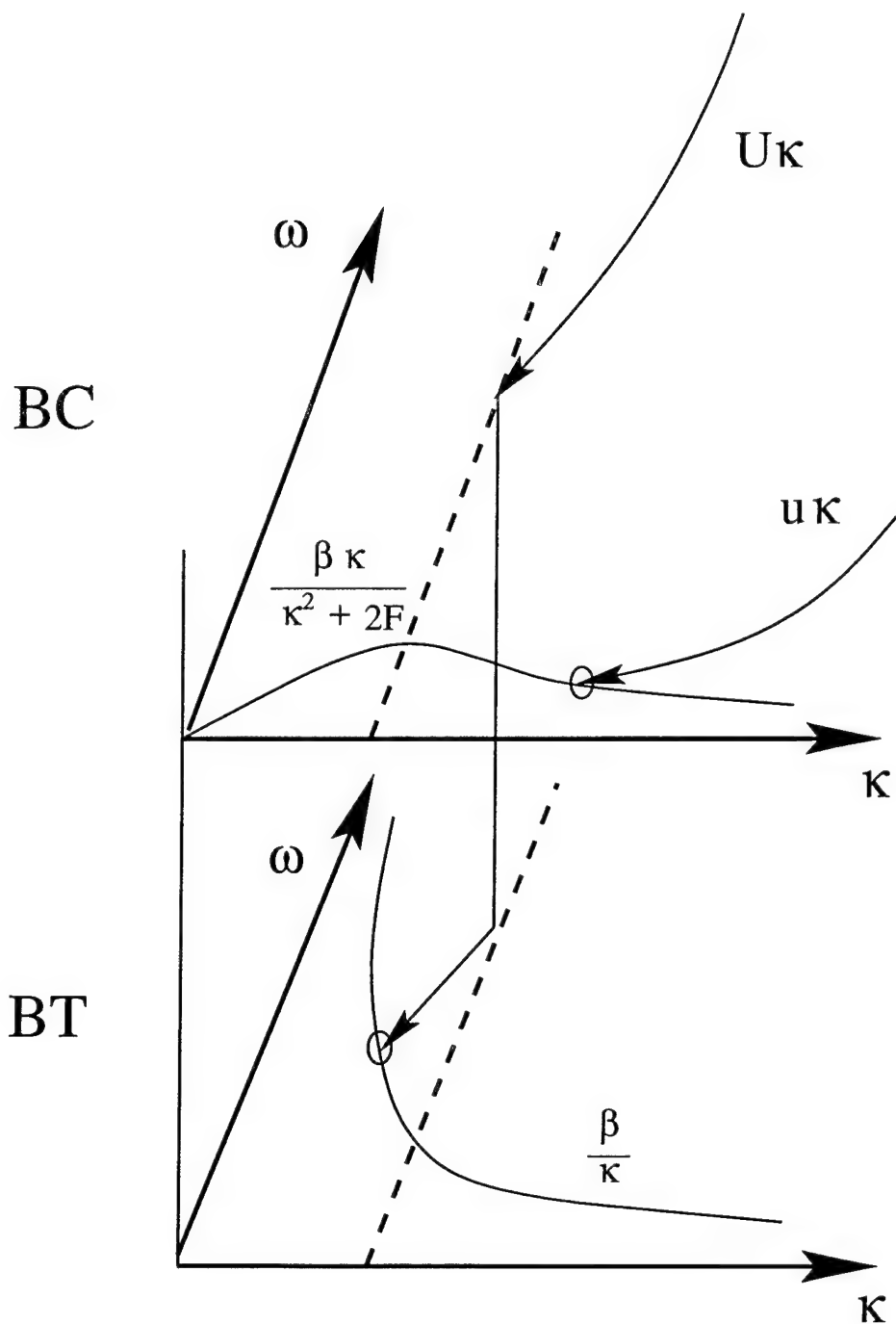
Figure 4.24: The arrest to planetary waves from a small scale initial flow, redrawn from Rhines (1977). The dashed lines mark the mean deformation wavenumber and the layer depths are assumed equal.

somewhat as they approach the deformation scale, indicated by the dashed line. On the upper path (the more energetic initial flow), baroclinic energy undergoes a "barotropic cascade" at the deformation scale, thereby making a transition to the lower plane. Thereafter it proceeds on a nearly straight line (baroclinic energy is small by assumption so barotropic kinetic energy is conserved) towards larger scales and lower frequencies. However, when it encounters the barotropic (and isotropic) Rossby dispersion curve, the cascade arrests as waves become competitive. The arrest scale from this argument is then at $\kappa_\beta = \sqrt{(\frac{\beta}{U})}$, where U is the velocity *at deformation scale* (not the initial velocity).

The second curve, also discussed by Rhines (1977), is for weaker initial velocities. In this case the baroclinic energy is arrested by baroclinic Rossby waves at a scale smaller than the deformation radius. The dividing line between baroclinic and barotropic arrests is the path which intersects the baroclinic curve at its maximum, i.e. when $\kappa^2 = 2F$ in the equal layer depth case. Thus the condition for baroclinic arrest is:

$$U\sqrt{2F} < \frac{\beta\sqrt{2F}}{4F} \quad \rightarrow \quad U < \frac{\beta}{4F}. \qquad (4.10)$$

For $\beta = 2.1 \times 10^{-11}$ and a deformation radius of 30 km, the velocity scale must be less than about .5 cm/s. Only very weak flows can arrest in this manner; the more common path then is the upper one.

The topographic case is different because there is only one dispersion curve. The analagous diagram may be drawn as in figure (4.25) where now the upper plane denotes upper layer motion and the lower is deep motion. One should note that these diagrams are only qualitative, for a surface trapped initial flow has both baroclinic and barotropic parts, which would change the previous diagram.

183

Likewise here the waves have a surface representation, but we require deep motion to excite them so the curve is only drawn for the bottom layer.

Again two paths are shown: a more energetic path and a less energetic path. In the former case, the evolution is very much like the arrest to barotropic planetary waves; a cascade to the deformation scale, a barotropic cascade, then a nearly barotropic arrest to topographic waves of large vertical extent. The arrest scale is then $\kappa = \sqrt{\frac{\beta_2}{U}}$ where now $U = U_1 = U_2$ is the (barotropic) velocity at the deformation scale. As explained earlier, knowing this scale *a priori* requires knowledge of where the upper portion of the curve intersects the dashed line at the deformation scale.

The second case with weaker initial flow reaches the deformation radius, but at a frequency below that of the isotropic topographic waves. Wave radiation occurs faster than the growth of deep disturbances and the barotropic cascade is thus blocked. However, energy is still lost to *anisotropic* waves of grave (topographic) zonal extent. So the curve arrests at the deformation radius in the upper layer while energy leaks away at the same frequency in the lower layer.

Note that changing the slope shifts the dispersion curve up and down, so stronger slopes require stronger initial flows for a "barotropic" arrest. The strong initial flow case above is equivalent to the "weak slope" case in the text, and less energetic initial flow is the "strong slope" case. The dividing line between the two paths can be deduced as in the planetary β case. The condition for the baroclinic arrest is approximately:

$$U\sqrt{F} < \frac{\beta_2\sqrt{F}}{2F}(\frac{2F}{3F}) \rightarrow U < \frac{\beta_2}{3F} \rightarrow \Lambda < \frac{1}{3}. \qquad (4.11)$$

Thus the diagram predicts the Λ-dependence. Moreover, it suggests a similar

184
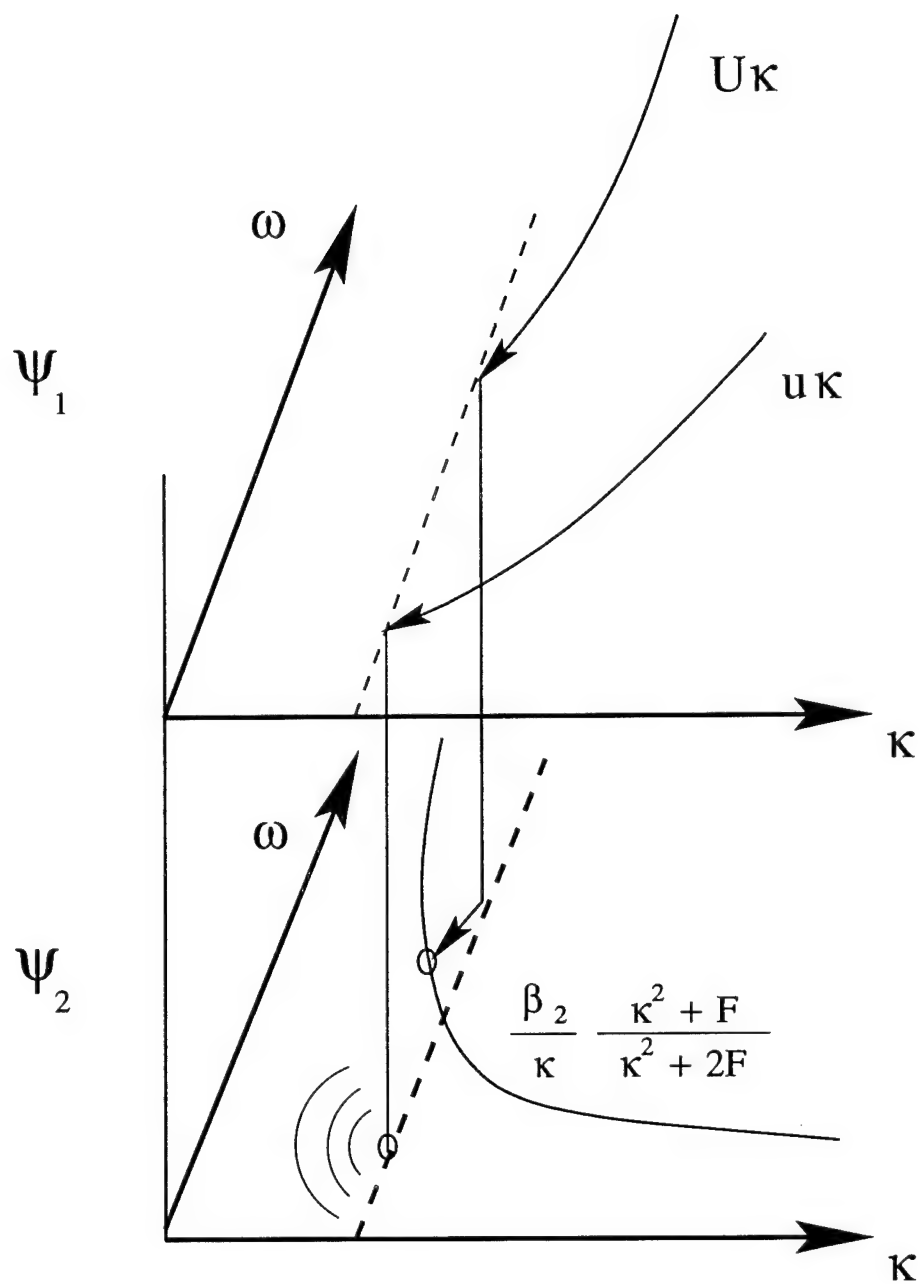
Figure 4.25: The arrest to topographic waves from small scale initial flow. Again the dashed line indicates the deformation wavenumber and layer depths are assumed equal.

value of Λ for transition to the value of $\frac{1}{2}$ assumed before (and found from various experiments).

The principal difference between the two cases is the difference in the dispersion curves, and this stems from the symmetry/asymmetry of the PV gradients. The planetary waves have two dispersion curves, but the topographic waves only one because the gradient only acts in one layer. One might think that restoring the planetary β effect to the topographic case would alter the development. However, as discussed in Chapter 5, if the slope is large, the same picture holds, with the modification that weak surface flows ($U = O|.5|$ cm/s) may arrest in surface planetary waves.

4.5.2 Vortices

A second consequence of the asymmetry of the mean PV gradient is that vortices tend to be dispersed at depth, but not at the surface. Thus in both "weak" and "strong" slope cases one finds a collection of isotropic, long-lived vortices in the surface PV field at later times. These vortices dominate the flow in the strong slope case because the growth in wave intensity is inhibited. In the weak slope case they appear to play a secondary role, but are significant nevertheless because they represent an energetic, isotropic component of the flow only present at the surface. As noted in the text, the potential vorticity is a convenient way of separating the vortex and "wave" portions of the flow simply because the waves have no surface PV and are thus filtered out in plots of q_1.

The statistics (mean size, strength) of these vortices has been calculated and compared to previously published results of McWilliams (1990). I find that in all cases the decay of the number of vortices due to mergers is approximately the same, suggesting that the rate of vortex collision is not strongly affected by the presence of waves in the domain. However, the number of vortices in these

runs is relatively small (order 100), so it is difficult to identify small differences between runs. As explained, one expects the rate of decrease to slow with the one and a half layer and strong slope cases due to the inhibition of mergers between deformation scale vortices.

The mean peak potential vorticity is nearly constant in all cases, consistent with McWilliams and with the assumption of Carnevale et al. (1991b). However, the size of the vortices is found to be strongly sensitive to the slope, and the dependence of size on slope is not monotonic. A small slope favors smaller vortices because the arrest to topographic waves weakens the surface vortices, making them more prone to filamentation by other vortices, and perhaps by the waves. Increasing the slope (but with $\Lambda > 1$) decreases the mean area of the vortices by shifting the arrest scale to smaller scales. However, increasing the slope further (so that $\Lambda < 1$) leads to an *increase* in vortex scale. Over very large slopes the mean area exceeds that in the flat bottom case because filamentation is suppressed, as in the one and a half layer case (Polvani et al., 1991b). As is shown in Appendix B, the same effect can be achieved with a flat bottom and a bottom Ekman layer; increasing the strength of damping decreases vortex areas to a degree, but then causes them to increase.

4.5.3   Potential vorticity: the RMS PV diagram

Given the complexity of a turbulent system, particularly one with baroclinicity and topography, it is useful to collapse the data. The potential vorticity, which separates out the two components of the flow, can be exploited to this end. A diagram which captures many aspects of the cascades over the slope may be constructed by plotting the root mean square (rms) potential vorticity in each layer, or root of the mean potential enstrophy, against the mean zonal and meridional wavenumbers, defined as:

$$
(\bar{k}_i, \bar{l}_i) \equiv \frac{\sum_k \sum_l (k, l) |\hat{q}_i|^2}{\sum_k \sum_l |q_i|^2} . \tag{4.12}
$$

These reflect the mean scales of the vorticity in each layer. By using the separate wavenumbers in this way, anisotropy may also be differentiated.

The four cases referred to in this chapter are shown in figure (4.26): the flat bottom case, the $\Lambda = 4$ case, the $\Lambda = .1$ case and the one and a half layer case. The rms PV is on the y-axis, and the mean wavenumbers on the x-axis. The upper layer points are shown with dots, and the lower layer points are $\bar{k}$ (x) and $\bar{l}$ (o).

One sees immediately that the upper layer is isotropic, whereas the lower layer is only isotropic over a flat bottom; otherwise it becomes anisotropic. The upper layer rms PV is decreasing monotonically due to the forward cascade of enstrophy, and dissipation at small scales. It is found to stall near wavenumber 10 in the flat bottom case, as the energy feels the size of the domain. It reaches larger scales in the one and a half layer case due to the suppression of filamentation. In the slope case the inverse progress is blocked, probably by wave-induced filamentation. The most strikingly different case with respect to the surface PV is the weak slope case, in which the rms PV is decreased somewhat and the mean scale increased substantially, both the result of increased filamentation due to slope-induced enhanced instability.

The lower layer evolution varies even more substantially. In the flat bottom case, $|q_2|^2$ is conserved and is found to decay away due to dissipation and filamentation by the deep vortex flows. The initial forward cascade is a signature of a forward enstrophy cascade at depth, which was not discussed in the text (the return to larger scales occurs when dissipation removes small scales). In the slope cases the deep enstrophy is no longer conserved, but increases. In the $\Lambda = 4$ case,
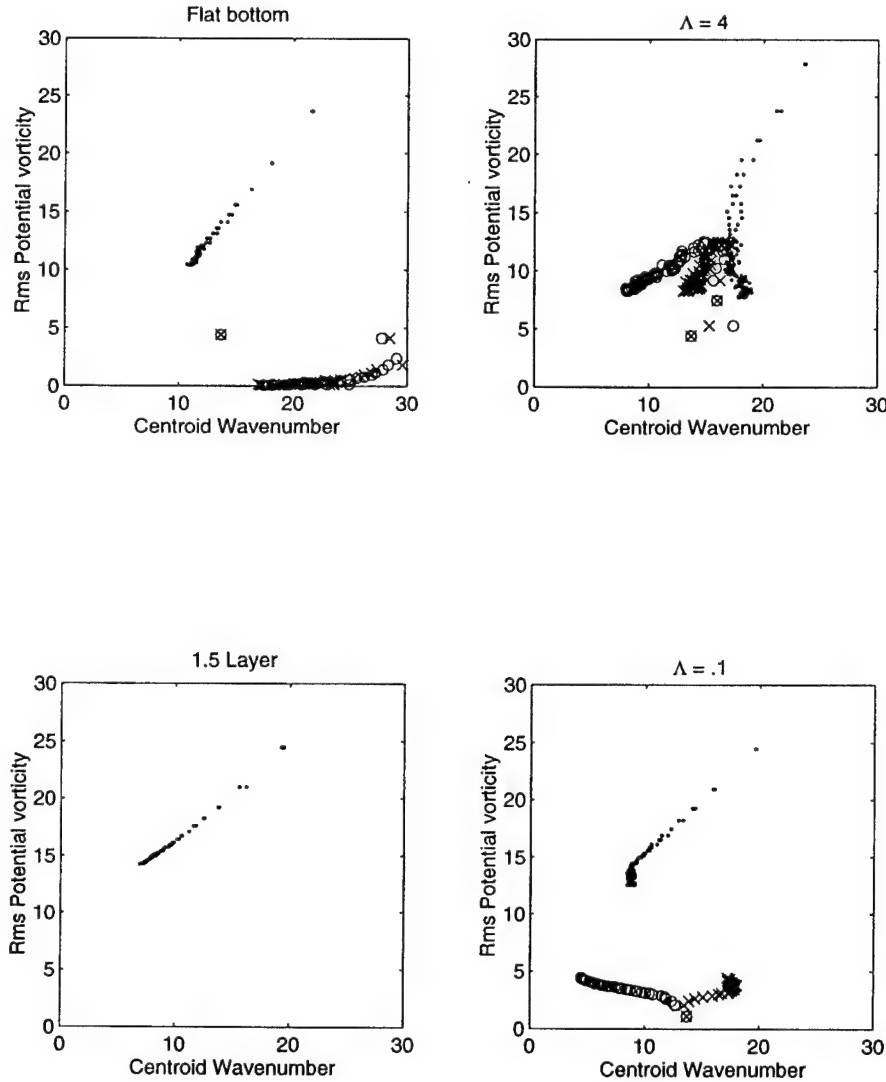
188

Figure 4.26: The rms PV in each layer vs the mean wavenumbers in the along-slope and cross-slope directions. The upper layer points are designated by (.), and the lower layer points are for wavenumber k (x) and l (o). The upper layer wavenumbers were not differentiated because of the isotropy in that layer. Points are marked every time step and all runs are to $t = 40$.

189

one finds that the initial increase is isotropic, but after intersecting the decreasing surface points, it decreases and becomes anisotropic. Note that bottom and surface rms PV are approximately equal at the end of the run, with the deep PV at larger scales. With $\Lambda = .1$ this is no longer true, as the surface PV dominates at all times. The lower layer rms PV spins up from an initial scale around wavenumber 15; the zonal wavenumber decreases thereafter, but the meridional wavenumber settles down in the vicinity of wavenumber 18. The latter is slightly smaller in scale than the scale of waves/jets seen in the streamfunction plots, as the PV in finer scaled.

While the plots present a useful summary of the principal features of the evolutions, they must nevertheless be viewed with caution for they do represent mean quantities. In the $\Lambda = 4$ case, the surface enstrophy was found to span a wide range of scales, so a single scale representation is perhaps dubious. The representation is more correct for the lower layer, where the wave energy tends to be dominated by a single scale (as noted also by Rhines, 1975).

4.5.4   Observations

One expects that both strong and weak slope regimes exist in the ocean. An approximate feel for the size of slopes required can be gained by considering the parameter, Λ. Rewriting it thus:

$$\Lambda = \frac{F_2 U_1}{\beta_2} = \frac{f^2 U_1 H_2}{g' H_2 f \partial_y H} = \frac{f U_1}{g' \partial_y H} \tag{4.13}$$

and substituting typical values for $f = 1 \times 10^{-4} s^{-1}$ and $g' = 2.5 \times 10^{-2} m/s^2$ yields $\Lambda \approx .004 \frac{U_1}{\partial_y H}$. For 1 m/s surface velocities, a slope which is larger than about .8 percent is "strong". This is a significant slope, but not huge. On the other hand,

if the velocities are only order 10 cm/s, a .08 percent grade is "strong"; this is a more modest grade.

In terms of observations, an ocean in an arrested barotropic state would have anisotropic, nearly barotropic flow oriented with the isobaths. In the Rhines planetary β case, the arrested barotropic state has zonally oriented flow. If, on the other hand, the ocean were closer to the strong slope regime, one would expect strongly surface-intensified isotropic flow with the dominant length scale being the deformation radius. This flow would be coupled to bottom-intensified topographic waves, continually draining energy away.

While there is good reason to expect both regimes in the ocean, several known characteristics agree with the strong slope scenario. The surface intensification of oceanic currents is well-known. Oceanic features such as warm core rings are much stronger at the surface than at depth (e.g. Joyce, 1984). However, a counter-example is that Agulhas eddies may be as much as 50% barotropic (Clement and Gordon, 1995) which suggests at least formation in a weak slope environment. Nevertheless, Wunsch (1983) notes the suppression of deep eddy kinetic energy over the mid-Atlantic ridge which certainly fits with a strong slope picture.

From altimeter data it appears that horizontal wavenumber spectra of the ocean surface are consistent with classical two-dimensional turbulence (Stammer and Boning, 1992). These authors also found that the dominant scale of eddy variability at the surface was linearly related to the first baroclinic deformation radius, again consistent with the strong slope scenario. Of interest is that their results suggested turbulence over most of the ocean, rather than just localized in the region of the western boundary current.

Lastly, as noted in Chapter 3, there are numerous observations of topographic waves on the continental slope of the eastern United States (Hogg, 1981; Smith, 1983; Pickart, 1995). These waves are bottom-intensified and radiating in from

offshore. Moreover, Pickart established a correlation between occurrences of the waves and meanders in the Gulf stream. While one must be quick to note that jet dynamics are not captured by the turbulence model, there is a strong resemblance to energy leakage in the latter to bottom topographic waves. However, one must also note that if the turbulence is *localized* (see below), both scenarios will produce radiating waves. The difference is that weak slope waves are more likely to be nearly barotropic.

Hence, while it is not possible to say the ocean "favors" one scenario, there are many observations which agree with the strong slope case. If this is so, then the deformation radius may be the upward bound on oceanic cascades. This is quite a different picture from that of Rhines (1975) in which the dominant length scale is the planetary arrest scale and the motion inevitably barotropic. Likewise it is different from the f-plane, flat-bottom flow predicted by Larichev and Held (1995) in which the dominant length scale is the domain scale and the motion again barotropic. Of course, the present work is also on the f-plane, but as described in Chapter 5, if the lower layer is inhibited from spinning up, the energy cascade to a planetary arrest or the domain scale is *blocked.*

In terms of flow over the continental shelf and slope, i.e. regions of the ocean which are well within the strong slope range, the results suggest greater variability at the surface than at the bottom. If, for instance, the relaxation of an upwelling front yields vortices, one imagines that the surface features could last long periods of time, after initially radiating waves. Likewise, the shelfbreak region could be highly variable at the surface, and eddies could persist there well after the time lower energy had been radiated away (on the time scale of order several days).

Appendix B: Geostrophic turbulence with a bottom Ekman layer

A bottom slope alters a baroclinic turbulent cascade by allowing for the dispersal of energy at depth by topographic waves essentially without removing the surface PV. A bottom Ekman layer *dissipates* energy at depth without directly altering the surface PV. To see this, consider the linear two layer equations:

$$\frac{\partial}{\partial t} q_1 = 0 \, , \tag{4.14}$$

$$\frac{\partial}{\partial t} q_2 = -R \, \nabla^2 \, \psi_2 \, . \tag{4.15}$$

The equations have two solutions, a decaying one with $q_1 = 0$ and a stationary one which carries the surface PV. Solving the bottom equation with $q_1 = 0 \rightarrow \hat{\psi}_1 = \frac{F_1}{\kappa^2 + F_1} \hat{\psi}_2$ yields:

$$\frac{\partial}{\partial t} q_2 = -\frac{R(\kappa^2 + F_1)}{(\kappa^2 + F_1 + F_2)} \psi_2 \, . \tag{4.16}$$

Thus $\psi_2 \, \alpha \, e^{-\sigma t}$ where the decay time is weakly dependent on scale, i.e. $\sigma \rightarrow \frac{R}{2}$ for long waves and $\sigma \rightarrow R$ for short waves. Note that the damping decreases the surface streamfunction too, exactly as the waves project onto ψ_1.

As the Ekman layer "acts" on the same portion of the flow as occupied by the topographic waves in the slope case, it can be exploited as an alternate way to study the effect of layer decoupling on the baroclinic cascade. In a sense, it

can be thought to mimic the loss of topographic waves to the far field. It has the advantage of having no re-entrant waves to disturb the surface vortices, and so is perhaps better suited for a doubly periodic model than a slope. Due to this latter fact, lower resolution runs were possible because the surface vortices were not sheared out by the waves.

Both weak slopes and weak bottom Ekman layers can destabilize a surface flow. Hart (1975) noted a decrease in the short-wave cut-off for vortex instability over a weak slope, and Pedlosky (1983) showed that *any* shear was unstable with a bottom Ekman layer, albeit with growth rates that depend on the scale of the motion and strength of shear. A very dissipative Ekman layer can stabilize a surface flow by defeating the growth of energy at depth. Scaling the lower layer PV equation as in Chapter 4, one finds that the ratio of the advection of thickness at depth to dissipation scales as:

$$\Lambda_R \equiv \frac{F_2 U_1 L}{R}.$$

(4.17)

This stability parameter is as in the slope case, but with R replacing $\beta_2 L$. In the cases studied in Chapter 4, the dominant length scale was the deformation radius which had a value of $\frac{1}{\sqrt{F}} = .1$. Thus one only requires R to be one-tenth the size of β_2 to obtain similar results, which in turn allows for a larger time step.

Of course, the action of dissipation is different from that of a mean PV gradient. No distinct arrest occurs with dissipation, for instance, because there is no scale-dependent change in the efficiency of the cascade. Rather energy is simply depleted at all scales of deep motion. However, the Ekman case, as another system with asymmetric layer forcing, serves as a good comparison.

A number of low resolution runs (128^2 grid points) were made with various values of R. The effects of an increasingly strong Ekman layer can be seen in plots

194

of the total energy and integrated surface potential enstrophy, shown in figure (4.27). The relation between energy and damping is not monotonic, as it would be in the barotropic case. For small values of damping, increasing R increases the rate at which energy is removed. But past a certain point, increasing R decreases the rate by inhibiting the transfer of energy to the lower layer.[8] The parameter Λ_R is order one around $R = 10$ if the dominant length scale is the deformation radius, which appears to be an appropriate dividing line in the response.

At the largest values of R, the total energy approaches the 1.5 layer curve in which no energy is lost to the lower layer. However the Ekman layer does not eliminate instability, it only inhibits it. By reasoning similar to that in Chapter 4, one may argue that interfacial motion drives motion at depth, and thus causes dissipation of energy. Therefore the total energy curves should approach the 1.5 layer case asymptotically as $R \to \infty$, but there will always be energy loss for finite values of R.

The lower plot indicates the degree of filamentation in the surface potential vorticity field. The bottom Ekman layer, by defeating barotropic motion, hinders large vortex interactions. Hence there is much less filamentation in the 1.5 layer case and in the large dissipation cases. In weaker dissipation cases this is also true initially, but then the loss is increased at later times due to later instability. However, the surface enstrophy is approximately the same for all cases with $\Lambda_R > 1$.

The mean vortex area is shown in figure (4.28). Again the vortices are found by grouping grid points with surface potential vorticity greater than a fixed threshold value (here 10). Here to there is a non-monotonic dependence on R. Weak dissipation, like the weaker bottom slopes, causes a decrease in mean area by weakening the surface flows, which favors filamentation, and by destabilizing

---

[8]A similar effect was noted with baroclinic Kelvin waves in the presence of a bottom Ekman layer in Allen (1984).
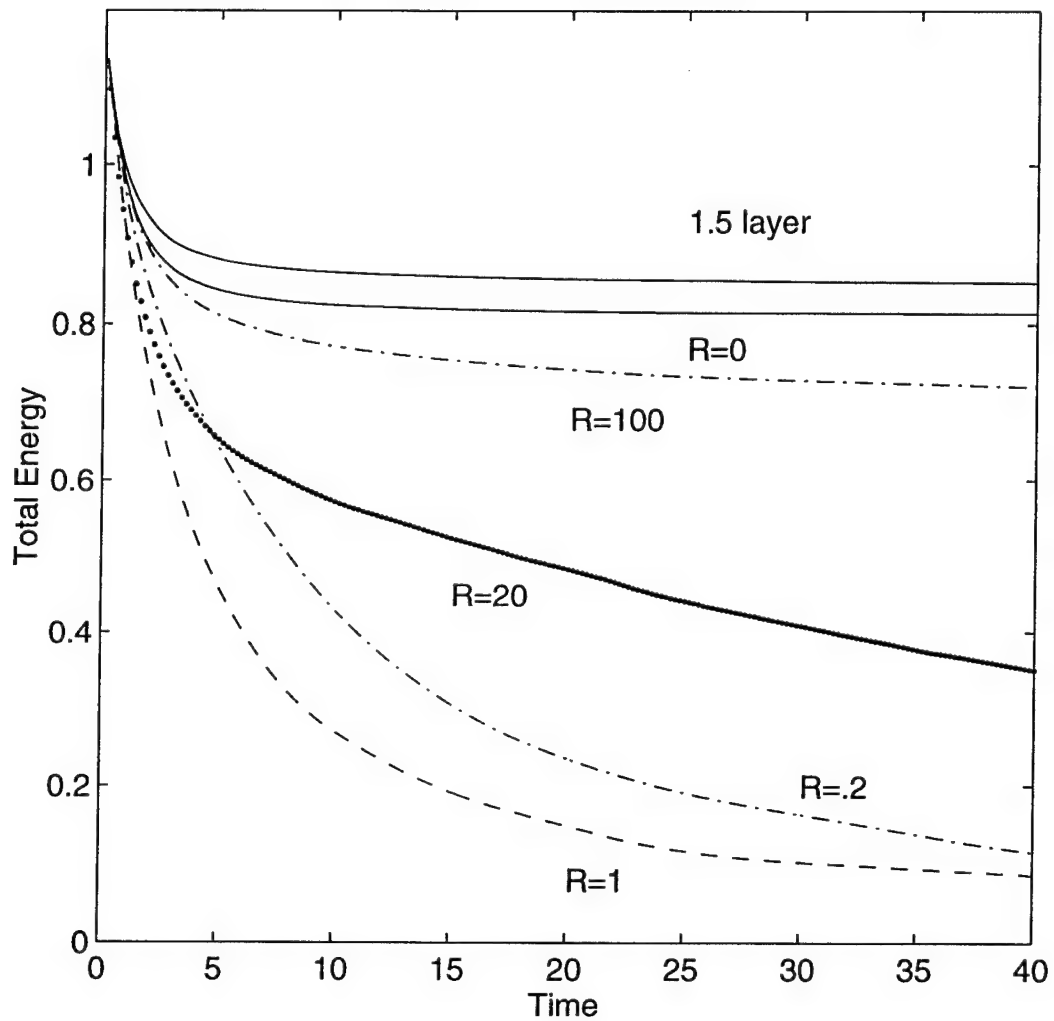
Figure 4.27: The total energy for the bottom Ekman layer cases. The total loss of energy is increased in these cases due to the lower resolution used (128^2 grid points). The two layer flat bottom case and the one and a half layer case are shown for comparison.

them by removing the deep flow. The mean area is less with slightly larger values of R because bottom dissipation occurs faster, so the surface vortices do not have time on average to grow. When $\Lambda_R < 1$ the mean area again increases, and the asymptotic limit is the 1.5 layer case. Here, filamentation is suppressed as in Polvani et al. (1991) and the vortices are ceasing to interact with vortices far away from themselves. As before, it is the defeat of the barotropic mode which is responsible for the shift. Note that the increase in mean area is then again consistent with the barotropic results of M90, suggesting mergers continue, and one observes that the number of vortices is also decreasing. A longer integration ought to show a deviation from the barotropic merger rate as deformation-scale vortices more and more cease to interact.

As mentioned above, comparing Λ and Λ_R shows that the Ekman case is like the slope case, but for the substitution $\beta_2 L \rightarrow R$ which is a change in time scales from the topographic wave period to the Ekman decay time scale. If a strong bottom slope is on the order of $100\,\beta$ and the length scale of order $10\ km$, the equivalent Ekman damping time is roughly *one day*. In other words, a strong bottom slope disperses energy at the same rate as a rather viscous bottom boundary layer. This suggests that bottom topography may provide an effective means of removing energy from the surface layer.

In summary, similar results are obtained with baroclinic turbulence and a viscous bottom Ekman layer and with a bottom slope. In one case energy is dispersed as topographic waves, and in the other it is dissipated. A stability parameter was defined, $\Lambda_R = \frac{F_2 U_1 L}{R}$, which determined the evolution. If small, active instability occurs and the surface vortices continually break into smaller ones as their lower halves are dissipated. If large, instability is hindered and vortex growth resumes, but the motion in the surface layer is sluggish due to the loss of the barotropic mode, as in the one and a half layer case.
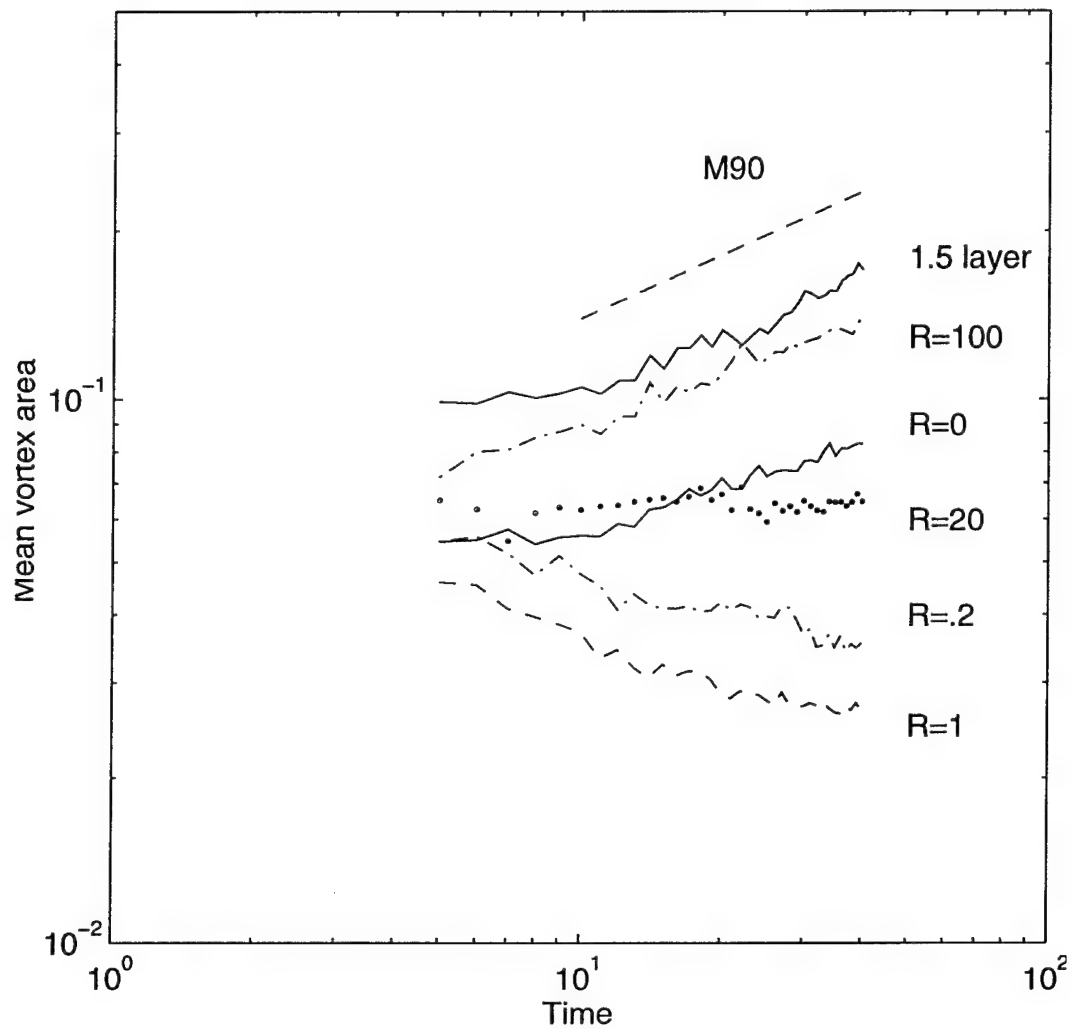
Figure 4.28: The mean areas for vortices in the Ekman cases. The vortices are elliptical groups of grid points with $q_1 \geq 10$. The dashed line is from the barotropic study of McWilliams (1990).

198

Chapter 5

Conclusions

The fundamental dynamical element which underlies the results presented is that the mean potential vorticity gradient due to bottom topography varies vertically, exerting an influence on flow at depth but not directly influencing flow at the surface. The result is that at the surface, vorticity anomalies tend to relax to a state in which the streamlines and isolines of potential vorticity coincide. These vortices are steady state solutions of the upper layer PV equation, and so may be long-lived. In contrast, vortices are not a possible steady state at depth, but will evolve and even disperse into waves under the influence of the restoring force. Thus the vertical asymmetry of the mean PV gradient translates directly into a vertical asymmetry in the character of the flow.

The case of barotropic, β-plane turbulence is a good counter-example. At small scales, the effect of β is weak and one finds vortices. However, as the inverse cascade to larger scales proceeds, the effect of β also increases, favoring waves; this is the central idea of Rhines (1975). In freely evolving turbulence, one finds that the vortices eventually all disperse when the scales become too large (McWilliams, 1984). In the (f-plane) slope case, there is no PV gradient at the surface, regardless of the size of the motion, so vortices there do not disperse. It is as if there is a co-existence between β and non-β turbulence. There are

199

other examples of spatially varying PV gradients, an example being that due to a sheared mean flow. One similarly expects to find more vortices in regions where the mean gradient is weak or vanishes; indeed, it has been suggested that the reason the Great Red Spot on Jupiter is so long-lived is that it resides in a region in which the total PV gradient vanishes (see Flierl, 1987).

The slope case is special because of the *coexistence* between the surface vortices and waves. Though vortices may be "favored" at the surface, they interact with topographic waves intensified at the bottom, and even lose energy to them. The present results are essentially just a characterization of this interaction, under various conditions.

Two advective parameters found by scaling the lower layer PV equation play central roles in both single vortex and turbulence cases. These parameters are $\frac{U_2}{\beta_2 L^2}$ and $\Lambda \equiv \frac{F_2 U_1}{\beta_2}$. The former parameter, which measures the importance of the advection of relative vorticity at depth, is more important when the motion is nearly barotropic (and thus stretching weak). When it is small, an initially barotropic vortex behaves as we expect from previous flat bottom results; the baroclinicity of the evolution depends only on whether the vortex is larger than deformation scale or not. If the parameter is large, the evolution is *always* baroclinic as the vortex breaks into surface vortex and waves.

In the turbulence case, the scale of motion changes and so then does $\frac{U_2}{\beta_2 L^2}$. The cases considered in chapter 4 had initially small scale motion, so the parameter was initially large, but decreased in time. As in the single vortex case, the flat bottom thinking applies initially; however, the scale reaches a value at which the parameter is order one at which point the flow divides again into surface vortices and waves. Due to the inverse cascade then, the flow always evolves to a baroclinic state. This baroclinic state may appear nearly barotropic if the waves are much larger than deformation scale, but there is always a baroclinic component, and surface-trapped vortices.

The second parameter, Λ, is a measure of the importance of stretching. Thus it is the more important parameter when there is little relative vorticity at depth, such as in the case of a surface-trapped flow. In the single vortex case, the size of the parameter dictated whether the surface vortex was stable or not, provided that the vortex was not immensely larger than deformation scale. In other words, a large vortex is able to relax into an axisymmetric state which is steady and stable over a strong slope.

In the turbulent case, the vortices are never perfectly steady due to the continual perturbations applied by other vortices. In this case, arguably the more general in forced systems such as the ocean, Λ determines the *rate* at which potential energy is lost from the surface layer. As in the single vortex case, if $\Lambda > 1$ then baroclinic instability is not inhibited and energy loss is as rapid as in the flat bottom case. If it is smaller than unity, instability is impeded and the energy is lost more slowly to topographic waves. The flow does not achieve barotropy in this case, but remains surface-intensified while radiating energy away.

The flow separates most naturally into the surface and bottom constituents when viewed from the perspective of *potential vorticity*. After all, the asymmetric forcing element is a PV gradient, so it follows that the effects are most clearly seen in PV. Considering the layer streamfunctions or the barotropic and baroclinic modes obscures the picture because both the vortices and waves may have non-zero flow in the opposite layers. The streamfunction perspective can then lead to a view of the flow which is more complicated than it ought to be.

Of course, the preceding discussion focusses on the f-plane case, in which there is zero background PV gradient at the surface. With the addition of the planetary β-effect, that gradient is no longer zero, and one might expect certain changes. Likewise, one wonders what modifications are required to encompass continuous stratification. Therefore two short sections are presented which discuss these additions.

5.1 Continuous Stratification

In two layers, the slope acts as a potential vorticity gradient which acts throughout the depth of the lower layer. In a continuously stratified system, the slope PV gradient is essentially a delta function at the bottom; on the f-plane then there is no gradient of PV throughout the entire water column. Therefore some changes may be expected. Here the properties of linear waves are compared to anticipate such changes.

The quasi-geostrophic equations with continuous stratification on the f-plane over a linearly sloping bottom are (e.g. Pedlosky, 1987):

$$\partial_t \partial_z \psi + J(\psi, \partial_z \psi) = 0 \quad at \ z = 0 \,, \tag{5.1}$$

$$\partial_t \bigtriangledown_3^2 \psi + J(\psi, \bigtriangledown_3^2 \psi) = 0 \,, \tag{5.2}$$

$$\partial_t \partial_z \psi + J(\psi, \partial_z \psi) + \frac{N^2}{f} \partial_y h \ \partial_x \psi = 0 \quad at \ z = -H \,, \tag{5.3}$$

where $\bigtriangledown_3^2 \psi \equiv (\bigtriangledown^2 + f^2 \partial_z (1/N^2 \partial_z))\psi$ is the potential vorticity in the interior, N^2 the Brunt-Väisälä frequency and $\partial_y h$ is the bottom slope.

Topographic waves (Rhines, 1970) are solutions to the linear version of these equations. As in the two-layer case, there are two solutions on the f-plane: a stationary solution and a propagating solution. The latter are bottom-trapped with a general solution $\psi \ \alpha \ sin(kx + ly - \sigma t)cosh(m(z + H))$ and dispersion relation:

$$\sigma = -\frac{N^2 H \ k \ \partial_y \tilde{h}}{f \ m \ tanh(m)} .$$ (5.4)

As stated, these waves have zero interior PV, so that $\nabla_3^2 \psi_w = 0$. As in the two-layer case, any flow with vorticity in the interior projects onto the stationary mode. However, as in the two layer case, the waves and interior flows may interact because the waves extend up into the water column and have a vertical height which scales with the stratification and their horizontal scale, i.e. $H \ \alpha \ \frac{fL}{N}$.

Scaling equation (5.3) with the wave period yields a single advective parameter because there is only one advective term. Assuming a single velocity scale, horizontal scale and vertical scale, the parameter is:

$$\frac{1}{S} \frac{U}{\beta_2 L^2}$$ (5.5)

where S is the Burger number $\frac{N^2 H^2}{f^2 L^2}$ and $\beta_2 \equiv \frac{f \partial_y h}{H}$ is a measure of the bottom slope. The parameter serves the dual role of $\frac{U_2}{\beta_2 L^2}$ and Λ, as can be seen by rewriting $\frac{1}{SL^2} \to F$. Note that strong stratification or small horizontal scales increases the effective slope while simultaneously yielding shorter topographic waves which are in turn less able to deform surface flows. The reduction to a single linearity parameter is perhaps the most striking difference with the two layer model, and is related to the continuous vertical variation of the density and of the interior flow. The latter implies that the importance of nonlinearity changes smoothly from surface to bottom, so that evaluating stability requires knowledge of the vertical shear. More work on the stability of continuously stratified flow over a slope is required to understand the sensitivity to the slope severity.

Lastly, unsteady surface flow in the two-layer case always drives topographic waves; the same is true under continuous stratification on the f-plane. Consider the vertical integral of the linear interior PV equation:

$$\frac{N^2}{f^2} \int_{-h}^{0} \nabla^2 \partial_t \psi \, dz \;=\; \partial_t \psi|_0 - \partial_t \psi|_{-h} = \partial_t \psi|_{-h} \,. \tag{5.6}$$

By the linear bottom boundary condition, the last term on the right-hand side is proportional to cross slope motion. Thus temporal changes in interior flow are likely to excite topographic waves which will deplete the energy of that flow.

Thus it appears the major characteristics of the adjustment on the f-plane carry over to the continuously stratified case. Vortices at the surface of the fluid could excite waves and thereby lose energy, but those waves could not deplete the vortex potential vorticity. The vertical extent of the waves also scales with horizontal extent, so long waves may disturb interior flows all the way to the surface. Likewise, unsteady motion in the interior implies wave radiation. The primary difference is that the slope PV gradient is now trapped to the slope, so that comments pertaining to surface PV anomalies now essentially apply to anomalies anywhere in the interior of the fluid, opening the possibility of long-lived, sub-surface vortex features.

5.2   Planetary β

Unlike the bottom slope, the variation of the Coriolis parameter yields a PV gradient which acts symmetrically on both vertical layers. The waves which exist with both types of gradient present are described in Rhines (1970) and in Pedlosky (1987). For simplicity, assume the topography shallows in the y direction as in the latter reference. The wave structure is found to depend on

stratification, scale and strength of the bottom slope. If the stratification is weak, the waves are essentially barotropic Rossby waves with β replaced by the sum of planetary and topographic gradients, i.e. $\beta + \beta_2$. If the slope is strong, a topographic wave much like the f-plane wave coexists with an infinite number of planetary waves which have a node at the bottom. Analogs of these waves are present in the two-layer case, presented here for comparison.

The linear QG PV equations (equal layer depths) now are:

$$\frac{\partial}{\partial t} q_1 + \beta \frac{\partial}{\partial x} \psi_1 = 0 \,, \tag{5.7}$$

$$\frac{\partial}{\partial t} q_2 + (\beta + \beta_2) \frac{\partial}{\partial x} \psi_2 = 0 \,. \tag{5.8}$$

Substituting in a wave-like solution, $\psi_i \,\alpha\, e^{ikx + ily - i\omega t}$, one obtains the dispersion relation:

$$\omega = -\frac{(2\beta + \beta_2)k}{2\kappa^2} \left(\frac{\kappa^2 + F}{\kappa^2 + 2F} \right) \pm \frac{\sqrt{\gamma}}{2\kappa^2(\kappa^2 + F)} \tag{5.9}$$

where the radical is defined as:

$$\gamma \equiv (\beta_2(4\beta + \beta_2)(\kappa^2 + F)^2 + 4\beta^2 F^2)k^2 - 4\beta\beta_2 k^2 \kappa^2 (\kappa^2 + 2F) \,. \tag{5.10}$$

In the limit of weak stratification $(F \to 0)$, the fast waves have the dispersion relation:

$$\omega = -\frac{(\beta + \beta_2)k}{\kappa^2} \tag{5.11}$$

which are barotropic Rossby waves with the combined gradients. A vortex in such an environment would translate under the combined influences of topography and β in a manner like that suggested by Smith and O'Brien (1983), i.e. in a direction between northwest and the topographic northwest. Similarly, cascading turbulence would arrest at a wavenumber proportional to the root of the sum of gradients.

In the large slope limit $(\beta_2 \gg \beta)$, there are two solutions. A "fast" bottom mode in Rhines's terminology with:

$$\omega_+ \approx -\frac{(2\beta + \beta_2)\,k}{\kappa^2}\left(\frac{\kappa^2 + F}{\kappa^2 + 2F}\right) + \frac{\beta\,k}{\kappa^2 + F} \tag{5.12}$$

which is similar to the topographic wave phase speed in the f-plane ocean. With $\omega \approx \beta_2 \gg \beta$, equation (5.7) reduces effectively to $\partial_t q_1 = 0$, so these waves again carry no surface PV. Of interest is the other mode:

$$\omega_- = -\frac{\beta\,k}{\kappa^2 + F}\,. \tag{5.13}$$

Substituting the frequency into equation (5.8), one finds:

$$\frac{i\beta F}{\kappa^2 + F}\psi_2 = 0 \rightarrow \psi_2 = 0\,. \tag{5.14}$$

206

In other words, the other mode in this case is the one and a half layer Rossby wave. This means that a vortex over a slope which radiates its lower portion away is no longer stationary, but will thereafter evolve as a one and a half layer vortex on the β plane. Such a vortex, studied by McWilliams and Flierl (1979), translates like the barotropic β vortex, but at a speed which is bounded by the baroclinic wave speeds, and slower than a barotropic vortex on the β-plane. The mechanism is what allowed the modelled Agulhas Eddy in Kamenkovich et al. (1996) to continue to translate after passing over the ridge, except in cases where topographic wave radiation depleted the surface streamfunction too severely. Note that McWilliams and Flierl (1979) found their surface-intensified vortices in two layers to approach compensation: this was due presumably to a deep lower layer and weak deep flows so that dispersal of the deep flow occurred even on the planetary β plane. A topographic slope would simply hasten the effect. In any event, the presence of β in the single vortex case yields dispersal, albeit slow, of the surface vortex.

The turbulent arrest would only be slightly altered under the addition of the planetary β-effect. In the "weak slope" case (equivalently weak stratification), a barotropic arrest should occur at a scale which derives from the sum of topographic and planetary PV gradients; if the slope is meridional, the slope either increases or decreases the scale, depending on which way the slope rises. The essential point is that a barotropic arrest is still expected. It may be that when the bottom is no longer meridional, the arrest may have unusual characteristics, because then the mean PV gradient in essence twists with depth. This would be an interesting subject for future study.

If the slope is strong, the only modification is the addition of the slow baroclinic Rossby wave mode at the surface. As noted in Chapter 4, this mode can lead to the arrest of very weak surface flows ($U_1 < 1cm/s$). But more energetic flows will either arrest at the deformation scale or undergo a barotropic arrest

over the strong slope. In other words, the diagram in figure (4.25) would only change in that the baroclinic wave mode would be added on the surface plane.

In addition, one can show that the presence of β does not change the fact that unsteady surface flow generates motion at depth. So the addition of β would also have little impact on the radiation of energy to topographic waves.

Thus the addition of a planetary PV gradient is likely to alter the overall picture only in cases when the bottom slope is weak, and substantial vertical coupling occurring. The differences may be most profound when planetary and slope gradients are non-parallel, leading to a twisting of the mean gradient with depth. Over strong topography or in cases with significant layer decoupling, the primary change is that the stationary surface mode is no longer stationary, and thus surface PV anomalies will slowly disperse to one and a half layer Rossby waves. As such, surface vortices could translate after radiating their deep flow by developing β-gyres. Cascading turbulence would change only in that weak surface flows could arrest to surface Rossby waves.

5.3   Modifications and Future Work

While there are numerous elements that could be changed or improved, I will point out a few in particular. First, the choice to consider freely evolving flows entails a choice of *initial conditions.* In the single vortex case, it was possible to consider a wide variety of initial conditions (though the barotropic and surface vortex were the primary focus). Numerical limitations resulted in a more restricted set of turbulent cases however; the choice of small scale surface flow was motivated partly by desire to clarify energy transfers and partly because the ocean is forced at the surface. However, the ocean is not forced at scales smaller than the deformation radius, but at much larger scales by the wind. In a free evolution, one expects similar results with initially large eddies or, say, an unstable

208

zonal surface current; if Λ is large, instability occurs and the large eddies break into deformation scale eddies and then cascade up to the topographic arrest scale. If Λ is small, instability is blocked, but if the surface flow is unsteady, energy is still lost to deep waves. In this case the scale of motion at the surface could feasibly exceed the deformation scale, and rather would be set by the forcing.

If the flow is *forced*, then Λ is no longer fixed because U_1 can vary. Consider a spin-up from rest. Then $\Lambda = 0$ initially, but increases as the surface spins up. If the primary sink of energy is a bottom Ekman layer, baroclinic instability must ensue to spin up the deep layer. If energy is injected slowly, it may be that a leakage of energy to topographic waves is sufficient to balance the input in which case the flow may remain in the "strong slope" regime. However, if the forcing is too intense, one expects $\Lambda \to 1$. However, even in this case the early spin-up may resemble the strong slope case in that grave zonal scales are excited. Work has been done with such systems before, but it would be useful to reconsider them in light of a spin-up. In addition, it will be interesting to examine the potential vorticity to discover whether surface vortices emerge and to determine their role.

The present study also presumes a sloping bottom and homogeneous turbulence which fill the domain. One might imagine differences with *inhomogeneous* turbulence. With a doubly periodic domain and homogeneous turbulence, energy is transferred to the wave field and the latter also shifts to larger scales. The zonal jet-like structures found in the strong slope case are made possible by periodicity. If the turbulence were inhomogeneous, the waves could simply radiate away, leaving the turbulent surface flow behind and unmolested. Recall that removing the sponge layer with the single vortex case in which $\Lambda < 1$ (Chapter 3) resulted in a zonal elongation of the vortex and a jet at depth. Perhaps with inhomogeneous turbulence, the size of Λ would simply indicate how quickly energy was lost to waves. Presumedly the turbulence would evolve to a state in which energy loss was minimized; the results in chapter 4 suggest that state may be a collection

209

of sub-deformation scale surface vortices. But the problem is more complicated because inhomogeneity can hinder cascades, as noted by Rhines (1977). Further study is certainly warranted with such a system.

Additional complexity is expected with varying topography. As noted above, the arrest might be unusual in the case when $\beta_2 \approx \beta$ but the slope not parallel to the planetary gradient. Further complications are expected when the topography is no longer a linear, domain-filling slope. The flow might be stabilized over portions of the topography and not over others, leading to "local instability" (Samelson and Pedlosky, 1994) and perhaps inhomogeneous turbulence. The observed surface variability downstream of topography in the ACC might be a manifestation of such an effect (Gille, 1995). In addition, there is the question of the development of mean flow anti-correlated with bumpy topography (Bretherton and Haidvogel, 1977; Holloway, 1978). Treguier and McWilliams (1990) have noted that such flow has a vertical scale which depends on the size of the bump, and Treguier and Hua (1987) noted that the slope of the topography was important to the spin-up of this flow, so the present work may have relevance.

With regard to the single vortex problem, it would beneficial to have a more complete linear stability theory of a surface vortex over a slope. The work would augment the Hart (1975) study by examining larger slopes. The present results suggests an interesting dependence on slope and a more subtle dependence on vortex size, and such a study would help quantify these aspects. Furthermore, one imagines that a central dependence on Λ might emerge as well.

The quasigeostrophic assumption limits accessible bottom slopes, as stated in Chapter 2. Therefore it is reasonable to wonder what would happen over more realistically large slopes. For instance, the cold core ring observed by Cheney and Richardson (1974) moved over the steep Blake escarpment into water which was as deep as the left-over surface vortex. As such, the topography essentially introduces a change in geometry to which the vortex must adjust. How would the

210

vertical structure change under such a change? Perhaps the vortex would become even more surface-trapped, such as the extremely shallow anticyclone observed over the California shelf by Washburn et al. (1993). As stated before, the observations of Largier et al. (1993) suggest variability over the California shelf which appears to have characteristics of the offshore eddies. Further observational work correlating offshore flow with shelf flows is definitely of interest.

Finally, the results of Chapter 4 and Appendix B suggest that topography may be an effective means of transporting energy put in by the wind on the gyre scale away from energetic regions to more quiescent regions. The observations of Hogg (1981), Smith (1983), Pickart (1995) and others suggest that topographic wave radiation may be driven by the unstable Gulf Stream. One wonders to what extent the waves carry away energy from the region, permitting dissipation elsewhere.

The present work suggests an ocean with topography might behave quite differently from one with a flat bottom. The alteration or even suppression of the barotropic mode by topography is the most serious aspect. If this occurs over substantial portions of the ocean, it may be necessary to rethink some of our notions about oceanic circulation.

REFERENCES

Adem, J. 1956 A series solution for the barotropic vorticity equation and its application in the study of atmospheric vortices. *Tellus*, **8**, 364-372.

Allen, J.S. 1984 A simple model for stratified shelf flow fields with bottom friction. *J. Phys. Oceanogr.*, **14**, 1200-1214.

Babiano, A., Basdevant, C., Legras, B. and Sadourny, R. 1987 Vorticity and passive-scalar dynamics in two-dimensional turbulence. *J. Fluid Mech.*, **183**, 379-397.

Basdevant, C., Legras, B., Sadourny, R. and Beland, M. 1981 a study of barotropic model flows: intermittency, waves and predictability. *J. Atmos. Sci.*, **38**, 2305-2326.

Batchelor, G.K. 1953 *The theory of homogeneous turbulence.* Cambridge University Press. 121 pp.

Batchelor, G.K. 1969 Computation of the energy spectrum in homogeneous two-dimensional turbulence. *Phys. Fluids Supp. II*, **12**, 233-239.

Benzi, R., Paladin, G., Patarnello, S., Santangelo, P. and Vulpiani, A. 1986 Intermittency and coherent structures in two-dimensional decaying turbulence. *J. Phys. A: Math. Gen.*, **19**, 3771-3784.

Benzi, R., Patarnello, S. and Santangelo, P. 1988 Self-similar coherent structures in two-dimensional turbulence. *J. Phys. A: Math. Gen.*, **21**, 1221-1237.

Bretherton, F. B. and Haidvogel, D. 1976 Two-dimensional turbulence over topography. *J. Fluid Mech.*, **78**, 129-154.

Canuto, C., Hussaini, M.Y., Quarteroni, A. and Zang, T.A. 1988 *Spectral methods in fluid mechanics.* Springer-Verlag. 567 pp.

Carnevale, G. F., Kloosterziel, R. C. and van Heijst, G. J. F. 1991a Propagation of barotropic vortices over topography in a rotating tank. *J. Fluid Mech.*, **233**, 119-140.

Carnevale, G.F., McWilliams, J.C., Pomeau, Y., Weiss, J.B. and Young, W.R. 1991b *Phys. Rev. Lett.*, **66**, 2735-2737.

Carton, X. 1989 In *Mesoscale/Synoptic Coherent Structures in Geophysical Turbulence* (Nihoul and Jamart, eds.), Elsevier.

Chan, J. C.-L. and Williams, R.T. 1987 Analytical and numerical studies of the beta-effect in tropical cyclone motion. Part I: Zero mean flow. *J. Atmos. Sci.*, **44**, 1257-1265.

Chapman, D.C. and Brink, K.H. 1987 Shelf and slope circulation induced by fluctuating offshore forcing. *J. Geophys. Res.***92**, 11741-11759.

Charney, J.G. 1971 Geostrophic Turbulence. *J. Atmos. Sci.*, **28**, 1087-1095.

Cheney, R. E. and Richardson, P. L. 1976 Observed decay of a cyclonic Gulf Stream ring. *Deep-Sea Res.*, **23**, 143-155.

Clement, A. C. and Gordon, A.L. 1995 The absolute velocity field structure of Agulhas eddies and the Benguela Current. *J. Geophys. Res.*, **100**, 22591-22601.

Davis, R.E. 1985 Drifter observations of coastal surface currents during CODE: The statistical and dynamical views. *J. Geophys. Res.*, **90**, 4756-4772.

Dewar, W.K. and Gailliard, C. 1994 The dynamics of barotropically dominated rings. *J. Phys. Oceanogr.*, **24**, 5-29.

Dickinson, R.E. and F.J. Clare 1973 Numerical study of the unstable modes of a hyperbolic-tangent barotropic shear flow. *J. Atmos. Sci.*, **30**, 1035-1049.

Faller, A.J. and von Arx, W.S. 1955 On the variation of the Coriolis parameter and its simulation in models of ocean circulation. Woods Hole Oceanographic Institution Technical Report, WHOI-55-13.

Ferrel, W. 1859 The motion of fluids and solids relative to the earth's surface. *Math. Mon.*, **1**, 300-307.

Fiorini, M. and Elsberry, R.L. 1989 Some aspects of vortex structure related to tropical cyclone motion. *J. Atmos. Sci.*, **46**, 975-990.

Fjortoft, R. 1953 On the changes in the spectral distribution of kinetic energy for two-dimensional non-divergent flow. *Tellus*, **5**, 225-230..

Flierl, G.R. 1977 The application of linear quasigeostrophic dynamics to Gulf Stream rings. *J. Phys. Oceanogr.*, **7**, 365-379.

Flierl, G.R., Larichev, V.D., McWilliams, J.C. and Reznik, G.M. 1980 The dynamics of baroclinic and barotropic solitary eddies. *Dyn. Atmos. Oceans*, **5**, 1-41.

Flierl, G.R., Stern, M.E. and Whitehead, J.A. 1983 The physical significance of modons: laboratory experiments and general constraints. *Dyn. Atmos. Oceans*, **7**, 233-263.

Flierl, G.R. 1987 Isolated eddy models in geophysics. *Ann. Rev. Fluid Mech.*, **19**, 493-530.

Flierl, G.R. 1988 On the instability of geostrophic vortices. *J. Fluid Mech.*, **197**, 349-388.

Frisch, U., Sulem, P.L. and Nelkin, M. 1978 A simple dynamical model of intermittent fully developed turbulence. *J. Fluid Mech.*, **87**, 719-736.

Gent, P.R. and McWilliams, J.C. 1986 The instability of barotropic circular vortices. *Geophys. Astrophys. Fluid Dyn.*, **35**, 209-233.

Gill, A.E. 1968 A linear model of the Antarctic Circumpolar Current. *J. Fluid Mech.*, **32**, 465-488.

Gill, A.E., Green, J.S.A. and Simmons, A.J. 1974 Energy partition in the large-scale ocean circulation and the production of mid-ocean eddies. *Deep-Sea Res.*, **21**, 499-528.

Gille, S.T. 1995 Dynamics of the Antarctic Circumpolar Current: evidence for topographic effects from altimeter data and numerical model output. Ph.D. Thesis, M.I.T./W.H.O.I. Joint Program in Oceanography. 216 pp.

Griffiths R.W. and Linden, P.F. 1981 The stability of vortices in a rotating stratified fluid. *J. Fluid Mech.*, **117**, 343-377.

Grimshaw, R., Broutman, D., He, X., and Sun, P. 1994 Analytical and numerical study of a barotropic eddy on a topographic slope. *J. Phys. Oceanogr.*, **24**, 1587-1607.

Haidvogel, D.B. and Held, I. M. 1981 Homogeneous quasigeostrophic turbulence driven by a uniform temperature gradient. *J. Atmos. Sci.*, **37**, 2644-2660.

Hart, J.E. 1975 Baroclinic instability over a slope. Part I: Linear theory. *J. Phys. Oceanogr.***5**, 625-633.

Haustein, J.R. 1981 The effect of shoaling bottom topography on the dynamics of the Gulf Stream cyclonic rings. Ph.D. Thesis, Texas A&M University. 254 pp.

Helfrich, K.R. and Send, U. 1988 Finite-amplitude evolution of two-layer geostrophic vortices. *J. Fluid Mech.*, **197**, 331-348.

Herring, J.R. 1977 On the statistical theory of two-dimensional topographic turbulence. *J. Atmos. Sci.*, **34**, 1731-1750.

Hogg, N.G. 1981 Topographic waves along 70°W on the continental rise. *J. Marine Res.*, **39**, 627-649.

Hogg, N.G. and Stommel, H. M. 1985 The heton, an elementary interaction between discrete baroclinic geostrophic vortices, and its implications concerning eddy heat-flow. *Proc. R. Soc. Lond. A*, **37**, 1-20.

Holloway, G. 1978 A spectral theory of nonlinear barotropic motion above irregular topography. *J. Phys. Oceanogr.*, **8**, 414-427.

Ikeda, M. 1981 Instability and splitting of mesoscale rings using a two-layer quasigeostrophic model on an f-plane. *J. Phys. Oceanogr.*, **11**, 987-998.

Joyce, T.M. 1983 Velocity and hydrographic structure of a Gulf Stream warm-core ring. *J. Phys. Oceanogr.*, **14**, 936-947.

Joyce, T.M. and Kennelly, M.A. 1985 Upper-ocean velocity structure of Gulf Stream Warm-core ring 82B. *J. Geophys. Res.*, **90**, 8839-8844.

Kamenkovich, I. V. and Pedlosky, J. 1996 Radiating instability of nonzonal ocean currents. *J. Phys. Oceanogr.*, **26**, 622-643.

Kamenkovich, V. M., Leonov, Y.P., Nechaev, D.A., Byrne, D.A. and Gordon, A. L. 1996 On the influence of bottom topography on the Agulhas Eddy. *J. Phys. Oceanogr.*, **26**, 892-912.

Kloosterziel, R.C. and Heijst, G.J.F. van 1991 An experimental study of unstable barotropic vortices in a rotating fluid. *J. Fluid Mech.*, **233**, 1-24.

Kraichnan, R. 1967 Inertial ranges in two-dimensional turbulence. *Phys. Fluids*, **10**, 1417-1423.

Kraichnan, R. 1971 Inertial range transfer in two- and three-dimensional turbulence. *J. Fluid Mech.*, **47**, 525-535.

Larichev, V.D. and Held, I.M. 1995 Eddy amplitudes and fluxes in a homogeneous model of fully developed baroclinic instability. *J. Phys. Oceanogr.*, **25**, 2285-2297.

Largier, J.L., Magnell, B.A., and Winant, C.D. 1993 Subtidal circulation over the Northern California shelf. *J. Geophys. Res.*, **98**, 18147-18180.

Lewis, J.K. and Kirwan, A.D. Jr. 1985 Some observations of ring-topography and ring-ring interactions in the Gulf of Mexico. *J. Geophys. Res.*, **90**, 9017-9028.

Louis, J.P. and P.C. Smith 1982 The development of the barotropic radiation field of an eddy over a slope. *J. Phys. Oceanogr.*, **12**, 56-73.

Malanotte-Rizzoli, P., Hogg, N.G. and Young, R.E. 1995 Stochastic wave radiation by the Gulf Stream: numerical experiments. *Deep-Sea Res.*, **42**, 389-423.

Maltrud, M.E. and Vallis, G.K. 1991 Energy spectra and coherent structures in forced two-dimensional and beta-plane turbulence. *J. Fluid Mech.*, **228**, 321-342.

Mandelbrot, B. 1974 Intermittent turbulence in self-similar cascades: divergence of high moments and dimension of the carrier. *J. Fluid Mech.*, **62**, 331-359.

Mariotti, A., Legras, B., and Dritschel, D. 1994 Vortex stripping and the erosion of coherent structures in two-dimensional flows. *Phys. Fluids*, **6**, 3954-3962.

McWilliams, J.C. and Flierl, G.R. 1979 On the evolution of isolated, nonlinear vortices. *J. Phys. Oceanogr.*, **9**, 1155-1182.

McWilliams, J.C. 1984 The emergence of isolated coherent vortices in turbulent flow. *J. Fluid Mech.*, **146**, 21-43.

McWilliams, J.C. and Gent, P.R. 1986 The evolution of sub-mesoscale, coherent vortices on the beta-plane. *Geophys. Astrophys. Fluid Dyn.*, **35**, 235-255.

McWilliams, J.C. 1990a The vortices of two-dimensional turbulence. *J. Fluid Mech.*, **219**, 361-385.

McWilliams, J.C. 1990b The vortices of geostrophic turbulence. *J. Fluid Mech.*, **219**, 387-404.

Mied, R. and Lindemann, G.J. 1979 The propagation and evolution of cyclonic Gulf Stream rings. *J. Phys. Oceanogr.*, **9**, 1183-1206.

Mory, M., Stern, M.E. and Griffiths, R.W. 1987 Coherent baroclinic eddies on a sloping bottom. *J. Fluid Mech.*, **183**, 45-62.

Nof, D. 1983 The translation of isolated cold eddies on a sloping bottom. *Deep-Sea Res.*, **30**, 171-182.

Olson, D.B., Schmitt, R., Kennelly, M. and Joyce, T. 1985 Two-layer diagnostic model of the long-term physical evolution of warm-core ring 82 B. *J. Geophys. Res.*, **90**, 8813-8822.

Olson, D.B. and Evans, R.H. 1986 Rings of the Agulhas Current. *Deep-Sea Res.*, **33**, 27-42.

Onsager, L. 1949 Statistical hydrodynamics. *Nuovo Cimento*, **6**, Suppl. 6, 279-287.

Owens, W.B. and Bretherton, F. P. 1978 A numerical study of mid-ocean mesoscale eddies. *Deep-Sea Res.***25**, 1-14.

Pankratov, K.K. 1994 Influence of topography on the dynamics of baroclinic oceanic eddies. Ph.D. Thesis, M.I.T./W.H.O.I. Joint Program in Oceanography. 189 pp.

Patterson, G.S. and Orszag, S.A. 1971 Spectral calculations of isotropic turbulence: efficient removal of aliasing interactions. *Phys. Fluids*, **14**, 2538-2541.

Pedlosky, J. 1983 The growth and decay of finite-amplitude baroclinic waves. *J. Atmos. Sci.*, **40**, 1863-1876.

Pedlosky, J. 1985 The instability of continuous heton clouds. *J. Atmos. Sci.*, **42**, 1477-1486.

Pedlosky, J. 1987 *Geophysical Fluid Dynamics*, Springer-Verlag, 710 pp.

Pickart, R. S. 1995 Gulf Stream-generated topographic Rossby waves. *J. Phys. Oceanogr.*, **25**, 574-586.

Polvani, L.M., Zabusky, N.J. and Flierl, G.R. 1989 Two-layer geostrophic V-states and merger. 1. Constant potential vorticity lower layer. *J. Fluid Mech.*, **205**, 215-242.

Polvani, L.M. 1991 Two-layer geostrophic vortex dynamics. Part 2. Alignment and two-layer V-states. *J. Fluid Mech.*, **225**, 241-270.

Polvani, L.M., McWilliams, J.C., Spall, M.A. and Ford, R. 1994 The coherent structures of shallow-water turbulence: Deformation-radius effects, cyclone/anticyclone asymmetry and gravity-wave generation. *Chaos*, **4**(2), 177-186.

Qui, B. 1990 Low-frequency shelf-slope response induced by localized offshore forcing. *J. Geophys. Res.*, **95**, 9447-9459.

Reznik, G. M. and Dewar, W. K. 1994 An analytical theory of distributed axi-symmetric barotroic vortices on the beta-plane. *J. Fluid Mech.*, **269**, 301-321.

Rhines, P.B. 1970 Edge-, bottom- and Rossby waves in a rotating, stratified fluid. *Geophys. Fluid Dyn.*, **1**, 273-302.

Rhines, P.B. 1975 Waves and turbulence on a beta-plane. *J. Fluid Mech.*, **69**, 417-443.

Rhines, P. 1977 the dynamics of unsteady currents. *The Sea*, vol. 6, Interscience, 189-318.

Richardson, P.L., Hufford, G.E. and Limeburner, R. 1994 North Brazil Current retroflection eddies. *J. Geophys. Res.*, **99**, 5081-5093.

Rossby, C. G. 1948 On the displacement and intensity change of atmospheric vortices. *J. Marine Res.*, **7**, 175-187.

Salmon, R. 1978 Two-layer quasigeostrophic turbulence in a simple special case. *Geophys. Astrophys. Fluid Dyn.*, **10**, 25-52.

Salmon, R. 1980 Baroclinic instability and geostrophic turbulence. *Geophys. Astrophys. Fluid Dyn.*, **15**, 167-211.

Samelson, R.M. and Pedlosky, J. 1994 Local baroclinic instability of flow over variable topography. *J. Fluid Mech.*, **221**, 411-436.

Santengelo, P., Benzi, R. and Legras, B. 1989 The generation of vortices in high-resolution, two-dimensional decaying turbulence and the influence of initial conditions on the breaking of self-similarity. *Phys. Fluids A*, **1**, 1027-1034.

Saunders, P.M. 1973 The instability of a baroclinic vortex. *J. Phys. Oceanogr.*, **3**, 61-65.

Shaw, P.T. and Divakar, S. 1991 Generation of topographic waves over the continental margin. *J. Phys. Oceanogr.*, **21**, 1032-1042.

Shepherd,T.G. 1987 Rossby waves and two-dimensional turbulence in a large-scale zonal jet. *J. Fluid Mech.*, **183**, 467-509.

Smith IV, D.C. and O'Brien, J.J. 1983 The interaction of a two-layer isolated mesoscale eddy with bottom topography. *J. Phys. Oceanogr.*, **13**, 1681-1697.

218

Smith IV, D.C. 1987 A numerical study of Loop Current eddy interaction with topography in the Western Gulf of Mexico. *J. Phys. Oceanogr.*, **16**, 1260-1272.

Smith, P. 1983 Eddies and coastal interactions. In *Eddies in Marine Science* (Robinson, ed.), Springer-Verlag. 609 pp.

Stammer, D. and Boning, C.W. 1992 Mesoscale variability in the Atlantic Ocean from Geosat Altimetry and WOCE high-resolution numerical modelling. *J. Phys. Oceanogr.*, **22**, 732-752.

Sutyrin, G.G. and Flierl, G.R. 1994 Intense vortex motion on the beta plane: Development of the beta gyres. *J. Atmos. Sci.*, **51**, 773-790.

Talley, L.D. 1983 Radiating barotropic instability. *J. Phys. Oceanogr.*, **13**, 972-987.

Thompson, R.O.R.Y. and Luyten, J.R. 1976 Evidence for bottom-trapped topographic Rossby waves from single moorings. *Deep-Sea Res.*, **23**, 629-635.

Treguier, A.M. and Hua, B.L. 1988 Influence of bottom topography on stratified quasigeostrophic turbulence in the ocean. *Geophys. Astrophys. Fluid Dyn.*, **43**, 265-305.

Vallis, G.K. and Maltrud, M.E. 1994 Generation of mean flows and jets on a beta-plane and over topography. *J. Phys. Oceanogr.*, **24**, 2305-2326.

van Ballegooyen, R.C., Grundlingh, M.L. and Lutjeharms, D. 1994 Eddy fluxes of heat and salt from the southwest Indian Ocean into the southeast Atlantic Ocean:a case study. *J. Geophys. Res.*, **99**, 14053-14070.

Vidal, V.M.V., Vidal, F.V. and Perez-Molero, J.M. 1994 Collision of a Loop Current anticyclone ring against the continental shelf-slope of the western Gulf of Mexico. *J. Geophys. Res.*, **99**, 2155-2172.

Wang, X. 1992 Interaction of an eddy with a continental slope. Ph.D. Thesis, M.I.T./W.H.O.I. Joint Program in Oceanography. 216 pp.

Warren, B.A. 1967 Notes on translatory movement of rings of current with application to Gulf Stream eddies. *Deep-Sea Res.*, **14**, 505-524.

Washburn, L., Swenson, M.S., Largier, J.L., Kosro, P.M. and Ramp, S. 1993 Cross-shelf sediment transport by an anticyclonic eddy off northern california. *Science*, **261**, 1560-1564.

Weiss, J.B. and McWilliams, J.C. 1993 Temporal scaling behavior of two-dimensional turbulence. *Phys. Fluids A*, **5**, 608-621.

Whitehead, J.A., Stern, M.E., Flierl, G.R. and Klinger, B.A. 1990 Experimental observations of baroclinic eddies on a sloping bottom. *J. Geophys. Res.*, **95**, 9585-9610.

Williams, G.P. 1978 Planetary circulations: I, Barotropic representation of Jovian and terestial turbulence. *J. Atmos. Sci.*, **35**, 1399-1426.

Willoughby, H.E. 1994 Nonlinear motion of a shallow water barotropic vortex. *J. Atmos. Sci.*, **24**, 3722-3744.

Winant, C.D., Beardsley, R.C. and Davis, R.E. 1987 Moored wind, temperature, and current observations made during Coastal Ocean Dynamics Experiments 1 and 2 over the northern California continental shelf and upper slope. *J. Geophys. Res.*, **92**, 1569-1604.

Wunsch, C. 1983 Western Atlantic Interior. In *Eddies in Marine Science* (Robinson, ed.), Springer-Verlag. 609 pp.

DOCUMENT LIBRARY

Distribution List for Technical Report Exchange – February 1996

University of California, San Diego
SIO Library 0175C
9500 Gilman Drive
La Jolla, CA 92093-0175

Hancock Library of Biology & Oceanography
Alan Hancock Laboratory
University of Southern California
University Park
Los Angeles, CA 90089-0371

Gifts & Exchanges
Library
Bedford Institute of Oceanography
P.O. Box 1006
Dartmouth, NS, B2Y 4A2, CANADA

Commander
International Ice Patrol
1082 Shennecossett Road
Groton, CT 06340-6095

NOAA/EDIS Miami Library Center
4301 Rickenbacker Causeway
Miami, FL 33149

Research Library
U.S. Army Corps of Engineers
Waterways Experiment Station
3909 Halls Ferry Road
Vicksburg, MS 39180-6199

Institute of Geophysics
University of Hawaii
Library Room 252
2525 Correa Road
Honolulu, HI 96822

Marine Resources Information Center
Building E38-320
MIT
Cambridge, MA 02139

Library
Lamont-Doherty Geological Observatory
Columbia University
Palisades, NY z10964

Library
Serials Department
Oregon State University
Corvallis, OR 97331

Pell Marine Science Library
University of Rhode Island
Narragansett Bay Campus
Narragansett, RI 02882

Working Collection
Texas A&M University
Dept. of Oceanography
College Station, TX 77843

Fisheries-Oceanography Library
151 Oceanography Teaching Bldg.
University of Washington
Seattle, WA 98195

Library
R.S.M.A.S.
University of Miami
4600 Rickenbacker Causeway
Miami, FL 33149

Maury Oceanographic Library
Naval Oceanographic Office
Building 1003 South
1002 Balch Blvd.
Stennis Space Center, MS, 39522-5001

Library
Institute of Ocean Sciences
P.O. Box 6000
Sidney, B.C. V8L 4B2
CANADA ·

National Oceanographic Library
Southampton Oceanography Centre
European Way
Southampton SO14 3ZH
UK

The Librarian
CSIRO Marine Laboratories
G.P.O. Box 1538
Hobart, Tasmania
AUSTRALIA 7001

Library
Proudman Oceanographic Laboratory
Bidston Observatory
Birkenhead
Merseyside L43 7 RA
UNITED KINGDOM

IFREMER
Centre de Brest
Service Documentation - Publications
BP 70 29280 PLOUZANE
FRANCE

50272-101

REPORT DOCUMENTATION PAGE	1. REPORT NO. MIT/WHOI 97-03	2.	3. Recipient's Accession No.

4. Title and Subtitle
Baroclinic Vortices Over a Sloping Bottom

5. Report Date
September 1996

6.

7. Author(s)
Joseph H. LaCasce, Jr.

8. Performing Organization Rept. No.

9. Performing Organization Name and Address

MIT/WHOI Joint Program in Oceanography/Applied Ocean Science & Engineering

10. Project/Task/Work Unit No.
MIT/WHOI   97-03

11. Contract(C) or Grant(G) No.
(C)   N00014-92-J-1643
(G)   N00014-92-J-1528

12. Sponsoring Organization Name and Address

Office of Naval Research

13. Type of Report & Period Covered
Ph.D. Thesis

14.

15. Supplementary Notes
This thesis should be cited as: Joseph H. LaCasce, Jr., 1996. Baroclinic Vortices Over a Sloping Bottom. Ph.D. Thesis. MIT/WHOI, 97-03.

16. Abstract (Limit: 200 words)

Nonlinear quasigeostrophic flows in two layers over a topographic slope are considered. The evolution depends on the size of two parameters which indicate the degree of nonlinearity at depth. The first measures the importance of relative vorticity advection and the second of stretching vorticity.

Two types of isolated vortex are used to examine the parameter dependence. An initially barotropic vortex remains barotropic only when the first parameter is large, otherwise topographic waves dominate at depth. An initially surface-trapped vortex larger than deformation scale is baroclinically unstable when the second is large, but is stabilized by the slope otherwise.

Both parameters are also relevant to cascading geostrophic turbulence. If the stretching parameter is large, a "barotropic cascade" occurs at the deformation radius (Rhines, 1977) and the cascade "arrests" when the relative vorticity parameter is order unity. If small, layer coupling is hindered and the cascade is arrested at the deformation scale, with the flow dominated by isotropic surface vortices.

In both cases, the distinction between vortices and waves is transparent when viewing potential vorticity. It is more difficult to identify waves and vortices from the streamfunction fields, because the waves are present in both layers.

17. Document Analysis   **a. Descriptors**

quasigeostrophy
vortex
turbulence

b. Identifiers/Open-Ended Terms

c. COSATI Field/Group

18. Availability Statement	19. Security Class (This Report) UNCLASSIFIED	21. No. of Pages 224
Approved for publication; distribution unlimited.	20. Security Class (This Page)	22. Price

(See ANSI-Z39.18)   *See Instructions on Reverse*   OPTIONAL FORM 272 (4-77)
(Formerly NTIS-35)
Department of Commerce